POSTSYNTHETIC CONTROL OF FUNCTIONALITY AND POROSITY IN METAL-ORGANIC FRAMEWORKS USING COVALENT, COORDINATIVE, AND ELECTROSTATIC INTERACTIONS

by

Chong Liu

B.S., Tsinghua University, 2006

Submitted to the Graduate Faculty of the

Kenneth P. Dietrich School of Arts and Sciences

in partial fulfillment

of the requirements for the degree of

Doctor of Philosophy

University of Pittsburgh

2016

UNIVERSITY OF PITTSBURGH

Kenneth P. Dietrich School of Arts and Sciences

This dissertation was presented

by

Chong Liu

It was defended on

June 23rd, 2016

and approved by

Haitao Liu, PhD, Assistant Professor, Department of Chemistry

Tara Y. Meyer, PhD, Associate Professor, Department of Chemistry

Rongchao Jin, PhD, Professor, Department of Chemistry, Carnegie Mellon University

Dissertation Advisor: Nathaniel L. Rosi, PhD, Professor, Department of Chemistry

POSTSYNTHETIC CONTROL OF FUNCTIONALITY AND POROSITY IN METAL-ORGANIC FRAMEWORKS USING COVALENT, COORDINATIVE, AND ELECTROSTATIC INTERACTIONS

Chong Liu, PhD

University of Pittsburgh, 2016

Metal-organic frameworks (MOFs) are a versatile family of hybrid materials. Research attention and industrial interest have focused on MOFs because of their diverse properties and their tunable host-guest interactions/chemistry. MOFs are intrinsically porous, and the porosity underlies many of their properties and applications. Methods for systematically controlling MOF porosity and functionality provide a gateway to new frontiers of MOF research. In this dissertation, I present four research projects aimed at fine-tuning MOF porosity and functionality in order to create materials with functionally- and structurally-complex pore environments.

Specifically, in Chapter 2, a versatile and nearly quantitative method is presented to covalently modify MOFs, especially mesoporous MOFs, with organic and biological molecules via strain-promoted click chemistry. In Chapter 3, a sequential postsynthetic ligand exchange protocol is presented for introducing up to three orthogonal functional groups into the MOF pore space. Subsequently, a new fluorescence-based method is implemented to experimentally reveal the macroscopic distribution of functional groups within individual MOF crystals by introducing fluorophore and quencher molecules. In Chapter 4, construction of porosity gradients within individual mesoporous MOF crystals via ligand exchange-based partial pore expansion is described. The product MOF crystals, bearing a hierarchical distribution of domains having differential porosity, are used to organize nano-sized molecules in a heterogeneous fashion. In

Chapter 5, a series of isoreticular rare earth MOFs having the well-known *fcu* topology is introduced. Based on their anionic nature, cation exchange experiments are applied to incorporate chromophore guest molecules. One of the incorporated dye compounds is used as an antenna molecule to sensitize Yb^{3+} in the MOF.

The research described represents a significant step forward in the development of MOF chemistry and will enable new studies that focus on using MOFs as platform materials for precisely organizing complex molecules and nanoscale materials in three-dimensional space.

TABLE OF CONTENTS

LIST OF TABLES

LIST OF FIGURES

PREFACE

ACKNOWLEDGEMENTS

Graduate school seemed to me like a very long but unknown journey with a lot of myths to be discovered when I first arrived in Pittsburgh, and now, my dissertation is almost complete. I am grateful for the start of this expedition, I am also grateful for the finish of it, particularly I am grateful to have lived through every precious moment of endurance, excitement, and even disappointment from time to time. I have grown both as a scientist and as an individual along the way. I believe it is the one of the best and most important decisions I have ever made, coming to Pitt and joining Professor Rosi's group.

With that, I want to express my deepest gratitude to my PhD advisor, Professor Nathaniel L. Rosi. Through his keen and creative scientific vision, encouraging and passionate work ethic, great attention to details and unyielding insistence of the highest quality, Professor Rosi has been an inspirational leader and mentor to me. I am grateful for his guidance, support, trust, friendship, and so many other things.

I am also grateful to have three outstanding scientists as my PhD committee members: Professor Tara Y. Meyer, Professor Haitao Liu, and Professor Rongchao Jin. I have benefited from their insightful counsel, some of which from the very beginning of my graduate study.

I have enjoyed the company of all the past and present colleagues and friends in the Rosi group. I extend my warmest gratitude to these people who have always selflessly helped me in many ways in all aspects of life: Dr. Kristy Gogick, Dr. Leekyoung Hwang, Dr. Tao Li, Tianyi Luo, Andre Merg, Patrick Muldoon, Soumitra Punekar, Ryan Ruenroeng, Jessica Sammons, Dr. Chengyi Song, Alex Spore, Dr. Chen Zhang, Yicheng Zhou.

I am lucky to have participated in several collaborative projects in which I have learned a lot from many amazing scientists with diverse backgrounds. To Chenjie Zeng, Yuxiang Chen, Dr. Anindita Das, Tatsuya Higaki, Renxi Jin, Shuxin Wang, Dr. Gao Li, Evan S. Feura, Emily A. Eikey, Dr. Svetlana V. Eliseeva, Dr. Hasan Babaei, Minyoung Jeong, Dr. Christopher M. Andolina, James E. Ellis, Jo Erika Narciso, and many others, I appreciate the opportunities to have worked with each and every one of you and am glad that our team efforts have or will come to fruition.

I have grown from a first-year graduate student who knew little about the powerful tool of X-ray diffraction to a fairly experienced crystallographer today, for which I want to thank Dr. Steven J. Geib for his guidance and assistance. I want to thank Dr. Susheng Tan at the Nanoscale Fabrication & Characterization Facility for his assistance on many techniques, including PXRD, Microspectrophotometry, and FTIR. I also want to thank Dr. Bhaskar Godugu for training and help with various MS techniques.

I am honored to have received a University of Pittsburgh School of Arts and Sciences Fellowship, a Graduate Excellence Fellowship, and a Safford Award for Excellence as a Graduate Student Teacher. I am especially honored to have worked with Dr. Ericka Huston in the preparation and revision of Organic Chemistry I Laboratory Manual which has been used by many students at Pitt.

Additionally, I gratefully acknowledge my friends outside of lab, namely Shaopeng Zhang, Feng Lang, Dong Wang, Dr. Zhiting Li, for their help and, as simple as, their presence.

Finally and most importantly, I thank my family. I could not have gotten this far if it were not for the continuous encouragement and genuine interest in my pursuits from my mom, Hong Li and my dad, Liu Guizhong. As their only child, I hope I could present this dissertation as a tribute to them to express my eternal gratitude for their everlasting contribution and sacrifices. My wife, Wang Disi, as a professional graphic designer and illustrator, has been an invaluable contributor and a trustworthy authority in the scientific figures and general aesthetic aspect of all my work. But more importantly, every day she has been supportive and understanding to the highest extent, for I may not have always been the most considerate person during these busy PhD days. With her standing by me, I feel genuinely happy and fueled (both literally and figuratively) to tackle the challenges I constantly face. Marrying her in 2014 is certainly going to be one of the highlights of my graduate life when I look back in years to come.

For the memories that do not dissolve

1.0 INTRODUCTION

1.1 METAL-ORGANIC FRAMEWORKS

Composite materials have different constituents organized together, which often leads to the emergence of new collective properties. Similar to common examples of complex systems such as organisms, it is the interaction between different constituents in multi-component composite materials that imparts properties beyond what can be expected within single-component materials. Therefore, much effort has been invested in studying composite materials, aiming to adjust and exploit desirable properties.

Hybrid materials are defined as composites organized on a nanometer or even molecular scale that push the control of constituent organization to the chemical limit.[1] Metal-organic frameworks (MOFs) have emerged as an important class of hybrid materials.[2-7] As an interconnected version of coordination complexes, MOFs are constructed by linking together metal-containing vertices with bridging ligands of various valence and geometry into one-dimensional, two-dimensional, or three-dimensional periodic networks (Figure 1).[8-9] Built upon the fundamental coordination chemistry between various elements on the periodic table and innumerable types of organic ligands, MOFs are an extraordinarily diverse class of materials. Importantly, each individual MOF can be carefully tailored at the molecular level. MOFs are crystalline and their structures and constitution can be precisely determined atom by atom, which

allows for prediction of and control over their properties. The diversity and adjustability of MOFs have made them an inexhaustible and complicated system.

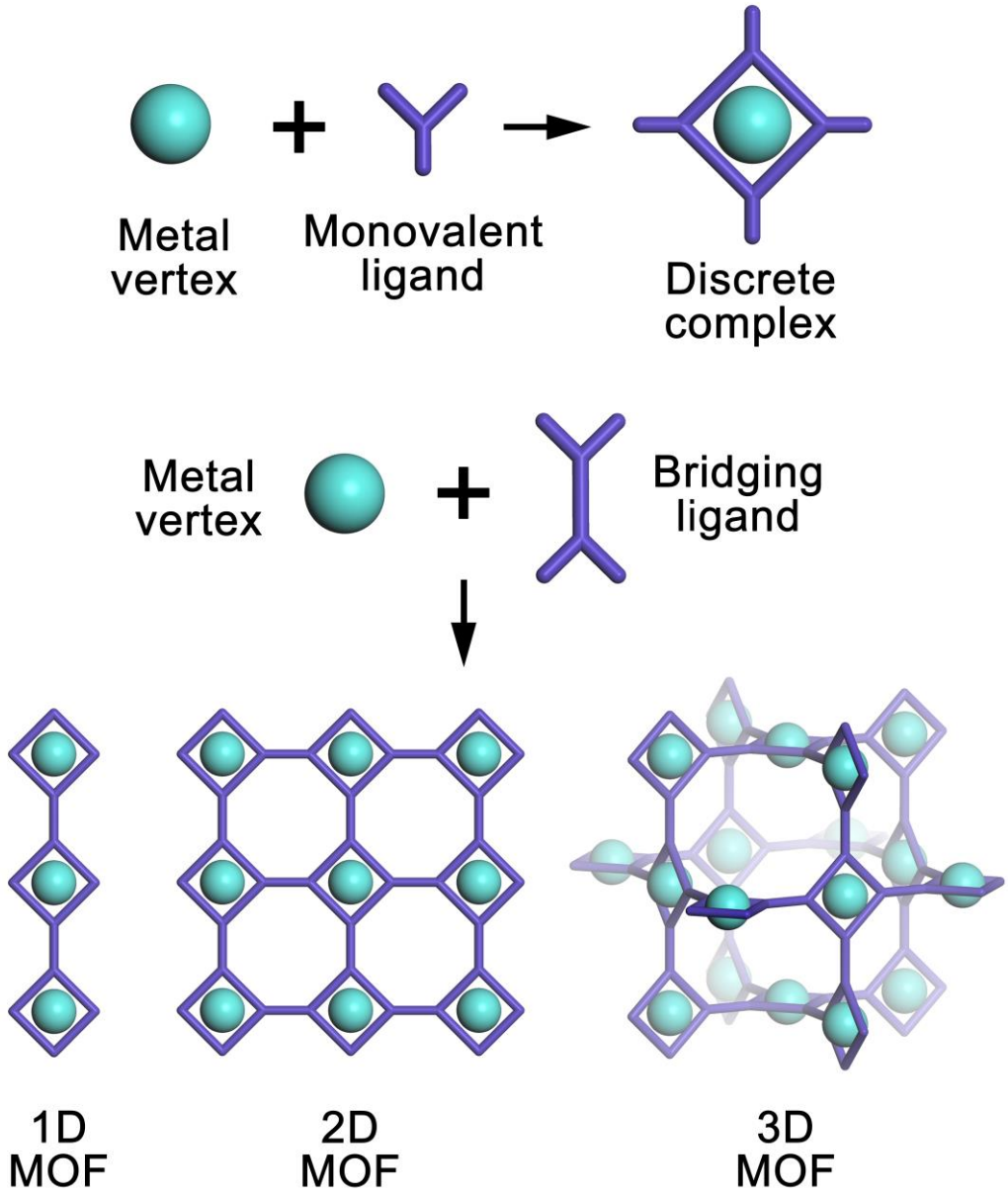

Figure 1. Organization of metal vertices in discrete complexes and MOFs.

1.1.1 Porosity in metal-organic frameworks

MOF building units are generally structurally and geometrically well-defined entities; therefore, when linked together into periodic networks, the spatial organization of these units must adhere to certain regular patterns that can be abstracted mathematically and are referred to as "nets".[10-12] Nets are simple, connected, graphic representations of different mathematical solutions to tessellation in three-dimensional space. The tiles that fill the space can be identical or a combination of different geometric shapes. The tiling mode is represented by the coordinates of vertices and edges of the tiles, which also constitute the core information of the nets. Using nets to describe MOF structures is to abstract the different structural units into virtual vertices and edges to fit the topological representation.[13] The topological arrangement of MOF structural units in space will inevitably yield porosity, which is regarded as the most important feature of MOFs.[14-16] As examples, three nets (*pcu*, *fcu*, and *csq*) are shown in Figure 2, all of which have been realized in MOFs. The vertices and edges are represented as points and sticks and the different pores are represented as space-filling spheres and rods. The pores and channels, defined by the metal-organic internal surfaces, dictate MOFs' interaction with all extrinsic elements, and consequently, their application.[17]

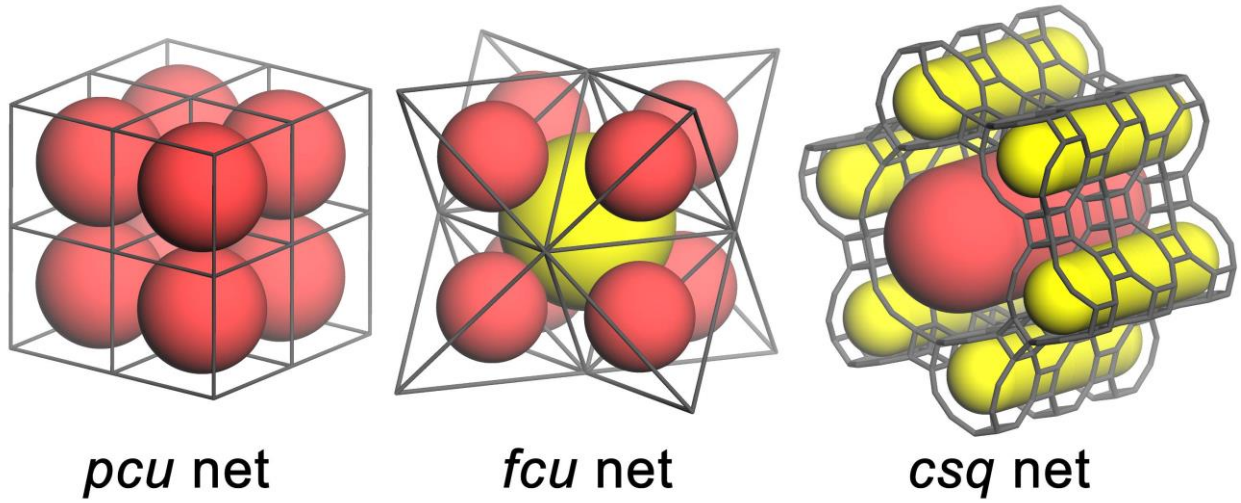

Figure 2. Schematic representation of connectivity and porosity in *pcu*, *fcu*, and *csq* nets.

Practically speaking, MOFs should be identified as porous only when the porosity can be probed with external molecules, which can be as small as simple gas molecules or as large as nano-sized objects. There are many parameters that can be used to assess MOFs' porosity, such as surface area, free volume, and pore size distribution. These parameters are typically determined via gas adsorption studies. Porous molecularly-tailorable MOF materials can potentially be fine-tuned and developed as host species to accommodate and organize more diverse guest entities.[18-19]

1.1.2 Postsynthetic methods for modifying MOFs

In order to develop MOFs for guest organization purposes, the internal pore space must be properly adjusted to meet varied needs. To that end, postsynthetic modifications on existing MOFs are identified to be convenient and versatile routes for adjusting MOF porosity and functionality, in addition to *de novo* MOF synthesis that entails a certain degree of

unpredictability. Based on the composition of MOFs, there are several possible pathways to modify the pore space, as shown in Figure 3: modification or replacement of metal-containing vertices, modification or replacement of ligands, and incorporation of pore-residing guests. Four specific types of MOF modification are introduced in the following sections: covalent chemical reactions, postsynthetic ligand exchange, coordinative modifications, and non-covalent pore infusion.[20-26]

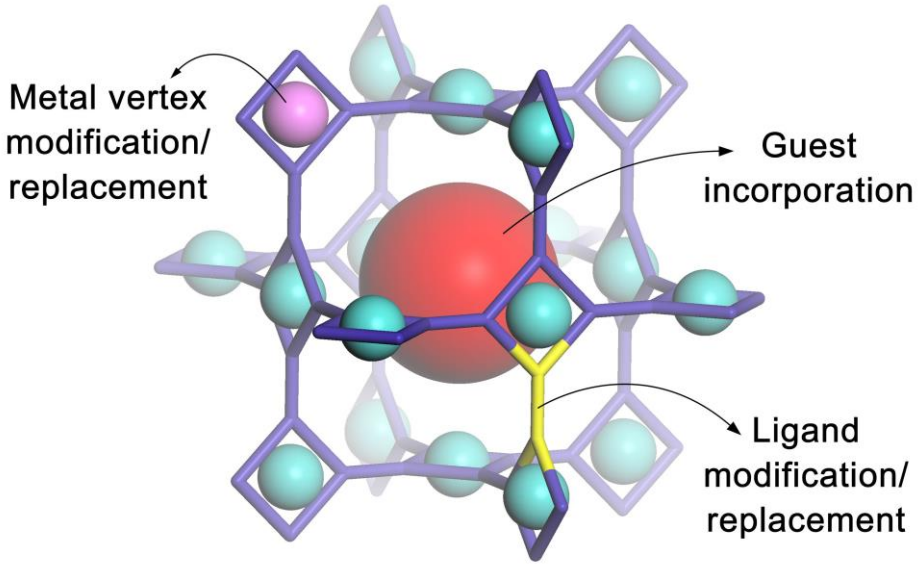

Figure 3. Possible pathways to modify MOF pore space.

1.2 COVALENT POSTSYNTHETIC MODIFICATION

As an intrinsic component in MOFs, the organic ligands possess the most fundamental feature: functional groups. It is not only logical to use various chemical reactions to alter existing

functional groups but also innovative in terms of opening up a new dimension for MOF diversification.

1.2.1 Comparison with pre-functionalization: advantages and limitations

Solvothermal synthesis is still the most common procedure for making MOFs, in which metal salts and organic ligands are usually mixed in solvents and heated for extended periods.[27] Multiple ligands can be obtained through conventional organic synthesis and then used in solvothermal MOF syntheses (Figure 4). This so-called "pre-functionalization" method has been successful in many examples.[28-30] However, an optimal MOF solvothermal condition is a product of careful adjustment of many factors, including temperature, concentration, solvent, pH. Therefore, the synthetic outcome is sometimes very sensitive to additional variables, including ligand functional groups. Therefore, modification of the ligand prior to MOF synthesis can affect product purity and product identity.

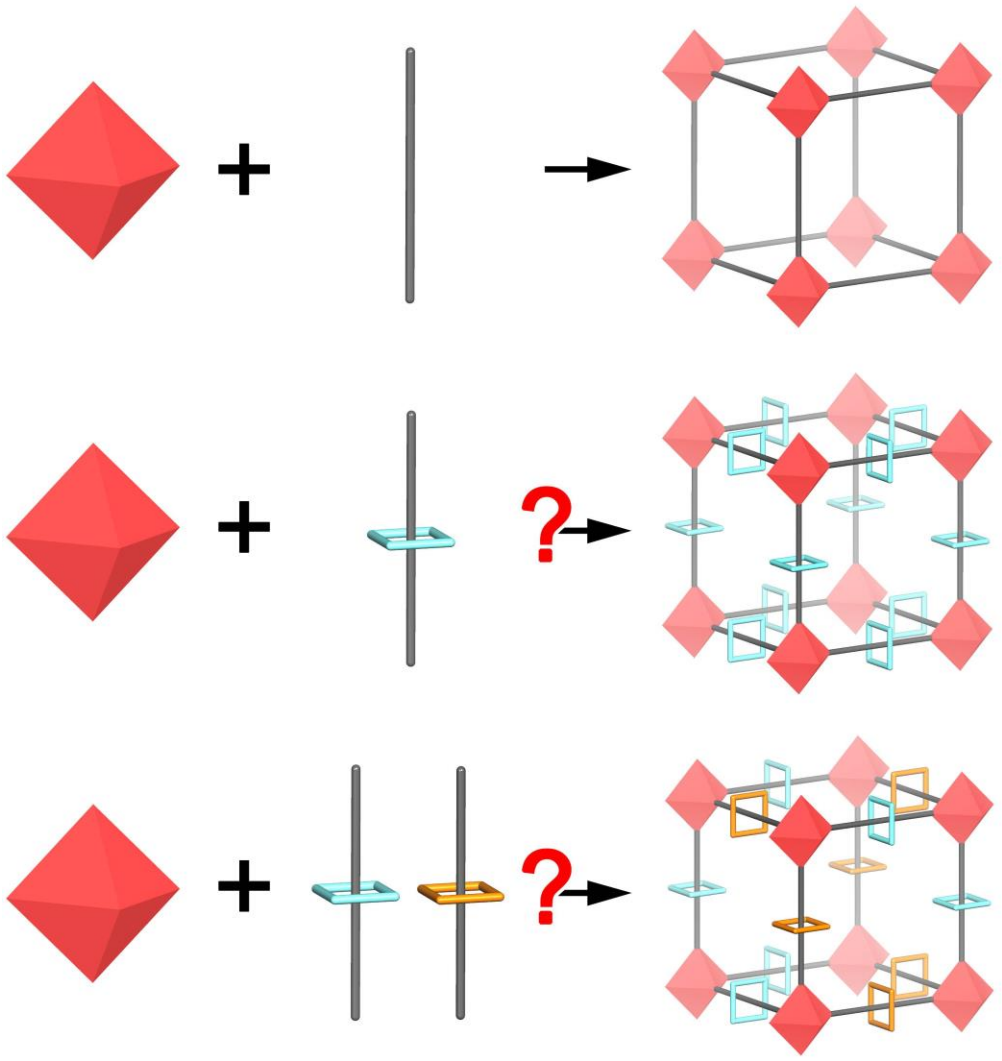

Figure 4. Pre-functionalization of ligand does not guarantee successful synthesis of analogous MOFs.

Alternatively, adapting a linear strategy, MOFs in their original forms can be prepared first and then they can be subjected to functional group conversion in a heterogeneous fashion (Figure 5). Clearly this postsynthetic modification (PSM) method overcomes the unpredictability of convergent syntheses.[24-26] But, PSM has notable limitations. While the whole arsenal of organic reactions are at one's disposal to synthesize a ligand, only reactions compatible with the MOF host can be used for PSM. Furthermore, it is very difficult to achieve full conversion or

controllable composition using PSM, possibly due to varied local environment that is highly dependent on physical diffusion throughout porous MOF crystals. In the following sections, reactions that are suitable for MOF PSM are introduced and strategies to overcome current limitations of PSM are discussed.

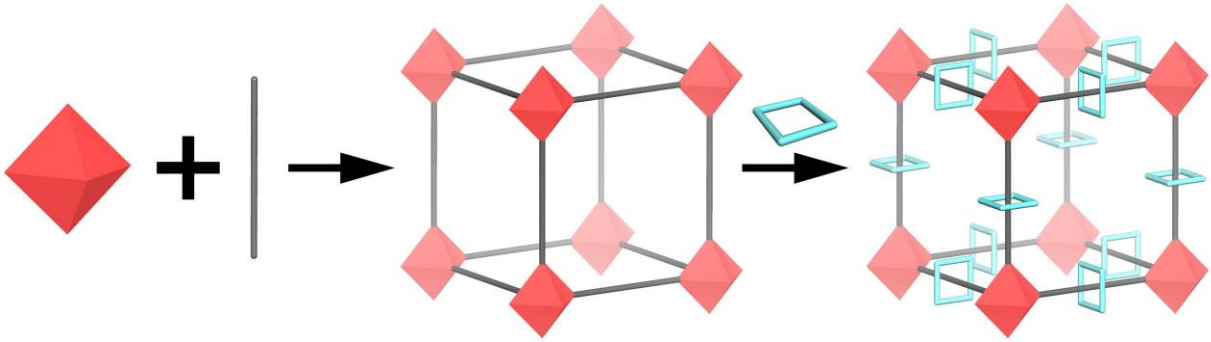

Figure 5. PSM enables ligand functionalization with structure conservation.

1.2.2 Current PSM reactions for MOFs

Many reactions have been tested for MOF PSM, including oxidation, condensation, addition, and elimination. In Figure 6, several examples are shown to illustrate the scope of available functional group transformations.[31-34] When evaluating PSM reactions, it is important to assess their efficiency. Higher conversion rates are usually expected with prolonged reaction time and excess reagents, both of which lower the overall efficiency. Additionally, they may also potentially compromise the structural integrity of the MOF substrates.[35] Aside from being inherently slow, another important reason for the inefficiency of some PSM methods is interference from side reactions.[36]

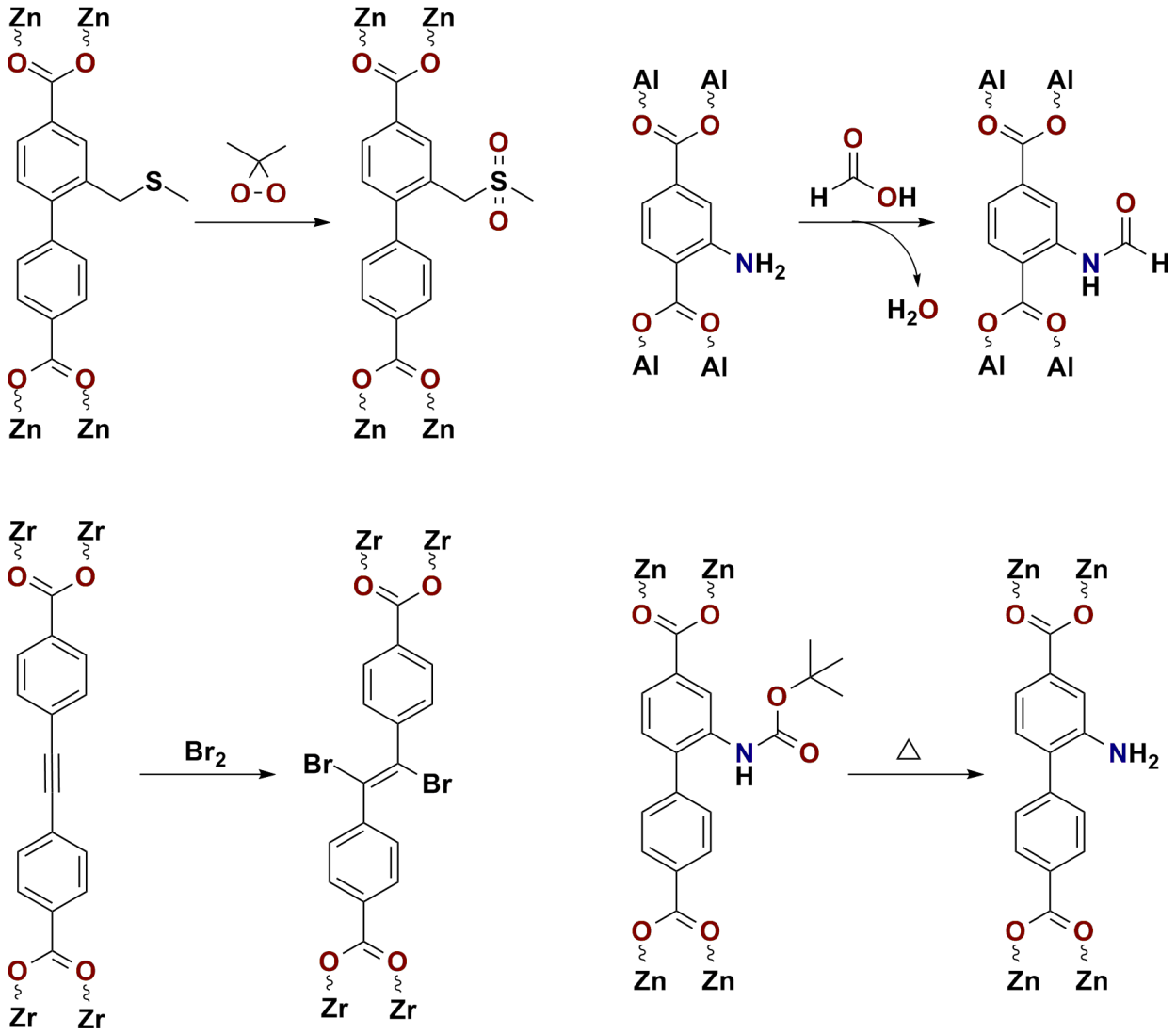

Figure 6. Examples of available PSM reactions in MOFs.[31-34]

Therefore, more orthogonal reactions need to be introduced for MOF modifications. Orthogonal reactions are more exclusive between the intended reactants and do not involve side reactions, therefore increasing the overall efficiency.[37] In fact, orthogonal modification methods have been developed for many disciplines in science, especially in complicated biological systems that involve multiple different functional groups. Cycloaddition reactions, which often require fewer reagents and produce fewer by-products, are an important category of orthogonal

reactions. Specifically, copper-catalyzed azide-alkyne cycloaddition (CuAAC), commonly referred to as click chemistry, has been used as a universal coupling tool in many different contexts.[38-40] Other cycloaddition reactions, including the Diels-Alder reaction, have also proven useful in complicated environments where orthogonality is required.[41] In Figure 7, it is shown that copper-catalyzed click chemistry and Diels-Alder chemistry have been used for MOF PSM.[42-45] From reported data, many of these reactions still demanded excess reagents, long reaction times, and/or elevated temperatures.[42-45] Further, the copper-based catalysts used in conventional click chemistry can, in some cases, interact with the framework in a dative fashion, or even integrate into the MOF irreversibly.[46] From review and analysis of the currently available PSM methods, it is concluded that an ideal PSM method should be free of catalyst, fast, orthogonal, and stoichiometrically efficient.

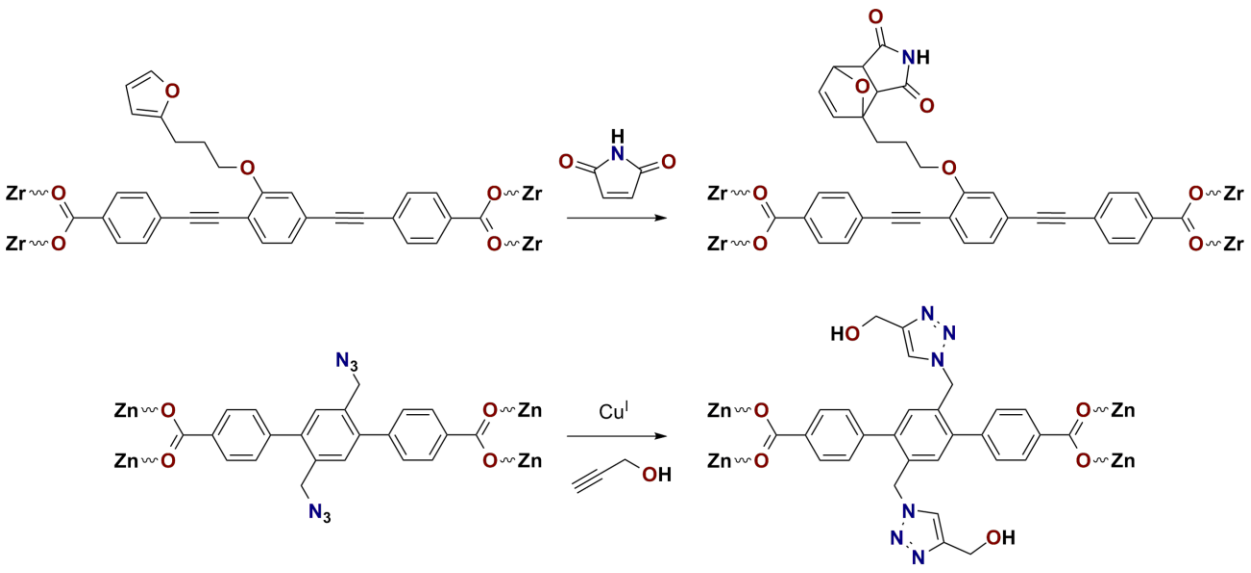

Figure 7. Examples of copper-catalyzed click chemistry (top) and Diels-Alder reaction (bottom) for MOF PSM.[42,45]

1.3 POSTSYNTHETIC LIGAND EXCHANGE

The crystallization of MOFs relies on reversible interactions that gradually organize the molecular building blocks into a periodic arrangement. For common molecular crystals, weak intermolecular interactions such as van der Waals forces and hydrogen bonding are responsible for crystallization. For MOFs, reversible coordination bonds are responsible.

1.3.1 Comparison with solvothermal synthesis and PSM

Many crystals can dissolve in suitable solvents, where solvent molecules disrupt the existing network of interactions between building units within the crystals. Similarly, dative reagents can disrupt the coordination network within MOF crystals. One extreme example is the dissolution of MOF crystals in strong acids. Acids having components bearing coordinative capabilities (e.g., HCl, HF) are particularly useful in dissolving MOFs. After dissolution, the chemical environment of the metal cations is completely changed (Figure 8, left). If another ligand of similar geometry and coordination capability as the original one is introduced, the MOF structure may not dissolve entirely, but it may be gradually converted to a new material in a piece by piece fashion (Figure 8, right) through kinetically controlled reversible coordination.[47]

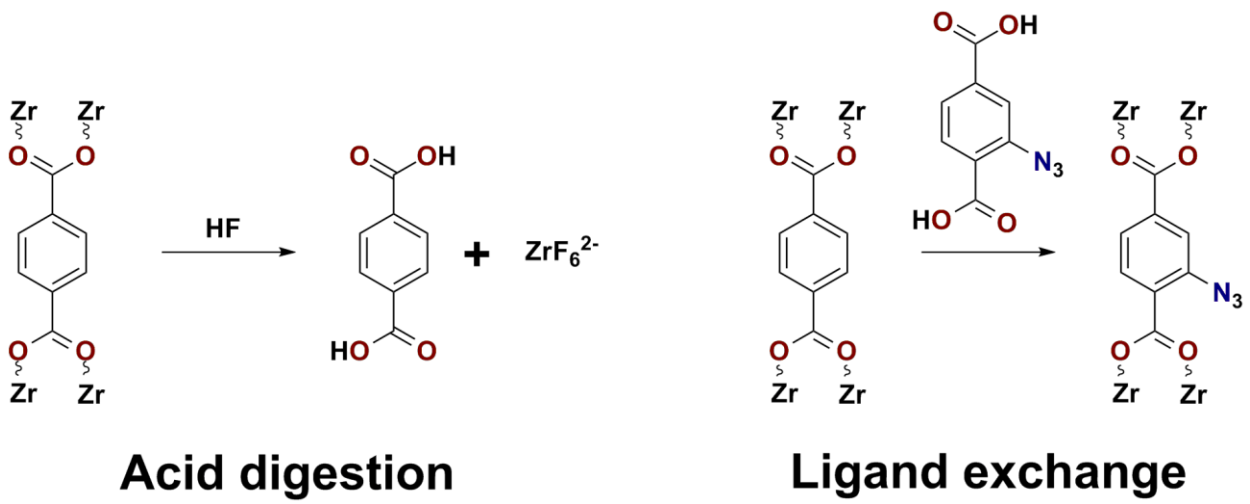

Figure 8. Acid digestion and ligand exchange in a Zr-based MOF.[47]

It has been established that postsynthetic ligand exchange is a reasonable process mechanistically and can occur in MOFs, but its practical value has not been fully exploited.[22-23] By circumventing *de novo* solvothermal synthesis, desirable structure can be preserved, but, similar to PSM, the ligands can be altered. On the other hand, unlike PSM in which chemical compatibility between the incoming reagent and the host MOF is a major concern, ligand exchange mainly depends on structural compatibility. Because of the inherently similar nature of various ligands involved, as long as the integration of the new ligand is thermodynamically acceptable, the reaction should proceed. Of course, possible chemical reactions involving functional groups on either ligand could interfere with the ligand exchange process.

1.3.2 Ligand exchange for functionalization

Permitted by structural and chemical compatibility, postsynthetic ligand exchange is clearly a useful tool for MOF functionalization. It combines the merits of *de novo* synthesis and PSM:

ligands are prepared in pure form via organic synthesis and the original MOF topology is preserved, as ligand exchange occurs after MOF synthesis.

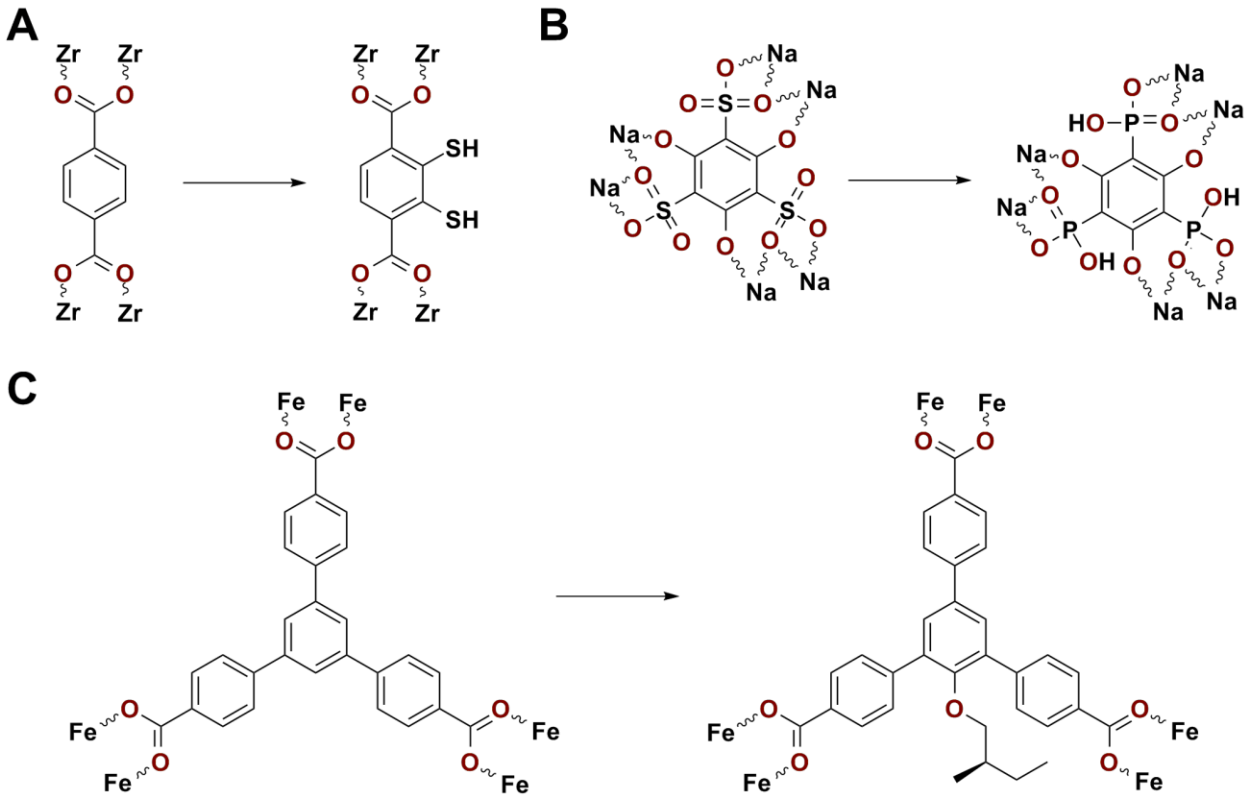

Figure 9. Examples of postsynthetic ligand exchange reactions for MOF functionalization.[48-50]

Many examples of ligand exchange reactions that introduce new functional groups to the MOFs have been demonstrated. As shown in Figure 9A, a Zr-based MOF was functionalized with thiol groups for subsequent coordinative modification; in Figure 9B, a Na-sulfonate MOF was functionalized with additional hydroxyl groups via exchange with phosphonic acid ligands for proton conduction; in Figure 9C, chirality was imparted into an achiral Fe-based MOF via ligand exchange.[48-50] In principle, one ligand exchange reaction can be used in tandem with other ligand exchange reactions or with PSM reactions to further expand and explore the diversity of MOF materials.

1.3.3 Ligand exchange for pore expansion

Families of isoreticular MOFs are typically synthesized from early approaches by employing ligands of similar geometry but different length/size.[28,51] Recently, MOF structural flexibility was exploited to enable pore expansion or compression via ligand exchange to achieve a series of isoreticular MOFs.[52-54] In a coordinative network like MOFs, the structural units can deviate slightly from their ideal positions. These deviations can create some mechanical strain, which is tolerable within certain limits. Therefore, taking advantage of the reversible coordination, longer ligands can replace the shorter, original ones, or vice versa, providing that the strain produced from introduction of the new ligand does not disrupt the structural integrity of the MOF. When a sufficient amount of the original ligands are replaced, the porosity of the MOF is effectively increased or decreased, depending on ligand length.

Pore compression has been realized in MOFs having different coordination chemistry between vertical and horizontal structural units (i.e., pillared MOFs). As shown in Figure 10, the pore contraction of pillared MOFs was possible because replacement of "pillar" ligands did not affect the structure of the horizontal planes, leading to one-dimensional compression.[52] Theoretically, pore expansion should also be feasible in such MOFs, and it was indeed realized in a later report.[53] Pore expansion via postsynthetic ligand exchange was first demonstrated in a series of more symmetric (*Ia-3d*) MOFs and the expansion was uniform in all three dimensions (Figure 11), showcasing the versatility and potential of this method.[54]

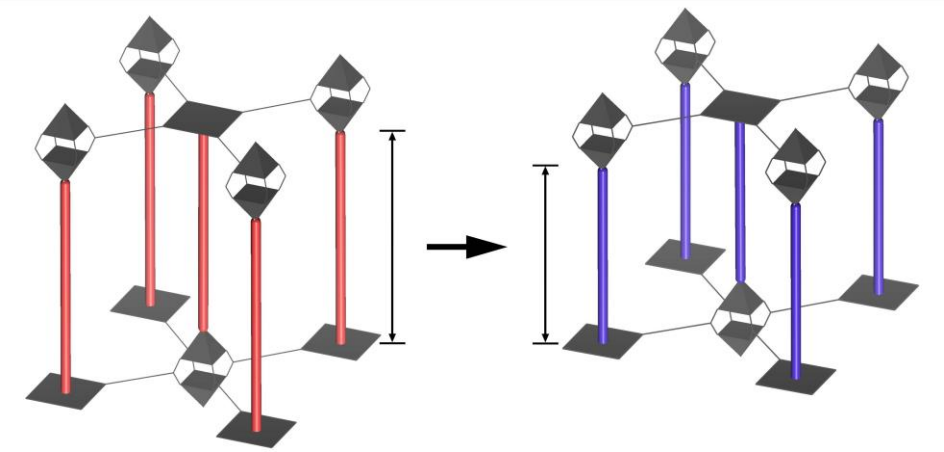

Figure 10. Pore contraction via ligand replacement in a pillared MOF.[52]

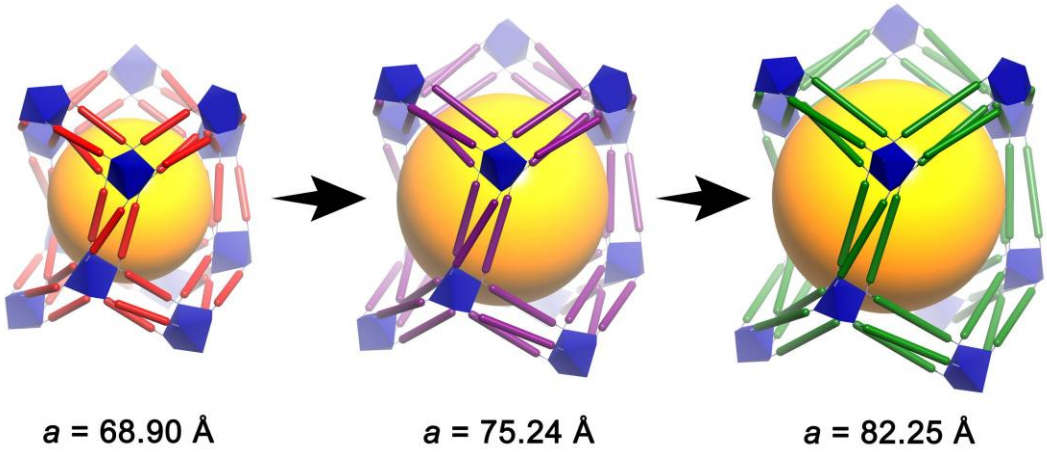

Figure 11. Pore expansion in a series of cubic MOFs via ligand exchange.[54]

1.4 COORDINATIVE MODIFICATION

In addition to PSM and ligand exchange, certain monovalent ligands that do not affect the topology of the MOF can be removed, added or replaced by others, enabling another way to fine-tune MOF properties.

1.4.1 Removal of non-bridging ligands

During solvothermal synthesis, solvent molecules or other additives may associate with the metal cations. It is possible to postsynthetically remove these associated molecules without disrupting the overall MOF connectivity. It has been shown from the beginning of MOF chemistry that this type of modification is capable of tuning the porosity and surface properties. HKUST-1 (HKUST = Hong Kong University of Science and Technology), exhibits a $Cu_2L_4(H_2O)_2$ building block (L = 1,3,5-benzenetricarboxylate) (Figure 12A). After removal of water molecules, coordination sites on the Cu^{2+} ions were exposed.[55] NU-1000 (NU = Northwestern University) has a $Zr_6(\mu_3\text{-}O)_4(\mu_3\text{-}OH)_4L_8(\text{benzoate})_4$ building block (L = 1,3,6,8-tetrakis(*p*-benzoate)pyrene and it is omitted from this representation for clarity) (Figure 12B). After treatment with HCl, benzoate anions were removed and ligands on the Zr^{4+} ions were transformed, yielding a new building block $Zr_6(\mu_3\text{-}OH)_8L_8(\mu_1\text{-}OH)_8$.[56]

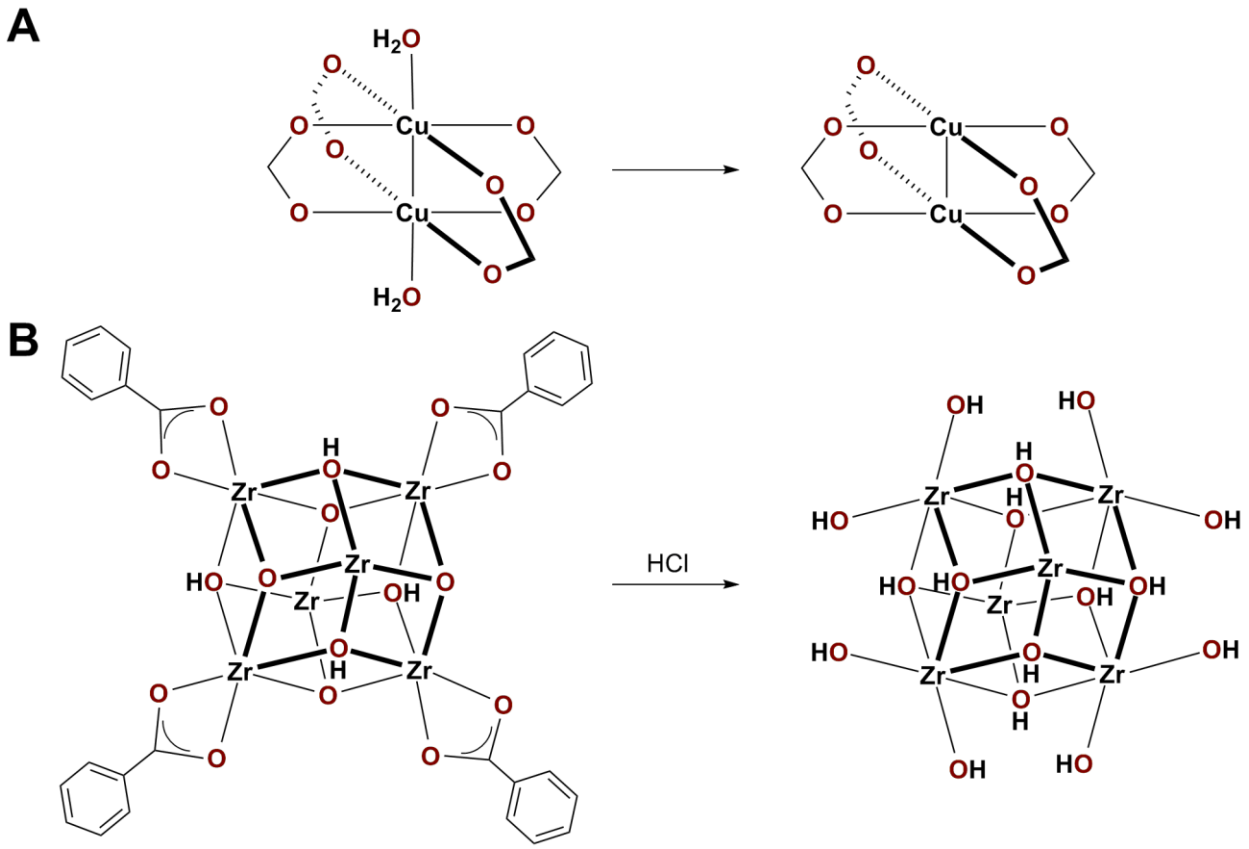

Figure 12. Postsynthetic removal of non-bridging ligands from HKUST-1 (A) and NU-1000 (B).[55-56]

1.4.2 Installation of additional monovalent ligands

Naturally, the removal of non-bridging ligands is also a reversible process, meaning that other monovalent ligands can be installed onto MOFs, similar to the process of postsynthetic ligand exchange. In the same examples described in the previous section, HKUST-1 and NU-1000 can also undergo this type of modification. Pyridine was incorporated into the anhydrous form of HKUST-1 (Figure 13A);[55] trifluoroacetic acid was used to mask the μ_1-OH groups in NU-1000

(Figure 13B). As a result, porosity and surface chemistry were adjusted accordingly in these materials.[57]

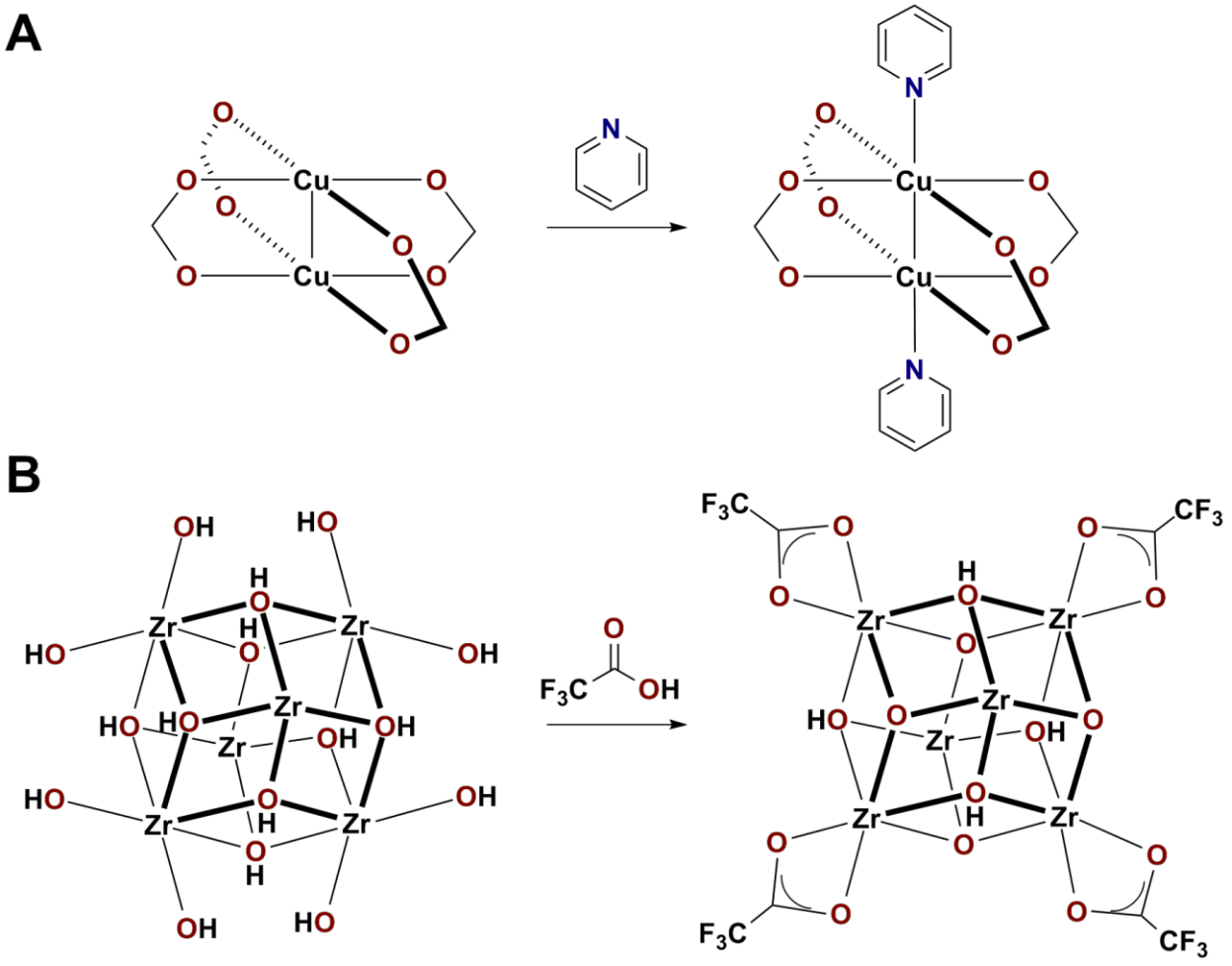

Figure 13. Postsynthetic installation of non-bridging ligands onto HKUST-1 and NU-1000.[55,57]

1.4.3 Additional metal coordination

Presence of coordination sites on ligands or the metal vertices provides additional possibilities for metal coordination. For example, 2, 2'-binaphthol (Figure 14A) and 2, 2'-bipyridine (Figure 14B) based ligands can undergo postsynthetic metalation.[58-59] In some cases,

the functional groups (e.g., carboxylate, hydroxyl groups) that coordinate the metal ion vertices are unsaturated and can coordinate to additional metal ions (Figure 15).[60-61] It is noteworthy that these types of modification are particularly useful for developing heterogeneous catalysts, utilizing the postsynthetically installed metal centers.[62-65]

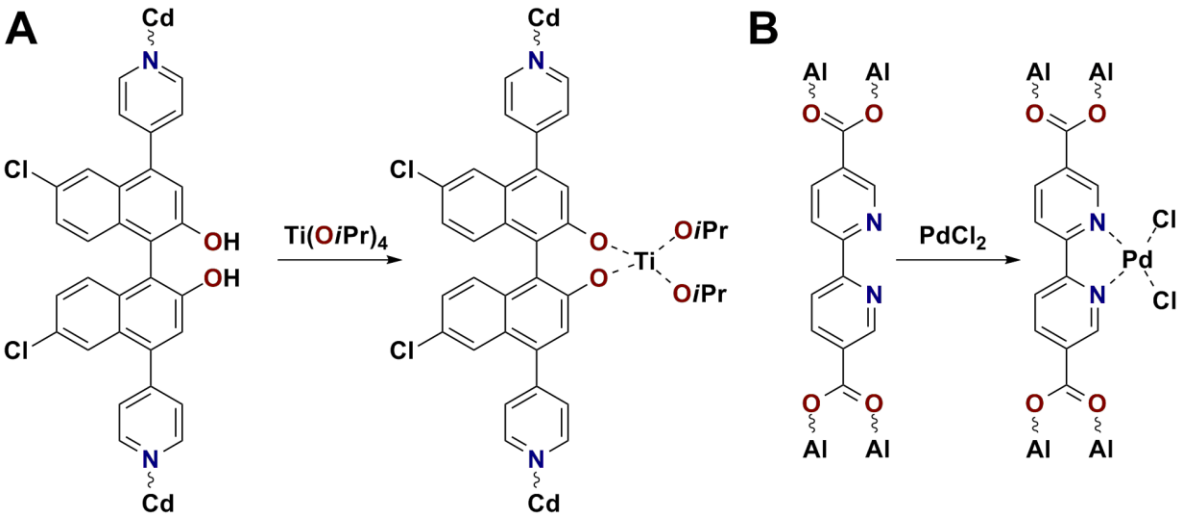

Figure 14. Postsynthetic metal coordination on organic linkers.[58-59]

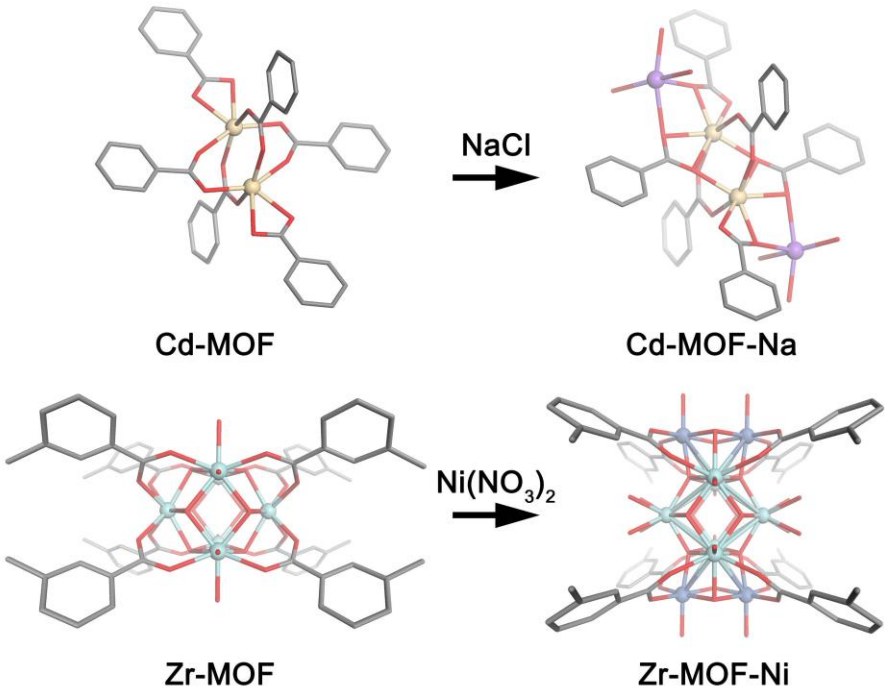

Figure 15. Postsynthetic metal coordination at metal vertices.[60-61]

1.5 NON-COVALENT PORE INFUSION

There are not just coordinative interactions present in MOFs. Due to their porous nature, external species can physically diffuse into MOFs. In addition, many MOFs are charged, so electrostatic attraction can also be used to incorporate guest molecules into the framework.

1.5.1 Physical diffusion

MOF pore space may be accessible through physical diffusion, if the pores are sufficiently large to accommodate the guest species. In fact, some MOFs can absorb guest molecules via this type of diffusion and organize them in a crystalline fashion.[66] The so-called "crystal sponge" MOFs have been found to be a powerful tool for determining absolute structures of many organic molecules, some of which were not able to be determined otherwise due to difficulty of crystallization.[67-69] For example, the absolute structure of a chiral drug compound santonin (Figure 16, left, IUPAC name (3*S*,3a*S*,5a*S*,9b*S*)-3,5a,9-trimethyl-3a,5,5a,9b-tetrahydronaphtho[1,2-*b*]furan-2,8(3*H*,4*H*)-dione) can be solved when it was incorporated in a "crystal sponge" MOF (Figure 16, right).[67] It was proposed that suitable internal environment and intermolecular forces of "crystal sponge" MOFs were responsible for positioning and orienting the guest molecules.[70-71]

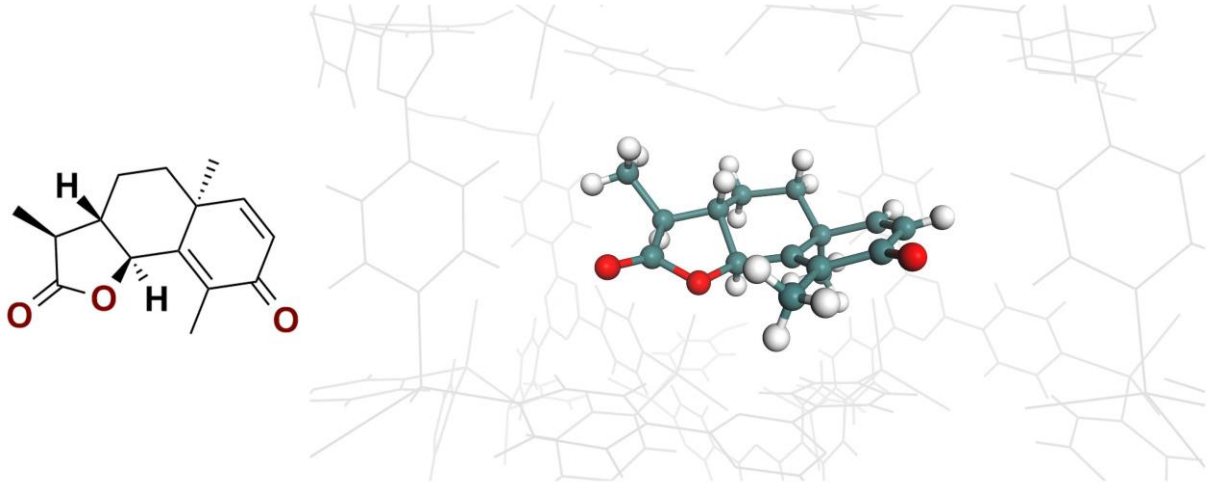

Figure 16. Molecular structure of santonin and its crystallographic visualization within a MOF.[67]

In other cases, to expedite the diffusion process, capillary force was found to be a sufficiently strong driving force to transport guest species into the MOF pores. For example, when a MOF with hydrophilic pores was completely evacuated and then exposed to hydrophobic solvent containing a small amount of aqueous solution, the aqueous solution was quickly absorbed into the pores, decreasing the surface tension. In this way, guest species were effectively transported into MOF pores.[72-73]

1.5.2 Electrostatic attraction

Positively charged MOFs have anions residing in the pores, which are usually the counter-ions of the metal salt precursor used during solvothermal synthesis.[74-75] Negatively charged MOFs have extra-framework cations residing in the pores, usually dimethylammonium that is a decomposition product of a common solvent *N*, *N*-dimethylformamide (DMF) for MOF

synthesis.[24,76] The locations of these counter-ions are usually difficult to determine as they move around freely.

Just like ion exchange in many other systems, the native counter-ions in MOFs can be intentionally replaced. For example, anionic MOFs can be charged with cations with higher practical value in terms of guest storage and porosity modulation. As shown in Figure 17, cationic drug compound procainamide HCl can be loaded into and controllably released from an anionic MOF, both via ion exchange process; cations with different sizes can be incorporated to adjust the accessible porosity of the MOF.[77-78] Charged MOFs can also be infused with ionic dye molecules to make solid state luminescent materials.[79-80] In other examples, ion exchange has been used to modify MOFs to optimize their applications in gas storage, catalysis, and as sensors.[81-83]

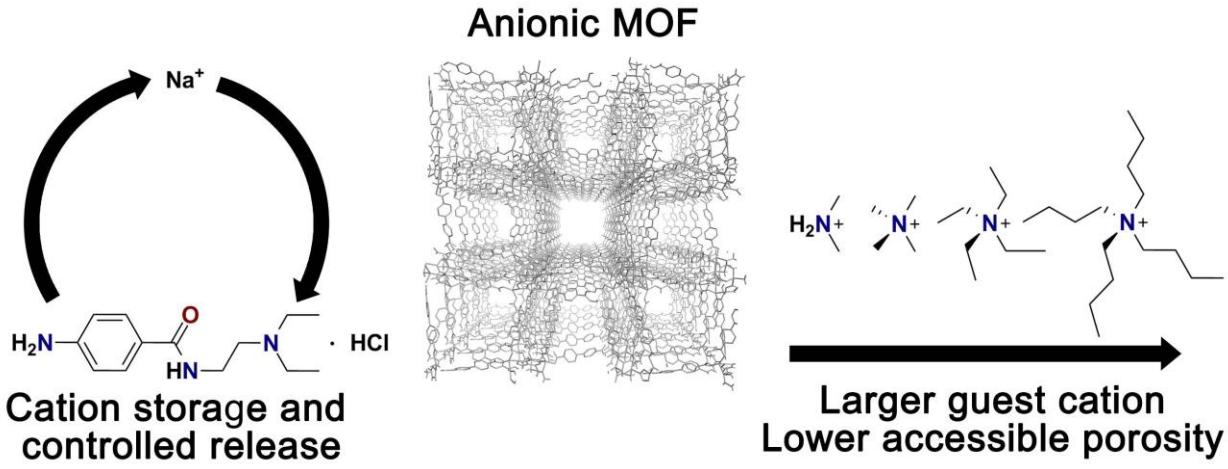

Figure 17. Cation exchange in an anionic MOF.[77-78]

1.6 POSTSYNTHETIC CONTROL OF FUNCTIONALITY AND POROSITY IN METAL-ORGANIC FRAMEWORKS

This dissertation focuses on the development of new MOF modification strategies and the implementation of these strategies toward systematic control of functionality and porosity in MOFs, which can be potentially used as scaffolds to accommodate complex functional species in 3-D space.

1.6.1 MOF modification via strain-promoted click chemistry

In Chapter 2, a powerful bioorthogonal tool was applied as a MOF modification method. Strain-promoted click chemistry was known for high reaction rate, quantitative efficiency, mild condition, and orthogonality, all of which were proven to be advantageous for the postsynthetic modification of mesoporous N_3-bMOF-100. Different functional groups were installed onto the MOF, including reactive groups that allowed for tandem modification, highlighting the efficiency and versatility of this method. The PSM method developed is an important foundational tool that can be used to incorporate highly complex molecular species into the MOF pore without compromising the 3-D structure.

1.6.2 Sequential ligand exchange for MOF multi-functionalization

A sequential postsynthetic ligand exchange process is introduced in Chapter 3. This process can be used to prepare a series of mono-, bi-, and tri-functionalized mesoporous MOFs. Through this process, orthogonal functional groups were installed and thereafter postsynthetically modified

with large dye and quencher molecules, which acted as surrogates for identifying the position of the specific ligands. Microspectrophotometric studies were used to determine the distribution of the two orthogonal functional groups within the MOF crystals. This is a new experimental approach for determining the spatial distribution of various moieties in heterogeneous MOFs. The results demonstrated how ligand exchange methods can be used to increase the diversity of MOF materials and they pointed toward the ability to place multiple different complex molecules in fixed positions with respect to one another in 3-D periodic space.

1.6.3 Porosity gradients in MOFs from controlled ligand exchange

Studies aimed at understanding the mechanism and process of ligand exchange-facilitated pore expansion in the three-dimensional bMOF-100 crystal are presented in Chapter 4. It is demonstrated that ligand exchange proceeded gradually from crystal periphery to crystal core and that the pore expansion occurred incrementally and depended on the magnitude of the ligand length step size. Halting the ligand exchange reactions resulted in MOF crystals bearing porosity gradients. The hierarchical distribution of porosity was then used for heterogeneous organization of gold nanoclusters. It was shown that carefully selected clusters of proper sizes preferentially located in the periphery region where the pores were large enough to accommodate them, as revealed by microspectrophotometric measurement.

1.6.4 Isoreticular rare earth MOFs with *fcu* topology and dye-MOF interactions

A series of isoreticular MOFs with the well-known *fcu* topology is reported in Chapter 5. They were synthesized with commercially available ligands of different lengths and 10 different rare earth metal ions. It was discovered that the presence of a new modulator (2,6-difluorobenzoic acid) was critical to enable the formation of these MOFs. These MOFs were anionic in nature, therefore cation exchange was performed with 5 different dye molecules. Loading efficiency was related to the porosity of the MOFs as well as cation exchange time. Spectroscopic studies showed that an incorporated cationic dye could sensitize Yb^{3+} emission with significantly red-shifted excitation wavelength compared to sensitization through MOF ligands.

2.0 STRAIN-PROMOTED CLICK MODIFICATION OF A MESOPOROUS METAL–ORGANIC FRAMEWORK

This work, written in collaboration with Tao Li and Nathaniel L. Rosi*, has been published in the *Journal of American Chemical Society*, **2012**, *134*, 18886-18888.[84]

Tao Li assisted with characterization of some of the MOF materials.

2.1 INTRODUCTION

As described in Chapter 1, MOFs are potential centerpiece materials for various applications in fields ranging from energy to medicine. Their signature attributes include permanent porosity, periodicity, and structural diversity. When it comes to guest organization, MOFs with different degrees of porosity perform differently. Microporous MOFs[85-86], with smaller pore diameters (≤ 2 nm), will limit the size and complexity of molecules that can be incorporated into the framework. Mesoporous MOFs, especially those with continuous mesoporous channels, can serve as better scaffolds for organizing large and complex molecules, thus enabling the creation of periodic porous materials with unprecedented levels of pore complexity.[87-89] The straightforward introduction of increasing levels of functional diversity and complexity into

MOF mesopore environments, beyond that which is currently possible for microporous MOFs, will lead to a step change in the overall application scope of MOF materials.

Facile incorporation of molecular complexity into mesopore environments requires postsynthetic modification (PSM) strategies. An ideal strategy would enable covalent pore modification with a variety of species ranging from simple organic molecules and catalysts to nanoparticles and biomolecules. Elaborating on the points made in Section 1.3, the synthetic approach should: i) be highly efficient under mild conditions; ii) be "clean", in that it should not yield byproduct or require input of additional reagents or catalysts; iii) not impact the structural integrity of the scaffold MOF; and iv) be orthogonal to a wide range of possible functional groups that one might choose to introduce. However, the most common methods either required catalysts (e.g., Cu^{+} for the Huisgen cycloaddition),[35,42-43] produced byproduct (e.g., H_2O or HCl),[36,90-92] or required the removal of protecting groups to unmask the desired functional moieties;[34,93-94] in some cases, these reagents and byproducts can cause degradation of the scaffold MOF. It should be noted that Diels-Alder-based PSM reactions have been reported and these important and useful strategies yielded either no byproduct or simply N_2 gas.[44-45] In some cases, however, these reactions required either a large excess of reagent (dienophile), long reaction times (two or seven days), or elevated temperatures.

Considering that substrate modifications are important in many other disciplines of chemistry as well, useful tools developed for other systems might be easily translated to MOF chemistry. After examining the literature, it was found that the complexity of native biological systems can be related to MOF environments. Accordingly, bioorthogonal chemistry, designed to meet the strict criteria for biological investigation, was found to be potentially promising for MOF modifications.[37,95-96]

To investigate biological systems in their native settings, a modification method should: i) be fast under mild (physiological) conditions; ii) be inert to various molecules/functional groups available *in vivo*; and iii) involve as few external molecules as possible. Chemical reactions that meet all of the above requirements, identified as 'bioorthogonal', include: imide formation between ketones/aldehydes and amines, Staudinger ligation between azides and triaryl phosphines, tetrazine-alkene cycloaddition, alkyne-azide cycloaddition. Among these reactions, alkyne-azide cycloaddtion, also known as click chemistry, has been most widely used.[38-39] Even though the original click chemistry (copper(I)-catalyzed alkyne-azide cycloaddition, CuAAC) has found very limited use in living systems as a result of the cytotoxicity of Cu, its alternative, strain-promoted click chemistry, based on cyclooctyne derivatives, has emerged as a very versatile tool.

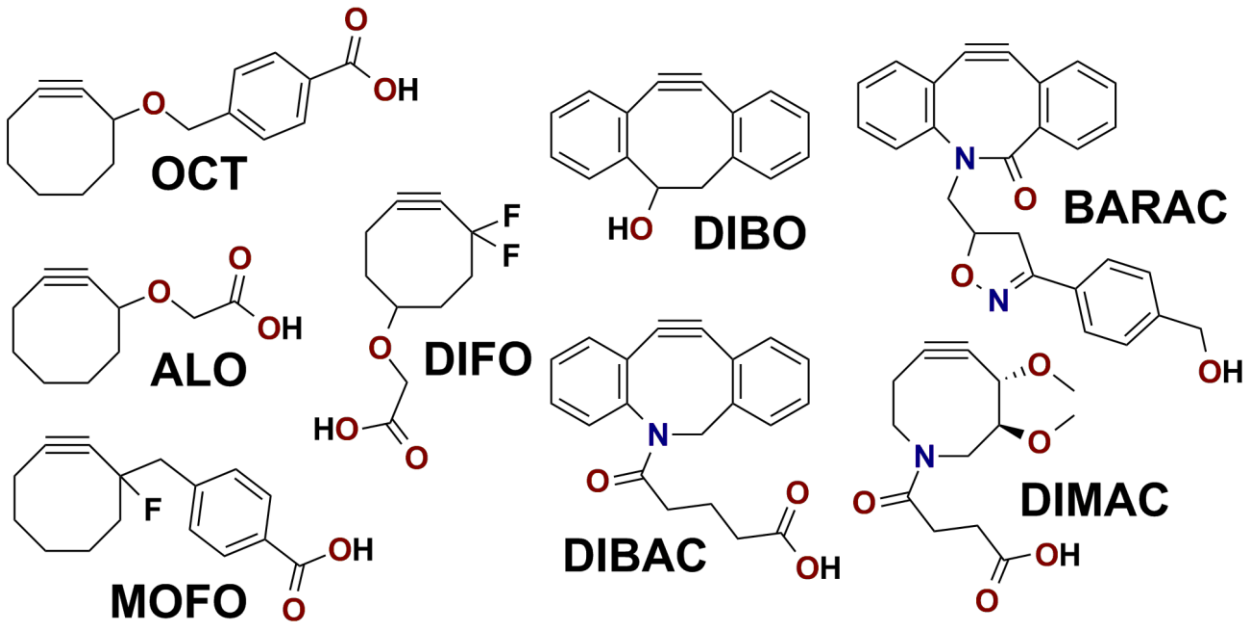

Figure 18. Different cyclooctyne-based compounds for strain-promoted click chemistry.[97-103]

Originating from the explosive reaction between neat cyclooctyne and azidobenzene studied in 1961,[104] a series of strained molecules have been synthesized and tested in biological systems (Figure 18).[97-103] The reaction proceeded very quickly and efficiently *in vivo* and exclusively between azide and cyclooctyne moieties; therefore, it did not interfere with the other processes in the living organisms. Cell, zebrafish, and mouse models were investigated, successfully confirming the bioorthogonality of this method.[97,105-106]

Based on the success of these reactions for the innocent modification of biological systems, it was reasoned that they could serve as ideal reactions for a new universal porous MOF modification strategy. Such a strategy should allow for the straightforward introduction of diverse molecules and functional groups into MOF pores. Further, it was noted that the size of typical cyclooctyne derivatives would make this strategy most useful for PSM of mesoporous MOFs.

2.2 RESULTS AND DISCUSSION

2.2.1 Platform mesoporous MOF material: N_3-bMOF-100

Azide-modified mesoporous bMOF-100 was chosen as the scaffold MOF for this study. Originally reported in 2012, bMOF-100 is a permanently mesoporous material consisting of Zn^{2+}-adeninate tetrahedral building blocks connected together through biphenyldicarboxylate (BPDC) linkers into an open augmented *lcs* network.[107-109] The synthetic condition for bMOF-100 is shown in Figure 19, as is the augmented *lcs* topology of the product. The Zn^{2+}-adeninate secondary building unit (SBU) is abstracted as a tetrahedron; the three bundled BPDC linkers are

abstracted as a line. Featuring mesoporous channels with a diameter of 2.5 nm, bMOF-100 is usually represented as Figure 20. In fact, bMOF-100 has mesoporous channels run along [101], [011] and [110], as shown in Figure 21, granting unprecedented accessibility to the internal space, which should allow for the unimpeded diffusion of large molecules.

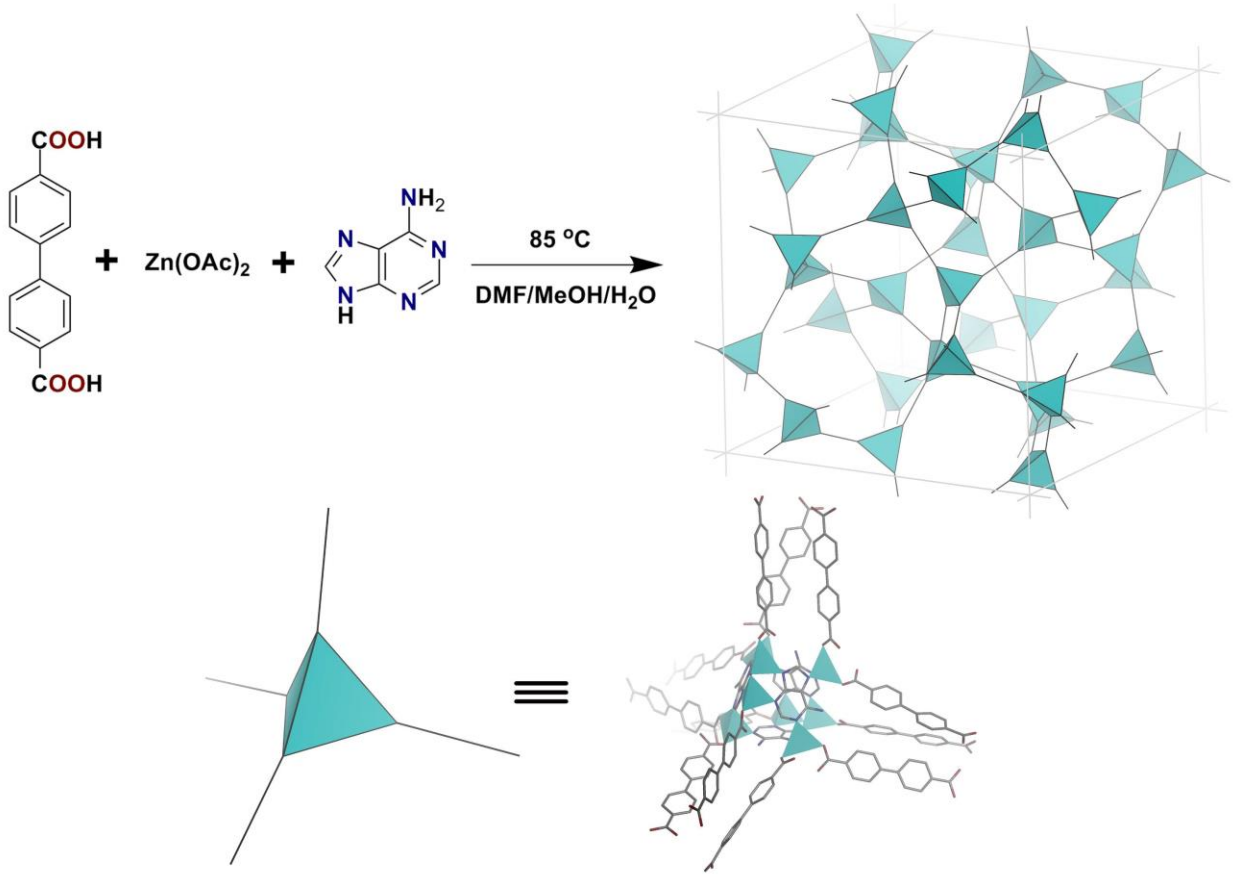

Figure 19. Synthetic condition and structural anatomy of bMOF-100 (bottom right: Zn: dark cyan polyhedron; C: grey; N: navy blue; O: maroon).[108]

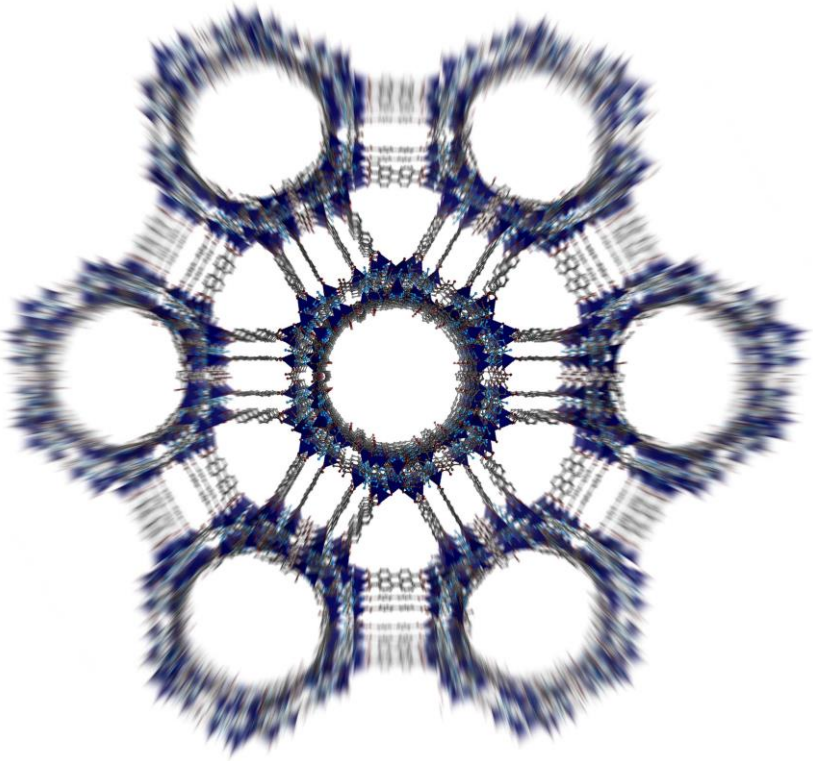

Figure 20. Schematic representation of bMOF-100 featuring mesoporous channels.[108]

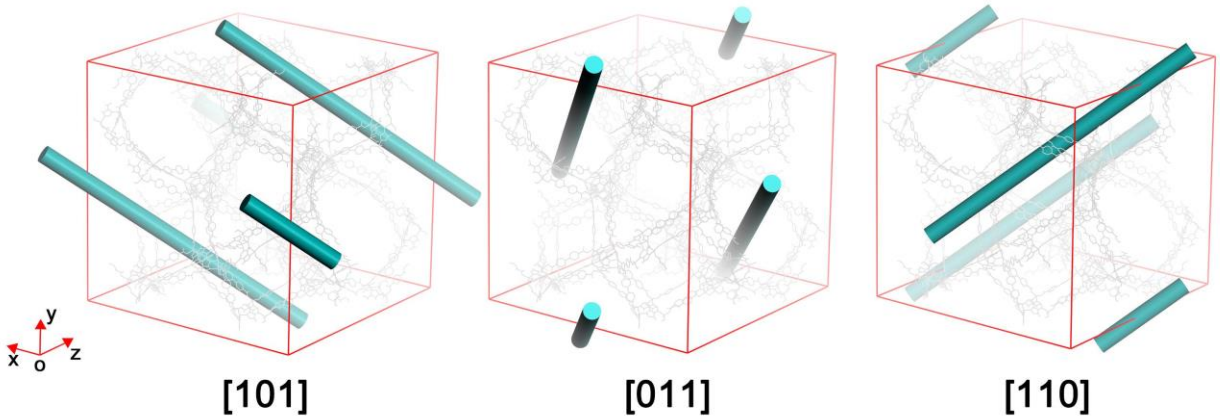

Figure 21. Mesoporous channels running along three directions in bMOF-100.

To prepare the azide-modified version of bMOF-100, biphenyldicarboxylic acid was replaced with 2-azidobiphenyldicarboxylic acid in the synthetic condition (Figure 22). Powder

X-ray diffraction (PXRD) was used to confirm that the product material was isostructural to bMOF-100 (Figure 23). CHN elemental analysis (Experimental Section 2.4.3) of a dried product sample was used to determine the composition: $Zn_8(Ad)_4(N_3\text{-}BPDC)_6O_2 \cdot 2(Me_2NH_2) \cdot 6.25(CH_2Cl_2)$ (Ad = adeninate; N_3-BPDC = 2-azidobiphenyldicarboxylate). Every azide group is exposed to the accessible space inside the channels. Essentially the mesopores of the structure are densely lined with azide groups (Figure 22); this is an aspect that should allow for dense coverage of desired functional molecules after PSM using alkyne-azide click chemistry.

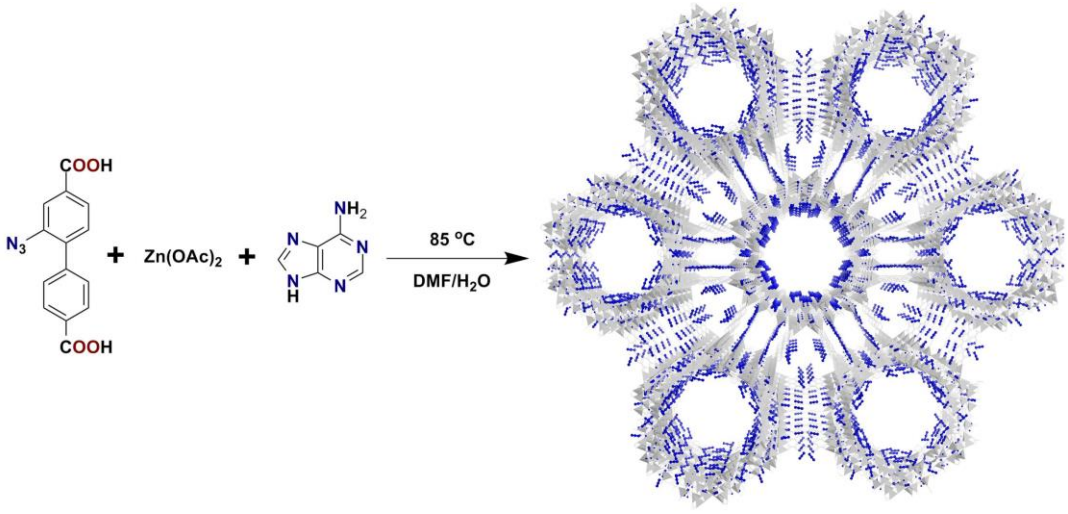

Figure 22. Synthetic condition and structure scheme for N_3-bMOF-100.

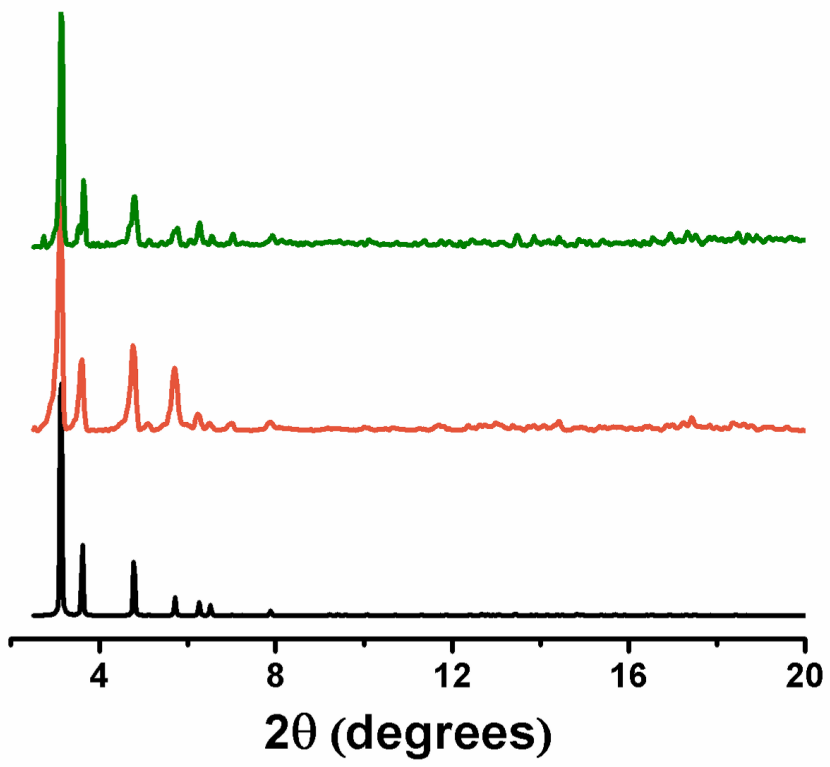

Figure 23. Comparing PXRD patterns of simulated bMOF-100 (black), experimental bMOF-100 (orange) and experimental N_3-bMOF-100 (green).

2.2.2 Synthesis of strained alkyne molecules

Among all the molecules shown in Figure 18 that have been tested for strain-promoted click chemistry, DIBAC was chosen for our study because it had one of the highest reaction rates and the synthetic route for various DIBAC compounds was well-documented.[103,110-111] Additionally, with the aid of recently developed DIBAL-H-promoted reductive rearrangement,[112] the route used in this study was further shortened. The slow (1 to 3 days), low-yielding Beckmann rearrangement was circumvented, so the overall efficiency of the synthesis was increased (Figure 24). Using the improved synthetic strategy, methyl 4-(11,12-

didehydrodibenzo[*b*,*f*]-azocin-5(*6H*)-yl)-4-oxobutanoate (**1**) and *N*-dodecanoyl-5,6-dihydro-11,12-didehydrodibenzo[*b*,*f*] azocine (**2**) were first prepared, for proof-of-principle PSM studies (Figure 25).

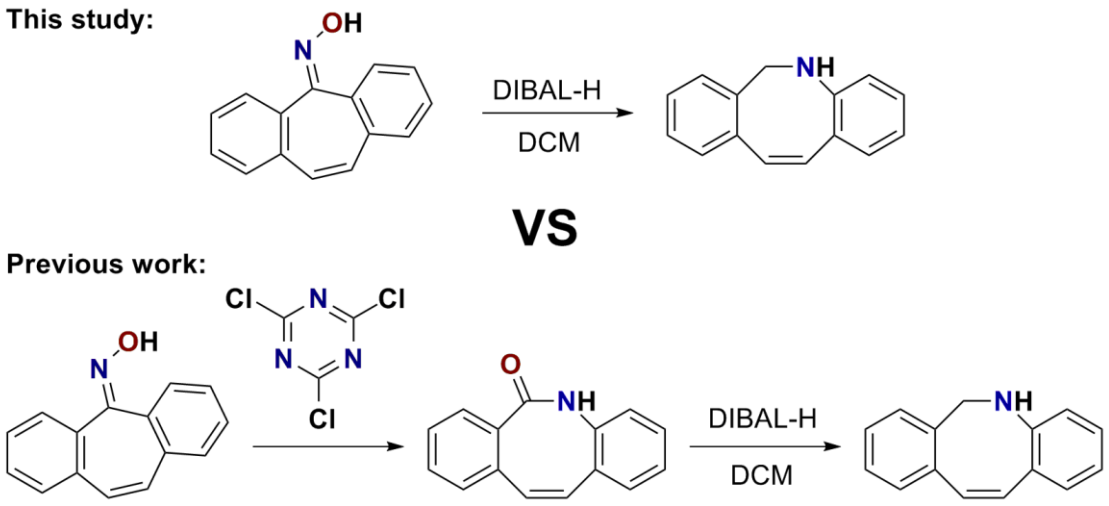

Figure 24. Improvement of DIBAC synthesis by application of reductive rearrangement (top) and elimination of Beckmann rearrangement (bottom).[111]

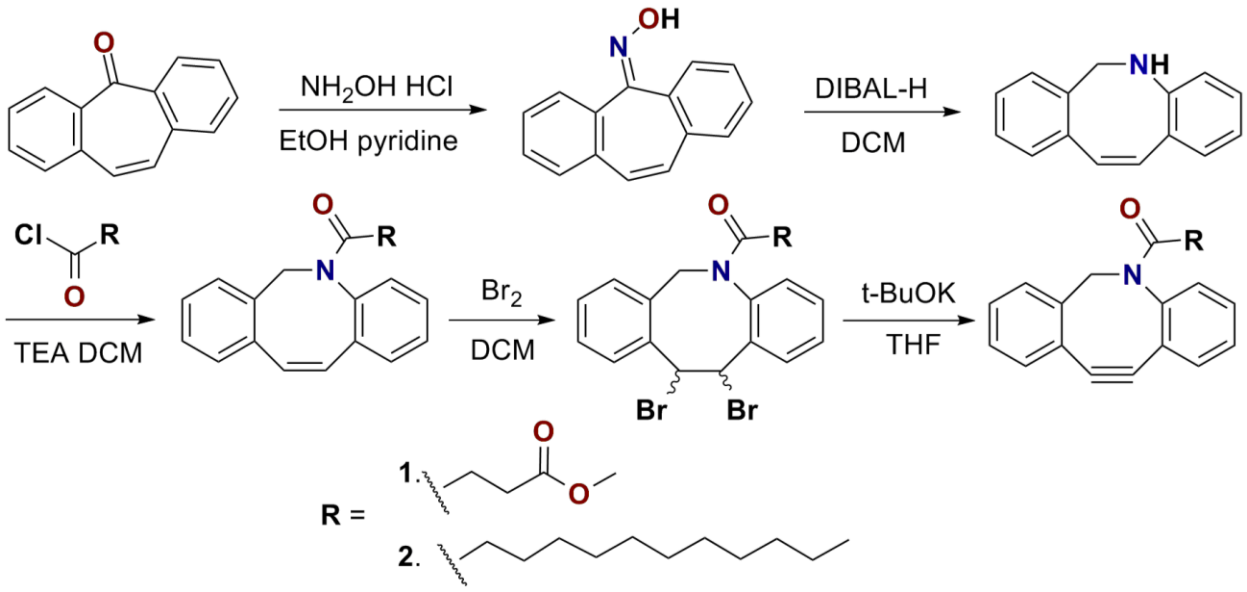

Figure 25. Synthesis of compounds **1** and **2**.

2.2.3 Strain-promoted MOF PSM and comparison with CuAAC

For solvent exchange, typically a sample of as-synthesized N_3-bMOF-100 was thoroughly washed with DMF followed by dichloromethane (DCM) and then stored in DCM prior to reaction. A solution containing 1 equivalent (i.e., 1 mole of alkyne per 1 mole of azide in MOF sample) of either **1** or **2** in DCM was added to respective vials containing samples of solid DCM-exchanged N_3-bMOF-100, and these mixtures were allowed to stand overnight at room temperature. The following day, the supernatants were removed and the MOF crystals were thoroughly washed with DCM to remove any unreacted **1** or **2**. Light microscopy images (Figures 26) provided visual proof that the modified MOF crystals remained intact throughout the PSM reactions, and PXRD patterns of the product materials indicated retention of crystallinity (Figure 27).

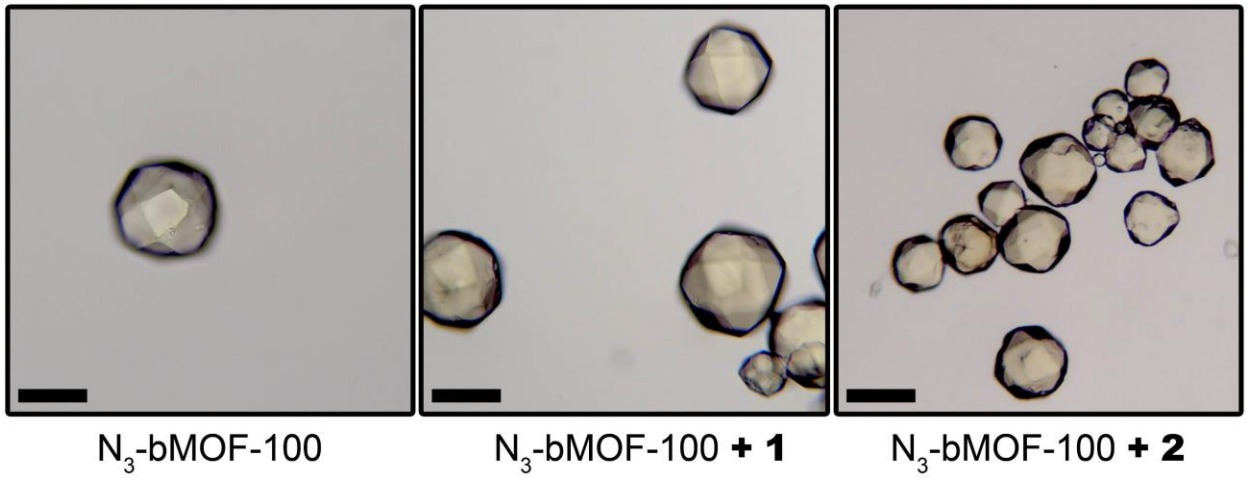

Figure 26. Light microscopic images of N_3-bMOF-100 and products after reaction with compounds **1** and **2** (scale bar: 80 μm).

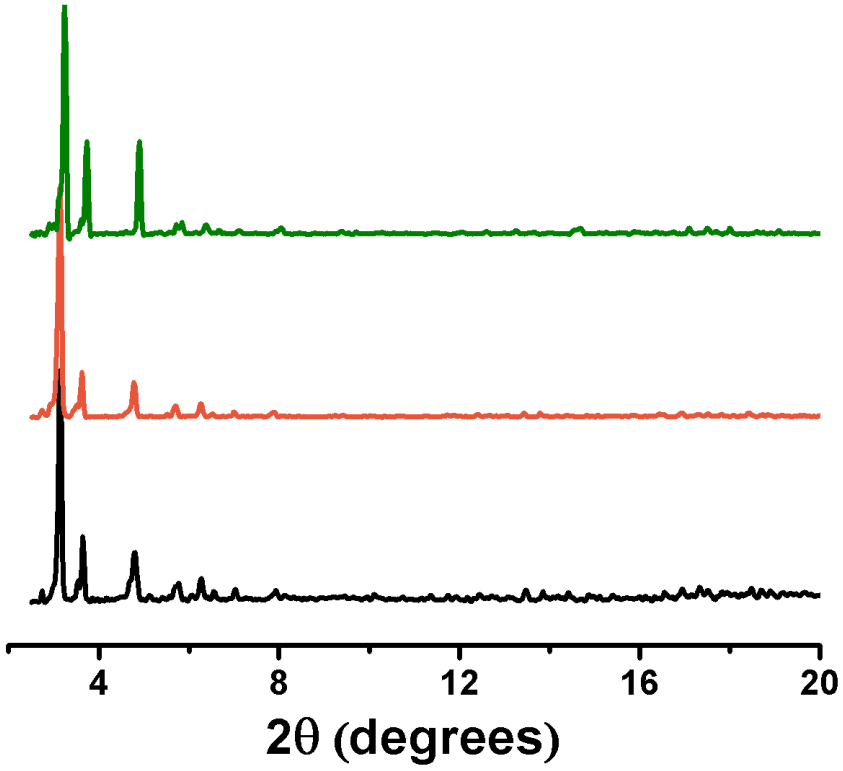

Figure 27. Comparing PXRD patterns of N_3-bMOF-100 (black) and PSM products with **1** (orange) and **2** (green).

Fourier-transform infrared (FTIR) spectroscopy (Figure 28) revealed that the strain-promoted click PSM procedure, in both cases, was nearly quantitative because the azide stretch (2116 cm^{-1}) present for the reactant MOF was nearly absent in the product MOFs after reaction with compounds **1** and **2**. Comparison of the thermogravimetric analysis (TGA) data for N_3-bMOF-100 to those for both **1**-bMOF-100 and **2**-bMOF-100 revealed a significant decrease in the amount of included solvent (Figure 29). This is reasonable considering the bulkiness and quantity of **1** and **2** now covalently attached to the framework. However, the MOFs can still be considered porous, which indicated there was still room in the pores for further modification.

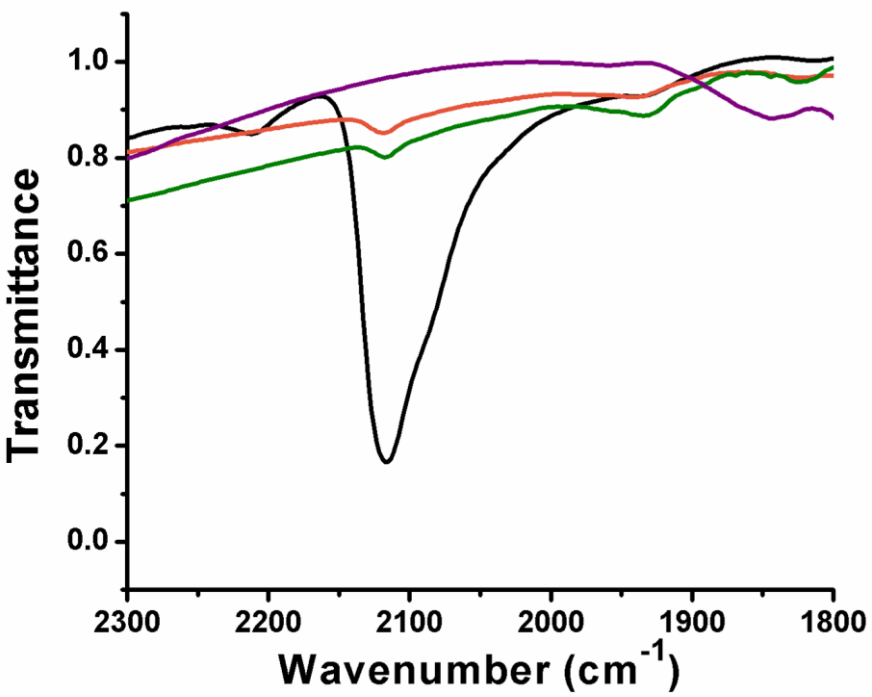

Figure 28. FTIR spectra comparing bMOF-100 (violet), N_3-bMOF-100 (black) and PSM products with **1** (orange) and **2** (green).

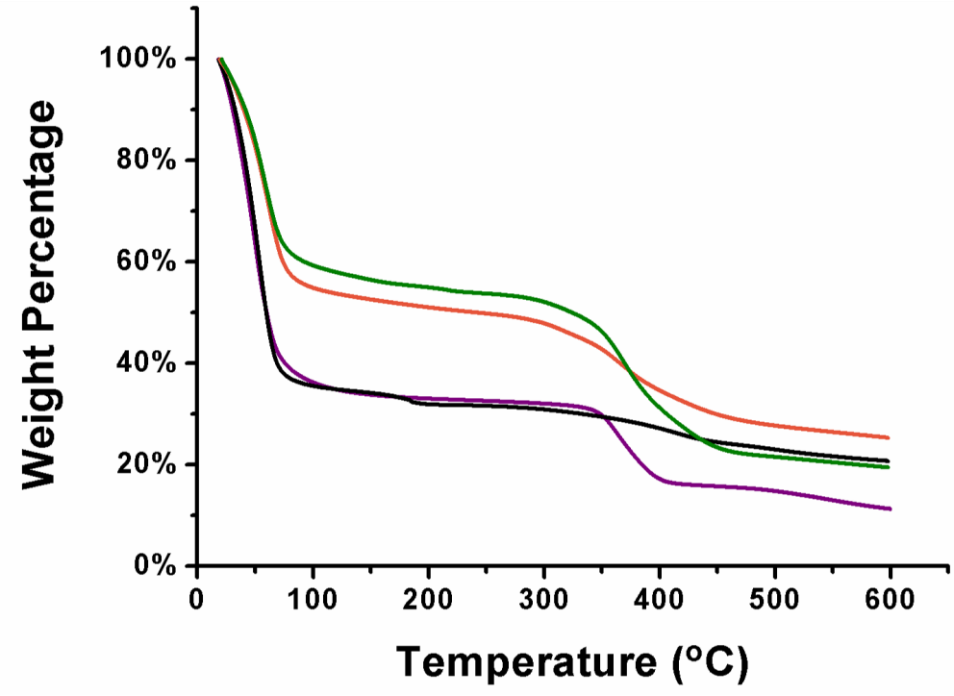

Figure 29. TGA plots comparing bMOF-100 (violet), N_3-bMOF-100 (black) and PSM products with **1** (orange) and **2** (green).

To further study the yield of the PSM reaction, the product MOFs were dissolved in dilute HCl/acetonitrile mixture and the resulting solution was analyzed using liquid chromatography coupled with mass spectrometry (LC-MS). For both samples, the negative mode total ion current (TIC) plots obtained from this analysis showed peaks for the click-modified BPDC molecules; the peak associated with unreacted 2-azidobiphenyldicarboxylic acid (m/z = 282) was nearly absent in both samples (Figures 30 and 31). For both PSM reactions with **1** and **2**, mass spectra of integrated chromatographic peaks also revealed the PSM products were indeed the major components in the mixture (Experimental Section 2.4.5).

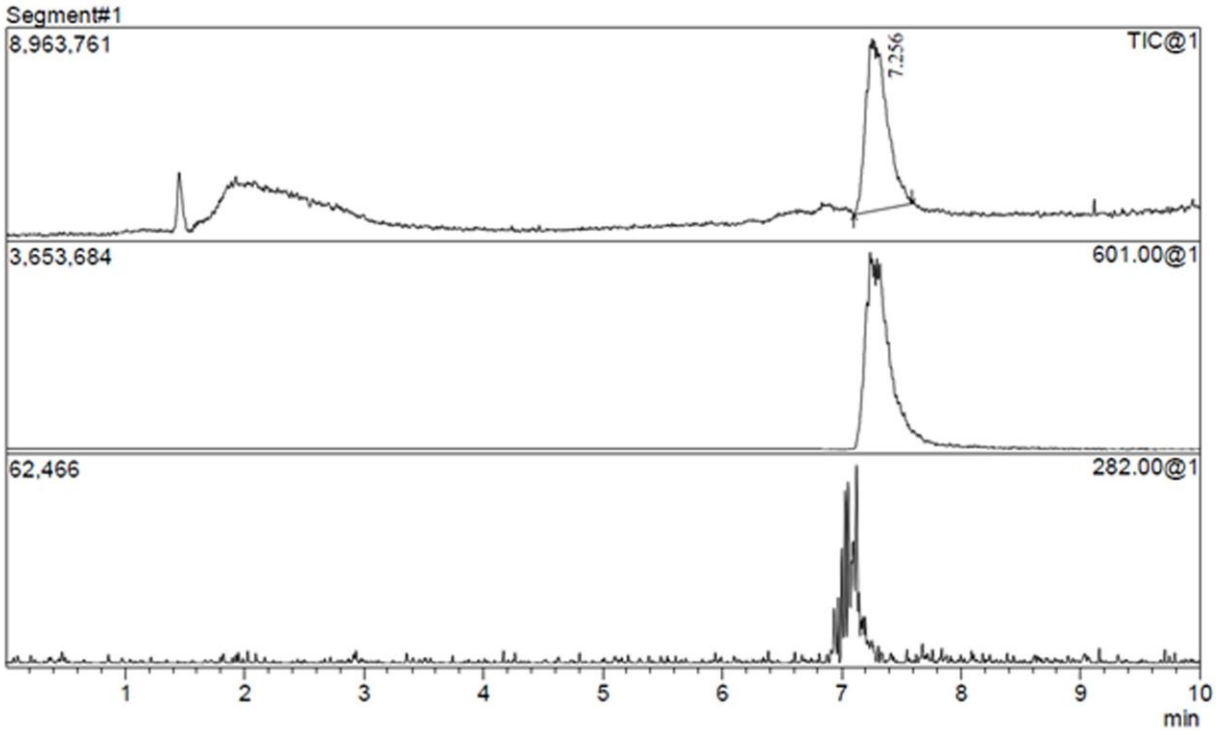

Figure 30. TIC chromatogram showing the presence of PSM product with **1** (m/z = 601) and very small quantity of unreacted H_2-N_3-BPDC (m/z = 282).

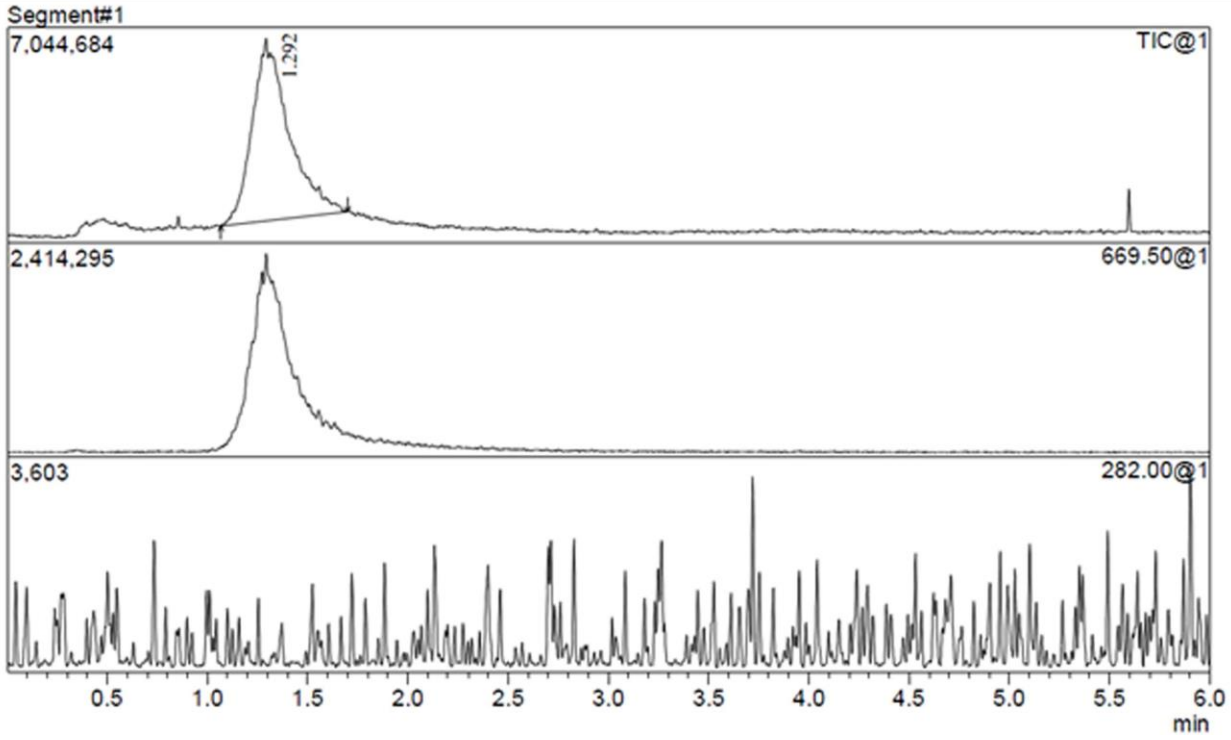

Figure 31. TIC chromatogram showing the presence of PSM product with **2** (m/z = 669.5) and absence of unreacted H_2-N_3-BPDC (m/z = 282).

Finally, the efficiency of this new strain-promoted click PSM methodology was compared to the established CuAAC PSM method. In short, a sample of N_3-bMOF-100 was reacted with 2 equivalents of 1-hexyne (i.e., 2 moles of 1-hexyne per 1 mole of azide in MOF sample) in the presence of CuI catalyst (Experimental Section 2.4.6). An FTIR spectrum of the product revealed a significant azide stretch (Figure 32, black). Therefore, the CuAAC reaction with 50 equivalents of 1-hexyne was performed next; in this case, FTIR confirmed complete consumption of the azide (Figure 32, red). The CuAAC approach required a large excess of alkyne to achieve levels of conversion that are comparable to those achieved via the strain-mediated approach, which only required 1 equivalent of alkyne.

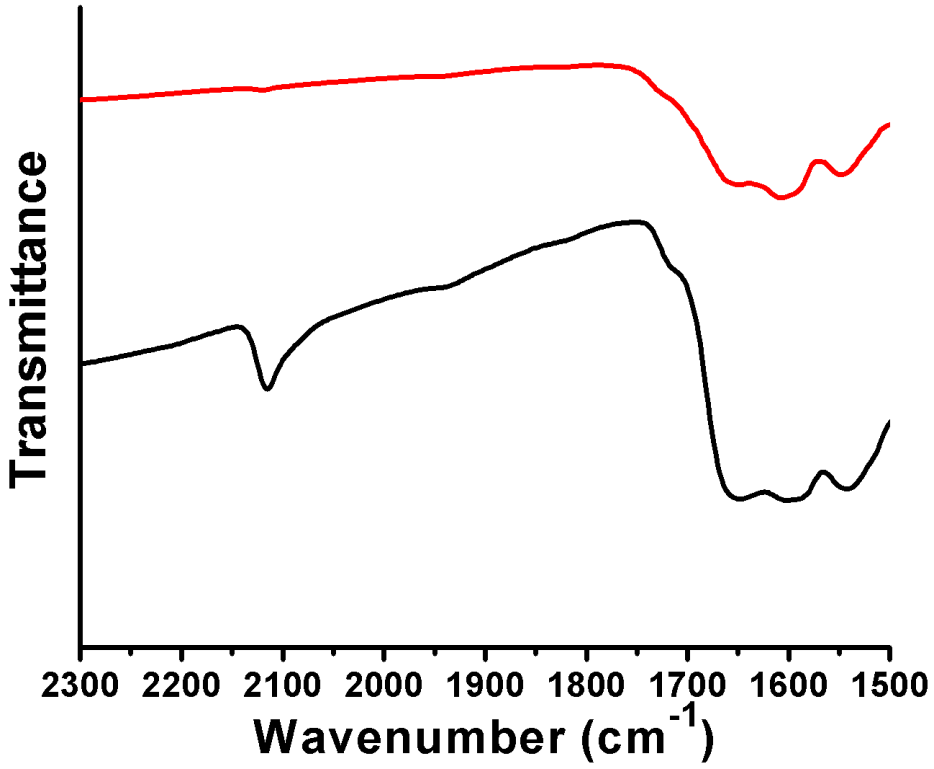

Figure 32. FTIR spectra characterizing CuAAC PSM products with 2 equiv. (black) and 50 equiv. (red) of 1-hexyne.

To summarize, these proof-of-principle studies demonstrated that strain-promoted click reactions in mesoporous N_3-bMOF-100 samples proceeded nearly quantitatively under ambient conditions and did not impact the structural integrity of the MOF. These reactions proceeded more efficiently than their Cu-catalyzed counterpart and they also had the added benefit of being free of byproduct (Cu^+, H_2O, or HCl, for example). It is important to realize that **1**, with its ester functionality, can easily be modified with other molecules and functional groups; therefore, **1** was an ideal platform molecule for this straightforward PSM methodology. In addition, a variety of other strained alkynes are commercially available, which should allow for the broad application of this strategy.

2.2.4 Tandem MOF PSM based on strain-promoted click chemistry

To exploit the orthogonality and scope of this PSM methodology, a succinimide-modified cyclooctyne derivative **3** was synthesized. Compounds like **3** are often used for coupling to primary amines, such as those at the N-termini of peptides. Reaction of **3** with N_3-bMOF-100 yielded the succinimide-decorated product MOF. Then this MOF was soaked in a solution of di-L-phenylalanine, a bulky dipeptide, yielded Phe_2-bMOF-100 with di-L-phenylalanine peptides anchored to its channel walls (Figure 33, Experimental Section 2.4.7). In principle, this straightforward bioconjugation strategy could be used to tether other peptides, proteins (including enzymes), polymers, dyes, and nanoparticles to the internal surface of a mesoporous MOF.

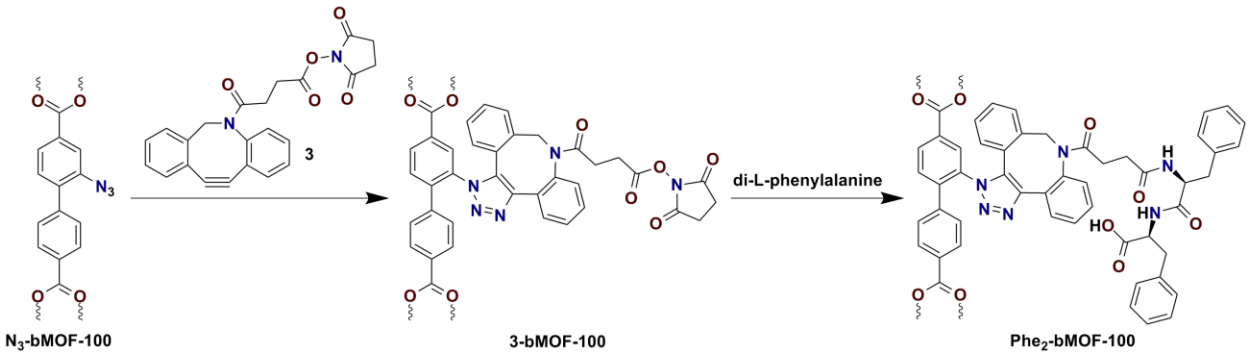

Figure 33. PSM with **3** and subsequent conjugation with Phe_2.

2.3 CONCLUSION

It was demonstrated that strain-promoted click chemistry was very efficient in postsynthetic modification of mesoporous N_3-bMOF-100. This modification strategy was mild, orthogonal and nearly quantitative. Different functional groups including reactive succinimide can be introduced

into the MOF using this method. Tandem modification can be achieved taking advantage of the reactive sites imparted.

Being a quantitative reaction that was also compatible with reactive groups, this method should allow us to achieve multi-functionalization via dose control and simple stepwise modification. As depicted in Figure 34, complex mesopores could be realized using this straightforward and orthogonal methodology.

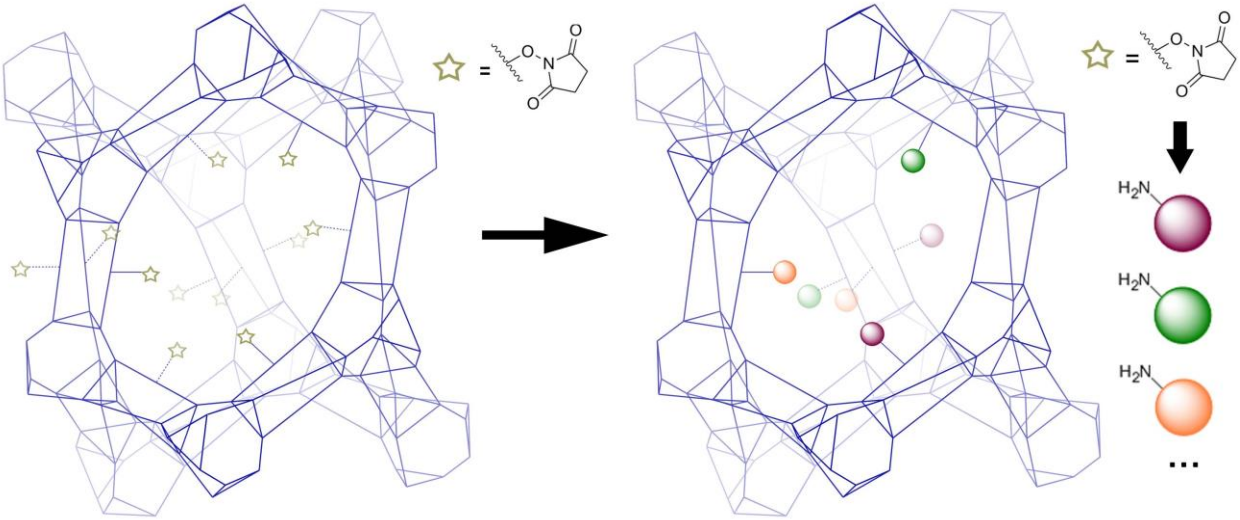

Figure 34. Schematic visualization of multi-functionalization via strain-promoted click PSM.

2.4 EXPERIMENTAL SECTION

2.4.1 General procedure

All purchased chemicals were used without further purification. The elemental analyses (EA) were performed by the University of Illinois, Department of Chemistry Microanalysis

Laboratory using an Exeter Analytical CE440. Powder X-ray diffraction (PXRD) patterns were collected using a Bruker AXS D8 Discover powder diffractometer at 40 kV, 40 mA for Cu Kα, (λ = 1.5406 Å) with a scan speed of 0.20 sec/step from 2.5 to 20 º at a step size of 0.02 º. ^{1}H NMR and ^{13}C NMR spectra were obtained using a Bruker Avance III 400 MHz and 500 MHz spectrometers. Chemical shifts are in parts per million using the residual solvent peak (Chloroform-*d* and DMSO-d_6) as the reference value. Liquid chromatography-mass spectrometry (LC-MS) analyses were performed on a Shimadzu LCMS-2020. Two LC methods were employed both using water and acetonitrile eluents. In the first method, the flow rate was held steady at 0.2 mL/min and acetonitrile was increased steadily from 10 % to 90 % over 0-9 min and then reduced to 10% acetonitrile for the final minute. In the second method, the flow rate was held steady at 0.2 mL/min and the acetonitrile:water ratio was held constant at 1:1 for the entire 6 min running time. The ionization interface was simultaneous ESI & APCI. FTIR experiments were performed on a Bruker Vertex-70LS FTIR spectrometer. About 2 mg of MOF sample was ground and mixed with ~250 mg KBr to make the sample pellets; the background pellet contained 250 mg KBr. All spectra were collected using the Opus software interface from 400 cm^{-1} to 4000 cm^{-1} with a resolution of 4 cm^{-1}; 16 scans were collected for both background and sample. Light microscopic images of crystals were collected using an Olympus BH-2 microscope. Thermogravimetric analyses (TGA) were performed using a TGA Q500 thermal analysis system. All TGA experiments were performed under a N_2 atmosphere from about 20 °C to 600 °C at a rate of 5 °C /min. Data were analyzed using the TA Universal Analysis software package.

2.4.2 Synthesis of ligand H_2-N_3-BPDC

The synthetic route of 2-azido-1,1'-biphenyl-4,4'-dicarboxylic acid (H_2-N_3-BPDC) is shown in Figure 35.[34,113-115]

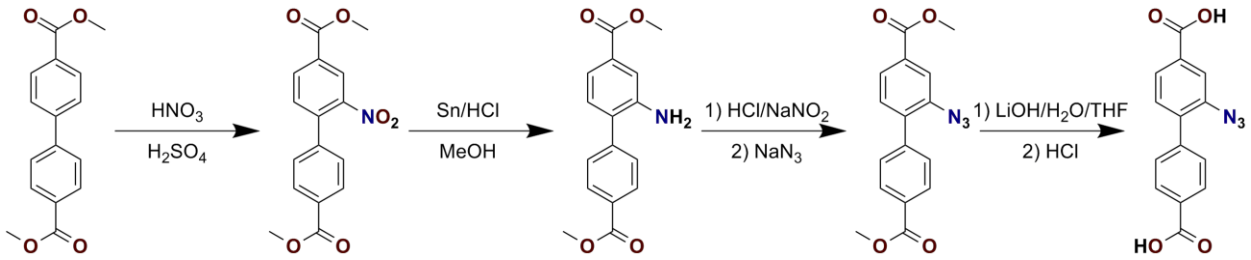

Figure 35. Synthetic route of H_2-N_3-BPDC.

2.4.2.1 Synthesis of dimethyl 2-nitro-1,1'-biphenyl-4,4'-dicarboxylate

2.00 g (7.40 mmol) dimethyl 1,1'-biphenyl-4,4'-dicarboxylate was dissolved in 15 mL concentrated H_2SO_4 with sonication and cooled to below 5 °C in an ice-water bath. A mixture of 482 µL of 69% HNO_3 (7.40 mmol) and 3 mL of concentrated H_2SO_4 was added to the above solution dropwise, while maintaining the temperature of the reaction mixture between 2 °C and 5 °C. After the addition was done, the reaction was allowed to proceed for another 20 minutes at <5 °C. Then the solution was poured onto ice (~300 mL), extracted with EtOAc three times, washed with water until pH = 7, dried over anhydrous $MgSO_4$, filtered and concentrated to dryness to afford a white solid. Yield 1.98 g (85%). ^{1}H NMR (400 MHz, $CDCl_3$) δ 8.56 (d, J = 1.6 Hz, 1H), 8.29 (dd, J = 8.0, 1.7 Hz, 1H), 8.12 (d, J = 8.6 Hz, 2H), 7.54 (d, J = 8.0 Hz, 1H), 7.40 (d, J = 8.6 Hz, 2H), 4.00 (s, 3H), 3.95 (s, 3H). ^{13}C NMR (100 MHz, $CDCl_3$) δ 166.68, 164.94, 149.17, 141.29, 139.72, 133.36, 132.34, 131.25, 130.72, 130.29 (2C), 128.11 (2C), 125.74, 53.12, 52.58.

2.4.2.2 Synthesis of dimethyl 2-amino-1,1'-biphenyl-4,4'-dicarboxylate

A solution of 2.00 g (6.35 mmol) dimethyl 2-nitro-1,1'-biphenyl-4,4'-dicarboxylate in 80 mL of MeOH was added Sn powder 4.40 g (36.67 mmol) while vigorous stirring, then was added 120 mL of 1M HCl. The mixture was heated to reflux for 5 hours before cooled down to room temperature and poured onto ice. 1M NaOH was then added to adjust the pH to around 10. The mixture was then filtered through a Büchner funnel and the collected dried residue was re-dispersed in hot EtOAc, then filtered through Celite in a Büchner funnel. The clear filtrate was then concentrated *in vacuo* to afford a white solid. Yield 1.16 g (64%). ^{1}H NMR (400 MHz, $CDCl_3$) δ 8.13 (d, J = 8.6 Hz, 2H), 7.55 (d, J = 8.6 Hz, 2H), 7.48 (dd, J = 7.9, 1.6 Hz, 1H), 7.45 (d, J = 1.6 Hz, 1H), 7.18 (d, J = 7.9 Hz, 1H), 4.15 (s, 2H), 3.95 (s, 3H), 3.91 (s, 3H). ^{13}C NMR (100 MHz, $CDCl_3$) δ 167.25, 166.98, 143.70, 143.58, 130.95, 130.74, 130.59, 130.46 (2C), 129.67, 129.11 (2C), 119.98, 116.92, 52.49, 52.39.

2.4.2.3 Synthesis of dimethyl 2-azido-1,1'-biphenyl-4,4'-dicarboxylate

A mixture of 963 mg (3.38 mmol) dimethyl 2-amino-1,1'-biphenyl-4,4'-dicarboxylate with 40 mL of concentrated HCl and 30 mL of H_2O was kept stirring at room temperature for 2 hours before cooled to ~0 °C. Then a solution of 242 mg (3.50 mmol) $NaNO_2$ in 5 mL of H_2O was added dropwise when the reaction mixture turned yellow and clear, indicating the formation of diazonium salt. Subsequently, a solution of 227 mg (3.50 mmol) NaN_3 in 5 mL of H_2O was added dropwise when white precipitates formed progressively. The mixture was kept at ~0 °C for additional 2 hours and at room temperature overnight before filtration. The residue was washed with H_2O and dried to afford an off-white solid. Yield 1.01 g (96%). ^{1}H NMR (400 MHz, $CDCl_3$) δ 8.09 (d, J = 8.1 Hz, 2H), 7.92 (s, 1H), 7.86 (d, J = 8.0 Hz, 1H), 7.52 (d, J = 8.2 Hz, 2H), 7.40 (d, J = 8.0 Hz, 1H), 3.95 (s, 3H), 3.93 (s, 3H). ^{13}C NMR (100 MHz, $CDCl_3$) δ

166.74, 165.93, 141.74, 137.80, 136.73, 131.21, 131.16, 129.70, 129.47 (2C), 129.43 (2C), 126.03, 119.92, 52.51, 52.24.

2.4.2.4 Synthesis of 2-azido-1,1'-biphenyl-4,4'-dicarboxylic acid

940 mg (3.02 mmol) dimethyl 2-azido-1,1'-biphenyl-4,4'-dicarboxylate was dissolved in 20 mL of THF when a solution of 380 mg (9.06 mmol) $LiOH \cdot H_2O$ in 10 mL of H_2O was added. The progress of the hydrolysis was monitored by either TLC or LC-MS. Upon completion, all volatiles were removed *in vacuo* and the remains were acidified with 1M HCl. The mixture was then filtered through a Büchner funnel and the residue was washed with H_2O before dried *in vacuo* to afford an off-white solid. Yield 819 mg (96%). ^{1}H NMR (400 MHz, DMSO-d_6) δ 13.23 (s, 2H), 8.02 (d, J = 8.2 Hz, 2H), 7.84 (s, 1H), 7.82 (d, J = 8.0 Hz, 1H), 7.64 (d, J = 8.2 Hz, 2H), 7.56 (d, J = 7.9 Hz, 1H). ^{13}C NMR (100 MHz, DMSO-d_6) δ 167.01, 166.27, 141.10, 137.15, 135.70, 131.88, 131.37, 130.22, 129.57 (2C), 129.18 (2C), 125.93, 119.86.

2.4.3 Solvothermal synthesis of MOFs and characterization

Crystals of bMOF-100 were synthesized based on literature.[108] Crystals of N_3-bMOF-100 were synthesized using the following procedure. Stock solutions of the starting materials were prepared: 0.05 M Zinc acetate dihydrate in DMF (A); 0.05 M adenine in DMF (B); and 0.1 M H_2-N_3-BPDC in DMF (C). In a glass tube, A (0.3 mL), B (0.1 mL), and C (0.1 mL) were mixed together and H_2O (0.05 mL) was added. The tube and its contents were frozen in liquid N_2 and evacuated *in vacuo*. The tube was then flame sealed and kept in an 85 °C oven for 10-14 hours to yield polyhedral crystals. Thereafter, the tube was opened and the crystals were transferred to a microcentrifuge tube and washed with DMF (5X) and then DCM (10X).

The crystals were allowed to dry under Ar flow to yield approximately 2 mg (67%). TGA and CHN elemental analysis were performed on combined samples prepared in this manner, respectively. CHN elemental analysis results: $C_{118.25}Cl_{12.5}H_{118.5}N_{42}O_{26}Zn_8$ = Zn_8(adenine)$_4$(N_3-BPDC)$_6O_2$•4Me_2NH_2, 6.25CH_2Cl_2. Calculated: *C*, 40.34; *H*, 2.56; *N*, 16.47. Found: *C*, 40.44; *H*, 2.23; *N*, 16.04. After extensive evacuation of the crystals *in vacuo*, ^{1}H NMR and LC-MS were performed after acid digestion using a small amount of concentrated DCl/D_2O in DMSO-d_6. FTIR was performed using KBr pellet that contains dried MOF. Powder X-ray diffraction and light microscope experiments were performed when these crystals were re-dispersed in DMF. The ^{1}H NMR spectrum (Figure 36) for the digested crystals confirmed the presence of N_3-BPDC and the expected composition of the material. The ratio of hydrogens on adenine to the ones on N_3-BPDC is as expected based on the formula.

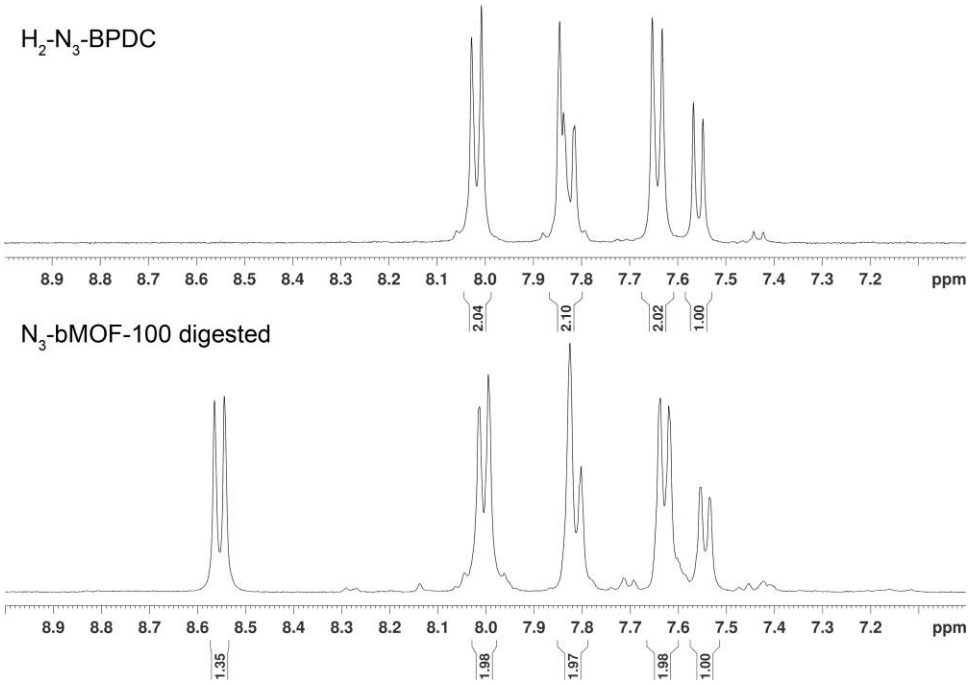

Figure 36. ^{1}H NMR spectra of H_2-N_3-BPDC and acid-digested N_3-bMOF-100.

2.4.4 Synthesis of DIBAC compounds

The synthetic route of DIBAC derivatives **1**, **2**, and **3** is shown in Figure 37.[111-112]

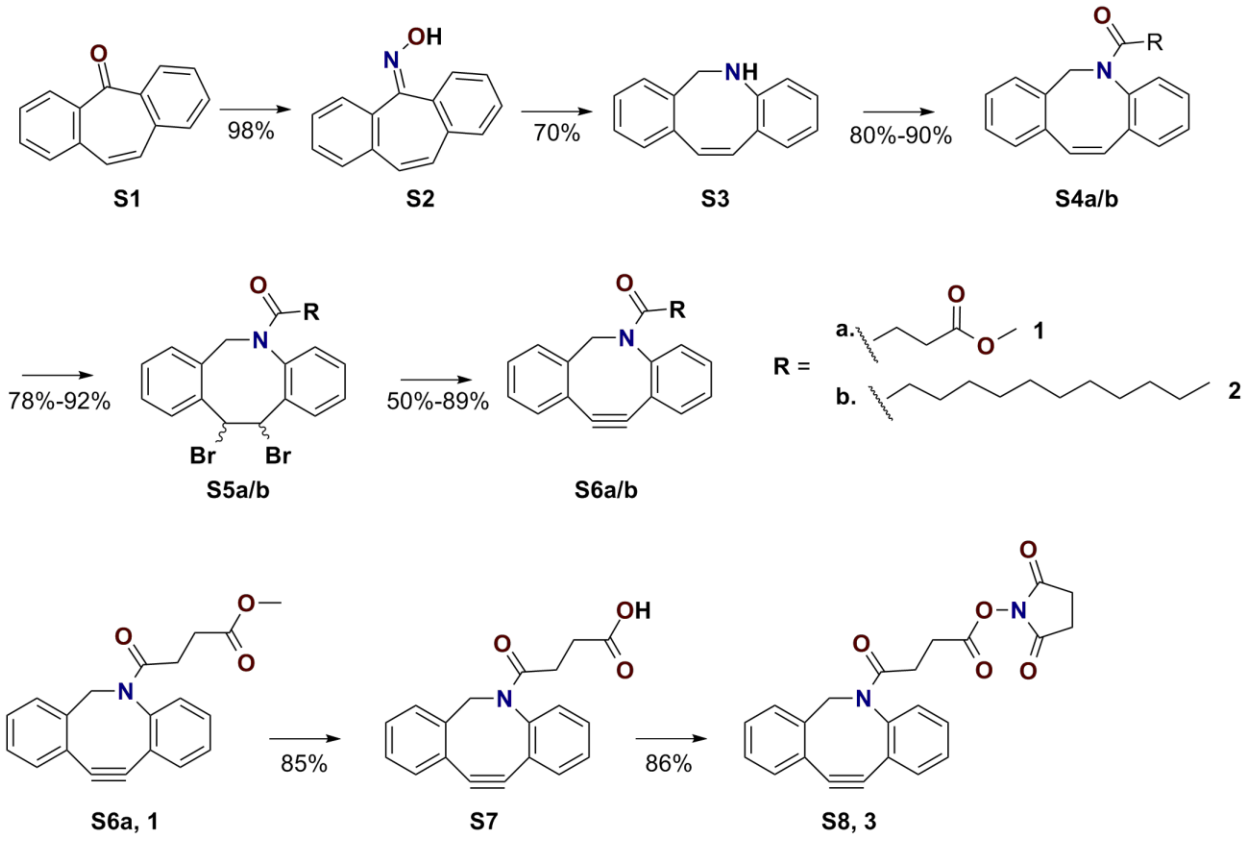

Figure 37. Synthetic route of DIBAC compounds **1**, **2**, and **3**.

2.4.4.1 Synthesis of 5*H*-dibenzo[7]annulen-5-one oxime (S2)

$NH_2OH \cdot HCl$ (1.04 g, 14.97 mmol) was dissolved in a hot mixture of absolute EtOH (7 mL) and pyridine (5 mL). To this solution was added dibenzosuberenone (**S1**) (1 g, 4.85 mmol) and pyridine (2 mL). The mixture was kept at reflux and monitored by TLC. When a complete disappearance of dibenzosuberenone was observed, all volatiles were removed *in vacuo*. The remains were re-dispersed between DCM and H_2O. The DCM phase was washed with another

portion of H_2O, dried over anhydrous $MgSO_4$, filtered, and concentrated *in vacuo* to afford a pinkish white solid. Yield 1.12 g (98 %). ^{1}H NMR (400 MHz, $CDCl_3$) δ 8.74 (s, 1H), 7.67 – 7.66 (m, 1H), 7.62 – 7.55 (m, 1H), 7.49 – 7.32 (m, 6H), 6.98 – 6.84 (m, 2H). ^{13}C NMR (100 MHz, $CDCl_3$) δ 156.62, 135.50, 134.62, 133.84, 130.87, 130.72, 130.56, 129.55, 129.23, 129.14, 129.04, 129.03, 128.92, 127.87, 127.74.

2.4.4.2 Synthesis of 5,6-Dihydrodibenzo[*b,f*]azocine (S3)

To a cool (< 5 °C) solution of oxime **S2** (2.26 mmol, 500 mg) in dry DCM (28 mL) under Ar was added DIBAL-H (16.5 mL of a 1 M solution in hexanes) via syringe while maintaining the temperature around 5 °C. The reaction mixture was kept at 5 °C for an additional 10 min and room temperature for 3 hours. The reaction completion was confirmed by TLC. Then the mixture was cooled to 0 °C followed by addition of NaF solid (3.38 g, 80.5 mmol) and H_2O (1.1 mL). The slurry was stirred at 0 °C for another 30 min before filtering through Celite in a Büchner funnel. The residue was thoroughly washed with EtOAc. The combined organic solution was concentrated *in vacuo* to yield a bright yellow-green solid. Yield 328 mg (70 %). ^{1}H NMR (400 MHz, $CDCl_3$) δ 7.29 – 7.22 (m, 1H), 7.21 – 7.14 (m, 3H), 6.97 (dd, J = 7.8, 1.5 Hz, 1H), 6.91 – 6.86 (ddd, J = 7.7, 7.2, 1.2 Hz, 1H), 6.60 (ddd, J = 7.7, 7.2, 1.2 Hz, 1H), 6.54 (d, J = 13.1 Hz, 1H), 6.47 (dd, J = 8.1, 1.2 Hz, 1H), 6.36 (d, J = 13.1 Hz, 1H), 4.58 (s, 2H), 4.35 (s, 1H). ^{13}C NMR (100 MHz, $CDCl_3$) δ 147.31, 139.47, 138.39, 134.94, 132.99, 130.38, 129.11, 128.20, 127.89, 127.64, 127.60, 122.01, 118.19, 117.98, 49.81.

2.4.4.3 Synthesis of Methyl 4-(dibenzo[*b,f*]azocin-5(6H)-yl)-4-oxobutanoate (S4a)

A solution of amine **S3** (200 mg, 0.97 mmol) and triethylamine (267 μL, 1.91 mmol) in DCM (6 mL) was cooled to 0 °C, followed by careful addition of methyl succinyl chloride (178

μL, 1.44 mmol). The reaction mixture was kept at 0 °C for an additional 30 min. and then at room temperature overnight. Thereafter, it was quenched with H_2O and diluted with DCM. The organic phase was washed with saturated $NaHCO_3$ solution (2X), 1M HCl (2X), brine (2X) and dried over anhydrous $MgSO_4$ and concentrated *in vacuo*. Then it was purified using column chromatography on 230-400 mesh silica (EtOAc:hexanes = 1:1) to yield a white solid. Yield 249 mg (80 %). ^{1}H NMR (400 MHz, $CDCl_3$) δ 7.31 – 7.27 (m, 5H), 7.21 – 7.13 (m, 3H), 6.82 (d, J = 12.9 Hz, 1H), 6.65 (d, J = 12.9 Hz, 1H), 5.55 (d, J = 15.0 Hz, 1H), 4.29 (d, J = 15.0 Hz, 1H), 3.65 (s, 3H), 2.68 – 2.60 (m, 1H), 2.55 – 2.40 (m, 2H), 2.11 – 1.98 (m, 1H). ^{13}C NMR (100 MHz, $CDCl_3$) δ 173.44, 170.87, 140.53, 136.50, 135.85, 134.60, 132.67, 131.83, 130.88, 130.18, 128.57, 128.28, 128.04, 127.31, 126.97, 54.50, 51.65, 29.57, 29.05.

2.4.4.4 Synthesis of N-dodecanoyl 5,6-dihydrodibenzo[*b,f*]azocine (S4b)

A solution of amine **S3 (**605 mg, 2.92 mmol) in DCM (15 mL) was cooled to 0°C followed by careful addition of lauroyl chloride (810 μL, 3.50 mmol). Then triethylamine (610 μL, 4.38 mmol) was added once solid precipitation was observed. Another 5 mL of DCM was added and the precipitation gradually disappeared. The reaction was allowed to stir at room temperature for 3 hours and TLC and LC-MS was used to monitor the reaction until complete conversion. The reaction was diluted with DCM and quenched by adding 1M NaOH solution and stirring for 20 min. The mixture was separated and the organic layer was washed with 1M NaOH solution (2X), 1M HCl (3X), brine (3X), dried over anhydrous $MgSO_4$, filtered, and then concentrated *in vacuo* before purification by column chromatography on 230-400 mesh silica (EtOAc:hexanes = 1:2) to afford a yellow oil. Yield 1024 mg (90 %). ^{1}H NMR (400 MHz, $CDCl_3$) δ 7.32 – 7.19 (m, 4H), 7.19 – 7.07 (m, 4H), 6.75 (d, J = 13.2 Hz, 1H), 6.56 (d, J = 13.2 Hz, 1H), 5.45 (d, J = 14.8 Hz, 1H), 4.18 (d, J = 14.8 Hz, 1H), 2.06 – 1.93 (m, 1H), 1.90 – 1.82

(m, 1H), 1.49 – 1.37 (m, 2H), 1.31 – 0.95 (m, 16H), 0.86 (t, J = 6.9 Hz, 3H). ^{13}C NMR (100 MHz, $CDCl_3$) δ 172.96, 141.40, 136.16, 135.86, 135.00, 132.47, 132.11, 131.38, 130.48, 128.26, 128.16, 127.69, 127.28, 127.27, 126.94, 54.61, 34.53, 31.89, 29.58, 29.55, 29.40, 29.31, 29.25, 29.01, 25.25, 22.67, 14.12.

2.4.4.5 Synthesis of methyl 4-(11,12-dibromo-11,12-dihydrodibenzo[*b*,*f*]azocin-5(6H)-yl)-4-oxobutanoate (S5a)

Amide **S4a** (317 mg, 0.99 mmol) was dissolved in DCM (16 mL) and cooled to 0 °C followed by careful addition of a solution of Br_2 (0.16 g, 0.99 mmol) in 5 mL DCM under Ar, while maintaining the temperature around 0 °C. The reaction mixture was stirred at 0 °C for 2 hours and quenched with saturated Na_2SO_3 solution (stirring for 20 min). The mixture was separated and the organic layer was washed with saturated Na_2SO_3 solution (3X), H_2O (2X), brine (1X), dried over anhydrous $MgSO_4$, and concentrated *in vacuo* before purification by column chromatography on 230-400 mesh silica (EtOAc:hexanes = 1:2 to 1:1.5) to yield a yellow-white solid (NMR showed that the product is actually a mixture of two stereoisomers with a ratio close to 9:1). Yield 370 mg (78 %). ^{1}H NMR (400 MHz, $CDCl_3$) δ 7.70 (d, J = 7.8 Hz, 1H), 7.30 – 6.97 (m, 6H), 6.87 (d, J = 7.4 Hz, 1H), 5.90 (d, J = 9.9 Hz, 1H), 5.80 (d, J = 14.9 Hz, 1H), 5.14 (d, J = 10.0 Hz, 1H), 4.17 (d, J = 14.9 Hz, 1H), 3.67 (s, 3H), 2.90 – 2.80 (m, 1H), 2.67 – 2.54 (m, 2H), 2.51 – 2.42 (m, 1H). ^{13}C NMR (100 MHz, $CDCl_3$) δ 173.58, 171.99, 138.32, 137.06, 136.94, 132.78, 130.81, 130.70, 130.65, 129.65, 129.49, 128.97, 128.90, 128.59, 60.10, 55.55, 52.56, 51.77, 30.65, 29.22.

2.4.4.6 Synthesis of N-dodecanoyl 5,6,11,12-tetrahydro-11,12-dibromodibenzo[*b,f*]azocine (S5b)

Amide **S4b** (1.016 g, 2.61 mmol) was dissolved in DCM (15 mL) and cooled to 0 °C followed by careful addition of a solution of Br_2 (0.418 g, 2.61 mmol) in 4 mL under Ar, while maintaining the temperature around 0 °C. The reaction mixture was stirred at 0 °C and monitored by LC-MS; additional Br_2 was added when necessary. After 12 hours, the reaction was quenched with saturated Na_2SO_3 solution (stirring for 20 min). The mixture was then separated and the organic layer was washed with saturated Na_2SO_3 solution (3X), H_2O (2X), brine (1X), dried over anhydrous $MgSO_4$, and concentrated *in vacuo* before it was purified using column chromatography on 230-400 mesh silica (EtOAc:hexanes = 1:4) to yield a yellow oil (NMR showed that the product is a mixture of two stereoisomers, but one of them is of only trace amount). Yield 1.315 g (92 %). ^{1}H NMR (400 MHz, $CDCl_3$) δ 7.70 (d, J = 7.7 Hz, 1H), 7.23 – 7.08 (m, 3H), 7.07 – 6.98 (m, 2H), 6.95 (d, J = 7.7 Hz, 1H), 6.86 (d, J = 7.4 Hz, 1H), 5.92 (d, J = 9.9 Hz, 1H), 5.80 (d, J = 14.9 Hz, 1H), 5.13 (d, J = 9.9 Hz, 1H), 5.13 (d, J = 9.9 Hz, 1H), 4.14 (d, J = 14.9 Hz, 1H), 2.32 – 2.21 (m, 1H), 2.11 – 1.99 (m, 1H), 1.68 – 1.63 (m, 2H), 1.32 – 1.10 (m, 16H), 0.85 (t, J = 6.8 Hz, 3H)..^{13}C NMR (100 MHz, $CDCl_3$) δ 173.80, 138.20, 137.45, 137.11, 133.09, 130.67, 130.46, 130.37, 129.58, 129.30, 128.90, 128.79, 128.60, 60.04, 55.71, 52.43, 35.98, 31.89, 29.59, 29.44, 29.40, 29.32, 25.24, 22.68, 14.12.

2.4.4.7 Synthesis of methyl 4-(11,12-didehydrodibenzo[*b,f*]azocin-5(6H)-yl)-4-oxobutanoate (S6a, Compound 1)

Compound **S5a** (101 mg, 0.21 mmol) was dissolved in anhydrous THF (10 mL) under Ar and cooled to around -40 °C in a dry ice-acetonitrile bath followed by careful addition of a solution of tBuOK (0.4 mL, 0.4 mmol, 1 M in THF) via syringe. After 2 hours at -40 °C, another

0.16 mL of tBuOK (1M in THF) was added dropwise via syringe. After another hour, LC-MS showed complete conversion. The reaction mixture was then poured into brine (25 mL) and extracted with DCM (3X). The combined organic phase was washed with brine (2X), dried over anhydrous $MgSO_4$, and concentrated *in vacuo* before purification by column chromatography on 230-400 mesh silica (EtOAc:hexanes = 1:2) to yield a yellow-white solid. Yield 34 mg (50%). ^{1}H NMR (400 MHz, $CDCl_3$) δ 7.67 (d, J = 7.5 Hz, 1H), 7.51 – 7.45 (m, 1H), 7.42 – 7.20 (m, 6H), 5.15 (d, J = 13.9 Hz, 1H), 3.66 (d, J = 13.8 Hz, 1H), 3.54 (s, 3H), 2.71 (ddd, J = 16.4, 8.2, 6.2 Hz, 1H), 2.59 (ddd, J = 17.2, 8.2, 6.1 Hz, 1H), 2.32 (dt, J = 17.1, 6.2 Hz, 1H), 1.94 (dt, J = 16.3, 6.1 Hz, 1H). ^{13}C NMR (100 MHz, $CDCl_3$) δ 173.31, 171.67, 151.45, 148.00, 132.26, 129.28, 128.51, 128.29, 128.11, 127.72, 127.09, 125.46, 123.13, 122.67, 114.93, 107.68, 55.46, 51.62, 29.51, 29.06.

2.4.4.8 Synthesis of N-dodecanoyl 5,6-dihydro-11,12-didehydrodibenzo[*b*,*f*]azocine (S6b, Compound 2)

Compound **S5b** (500 mg, 0.91 mmol) was dissolved in anhydrous THF (10 mL) under Ar and cooled to around -40 °C in a dry ice-acetonitrile bath followed by careful addition of a solution of tBuOK (1.82 mL, 1.82 mmol, 1 M in THF) via syringe. After 2 hours at -40 °C, another 0.6 mL of tBuOK (1M in THF) was added dropwise via syringe. After another hour, LC-MS showed complete reaction. The reaction mixture was then poured into brine (20 mL) and extracted with DCM (3X). The combined organic phase was washed with brine (2X), H_2O (1X), dried over anhydrous $MgSO_4$, and then concentrated *in vacuo* before purification by column chromatography on 230-400 mesh silica (EtOAc:hexanes = 1:4) to yield a yellow-green oil. Yield 314 mg (89 %). ^{1}H NMR (400 MHz, $CDCl_3$) δ 7.74 (d, J = 7.5 Hz, 1H), 7.51 – 7.19 (m, 7H), 5.19 (d, J = 13.8 Hz, 1H), 3.67 (d, J = 13.7 Hz, 1H), 2.18 (dt, J = 14.8, 7.3 Hz, 1H), 1.96 (dt,

J = 15.1, 7.5 Hz, 1H), 1.47 – 1.36 (m, 2H), 1.34 – 0.96 (m, 16H), 0.90 (t, J = 7.0 Hz, 3H). ^{13}C NMR (100 MHz, $CDCl_3$) δ 173.66, 152.13, 148.15, 132.38, 128.94, 128.26, 128.21, 127.82, 127.62, 127.02, 125.37, 123.15, 122.62, 115.15, 107.90, 55.20, 34.79, 31.91, 29.58, 29.51, 29.38, 29.31, 29.15, 28.83, 25.37, 22.68, 14.12.

2.4.4.9 Synthesis of 4-(11,12-didehydrodibenzo[*b,f*]azocin-5(6H)-yl)-4-oxobutanoic acid (S7)

A solution of compound **S6a (**40 mg, 0.12 mmol) in anhydrous THF (2.5 mL) was added to a solution of $LiOH{\cdot}H_2O$ (6.4 mg, 0.15 mmol) in H_2O (0.5 mL). The reaction was allowed to proceed under stirring at room temperature and monitored by TLC. Upon complete conversion, it was diluted with H_2O and subsequently adjusted to pH~14 using 2M NaOH solution. The mixture was washed with DCM (2X), acidified to pH~2 using 2M HCl solution and then extracted using DCM (4X). The combined organic phase was dried over anhydrous $MgSO_4$ and concentrated *in vacuo* to yield a yellow-white solid. Yield 33 mg (85 %). ^{1}H NMR (400 MHz, $CDCl_3$) δ 7.66 (d, J = 7.4 Hz, 1H), 7.47 – 7.19 (m, 7H), 5.14 (d, J = 13.9 Hz, 1H), 3.68 (d, J = 13.8 Hz, 1H), 2.70 (ddd, J = 16.5, 8.9, 5.2 Hz, 1H), 2.58 (ddd, J = 16.9, 8.9, 5.1 Hz, 1H), 2.34 (ddd, J = 16.9, 6.4, 5.3 Hz, 1H), 1.96 (ddd, J = 16.5, 6.3, 5.2 Hz, 1H). ^{13}C NMR (100 MHz, $CDCl_3$) δ 176.21, 172.36, 151.00, 147.68, 132.26, 129.10, 128.57, 128.41, 128.34, 127.87, 127.21, 125.58, 123.00, 122.67, 115.04, 107.45, 55.67, 29.49, 29.46.

2.4.4.10 Synthesis of 2,5-dioxopyrrolidin-1-yl 4-(didehydrodibenzo[*b,f*]azocin-5(6H)-yl)-4-oxobutanoate (S8, Compound 3)

To a solution of compound **S7** (12.6 mg, 0.043 mmol) in DCM (2 mL) was added *N*-hydroxysuccinimide (5.4 mg, 0.047 mmol) and a solution of EDC·HCl (9 mg, 0.047 mmol) in 1 mL of DCM. The reaction was allowed to proceed under stirring at room temperature and

monitored by TLC. Upon complete conversion, it was diluted with DCM, washed with saturated NaCl solution (3X), dried over anhydrous $MgSO_4$, and concentrated *in vacuo* to yield a yellow solid. The product was used without further purification. Yield 14.3 mg (86 %). ^{1}H NMR (500 MHz, $CDCl_3$) δ 7.67 (d, J = 7.6 Hz, 1H), 7.43 – 7.24 (m, 7H), 5.16 (d, J = 13.9 Hz, 1H), 3.67 (d, J = 13.9 Hz, 1H), 2.95 (dt, J = 17.5, 7.6 Hz, 1H), 2.84 – 2.77 (m, 1H), 2.77 (s, 4H), 2.65 – 2.58 (m, 1H), 2.06 (ddd, J = 16.8, 7.8, 5.4 Hz, 1H). ^{13}C NMR (100 MHz, $CDCl_3$) δ 170.26, 168.84, 168.29, 151.01, 147.77, 132.27, 129.09, 128.62, 128.36, 127.83, 127.23, 125.54, 123.03, 122.73, 115.01, 107.53, 55.58, 29.18, 26.42, 25.51.

2.4.5 Strain-promoted click PSM reactions and characterization

Based on the protocol described in 2.4.3, adenine (5×10^{-6} mol) is the limiting reagent in a typical synthesis of N_3-bMOF-100. Assuming 100% conversion, there should be a total of 7.5×10^{-6} mol of N_3-BPDC (7.5×10^{-6} mol azide groups) in the resulting product, based on the ratio of adenine:N_3-BPDC (4:6). Since the product yield is approximately 67%, approximately 5×10^{-6} mol azide groups should be expected in the final product. Based on this, 5×10^{-6} mol, or one equivalent, of either **1** or **2** was used for the PSM reactions.

In a typical strain-promoted click reaction, a DCM solution of 5×10^{-6} mol of **1** or **2** (1.6 mg and 1.9 mg, respectively) was added to a microcentrifuge tube containing pre-washed MOF crystals. After vortexing for a few seconds, the tube was allowed to stand at room temperature overnight. Then, the supernatant was removed and the crystals were washed with DCM (10X) to remove any unreacted **1** or **2**. Solvent was slowly removed by Ar flow. CHN elemental analysis was performed: $C_{240}Cl_{16}H_{224}N_{48}O_{44}Zn_8$ = Zn_8(adenine)$_4$(N_3-BPDC + **1**)$_6O_2$ • $4Me_2NH_2$, $8CH_2Cl_2$. Calculated: *C*, 56.83; *H*, 4.94; *N*, 10.97. Found: *C*, 57.08; *H*, 5.11; *N*, 11.02.

$C_{285}Cl_{22}H_{326}N_{48}O_{32}Zn_8$ = Zn_8(adenine)$_4$(N_3-BPDC + **2**)$_6O_2$ • 4Me_2NH_2, 11CH_2Cl_2. Calculated: *C*, 50.17; *H*, 3.49; *N*, 11.26. Found: *C*, 50.24; *H*, 3.51; *N*, 11.27.

After evacuation *in vacuo*, LC-MS (negative mode) was performed after acid digestion using acetonitrile and a small amount of concentrated HCl. FTIR was performed using KBr pellet that contained dried crystals. Powder X-ray diffraction and light microscope experiments were performed when these crystals were re-dispersed in DMF. Figure 38 and Figure 39 are averaged mass spectra of the integrated peaks indicated in Figure 30 and Figure 31, respectively. The major peaks in Figure 38 and Figure 39 correspond to the PSM products of N_3-bMOF-100 with **1** and **2**, respectively.

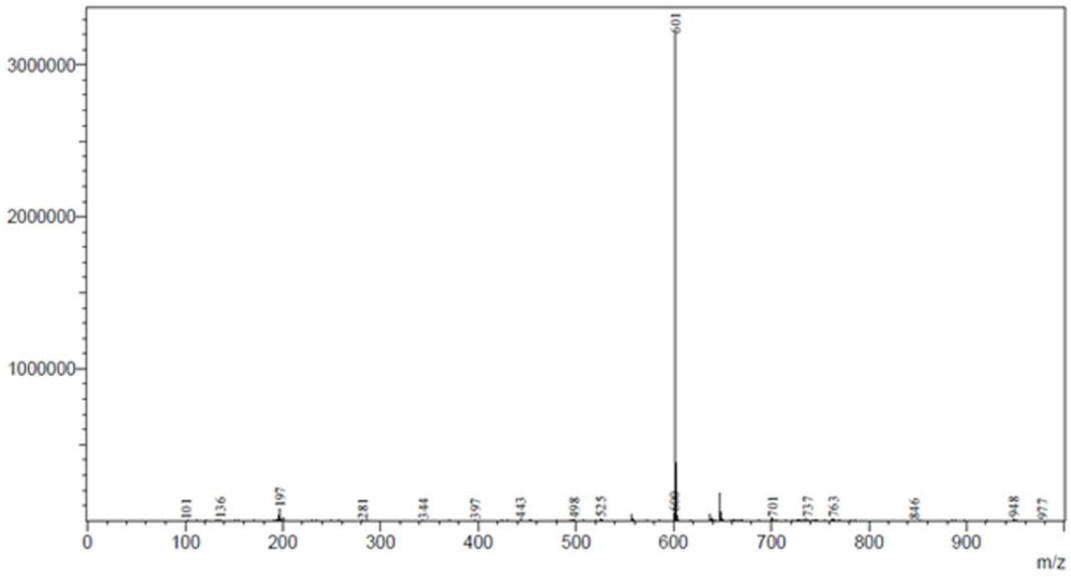

Figure 38. Mass spectrum for product of N_3-bMOF-100 and **1**.

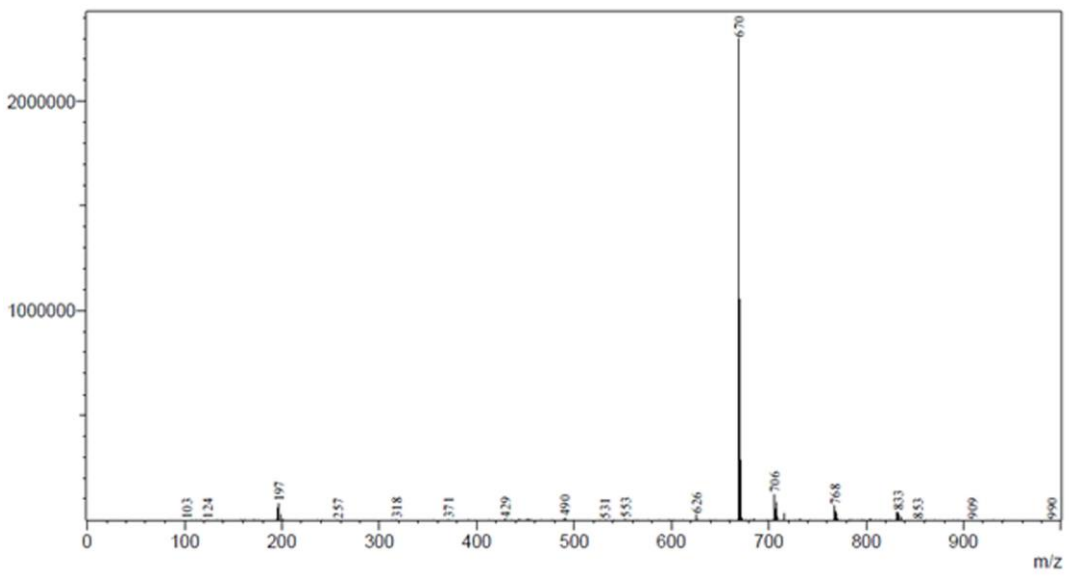

Figure 39. Mass spectrum for product of N_3-bMOF-100 and **2**.

2.4.6 Copper(I)-catalyzed click reactions of 1-hexyne with N_3-bMOF-100 and characterization

In a copper(I)-catalyzed click reaction, $2 \times (5 \times 10^{-6})$ mol (two equivalents to azide groups in MOF crystals) or $50 \times (5 \times 10^{-6})$ mol (fifty equivalents to azide groups in MOF crystals) of 1-hexyne was added to a microcentrifuge tube that contained pre-washed MOF crystals soaked in DCM (handled via the same procedure described in 2.4.3). Then, a visible amount of CuI was added. After vortexing for a few seconds, the tube was allowed to stand at room temperature for 48 hours. Thereafter, the supernatant was removed and the crystals were washed by DCM (10X) to remove any unreacted 1-hexyne. After removal of solvent using Ar flow, LC-MS was performed after acid digestion using acetonitrile and a small amount of concentrated HCl. FTIR was performed using a KBr pellet that contained ground dried crystals. Figures 40 to 43 are

negative mode mass spectra and TIC chromatograms (including MS peak search results), in which m/z = 281.6 is corresponding to the anion of unreacted H_2-N_3-BPDC, m/z = 363.7 is corresponding to the anion of the adduct of H_2-N_3-BPDC and 1-hexyne.

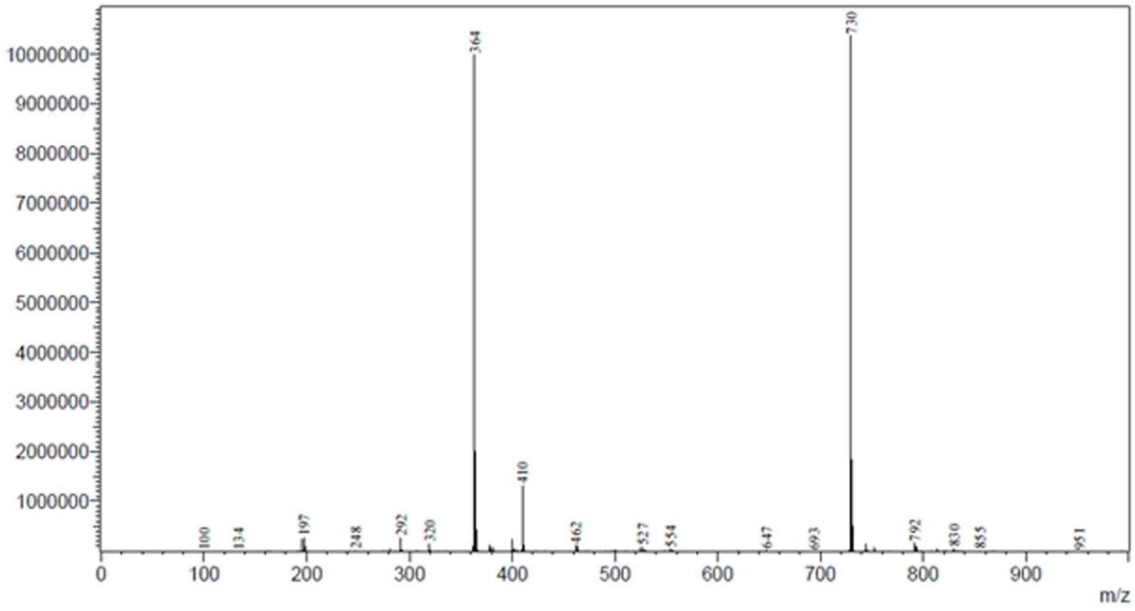

Figure 40. Mass spectrum of CuAAC product of N_3-bMOF-100 and 2 equiv. of 1-hexyne.

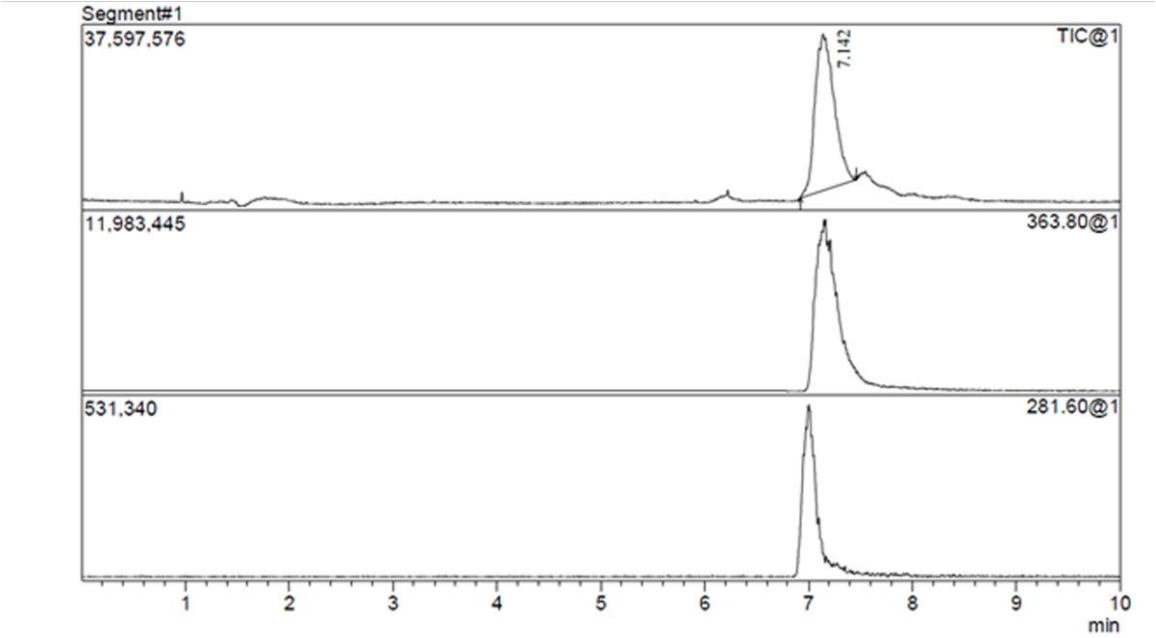

Figure 41. TIC chromatogram of CuAAC product of N_3-bMOF-100 and 2 equiv. of 1-hexyne.

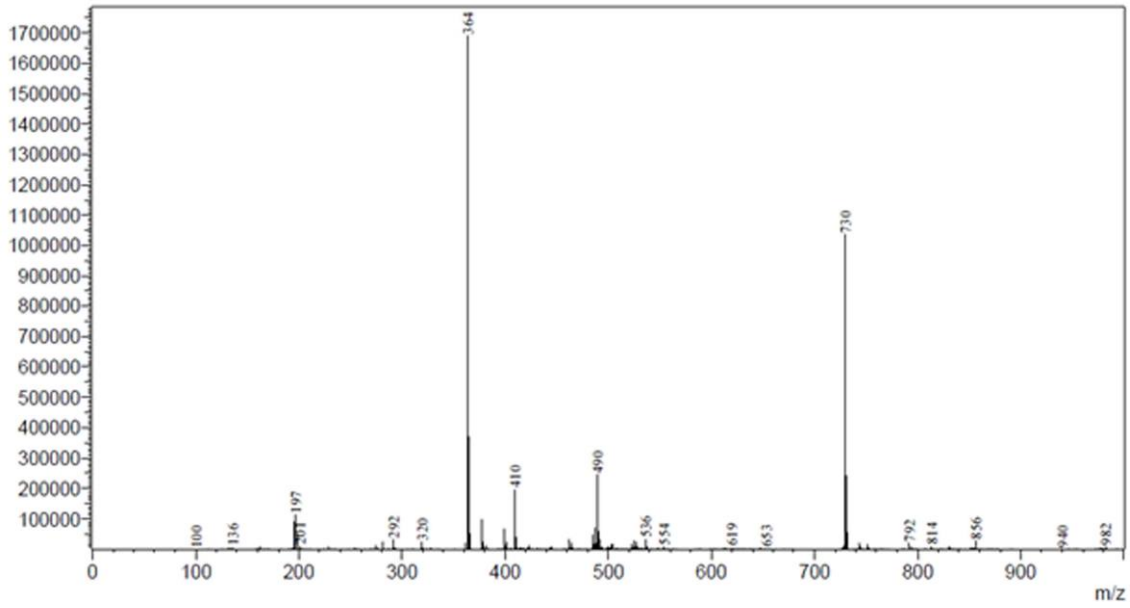

Figure 42. Mass spectrum of CuAAC product of N_3-bMOF-100 and 50 equiv. of 1-hexyne.

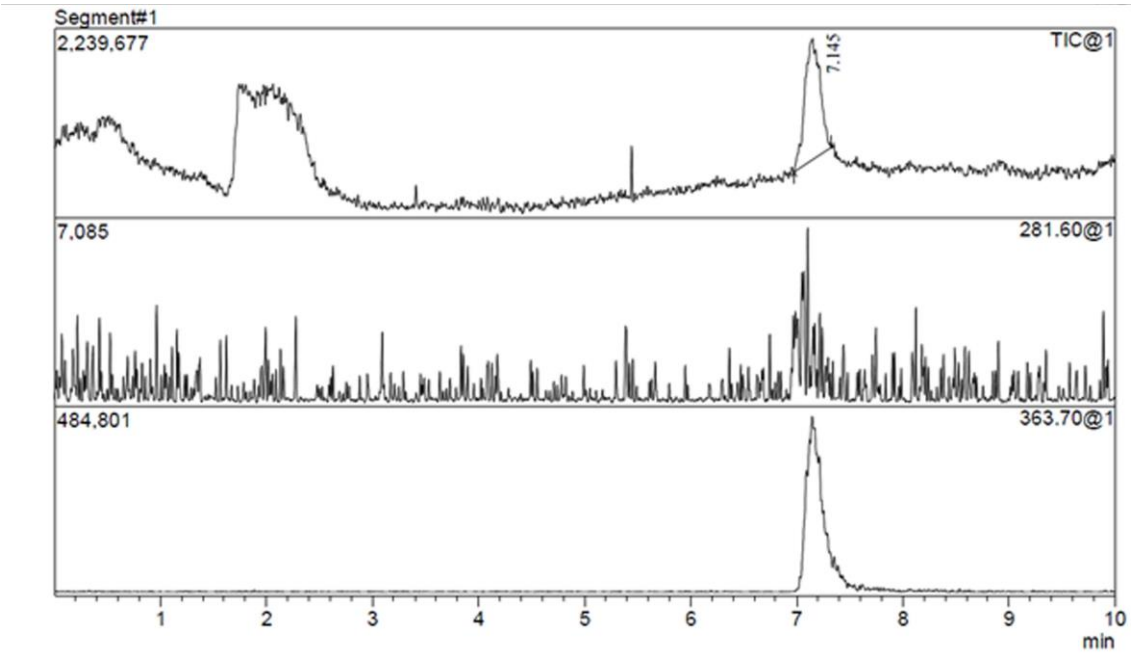

Figure 43. TIC chromatogram of CuAAC product of N_3-bMOF-100 and 50 equiv. of 1-hexyne.

2.4.7 Strain-promoted click PSM reaction with 3 and peptide coupling

Because of the limited amount of **3** available, less than 5×10^{-6} mol was used for this reaction. Pre-washed N_3-bMOF-100 crystals were soaked in a DCM solution containing about 1 mg of **3** and were allowed to stand at room temperature overnight. Then, a portion of the crystals were digested in 150 μL DMF containing 1 μL of conc. HCl. The resulting clear solution was subjected to LC-MS analysis (positive mode). The peaks with m/z = 686.00 and m/z = 708.00 correspond to the $[M+H]^+$ and $[M+Na]^+$ of the adduct of H_2-N_3-BPDC and **3**, respectively.

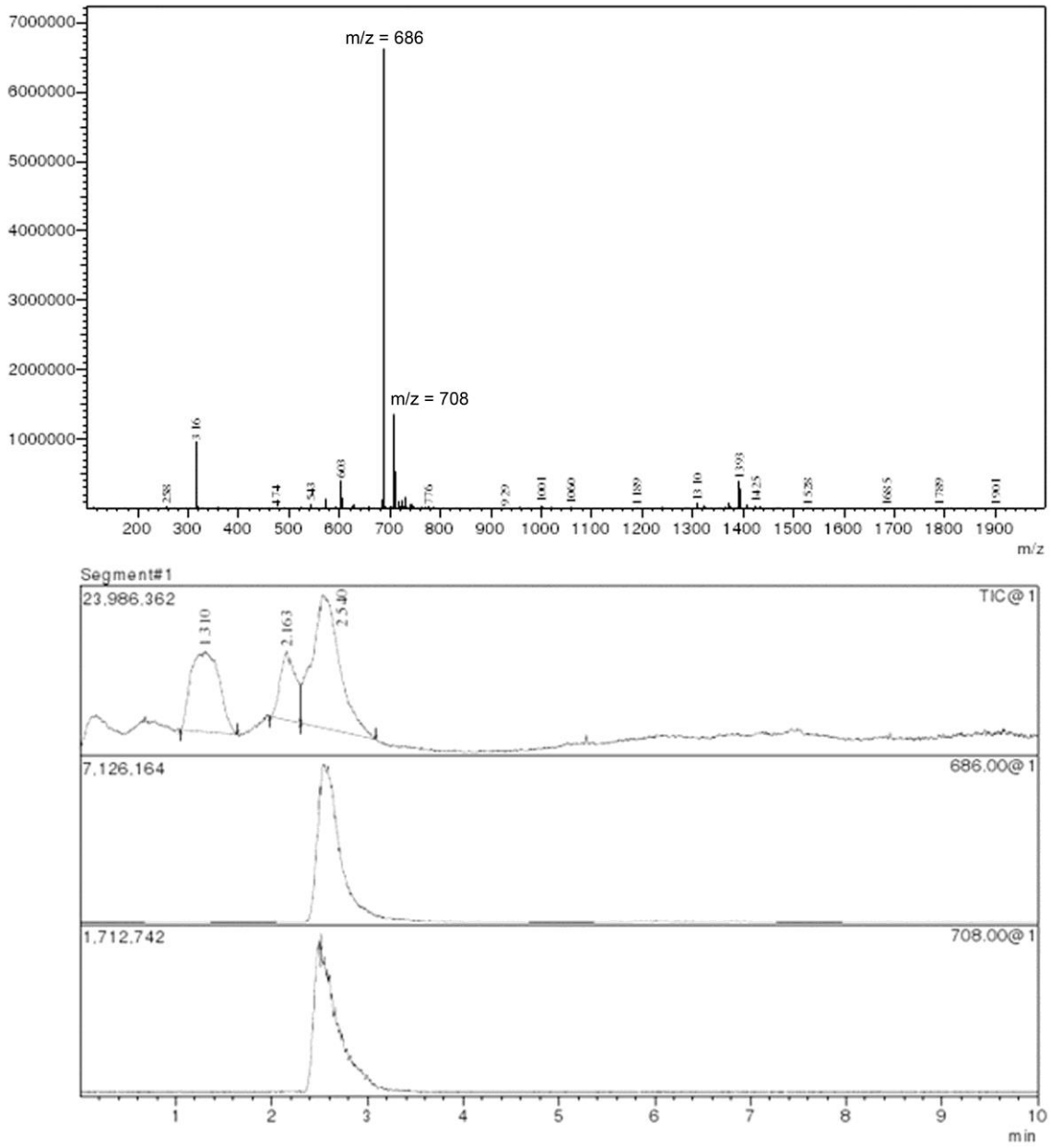

Figure 44. Mass spectrum (top) and TIC chromatogram (bottom) for product of N_3-bMOF-100 and **3**.

MOF crystals decorated by **3** were washed with DMF and then soaked in a DMF solution of dipeptide Phe-Phe. The molar amount of the peptide used was calculated to be equal to the amount of **3** used in the previous step. After reacting overnight at room temperature, a portion of

the crystals were digested using 150 μL DMF containing 1 μL of conc. HCl. The resulted clear solution was subjected to LC-MS analysis (positive mode). The peaks with m/z = 883.00 and m/z = 905.00 correspond to the $[M+H]^+$ and $[M+Na]^+$ of the compound Phe_2-bMOF-100 shown in Figure 33.

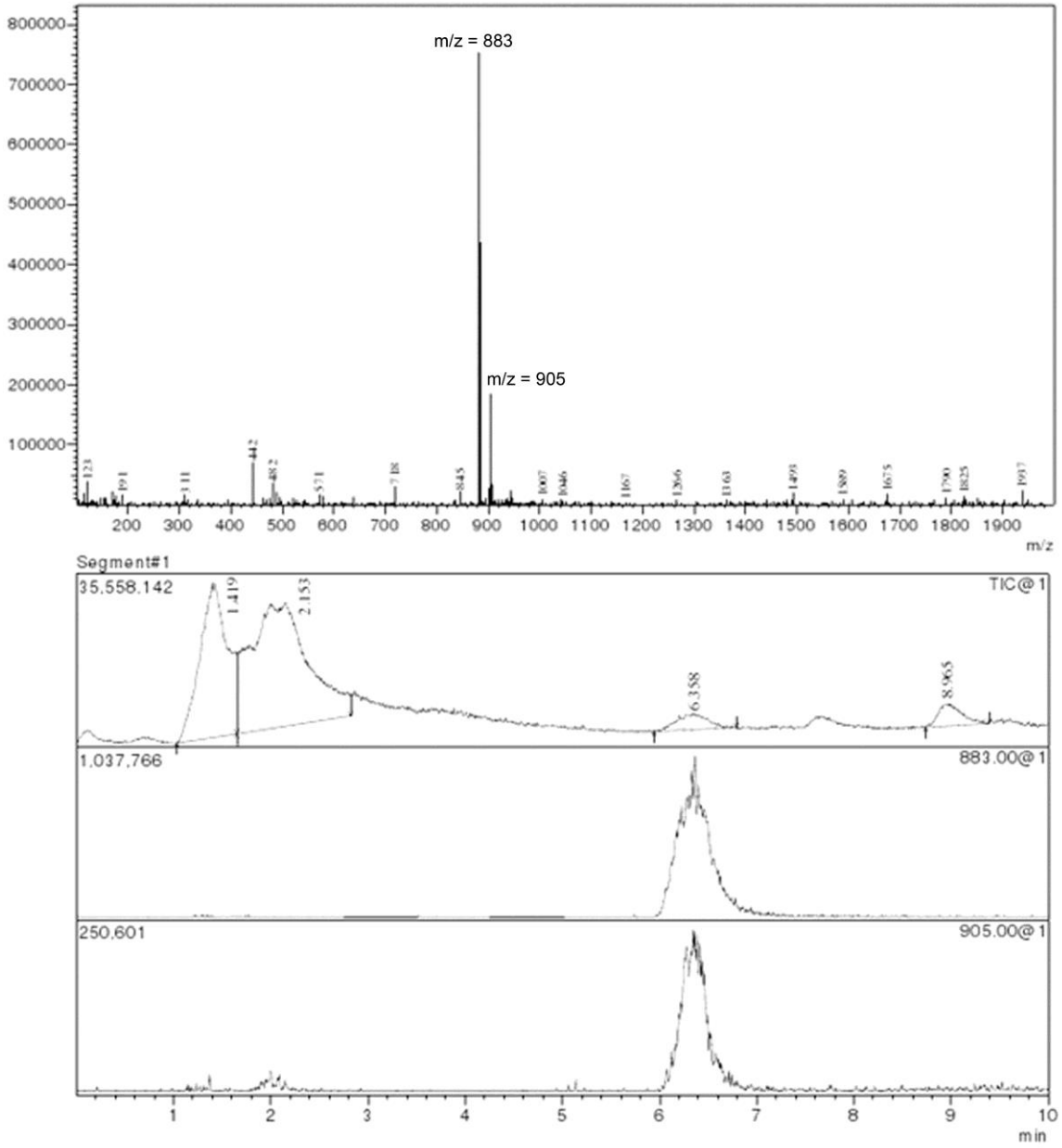

Figure 45. Mass spectrum (top) and TIC chromatogram (bottom) for Phe_2-bMOF-100.

3.0 ORTHOGONAL TERNARY FUNCTIONALIZATION OF A MESOPOROUS METAL−ORGANIC FRAMEWORK VIA SEQUENTIAL LIGAND EXCHANGE

This work, written in collaboration with Tian-Yi Luo, Evan S. Feura, Chen Zhang and Nathaniel L. Rosi*, has been published in the *Journal of American Chemical Society*, **2015**, *137*, 10508-10511.[116] Copyright 2015, American Chemical Society.

Tian-Yi Luo, Evan S. Feura, Chen Zhang assisted with preparation of some of the ligands and MOF samples. Tian-Yi Luo assisted with characterization of some of the MOF samples.

3.1 INTRODUCTION

The properties of complex molecular systems rely on the precise organization of functional molecular subunits in three-dimensional space. Typically, these subunits are found within a larger molecular architecture that serves as a scaffold for organizing the subunits with respect to one another. The scaffold structure and the individual molecular subunits are equally important in defining system properties.

As discussed in Chapter 1, MOFs are ideal scaffold materials for organizing molecules in 3-D space. Multiple different approaches have been developed for installing complex functional moieties onto MOF scaffolds, which have led to rapid expansion of MOF diversity.[7] These methods, which include postsynthetic modification and postsynthetic ligand exchange, allow

introduction of functional groups that are often incompatible with the solvothermal reaction conditions typically used for MOF synthesis. As detailed in previous chapters, multiple postsynthetic ligand modification reactions have been reported, including condensation reactions, cycloaddition reactions, and metalation.[24-26] To date, these have allowed for installation of up to two different functional moieties in a single MOF.[117-121] Ligand exchange is also a powerful method of tuning MOF composition, functionality, and porosity.[20,22-23] These two strategies can be used in tandem to further increase the diversity and complexity of MOFs.[122]

Both the porosity and the structure of the scaffold MOF affect the level of complexity achievable from postsynthetic ligand modification and ligand exchange methods. As discussed in Section 2.1, microporous MOFs are ideal scaffolds for organizing relatively "small" functional moieties in close proximity to one another.[85-86] New selective sorbents and complex heterogeneous catalysts have been created via postsynthetic modification of microporous MOFs. Mesoporous MOFs, on the other hand, are ideal scaffolds for organizing relatively "large" functional species, because the pore dimensions allow for facile entry and diffusion of larger and more complex molecules.[87-89] In terms of structure and bonding, most reported MOFs have a single ligand strut connecting neighboring metal clusters (Figure 46A). If multiple ligands link neighboring clusters (Figure 46B), one can imagine closely arranging multiple different functional groups, facilitating interactions between these groups that could lead to cooperative functionality. Having ligand clusters connecting neighboring metal clusters may be especially important for mesoporous MOFs, in which ligands surrounding the mesopores are spaced far apart. Motifs similar to Figure 46B would allow one to install functional groups in close proximity to one another in a mesoporous MOF. A platform material bMOF-100, which was

introduced in detail in Chapter 2, consists of Zn^{2+}-adeninate vertices interconnected through a bundle of three BPDC linkers (Figure 47) rather than a single ligand bridge.

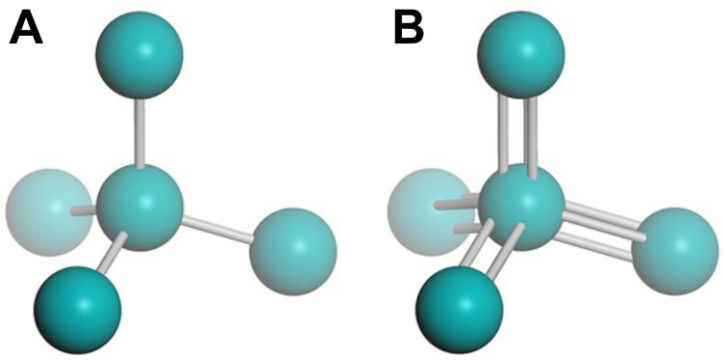

Figure 46. Representation of metal nodes (dark cyan spheres) linked by single-ligand struts (A) and multi-ligand struts (B).

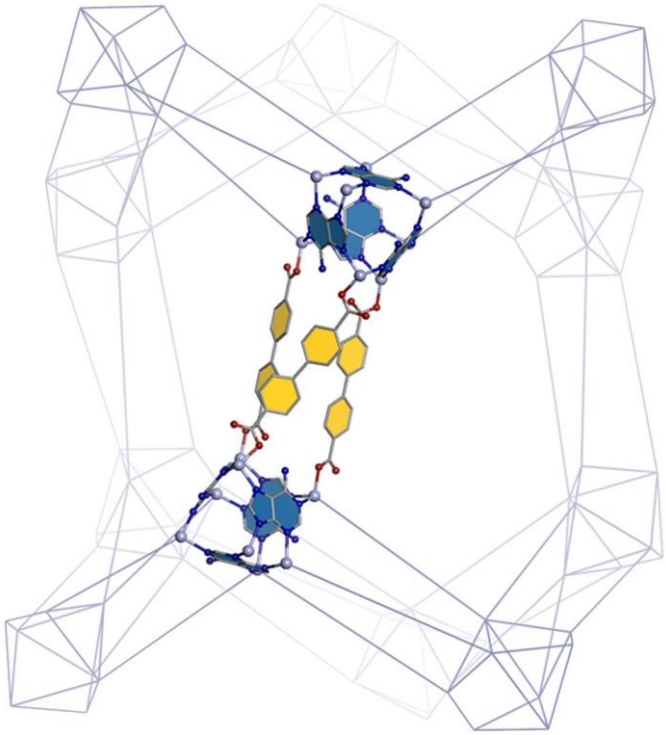

Figure 47. The underlying network and bundled three-BPDC strut in bMOF-100.

It was previously demonstrated that bMOF-100 could be postsynthetically modified with large and complex molecules, and its porosity could be systematically increased via stepwise ligand exchange reactions.[54,84] Beyond what has already been accomplished, the three-ligand bundle motif connecting the vertices coupled with the large mesopores still presents a unique opportunity to employ sequential ligand exchange reactions to install up to three different functional moieties in very close proximity in 3-D space (Figure 48A) and thereafter to use these moieties as sites for covalently attaching large complex molecules via postsynthetic ligand modification (Figure 48B).

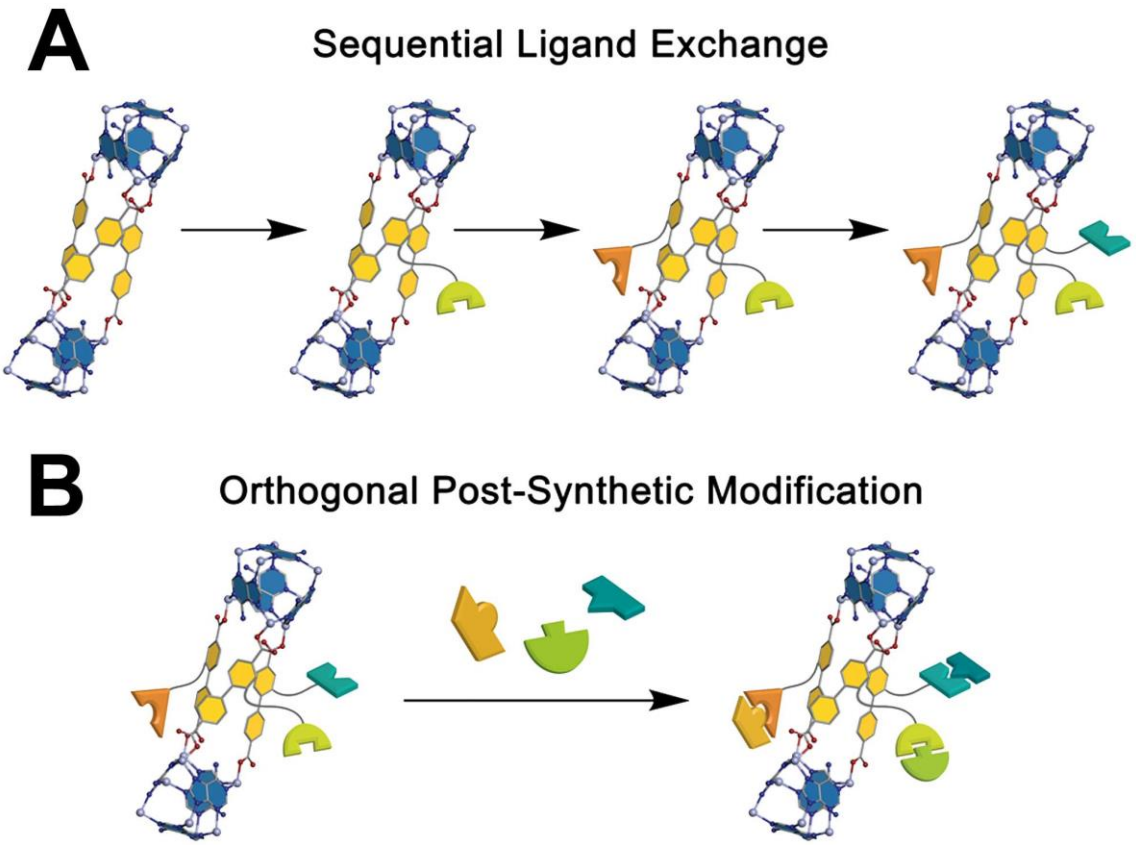

Figure 48. Proposed sequential ligand exchange process for installing multiple orthogonal functional groups (A) and subsequent covalent modification of the functional groups (B) in bMOF-100.

3.2 RESULTS AND DISCUSSION

3.2.1 Mono-functionalization of bMOF-100 via postsynthetic ligand exchange

Previous studies in our group have shown that bMOF-100 was amenable to facile and nearly quantitative ligand exchange reactions.[54] In this study, replacement of BPDC with BPDC linkers functionalized at the 2-position was planned to introduce new functionality to the pore space. Within the framework, the 2-carbon positions on the biphenyl struts are ≤ 7.5 Å from each other. Three linkers were synthesized: 2-amino-1,1′-biphenyl-4,4′-dicarboxylic acid (H_2-NH_2-BPDC), 2-azido-1,1′-biphenyl-4,4′-dicarboxylic acid (H_2-N_3-BPDC), and 2-formyl-1,1′-biphenyl-4,4′-dicarboxylic acid (H_2-F-BPDC). The formyl, azido, and amino groups were chosen because they are chemically orthogonal and can therefore be differentially addressed via postsynthetic modification reactions. Next, experiments were performed to examine whether bMOF-100 could withstand ligand exchange reactions with the functionalized linkers. Crystalline samples of bMOF-100 were heated at 75 °C for 24 hours in solutions of the individual linkers to prepare mono-functionalized materials. After reaction, the crystals were transparent (Figure 49) and retained their crystallinity, as determined by PXRD (Figure 50). Thoroughly washed products were dissolved in DMSO-d_6 and DCl/D_2O and analyzed via ^{1}H NMR to determine the linker ratios and extent of exchange. 43.7%, 47.2%, and 50.3% of the BPDC linkers in bMOF-100 were replaced with NH_2-BPDC, N_3-BPDC, and F-BPDC, respectively (Figure 51). These results indicate that the linkers in bMOF-100 can be exchanged and that the crystal structure is compatible with the chosen functionalized linkers.

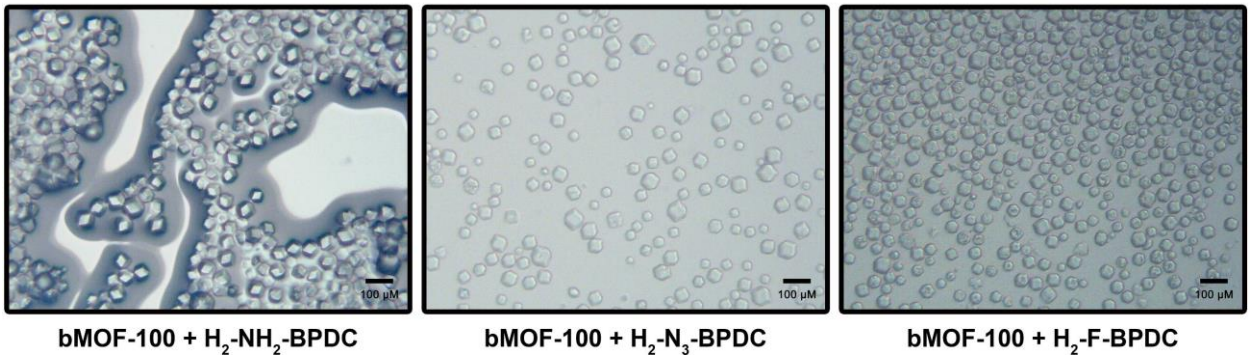

Figure 49. bMOF-100 crystals after exchange with functionalized BPDC ligands.

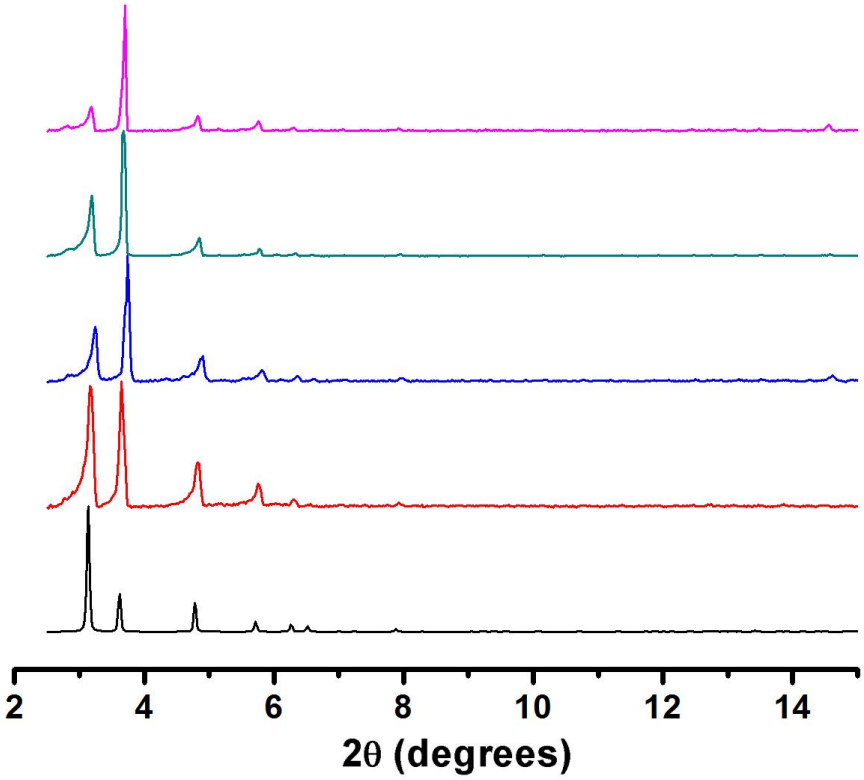

Figure 50. PXRD patterns for as-synthesized bMOF-100 crystals (red) and after ligand exchange with H_2-F-BPDC (blue), H_2-N_3-BPDC (dark cyan), and H_2-NH_2-BPDC (magenta). The pattern simulated from single crystal data for bMOF-100 is shown in black.

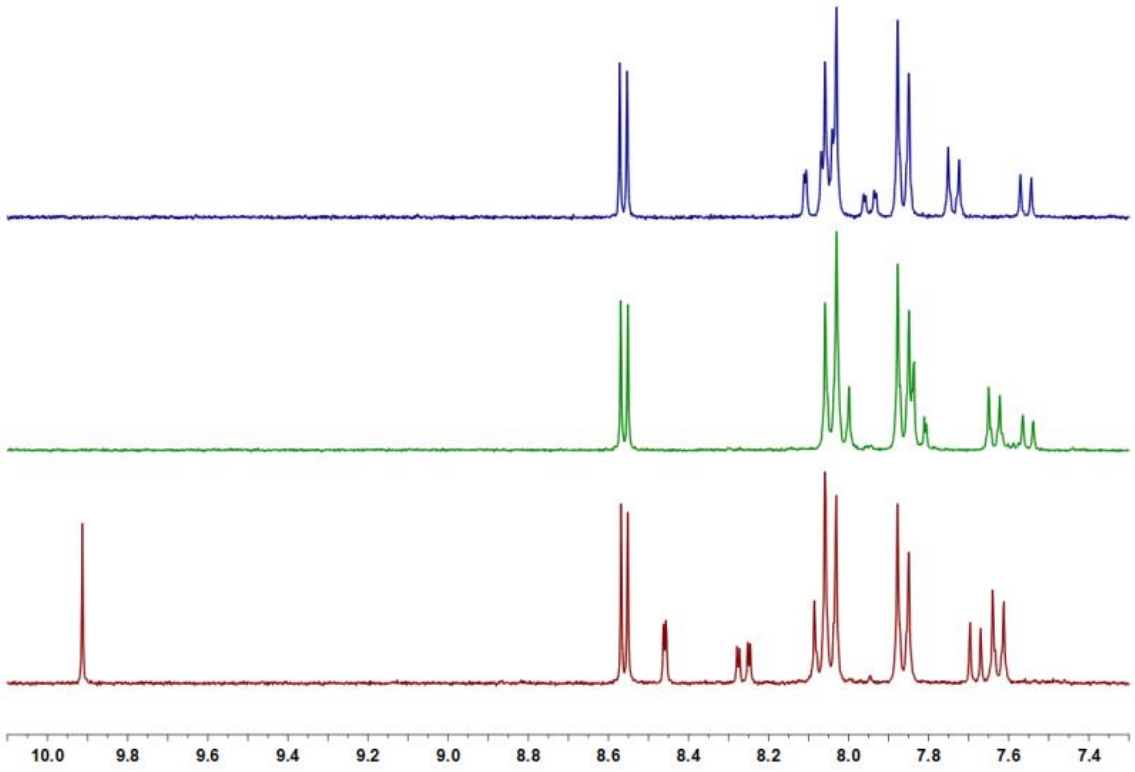

Figure 51. ^{1}H NMR spectra of dissolved bMOF-100 crystals after ligand exchange with H_2-NH_2-BPDC (blue), H_2-N_3-BPDC (green), and H_2-F-BPDC (red). The integration values of non-overlapping peaks for the two ligands were compared to determine the extent of ligand exchange.

3.2.2 Orthogonal bi-functionalization of bMOF-100 via postsynthetic ligand exchange

Having proven that bMOF-100 can be postsynthetically (mono-) functionalized via ligand exchange, its synthetically accessible analogue, N_3-bMOF-100,[84] was prepared next, and ligand exchange reactions to produce orthogonal binary functionalized MOFs were performed. In trial ligand exchange reactions, it was discovered that the N_3-BPDC linkers were much more labile

than BPDC. Therefore 35 °C was determined to be an optimal reaction temperature, permitting slower exchange and allowing for better control over the extent of ligand exchange. The reactions are shown in Figure 52, using H_2-NH_2-BPDC or H_2-F-BPDC. The exchange percentage depended on the reaction time, as analyzed by ^{1}H NMR (Figures 53 and 54). The MOFs remained crystalline throughout the reactions, as determined by PXRD (Figures 55 and 56).

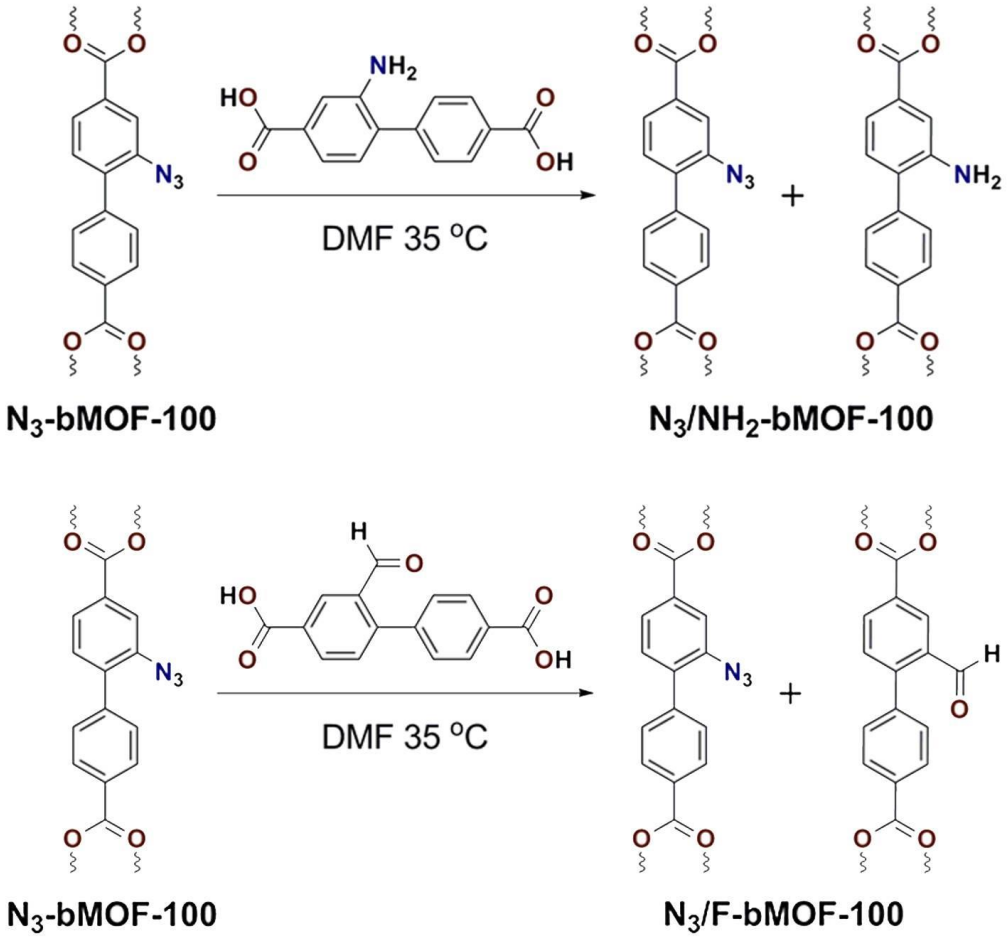

Figure 52. Ligand exchange reactions to produce N_3/NH_2-bMOF-100 (top) and N_3/F-bMOF-100 (bottom).

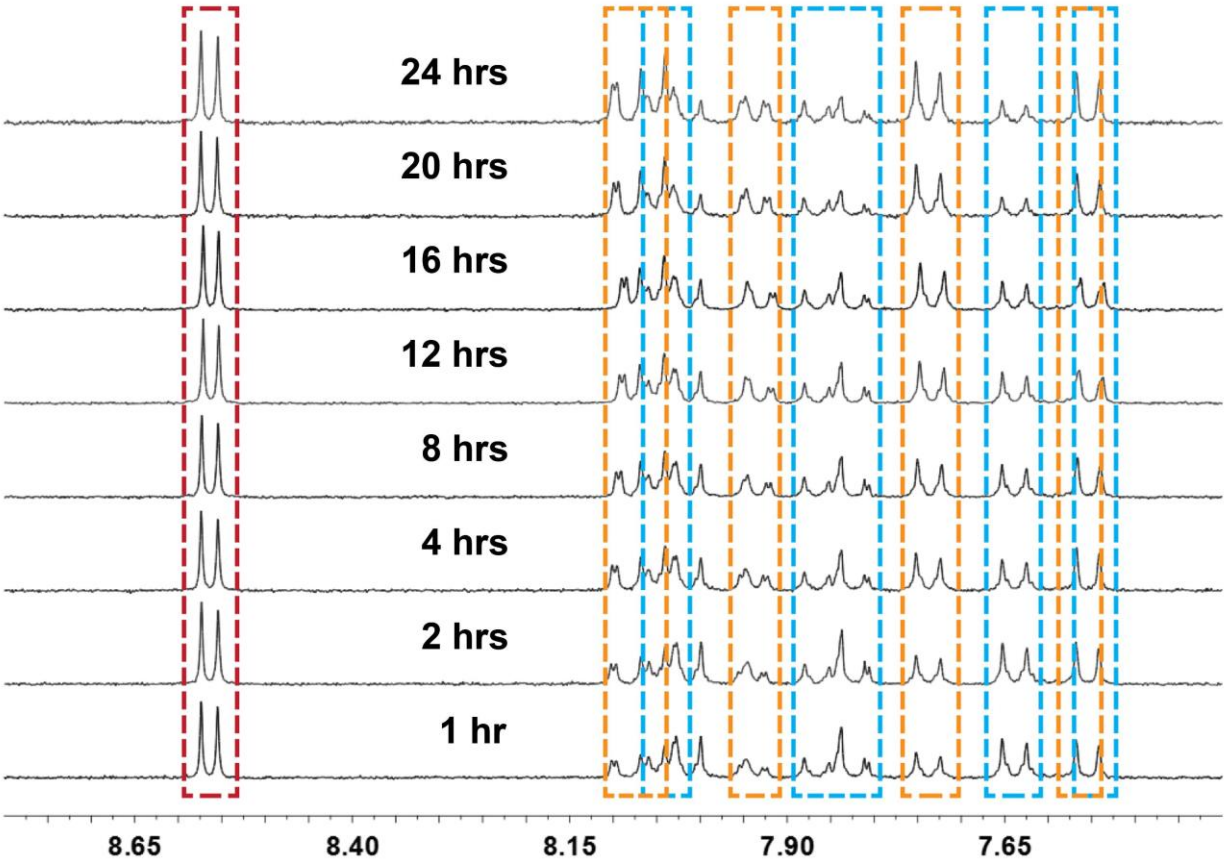

Figure 53. ^{1}H NMR spectra of dissolved N_3-bMOF-100 crystals after ligand exchange with H_2-NH_2-BPDC for different periods of time (red: adenine; blue: N_3-BPDC; yellow: NH_2-BPDC). The integration values of non-overlapping peaks for the two ligands were compared to determine the extent of ligand exchange.

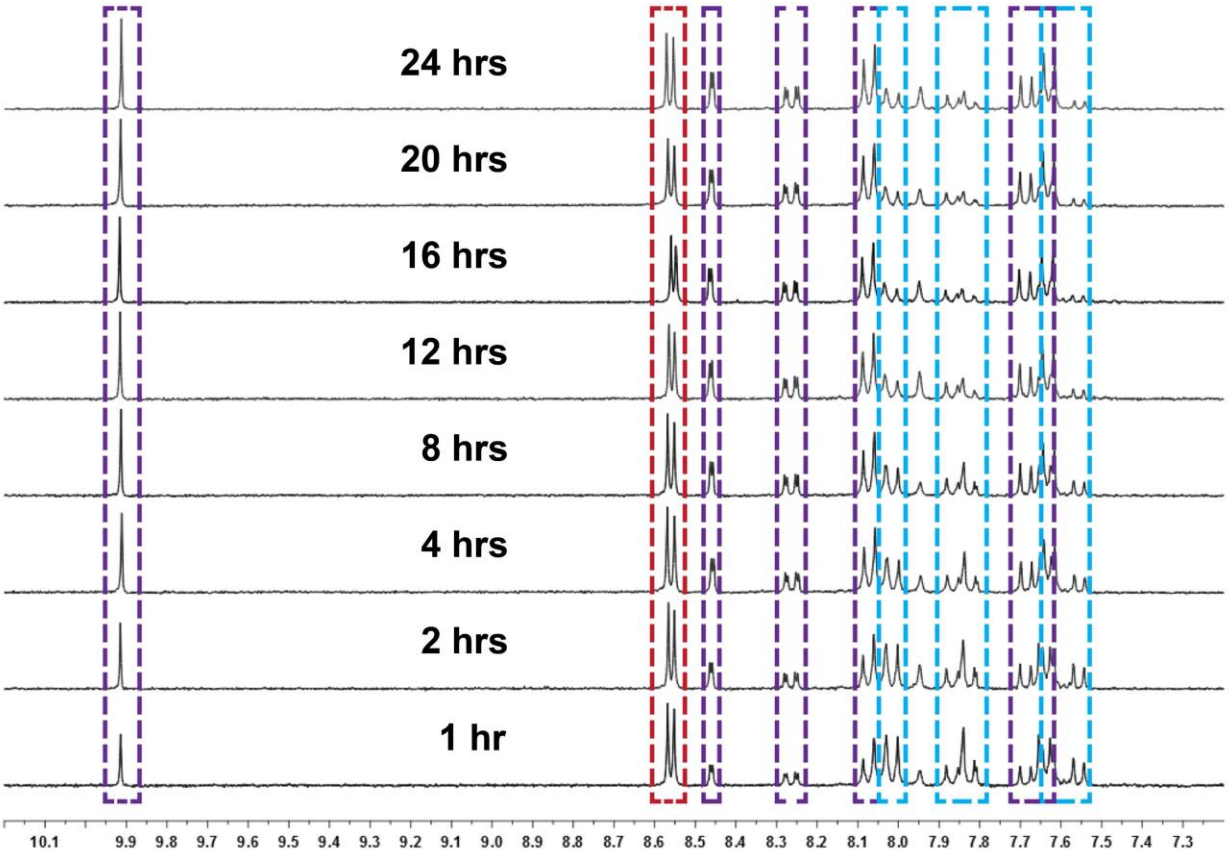

Figure 54. ^{1}H NMR spectra of dissolved N_3-bMOF-100 crystals after ligand exchange with H_2-F-BPDC for different periods of time (red: adenine; blue: N_3-BPDC; purple: F-BPDC). The integration values of non-overlapping peaks for the two ligands were compared to determine the extent of ligand exchange.

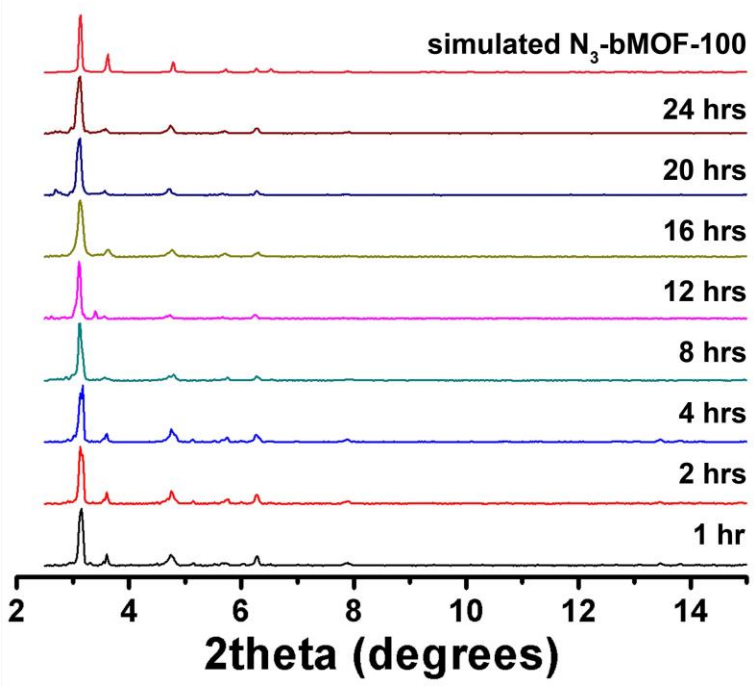

Figure 55. PXRD comparing N_3/NH_2-bMOF-100 samples at different ligand exchange time points with simulated pattern.

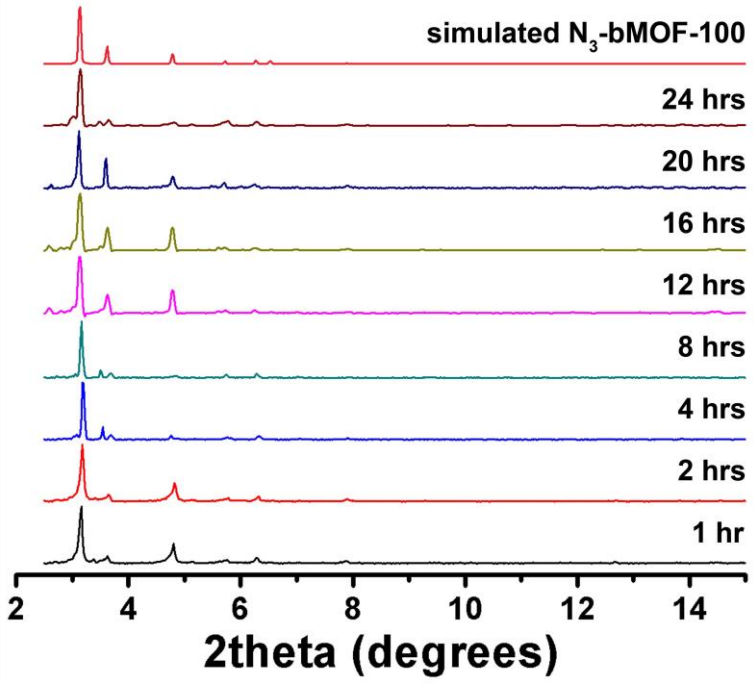

Figure 56. PXRD comparing N_3/F-bMOF-100 samples at different ligand exchange time points with simulated pattern.

In both cases, the ratios of the two ligands (N_3-BPDC:NH_2-BPDC or N_3-BPDC:F-BPDC) can be varied within a broad range. Close analysis of the exchange percentages for the two ligands as a function of reaction time revealed different exchange behavior. In the case of F-BPDC exchange, there appeared to be an upper limit of exchange (Figure 57A). Once the product crystal contained ~65% F-BPDC, no further exchange occurred. As the reaction time increased, the amount of crystals in the reaction visibly decreased. These observations suggested that if bMOF-100 contained too many F-BPDC ligands, it became thermodynamically unstable and eventually dissolved. A corollary to this observation is the F-BPDC bMOF-100 analogue could not be prepared via direct synthesis. The NH_2-BPDC exchange reaction proceeded linearly with time (Figure 57B). No visible crystal dissolution was observed regardless of reaction time, suggesting that there was not an upper limit for NH_2-BPDC exchange.

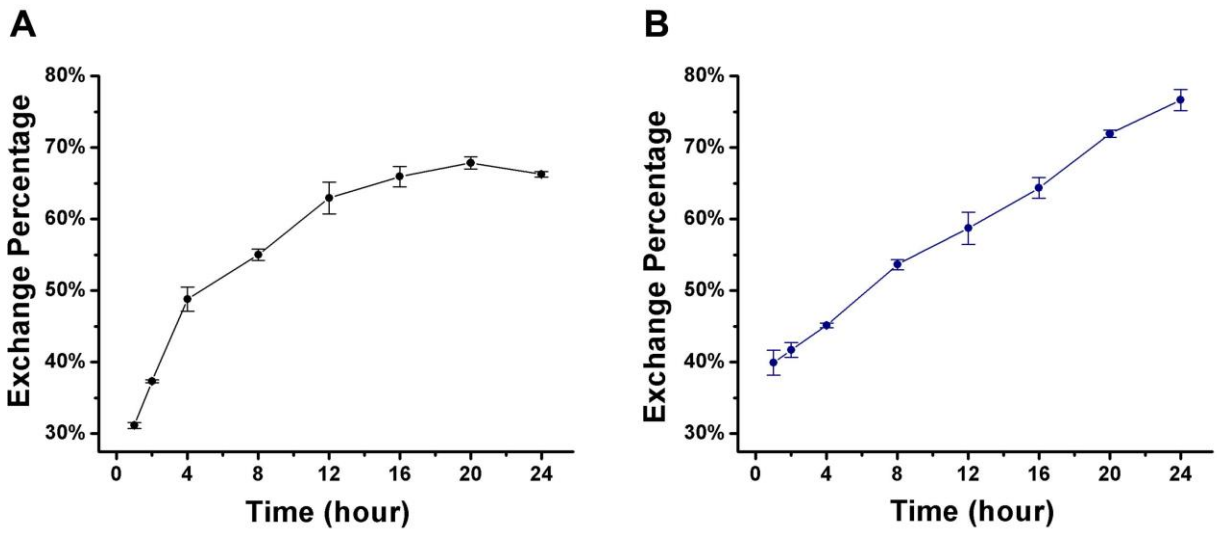

Figure 57. Percentage of F-BPDC (A) or NH_2-BPDC (B) in the ligand exchange product at different time points, based on ^{1}H NMR results.*

* Error bars in Figure 57 are standard deviations of two parallel sets of experiments.

3.2.3 Orthogonal tri-functionalization of bMOF-100 via postsynthetic ligand exchange

As shown in Figure 57A, after 4 h of ligand exchange, the ratio of N_3-BPDC to F-BPDC in the product crystals was approximately 1:1. These crystals were reacted with H_2-NH_2-BPDC to create a ternary MOF with three orthogonal functional groups (Figure 58A). Similarly, 1:1 N_3-BPDC:NH_2-BPDC samples, which were synthesized according to Figure 57B, were reacted with H_2-F-BPDC (Figure 58B). By varying the reaction time, the final ligand composition was tunable, as determined by ^{1}H NMR (Figures 59 and 60), and the crystallinity retained (Figure 61). As shown in Figure 62, N_3-BPDC was always present in the smallest amount after analyzing the ^{1}H NMR data from Figure 59 and Figure 60, suggesting that it could be the most labile of the three linkers. The ligand present in the largest amount in the final product was always the third ligand that was introduced. Therefore, it can be concluded that the ligand composition is mainly kinetically controlled.

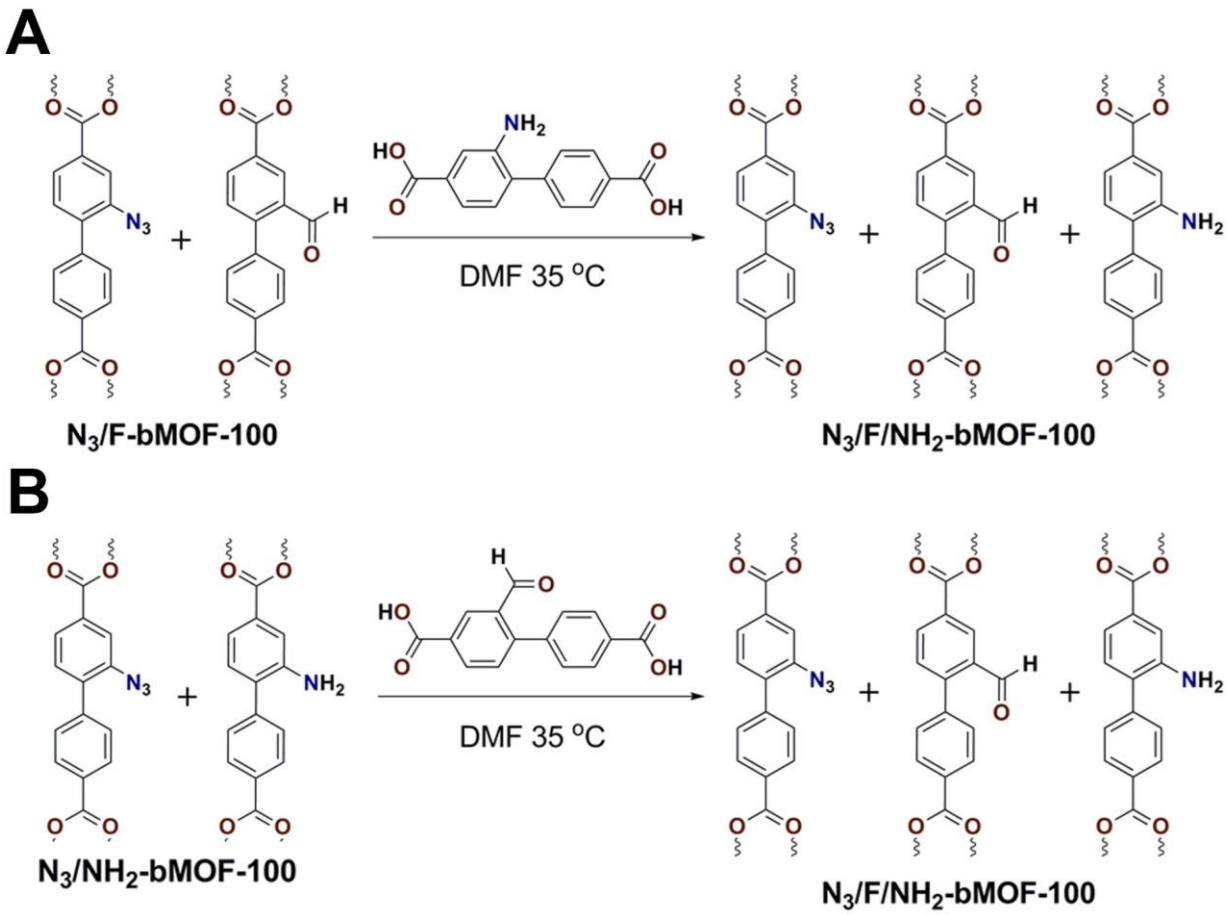

Figure 58. Ligand exchange reactions to produce N_3/F/NH_2-bMOF-100 starting from N3/F binary mixture (A) and N_3/NH_2 binary mixture.

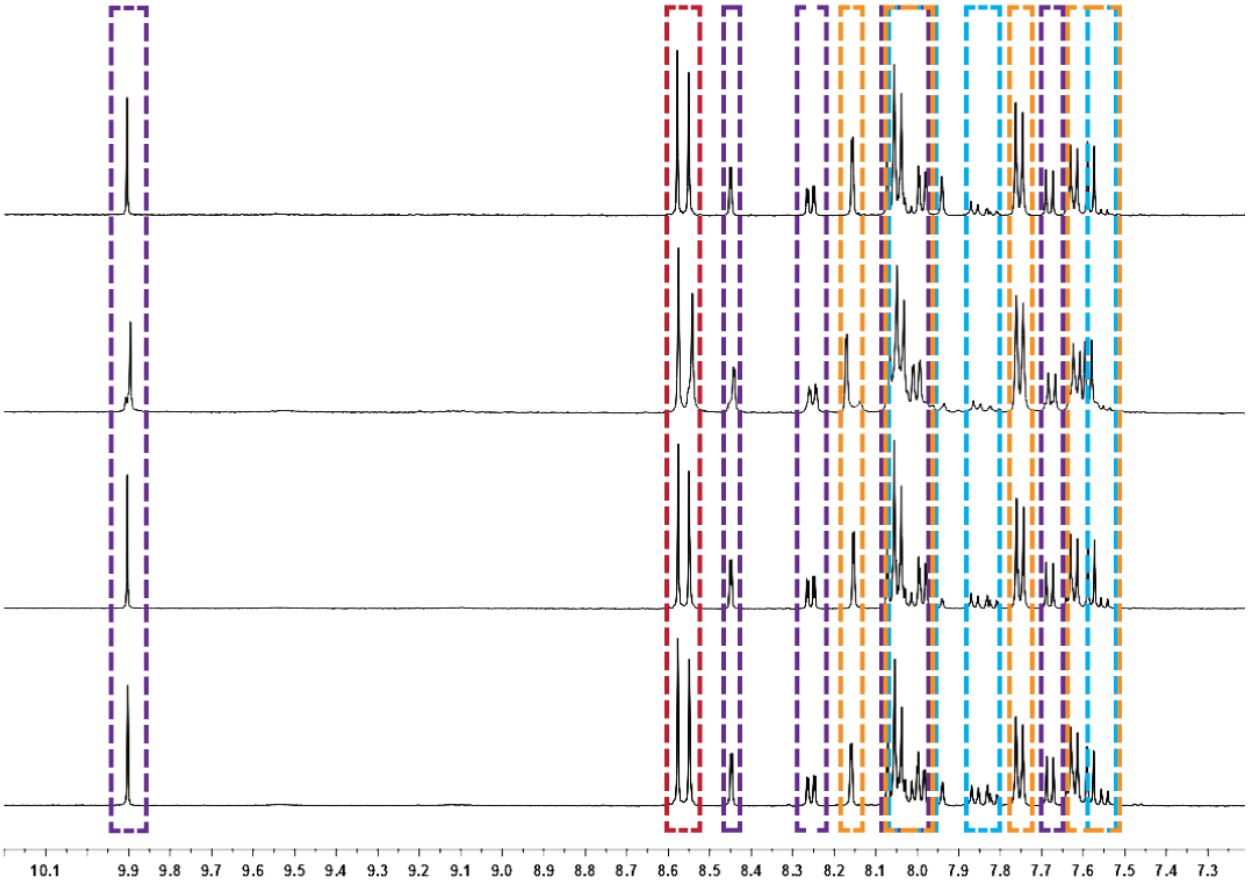

Figure 59. ^{1}H NMR spectra of dissolved MOF crystals after reaction shown on Figure 58A. From top to bottom: 6, 4, 2, 1 hour(s) exchange with H_2-NH_2-BPDC (red: adenine; blue: N_3-BPDC; purple: F-BPDC; yellow: NH_2-BPDC).*

* The integration values of non-overlapping peaks for the three ligands were compared to determine the composition. I note that no peaks were observed that correspond to the imine adduct of F-BPDC and NH_2-BPDC.

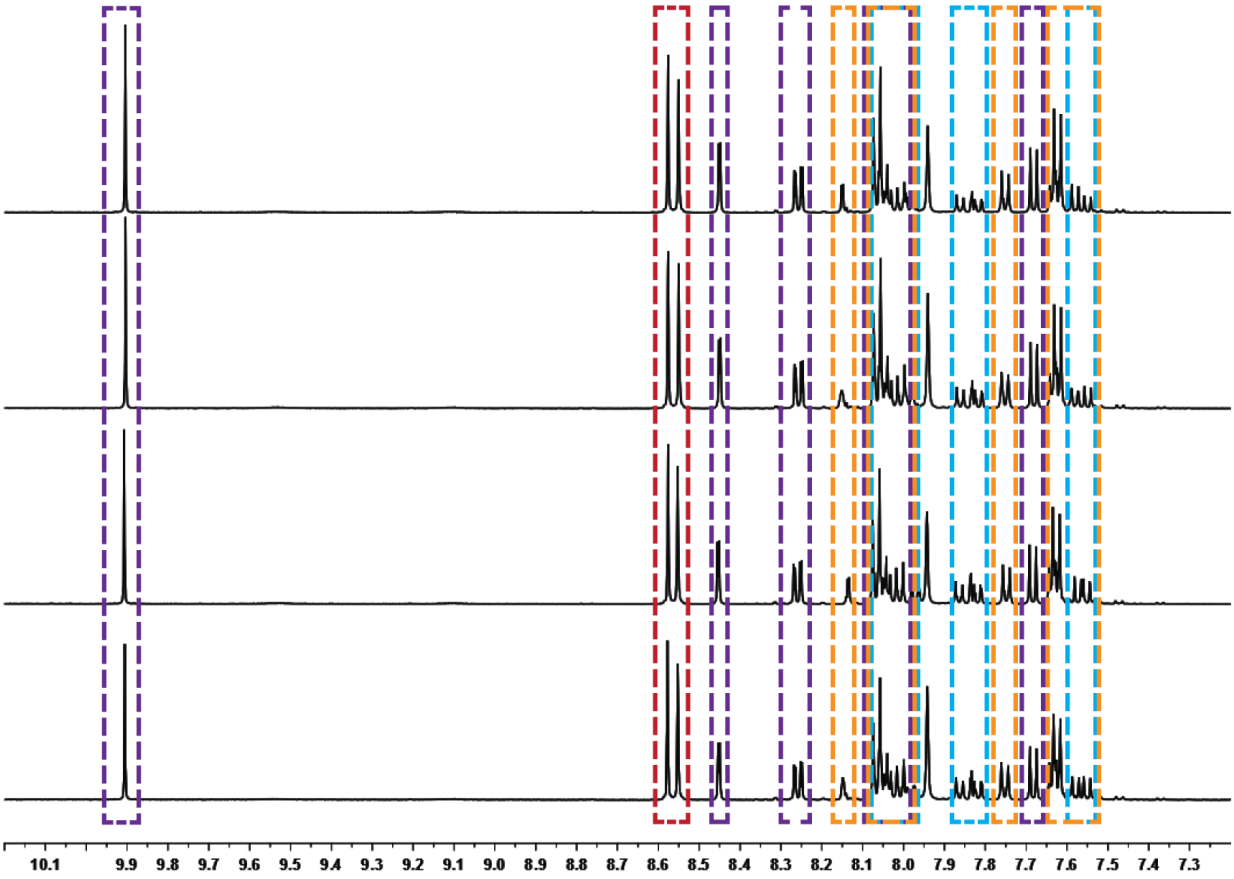

Figure 60. ^{1}H NMR spectra of dissolved MOF crystals after reaction shown on Figure 58B. From top to bottom: 6, 4, 2, 1 hour(s) exchange with H_2-F-BPDC (red: adenine; blue: N_3-BPDC; purple: F-BPDC; yellow: NH_2-BPDC).*

* The integration values of non-overlapping peaks for the three ligands were compared to determine the composition. I note that no peaks were observed that correspond to the imine adduct of F-BPDC and NH_2-BPDC.

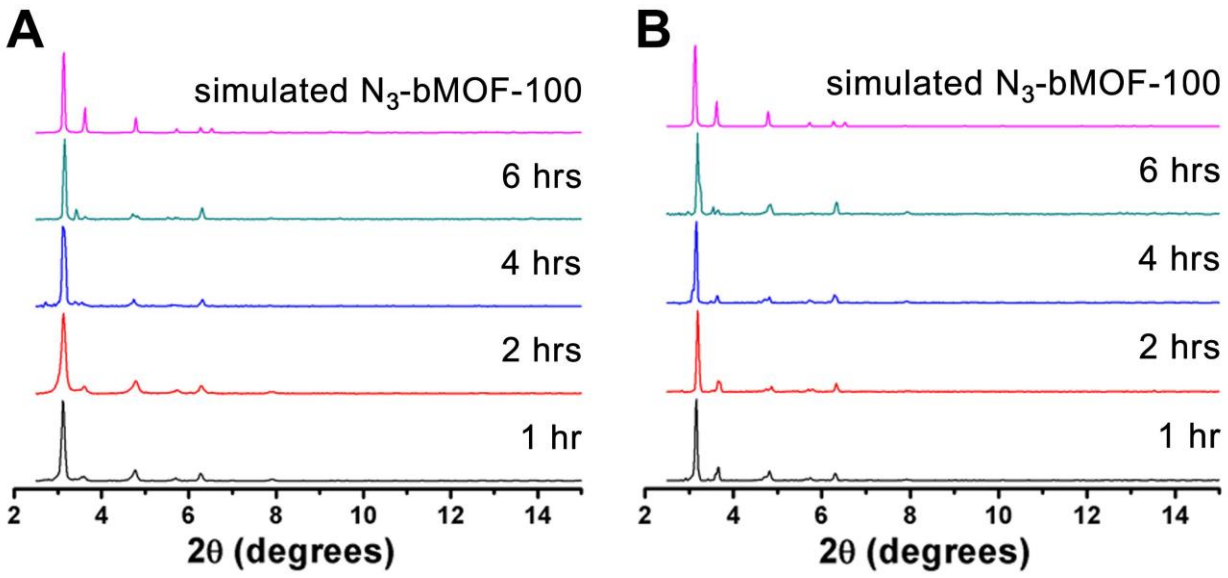

Figure 61. PXRD comparing MOFs at different exchange time points with simulated pattern. (A corresponds to Figure 58A; B corresponds to Figure 58B)

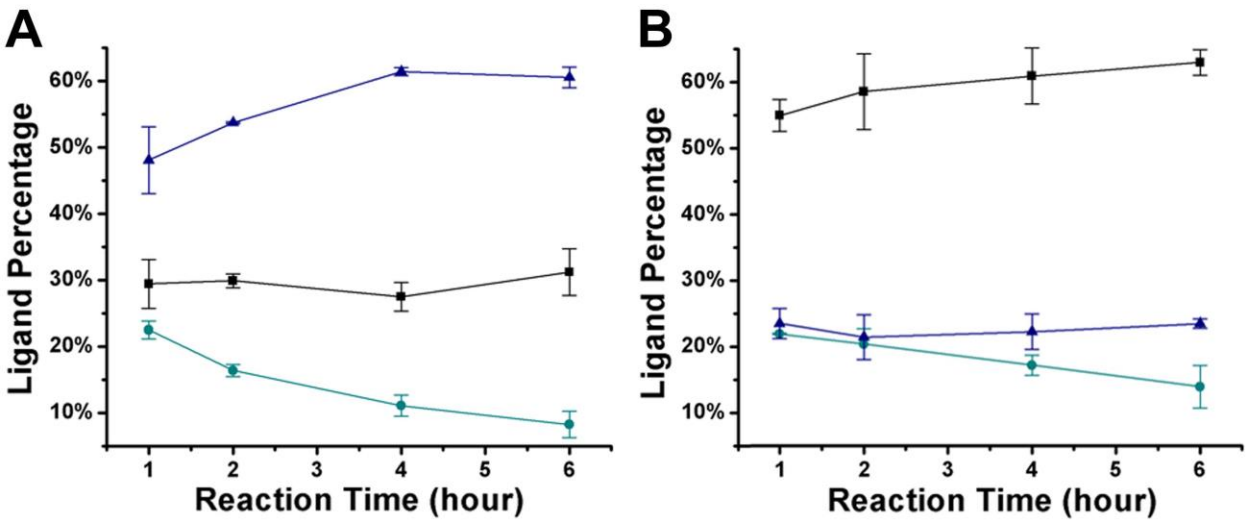

Figure 62. Percentages of all three functionalized BPDC ligands in the product as a function of reaction time (A corresponds to Figure 58A; B corresponds to Figure 58B).*

* Error bars in Figure 62 are standard deviations of two parallel sets of experiments.

3.2.4 Spatial distribution pattern of two functional groups after ligand exchange

For a heterogeneous material with multiple functional groups, it is important to understand the spatial distribution of the different groups. Several methods have been established to study the linker distribution in MOFs, including microscopic attenuated total reflectance (ATR) infrared spectroscopy, photothermal induced resonance (PTIR), and solid-state NMR.[123-126] In the case of ligand exchange, knowing the spatial distribution of functional groups may allow one to retroactively understand aspects of the exchange process, such as whether particular ligands cluster together into domains or whether they are homogeneously distributed. Moreover, information about the ligand distribution will also be important for guiding the development of potential applications.

First, four possible scenarios are proposed for how the two functional groups are distributed in the three-dimensional space within the bi-functionalized MOF. In Figure 63, the four scenarios are presented as simplified two-dimensional arrays; different components (i.e., functional groups) are shown as spheres of different colors. To reveal the spatial distribution of the two components, the degree and manner of clustering need to be determined. The first possible scenario is homogeneous distribution (Figure 63A) where no significant clustering is observed. The second possible scenario is the formation of small clusters (Figure 63B) where there is definitely clustering, but the dimension of the aggregates are below the spatial resolution or detection limit of the experimental probe applied; therefore, it is practically indistinguishable from the first scenario. Improvement of analytical technology would help recognize this distribution fashion. The third possible scenario is the formation of large clusters (Figure 63C) where the difference between the periphery and core regions of the clusters is detectable; therefore, it is possible to identify this distribution manner as opposed to the first two scenarios.

More specifically for MOF crystals, one extreme example of the "large clusters" scenario is the formation of a core-shell (or layered) structure where there are essentially two stratified "clusters" within one crystal, shown as the fourth scenario (Figure 63D).

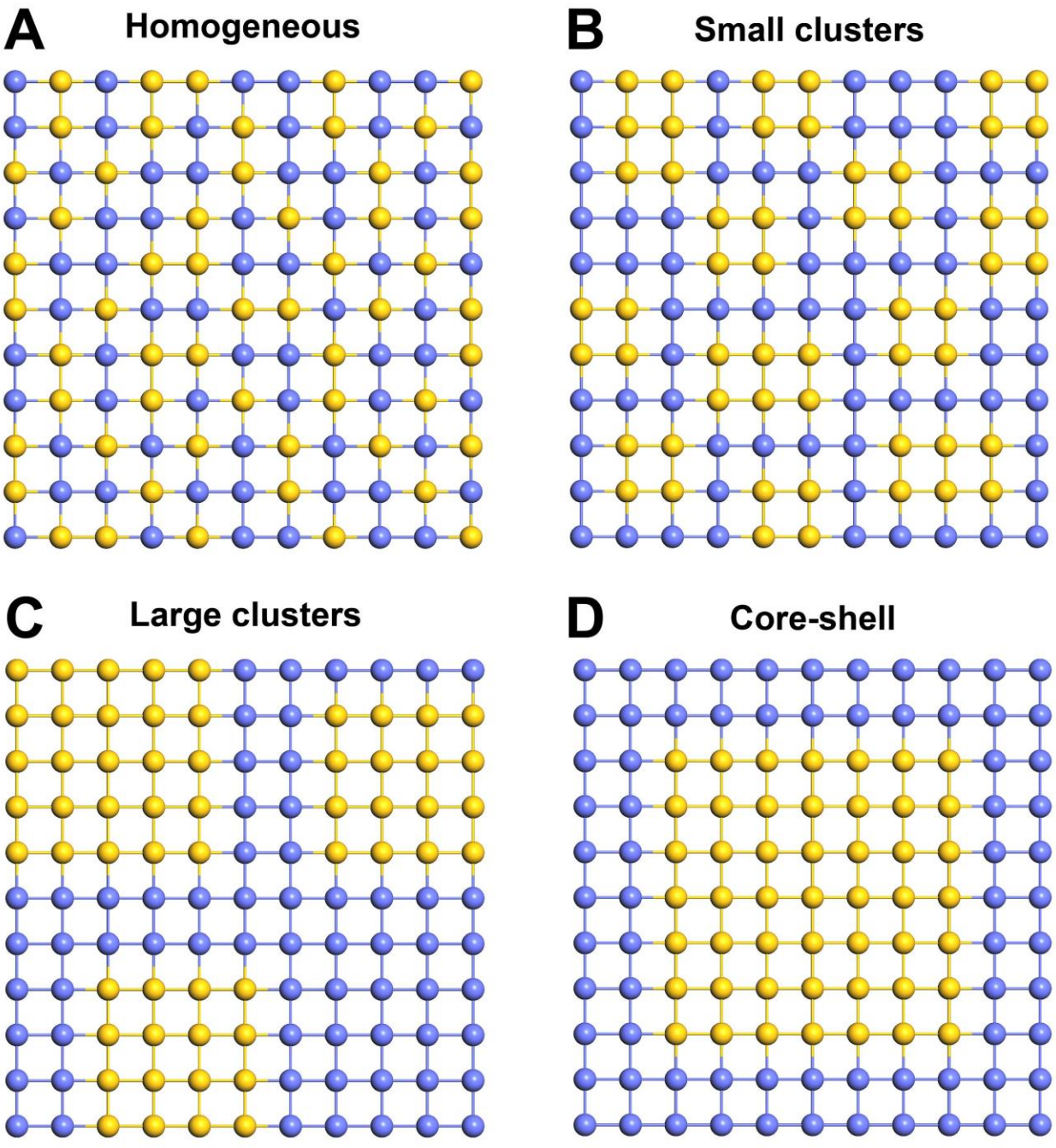

Figure 63. Four proposed scenarios of spatial distribution in a binary system.

To identify the correct model to describe the distribution of two functional groups in bi-functionalized bMOF-100, a dye-quencher approach was used. It was known that this dye-quencher pair needs to be ≤ 10 nm apart for FRET-based quenching.[127] Therefore there is a 10 nm spatial resolution limit in this method; clusters that are smaller than 10 nm would not be distinguishable from homogeneous mixture. Again the binary array model in Figure 63 is used to predict the possible outcome of this experiment, with the yellow sphere representing a fluorophore and the blue sphere representing a quencher. As shown in Figure 64, in the cases of homogeneous and small clustering distribution, because all the fluorophores would be sufficiently close to a nearby quencher, nearly all the fluorescence should be quenched (depicted as grey spheres). However, in the large clustering or core-shell distribution fashion, only when the fluorophores are at or near the interface will their fluorescence be quenched; significant residual fluorescence should still be observed. Considering each individual crystal contains very large numbers of fluorophore and quencher molecules, the difference between A/B and C/D should be obvious.

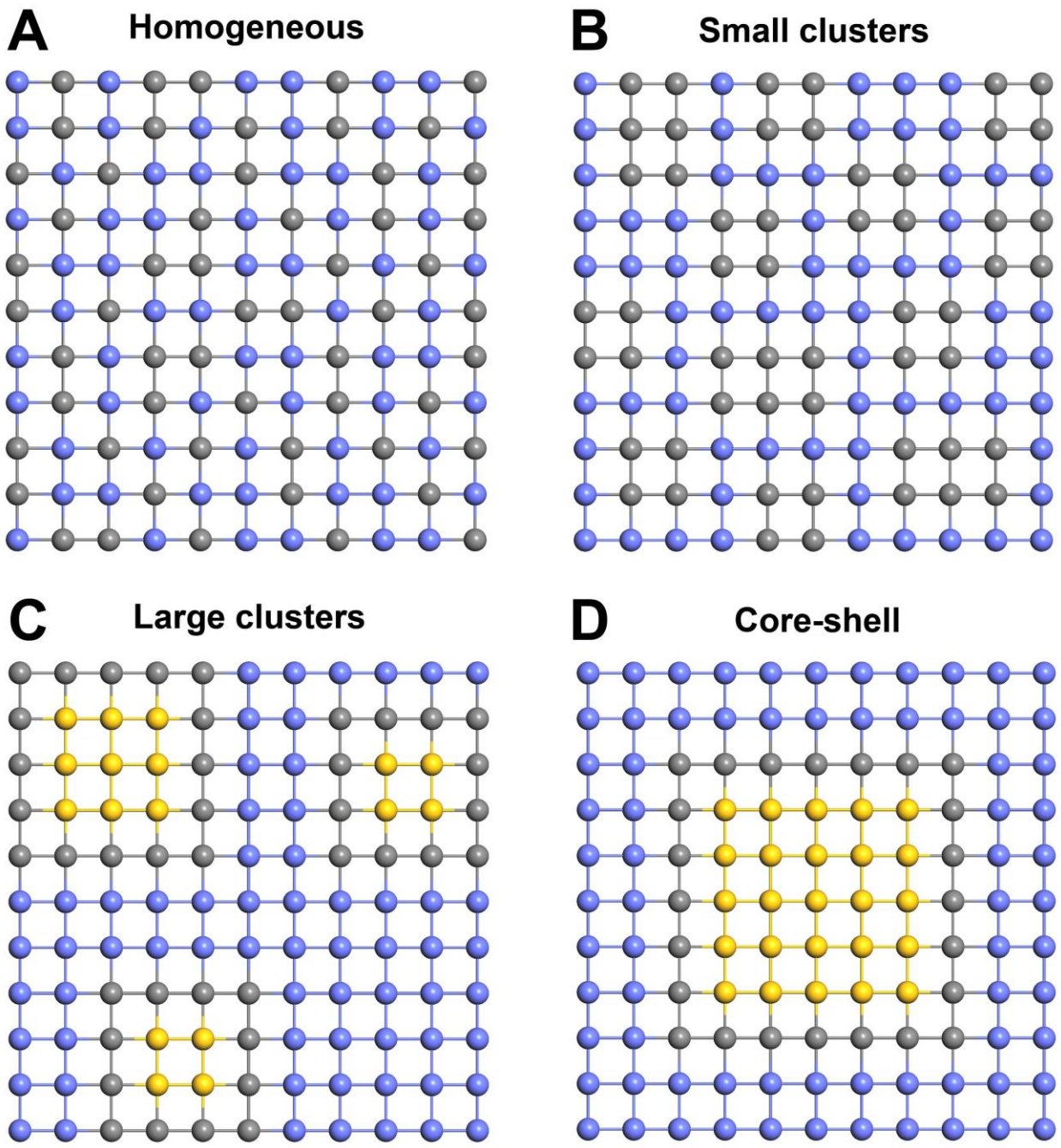

Figure 64. Four hypothesized scenarios of fluorescence quenching in a binary system.

Using ~1:1 azido:formyl bi-functionalized bMOF-100 as a scaffold, a fluorescent dye (carboxyrhodamine 110) was introduced via strain-promoted click chemistry and then a fluorescence quencher (BHQ-1) was attached via aldehyde-amine condensation (Figure 65). The

cavities of bMOF-100 can accommodate these large molecules (Experimental Section 3.4.5.1). After reaction with both dye and quencher, the MOF maintained its crystallinity (Figure 66). The crystals were copiously washed to remove unbound reactants, dissolved in dilute base, and then LC-MS was used to analyze the contents of the dissolved MOF. This analysis confirmed the presence of the BPDC linkers covalently modified with dye and quencher (Experimental Section 3.4.5.2 and 3.4.5.3).

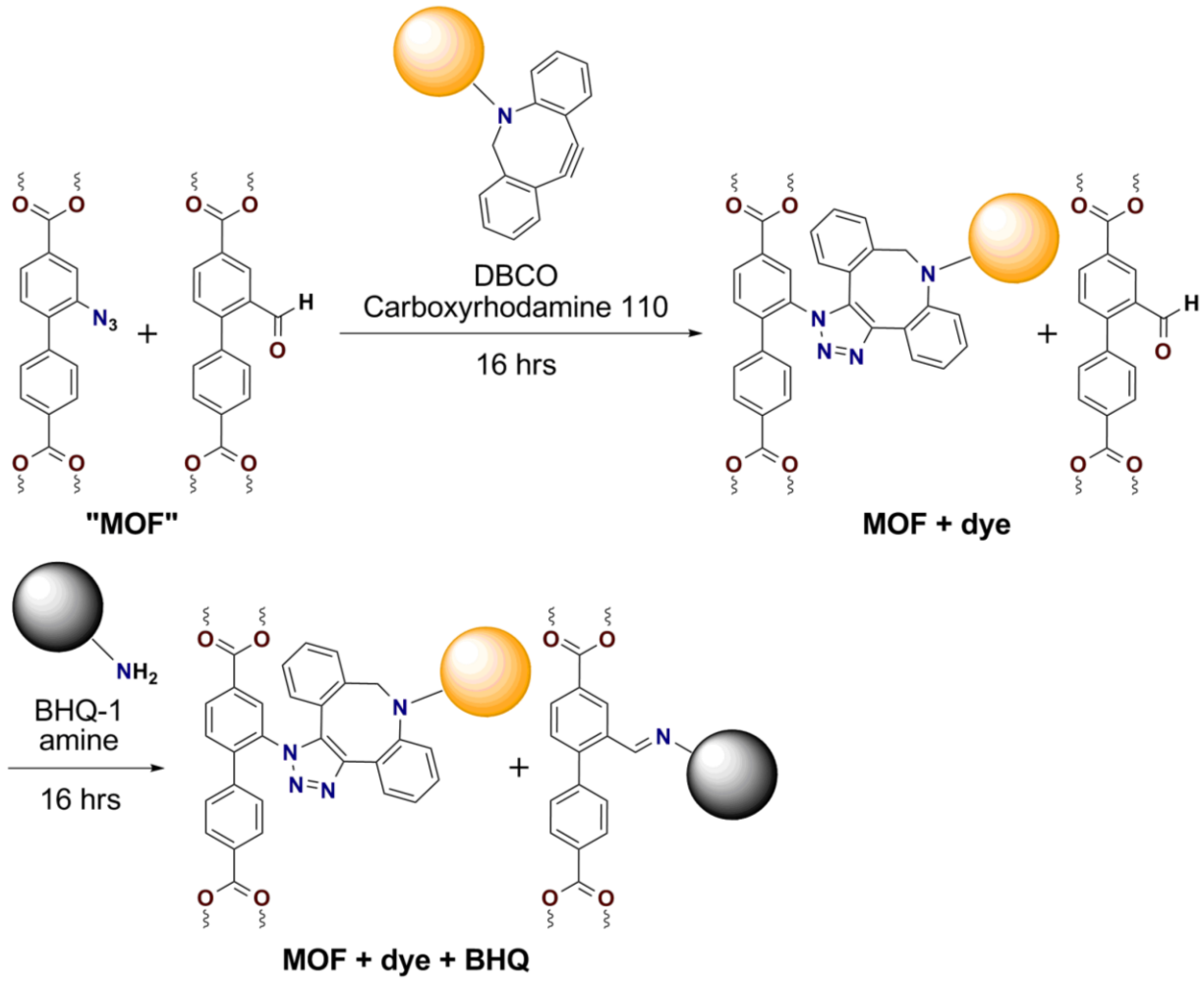

Figure 65. Tandem postsynthetic modification of ~1:1 N_3/F-bMOF-100 with dye and quencher.

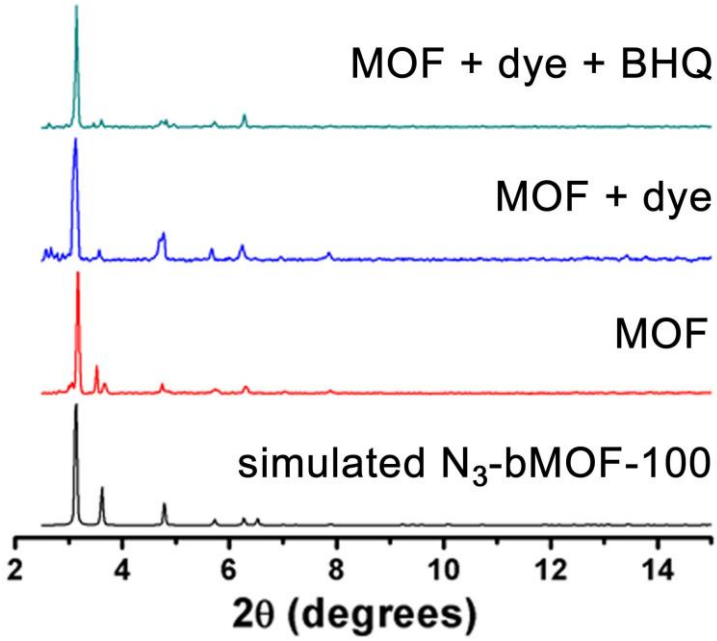

Figure 66. PXRD comparing patterns of MOFs before and after PSM to simulated pattern.

As previously mentioned, the dye-quencher pair needs to be ≤ 10 nm apart to enable FRET-based quenching. Therefore, if the azido and formyl groups were organized apart from one another in large discrete domains within the MOF (Figure 64C or Figure 64D), most of the fluorophores would be sufficiently far from the quenchers and quenching would only occur at or near the interface between fluorophore and quencher domains. On the other hand, if the two groups were randomly distributed or formed small (≤ 10 nm) domains in the macroscopic crystal, nearly complete fluorescence quenching would be observed. For example, in the case of 1:1 binary functionalized bMOF-100, the Zn^{2+}-adeninate clusters are interconnected by a three ligand bundle; therefore, there is a 75% chance that a dye and a quencher could be positioned in close proximity on two of these three ligands, if the distribution is absolutely random. The modified MOF crystals were analyzed via microspectrophotometry. In a typical experiment, MOF crystals were placed on a glass slide under the microspectrophotometer objective lens. The

corresponding fluorescence spectra and images were collected at the excitation wavelength of 420 nm. As shown in Figure 67, almost complete fluorescence quenching was observed in both intact crystals and ground samples. The same phenomenon was observed in parallel measurements (Experimental Section 3.4.6). These results suggested that the dye and quencher, which marked the positions of the azido and formyl functional groups respectively, were not distributed in a core-shell fashion or clustered into relatively large discrete domains ($\gg$10 nm), cases where effective quenching would be suppressed to some extent. Therefore, it was concluded that the azido and formyl groups were likely randomly distributed in the crystal or clustered into small domains within 10 nm of each other (Figure 64A or Figure 64B).

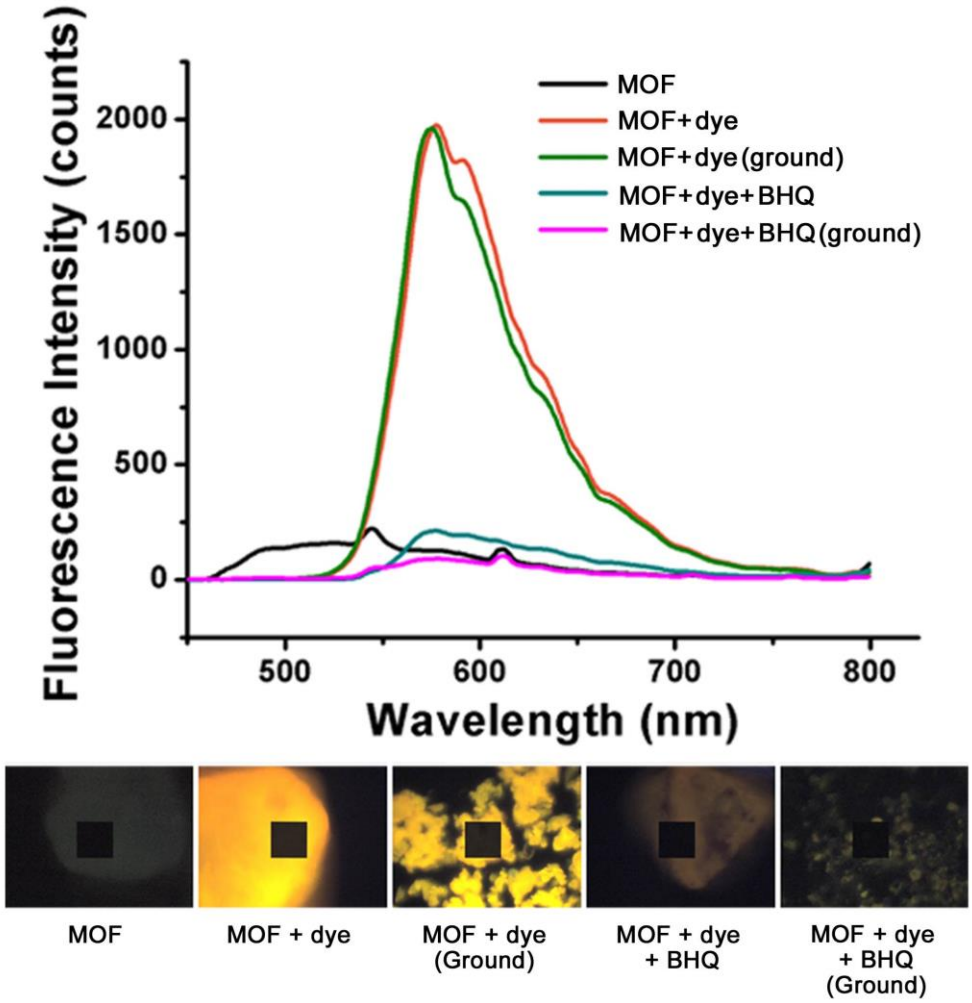

Figure 67. Top: fluorescence spectra (excited at 420 nm) of the MOF samples as determined by microspectrophotometry. Bottom: images of MOF samples excited at 420 nm.*

* black box: 31 × 31 μm^2 sampling area for spectroscopy

3.3 CONCLUSION

Successful mono-, bi-, and tri-functionalization was realized in a mesoporous MOF material, bMOF-100, via sequential postsynthetic ligand exchange reactions. The ratios of orthogonal functional groups were tunable with reaction time. Orthogonally functionalized crystals can be postsynthetically modified with large dye and quencher molecules to probe the distribution of functional moieties within the MOF. Spectrophotometric analysis of the dye-quencher MOF suggested a random distribution of functional groups in binary functionalized bMOF-100. These results represent a significant step forward in the development of ordered hierarchically structured and functionalized 3-D molecular materials.

3.4 EXPERIMENTAL SECTION

3.4.1 General procedure

All purchased chemicals were used without further purification except where otherwise stated. All DMF used for washing crystals was pre-dried over 4Å molecular sieves. Powder X-Ray diffraction patterns were collected using a Bruker AXS D8 Discover powder diffractometer at 40 kV, 40 mA for Cu Kα, (λ = 1.5406 Å) with a scan speed of 0.10 sec/step from 2.5 to 20 º at a step size of 0.02 º. The data were analyzed using the EVA program from the Bruker Powder Analysis Software package. The simulated powder pattern was calculated using Materials Studio from single crystal data of bMOF-100. ^{1}H NMR spectra were obtained using Bruker Avance III 300/400/500 MHz spectrometers. Chemical shifts are in parts per million using the residual

solvent peak (Chloroform-*d*, DMSO-d_6) as references. Microspectrophotometric experiments were performed on a CRAIC QDI 2010 microspectrophotometer equipped with a 420 nm filter. The sampling area was fixed at 31 × 31 μm^2, and the integration time was fixed at 971.60 ms for all acquired fluorescence spectra. Light microscopic images were obtained using an Olympus BH-2 microscope. LC-MS analyses were performed on a Shimadzu LCMS-2020 instrument. The LC method used was 6 minute running time with a constant ratio of 1:1 acetonitrile:water at a constant flow rate of 0.2 mL/min. In this method the samples do not pass through a chromatographic column; therefore, there is virtually no separation of the components. So in 3.4.5, the chromatograms are omitted, the mass spectra can sufficiently represent the samples' composition. The ionization interface was simultaneous ESI & APCI.

3.4.2 Syntheses of substituted H_2-BPDC ligands

3.4.2.1 Synthesis of dimethyl 2-amino-1,1'-biphenyl-4,4'-dicarboxylate

Dimethyl 2-amino-1,1'-biphenyl-4,4'-dicarboxylate was synthesized according to the literature.[84] ^{1}H NMR (400 MHz, $CDCl_3$) δ 8.13 (m, 2H), 7.55 (m, 2H), 7.48 (dd, J = 7.9, 1.4 Hz, 1H), 7.45 (d, J = 1.4 Hz, 1H), 7.18 (d, J = 7.9 Hz, 1H), 3.95 (s, 3H), 3.92 (s, 3H), 3.86 (s, 2H).

3.4.2.2 Synthesis of 2-amino-1,1'-biphenyl-4,4'-dicarboxylic acid (H_2-NH_2-BPDC)

Dimethyl 2-amino-1,1'-biphenyl-4,4'-dicarboxylate (990 mg, 3.47 mmol) was dissolved in THF (35 mL) and MeOH (25 mL). The resulting solution was then mixed with a solution of KOH (2 g, 35.7 mmol) in DI H_2O (40 mL). The reaction mixture was heated to reflux overnight. After all the volatiles were removed *in vacuo*, it was diluted with DI H_2O and acidified with 1M HCl solution until pH = 2. The precipitates were collected via centrifugation, washed with DI

H_2O, and dried in air. Compound **2** was collected as a yellow solid (857 mg, 96 %). ^{1}H NMR (400 MHz, DMSO-d_6) δ 12.92 (s, 2H), 8.01 (m, 2H), 7.57 (m, 2H), 7.41 (d, J = 1.5 Hz, 1H), 7.21 (dd, J = 7.9, 1.5 Hz, 1H), 7.11 (d, J = 7.9 Hz, 1H), 5.15 (s, 2H).

3.4.2.3 Synthesis of 2-azido-1,1'-biphenyl-4,4'-dicarboxylic acid (H_2-N_3-BPDC)

2-Azido-1,1'-biphenyl-4,4'-dicarboxylic acid was synthesized according to the literature.[84] ^{1}H NMR (400 MHz, DMSO-d_6) δ 13.26 (s, 2H), 8.03 (m, 2H), 7.85 (s, 1H), 7.83 (d, J = 8.0 Hz, 1H), 7.65 (m, 2H), 7.58 (d, J = 8.0 Hz, 1H).

3.4.2.4 Synthesis of methyl 4-bromo-3-formylbenzoate

Methyl 4-bromo-3-formylbenzoate was synthesized according to the literature.[128] ^{1}H NMR (300 MHz, $CDCl_3$) δ 10.39 (s, 1H), 8.54 (d, J = 2.2 Hz, 1H), 8.09 (dd, J = 8.3, 2.2 Hz, 1H), 7.75 (d, J = 8.3 Hz, 1H), 3.95 (s, 3H).

3.4.2.5 Synthesis of dimethyl 2-formyl-1,1'-biphenyl-4,4'-dicarboxylate

Methyl 4-bromo-3-formylbenzoate (729 mg, 3 mmol), 4-Methoxycarbonylphenylboronic acid (810 mg, 4.5 mmol), $Pd(dppf)Cl_2$ (66 mg, 0.09 mmol), and Cs_2CO_3 (2.93 g, 9 mmol) were mixed with DMF (10 mL) and stirred at 90 °C for 16 hours. DI H_2O (100 mL) was added and the mixture was extracted with DCM (25 mL, 3X). The organic layer was washed with DI H_2O (125 mL), brine (125 mL), and dried over $MgSO_4$. After filtration, the solution was concentrated and purified via column chromatography over 230-400 mesh silica gel (DCM : hexanes = 2 : 1 to DCM) to yield compound **5** as a yellow-white solid (465mg, 52 %). ^{1}H NMR (300 MHz, $CDCl_3$) δ 9.98 (s, 1H), 8.69 (d, J = 1.8 Hz, 1H), 8.31 (dd, J = 8.0, 1.8 Hz, 1H), 8.17 (m, 2H), 7.55 (d, J = 8.1 Hz, 1H), 7.48 (m, 2H), 3.99 (s, 3H), 3.97 (s, 3H).

3.4.2.6 Synthesis of 2-formyl-1,1'-biphenyl-4,4'-dicarboxylic acid (H_2-F-BPDC)

Dimethyl 2-formyl-1,1'-biphenyl-4,4'-dicarboxylate (239 mg, 0.8 mmol) was dissolved in THF (3 mL) and then mixed with a clear solution of $LiOH{\cdot}H_2O$ (201 mg, 4.8 mmol) in DI H_2O (1 mL) and MeOH (1 mL). The reaction mixture was stirred at room temperature for 24 hrs. Thereafter, all the volatiles were removed *in vacuo*, the reaction mixture was diluted with DI H_2O and acidified with 1M HCl solution. The precipitates were collected via filtration and dried *in vacuo*. Compound **6** was collected as an off-white solids (205 mg, 95 %). ^{1}H NMR (400 MHz, DMSO-d_6) δ 13.26 (s, 2H), 9.92 (s, 1H), 8.46 (d, J = 1.7 Hz, 1H), 8.27 (dd, J = 8.0, 1.7 Hz, 1H), 8.08 (m, 2H), 7.69 (d, J = 8.0 Hz, 1H), 7.63 (m, 2H).

3.4.3 Solvothermal MOF syntheses

Crystals of N_3-bMOF-100 and bMOF-100 were synthesized according to literature protocols.[84,108] The as-synthesized materials were washed as described in the following sections. The mass of MOFs used for subsequent experiments was determined after the DMF-washed crystals were dried under Ar flow to the point that they became free-flowing solids.

3.4.4 Ligand exchange experiments

3.4.4.1 Ligand exchange on bMOF-100

bMOF-100 (6 mg) was washed with DMF(6X) in a 1.5 mL centrifuge tube. After removing most of the solvent while keeping the crystals wet, a DMF solution of compounds H_2-NH_2-BPDC or H_2-N_3-BPDC or H_2-F-BPDC (0.05 M, 0.5 mL) was added. The tube was placed in a 75 °C oven for 24 hours. The crystals were imaged after the reaction (Figure 49). PXRD

patterns were collected to assess the crystallinity after reaction (Figure 50). For PXRD sample preparation, the crystals were washed with DMF (3X), soaked in DMF at 75 °C for 30 minutes, washed with DMF (3X), soaked in DMF at 75 °C for another 30 minutes, and finally washed with DMF again (3X) and stored under DMF. For ^{1}H NMR analysis (Figure 51), after following the DMF washing steps, the crystals were washed with DCM (3X), soaked in DCM at room temperature for at least 1 hour, washed with DCM (3X), and dried under Ar flow. Then, the crystals were dissolved in DMSO-d_6 (0.7 mL) and DCl in D_2O (37%, 0.006 mL) for ^{1}H NMR analysis to determine the ligand composition and exchange percentage.

3.4.4.2 Ligand exchange on N_3-bMOF-100: bi-functionalization

N_3-bMOF-100 (6 mg) was washed with DMF (6X) in a 1.5 mL centrifuge tube. After removing most of the solvent while keeping the crystals wet, a DMF solution of H_2-NH_2-BPDC or H_2-F-BPDC (0.05 M, 0.5 mL) was added. The tube was incubated in a 35 °C thermomixer (600 rpm) for various time periods. For PXRD characterization (Figures 55 and 56), the crystals were washed with DMF (3X), soaked in DMF at 75 °C for 30 minutes, washed with DMF (3X), soaked in DMF at 75 °C for another 30 minutes, and finally washed with DMF again (3X) and stored under DMF. For ^{1}H NMR analysis (Figures 53 and 54), after following the DMF washing steps, the crystals were washed with DCM (3X), soaked in DCM at room temperature for at least 1 hour, washed with DCM (3X), and dried under Ar flow. Then, the crystals were dissolved in DMSO-d_6 (0.7 mL) and DCl in D_2O (37%, 0.006 mL) for ^{1}H NMR analysis to determine the ligand composition and exchange percentage.

3.4.4.3 Ligand exchange on N_3-bMOF-100: tri-functionalization

For the reaction shown in Figure 58A, N_3-bMOF-100 (6 mg) was washed with DMF (6X) in a 1.5 mL centrifuge tube. After removing most of the solvent while keeping the crystals wet, a DMF solution of H_2-F-BPDC (0.05 M, 0.5 mL) was added. The tube was incubated in a 35 °C thermomixer (600 rpm) for 4 hours. The crystals were washed with DMF (3X), soaked in DMF at 75 °C for 30 minutes, washed with DMF (3X), soaked in DMF at 75 °C for another 30 minutes, and then washed again with DMF (3X). Then, the supernatant was removed and the crystals were added to a DMF solution of H_2-NH_2-BPDC (0.05 M, 0.5 mL) and incubated in a 35 °C thermomixer (600 rpm) for 1, 2, 4, or 6 hour(s). For PXRD characterization (Figure 61A), the crystals were washed with DMF (3X), soaked in DMF at 75 °C for 30 minutes, washed with DMF (3X), soaked in DMF at 75 °C for another 30 minutes, and finally washed with DMF again (3X) and stored under DMF. For ^{1}H NMR analysis (Figure 59), after following the DMF washing steps, the crystals were washed with DCM (3X), soaked in DCM at room temperature for at least 1 hour, washed with DCM (3X), and dried under Ar flow. Then, the crystals were dissolved in DMSO-d_6 (0.7 mL) and DCl in D_2O (37%, 0.006 mL) for ^{1}H NMR analysis to determine the ligand composition and exchange percentage.

For the reaction shown in Figure 58B, N_3-bMOF-100 (6 mg) was washed with DMF (6X) in a 1.5 mL centrifuge tube. After removing most of the solvent while keeping the crystals wet, a DMF solution of H_2-NH_2-BPDC (0.05 M, 0.5 mL) was added. The tube was incubated in a 35 °C thermomixer (600 rpm) for 6 hours. The crystals were washed with DMF (3X), soaked in DMF at 75 °C for 30 minutes, washed with DMF (3X), soaked in DMF at 75 °C for another 30 minutes, and then washed again with DMF (3X). Then, the supernatant was removed and the crystals were added to a DMF solution of H_2-F-BPDC (0.05 M, 0.5 mL) and incubated in a 35

°C thermomixer (600 rpm) for 1, 2, 4, or 6 hour(s). For PXRD characterization (Figure 61B), the crystals were washed with DMF (3X), soaked in DMF at 75 °C for 30 minutes, washed with DMF (3X), soaked in DMF at 75 °C for another 30 minutes, and finally washed with DMF again (3X) and stored under DMF. For ^{1}H NMR analysis (Figure 60), after following the DMF washing steps, the crystals were washed with DCM (3X), soaked in DCM at room temperature for at least 1 hour, washed with DCM (3X), and then dried under Ar flow. Then, the crystals were dissolved in DMSO-d_6 (0.7 mL) and DCl in D_2O (37%, 0.006 mL) for ^{1}H NMR analysis to determine the ligand composition and exchange percentage.

3.4.5 Postsynthetic modification with DBCO carboxyrhodamine 110 and BHQ-1 amine

3.4.5.1 Estimation of the molecular geometry of the dye and quencher

Models of the two molecules were created in ChemBio3D Ultra 11.0 and then imported into Scigress as c3xml files. Geometry optimization was done using B88LYP DFT functional and DGauss double zeta double valence polarization (DZVP) basis set. Then, the molecule was fitted into an orthorhombic box, with consideration of the atoms' van der Waals radii. The dimensions of the orthorhombic box were used to estimate the molecule's size (Figures 68 and 69). DBCO carboxyrhodamine 110 has a long flexible spacer chain between the DBCO and dye components. Therefore, the calculated box is only an approximation of possible molecular dimensions.

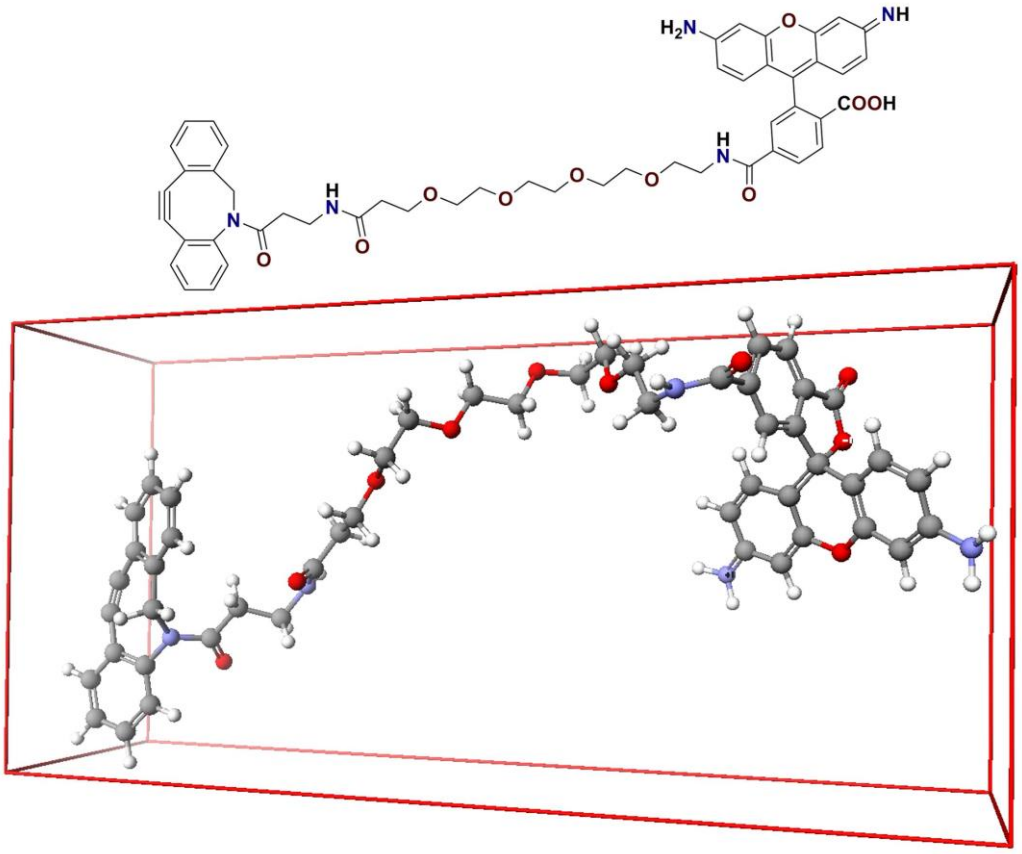

Figure 68. Structure and optimized geometry of DBCO carboxyrhodamine 110 (box dimensions: 8.489 Å × 15.283 Å × 31.636 Å).

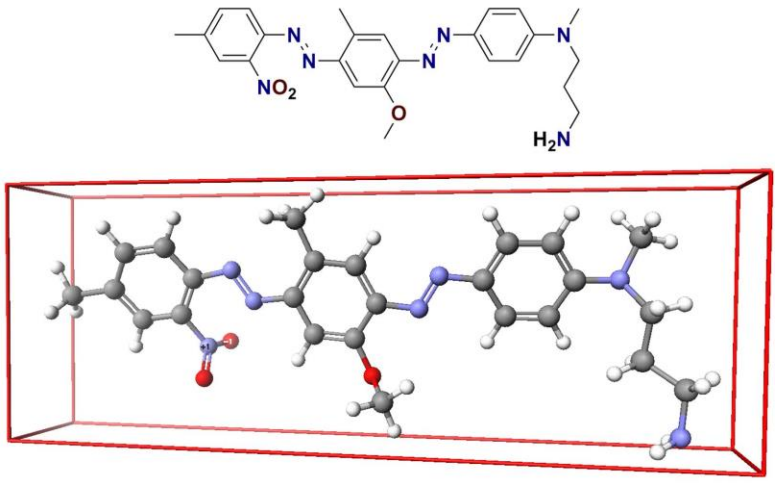

Figure 69. Structure and optimized geometry of BHQ-1 amine (box dimensions: 3.882 Å × 8.527Å × 23.761 Å).

3.4.5.2 DBCO carboxyhodamine 110 incorporation and LC-MS characterization

N_3-bMOF-100 (3 mg, containing 1.08×10^{-3} mmol N_3 groups) was washed with DMF (6X) in a 1.5 mL centrifuge tube. After removing most of the solvent while keeping the crystals wet, a DMF solution of H_2-F-BPDC (0.05 M, 0.5 mL) was added. The tube was incubated in a 35 °C thermomixer (600 rpm) for 4 hours. The crystals were washed with DMF (3X), soaked in DMF at 75 °C for 30 minutes, washed with DMF (3X), soaked in DMF at 75 °C for another 30 minutes, and then washed with DMF (3X). Then, the supernatant was removed and the crystals were added to a solution of DBCO carboxyrhodamine 110 (1 mg, 1.58×10^{-3} mmol) in DMF (0.2 mL) and incubated in a 25 °C thermomixer (600 rpm) for 16 hours.

After reaction, the supernatant was analyzed via LC-MS (Figure 70). The molecular weight of DBCO carboxyrhodamine 110 is 879.35 g/mol. In positive mode, m/z = 880 can be assigned to $[M+H]^+$, and m/z = 441 can be assigned to $[M+2H]^{2+}$. In negative mode, m/z = 878 can be assigned to $[M-H]^-$. In the negative mode, there were no peaks that correlated to the degradation product of the MOFs (e.g., H_2-N_3-BPDC or H_2-F-BPDC). After analysis of the supernatant, the crystals were washed with DMF (4X). The supernatant from the fourth wash was analyzed via LC-MS (Figure 71). A small amount of DBCO carboxyrhodamine 110 was present (note that the peak intensities are very low compared to Figure 70). Finally, the crystals were soaked again in DMF for 12 additional hours. The (fifth) supernatant was analyzed via LC-MS (Figure 72). No DBCO carboxyrhodamine 110 was present. Therefore, there was no significant leakage and any remaining dye molecules associated with the MOF were most likely covalently attached through the postsynthetic click modification. Next, approximately 20-30 crystals were digested in 0.15 mL DMF with a few drops of 1M NaOH/DI H_2O; the resulted solution was analyzed via LC-MS (Figure 73). In the negative mode, m/z = 1161 can be assigned

to the $[M-H]^-$ of the click product; m/z = 269 can be assigned to the $[M-H]^-$ of unreacted H_2-F-BPDC (not affected by the click reaction). There was no significant peak corresponding to H_2-N_3-BPDC (m/z = 282).

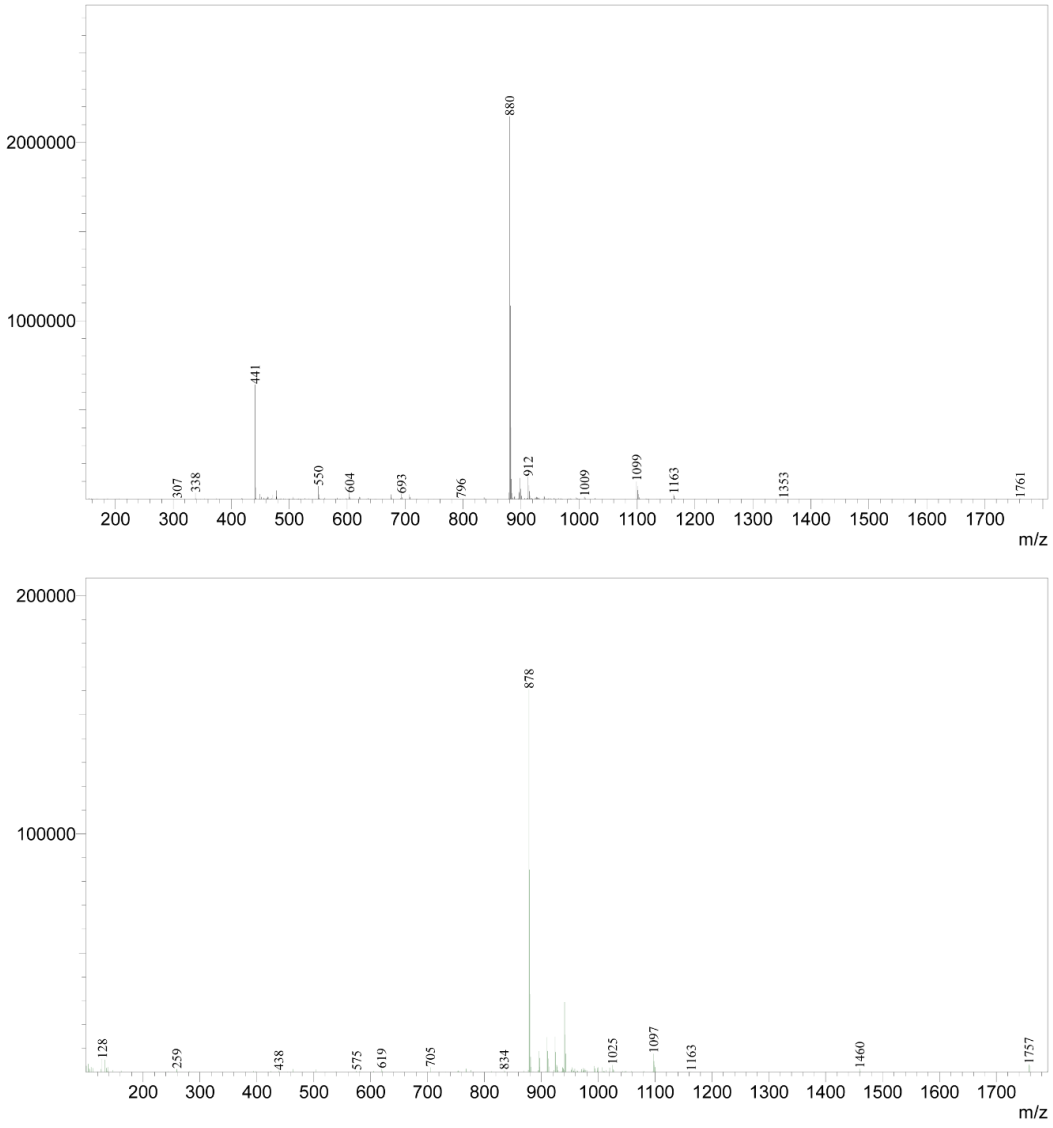

Figure 70. Mass spectra of supernatant immediately after DBCO carboxyrhodamine 110 incorporation reaction (top: positive; bottom: negative).

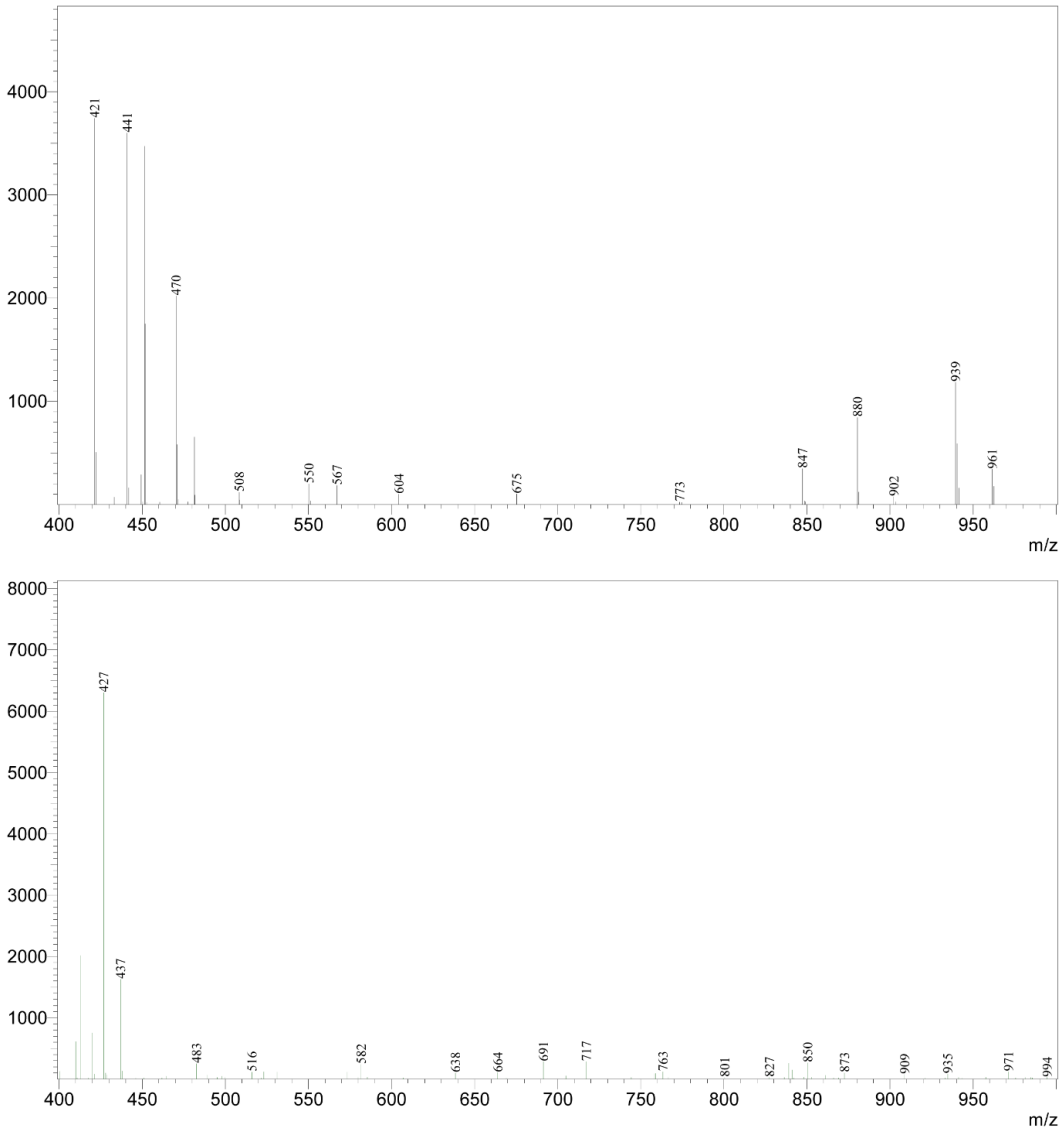

Figure 71. Mass spectra of supernatant after the fourth DMF wash after DBCO carboxyrhodamine 110 incorporation reaction (top: positive; bottom: negative).

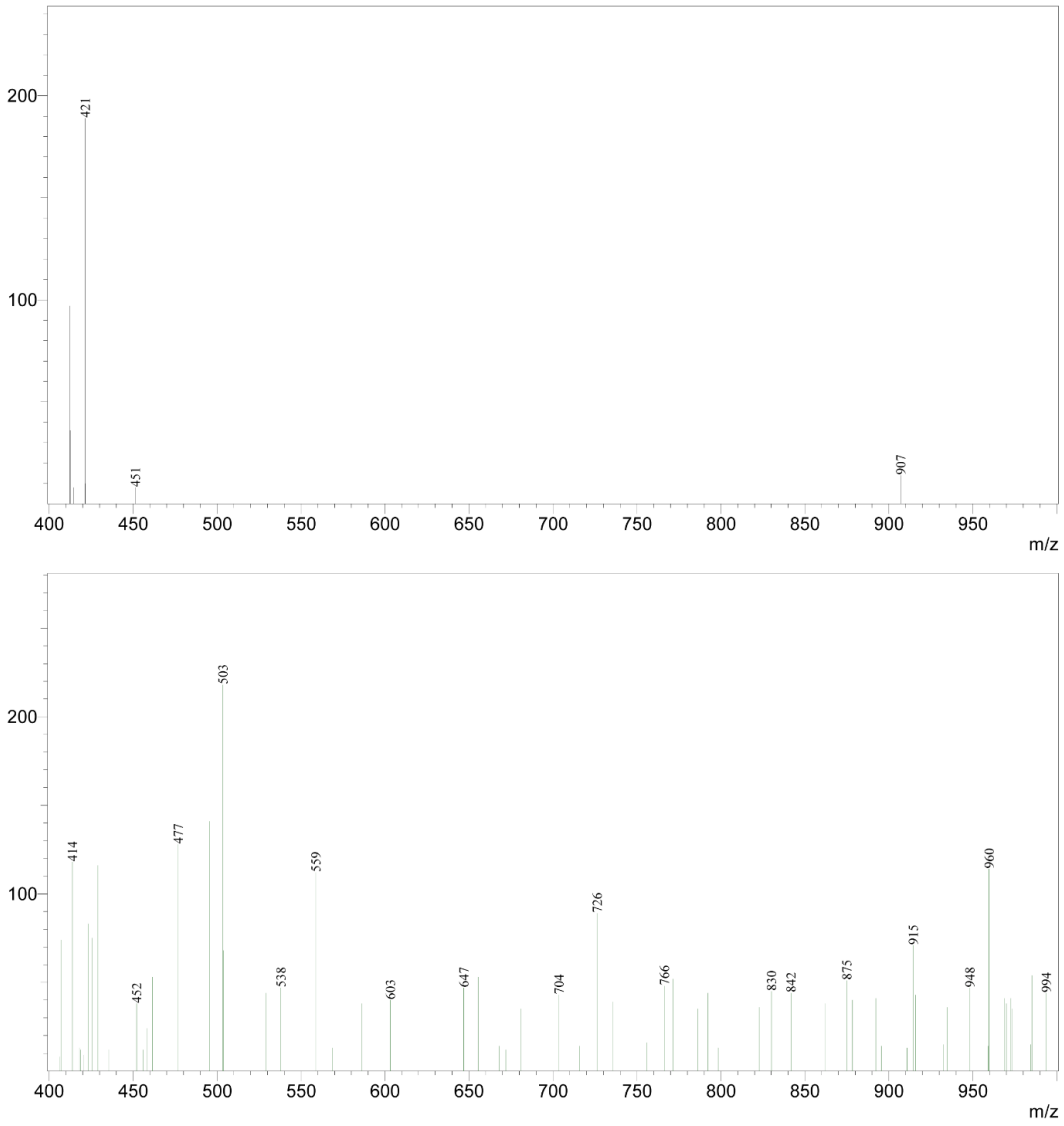

Figure 72. Mass spectra of the fifth supernatant after 12-hour leakage test (top: positive; bottom: negative).

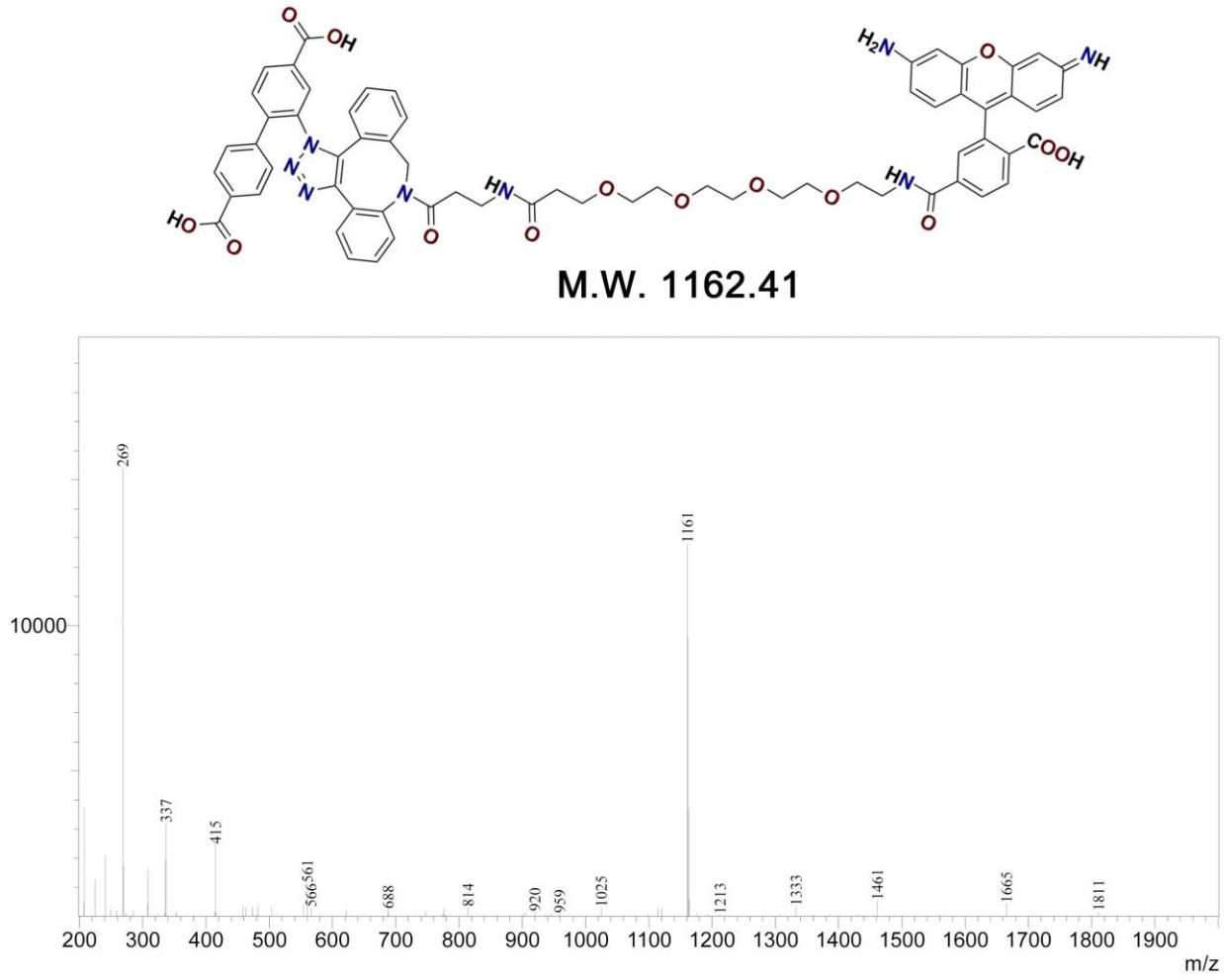

Figure 73. Mass spectrum of digested N_3/F-bMOF-100 after reaction with DBCO carboxyrhodamine 110 (negative mode).

3.4.5.3 BHQ-1 amine incorporation and LC-MS characterization

After the click reaction with DBCO carboxyrhodamine 110 and subsequent washing steps described in 3.4.5.2, the MOF crystals were soaked in a solution of BHQ-1 amine (2 mg, 4.21×10^{-3} mmol) in DMF (0.2 mL) and incubated in a 25 °C thermomixer (600 rpm) for 16 hours. Immediately after reaction, the supernatant was analyzed via LC-MS (Figure 74). The

molecular weight of BHQ-1 amine is 475.23. In positive mode, m/z = 476 can be assigned to $[M+H]^+$. In negative mode, m/z = 1161 (dye-BPDC product) and m/z = 269 (H_2-F-BPDC) indicated that the MOF was degrading to some extent, possibly due to the basic nature of BHQ-1 amine. After analysis of the supernatant, the crystals were washed with DMF (8X). The supernatant from the eighth wash was analyzed via LC-MS (Figure 75). Only a very small amount of BHQ-1 amine was present (m/z = 476, positive mode) (note that the intensities are very low compared to Figure 74). Finally, the crystals were soaked again in DMF for 8 hours. Then, the (ninth) supernatant was analyzed via LC-MS (Figure 76). Again, only a very small amount of BHQ-1 amine was present (m/z = 476, positive mode). Therefore it was concluded that most of the quencher molecules were likely covalently attached to the MOF through the postsynthetic aldehyde-amine condensation reaction. It was suspected that the MOF dissolution condition could reverse the formation of the imine linkage, releasing free BHQ-1 amine. Therefore, to confirm the imine formation between BHQ-1 amine and F-BPDC in the MOF sample, reduction of the imine bonds was attempted to obtain permanent adduct. Approximately 20-30 crystals were treated with 0.15 mL MeOH and a few drops of 1M $NaBH_4$/MeOH for 10 minutes. Then, the crystals were dissolved with 1M NaOH/H_2O and some DMF for LC-MS analysis (Figure 77). In the positive mode, m/z = 730 can be assigned to $[M+H]^+$ of the secondary amine (reduced imine product). m/z = 476 can be assigned to $[M+H]^+$ of BHQ-1 amine; its presence indicated the incomplete reduction of the imine. Some imine may have decomposed into the original BHQ-1 amine and F-BPDC, which was indeed found in the negative mode (m/z = 269). Also, in the negative mode, m/z = 1162 can be assigned to the $[M-H]^-$ (1161 rounded up by software).

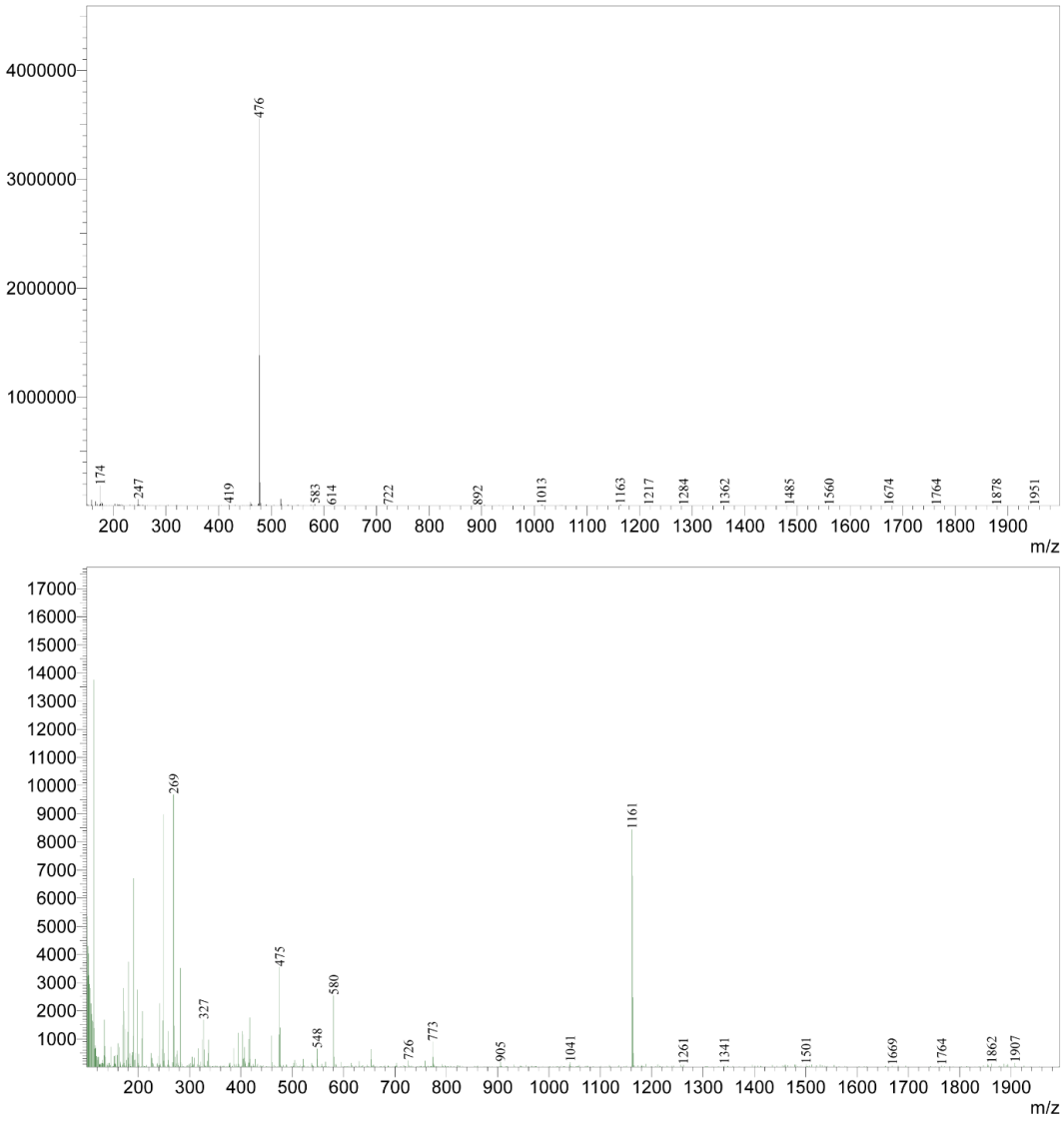

Figure 74. Mass spectra of the supernatant immediately after BHQ-1 amine incorporation reaction (top: positive; bottom: negative).

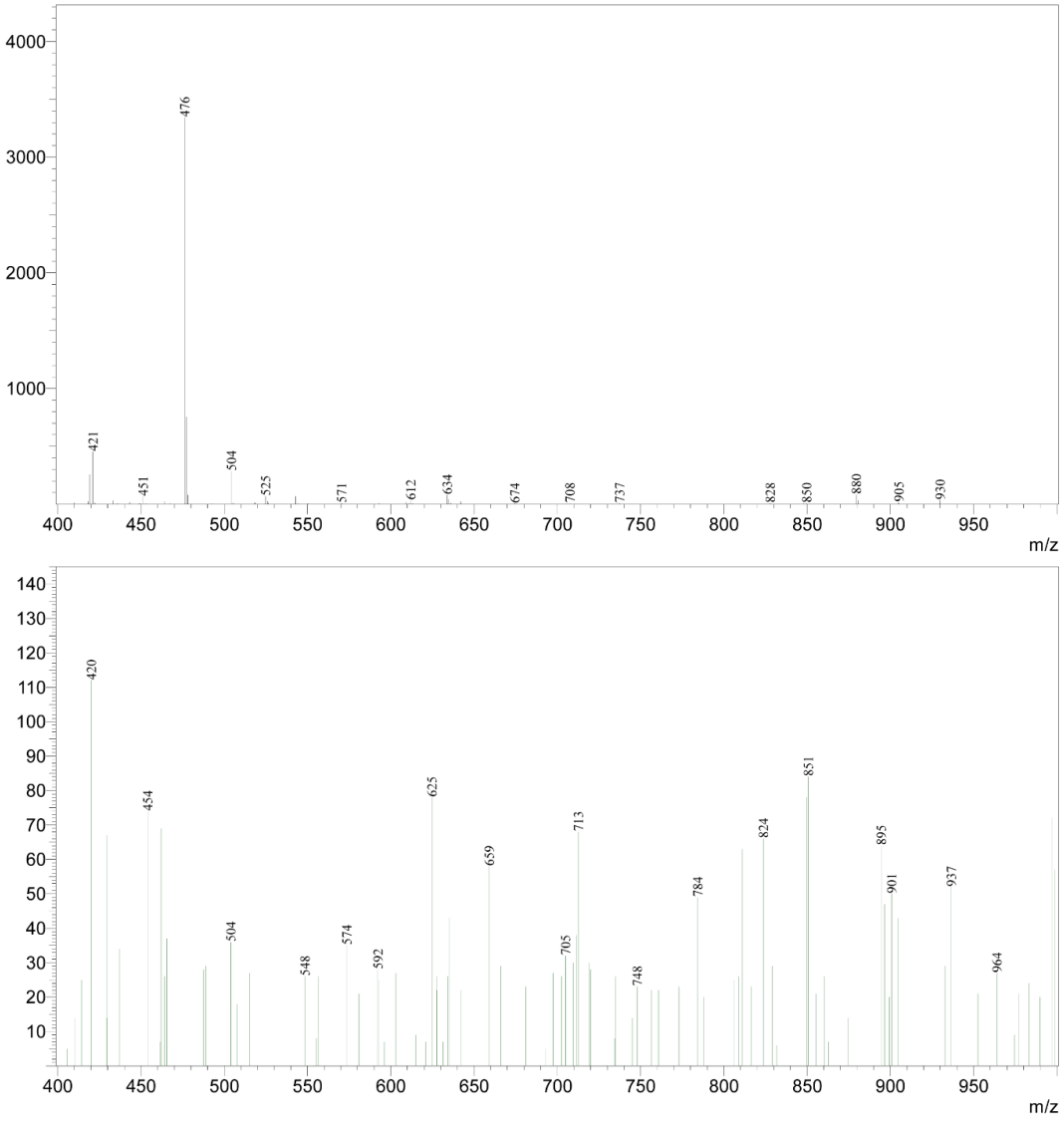

Figure 75. Mass spectra of supernatant after the eighth DMF wash after BHQ-1 amine incorporation reaction (top: positive; bottom: negative).

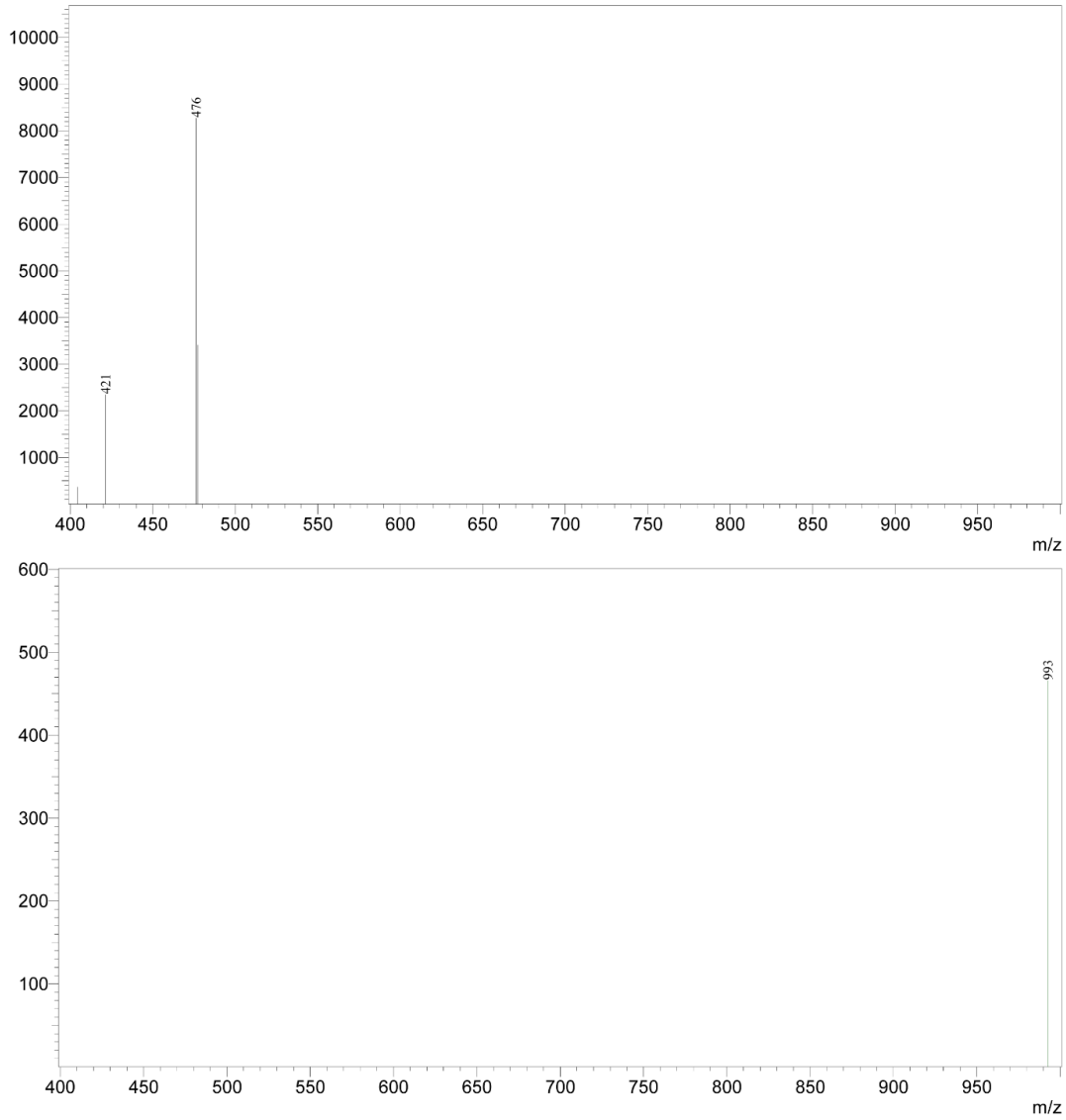

Figure 76. Mass spectra of the ninth supernatant after 8-hour leakage test (top: positive; bottom: negative).

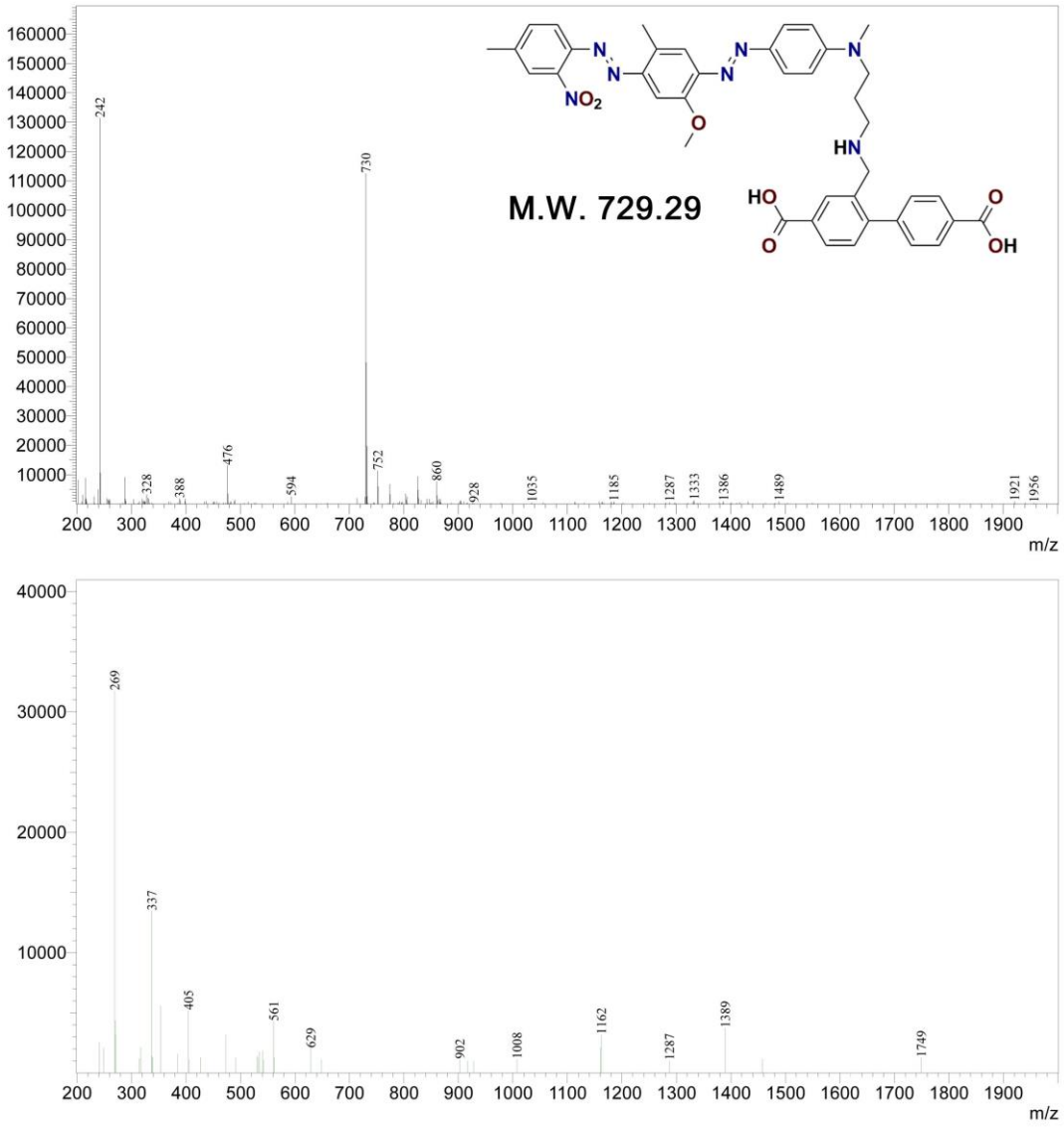

Figure 77. Mass spectra of digested N_3/F-bMOF-100 after reaction with DBCO carboxyrhodamine 110 and BHQ-1 amine (top: positive mode; bottom: negative mode).

3.4.5.4 Picture of MOFs before and after dye/quencher incorporation

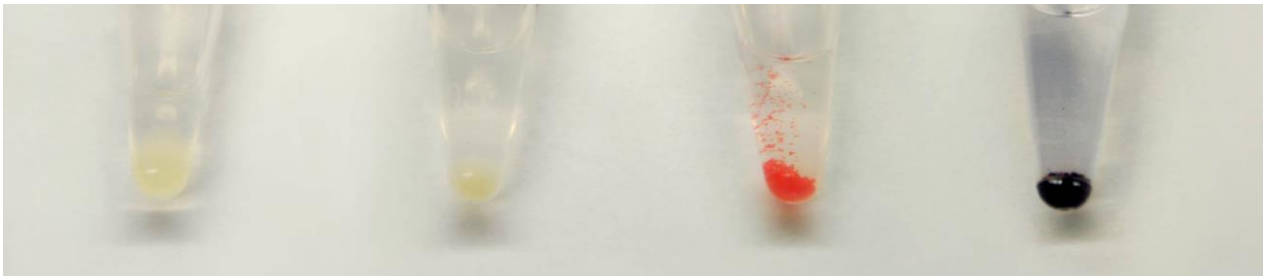

Figure 78. From left to right: N_3-bMOF-100, N_3/F-bMOF-100, dye-modified N_3/F-bMOF-100, dye/quencher-modified N_3/F-bMOF-100.

3.4.6 Microspectrophotometry

Using methods described in previous sections, all the MOFs used for microspectrophotometric experiments were properly washed with DMF and then dried *in vacuo*. N_3/F-bMOF-100 (abbreviated as MOF in this section), N_3/F-bMOF-100 with carboxyrhodamine 110 (abbreviated as MOF + dye), N_3/F-bMOF-100 with carboxyrhodamine 110 and BHQ-1 amine (abbreviated as MOF + dye + BHQ), and ground samples of the latter two were placed on glass slides for microspectrophotometric measurements. Aside from the spectra and images shown in Figure 67, two other parallel experiments were performed. The results are shown below in Figures 79-82.

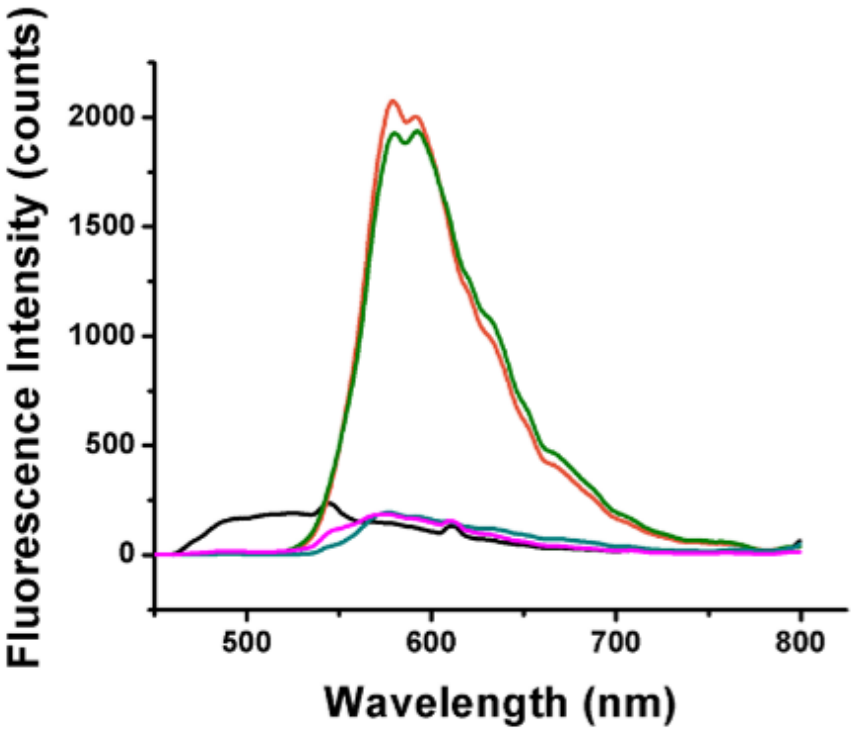

Figure 79. Fluorescence spectra excited at 420 nm. (black: MOF; orange: MOF + dye; olive: MOF + dye (ground); cyan: MOF + dye + BHQ; magenta: MOF + dye + BHQ (ground))

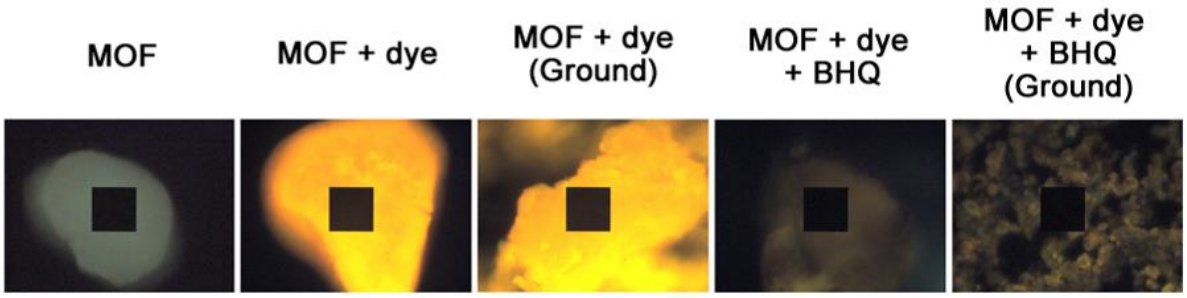

Figure 80. Microscopic images of the materials. The black squares represent the 31 × 31 μm^2 sampling area for spectroscopy.

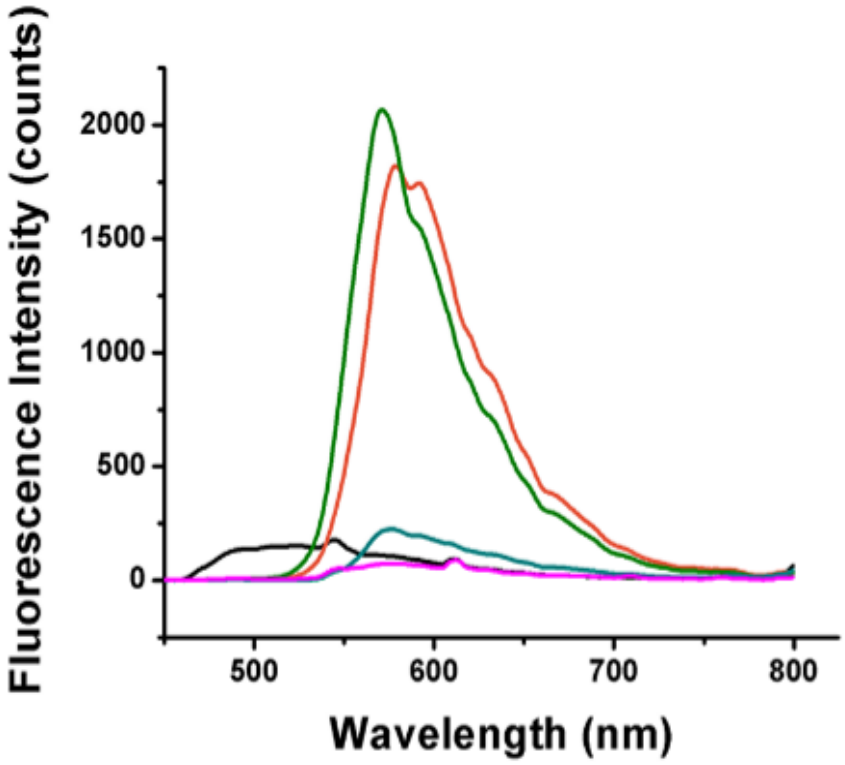

Figure 81. Fluorescence spectra excited at 420 nm. (black: MOF; orange: MOF + dye; olive: MOF + dye (ground); cyan: MOF + dye + BHQ; magenta: MOF + dye + BHQ (ground))

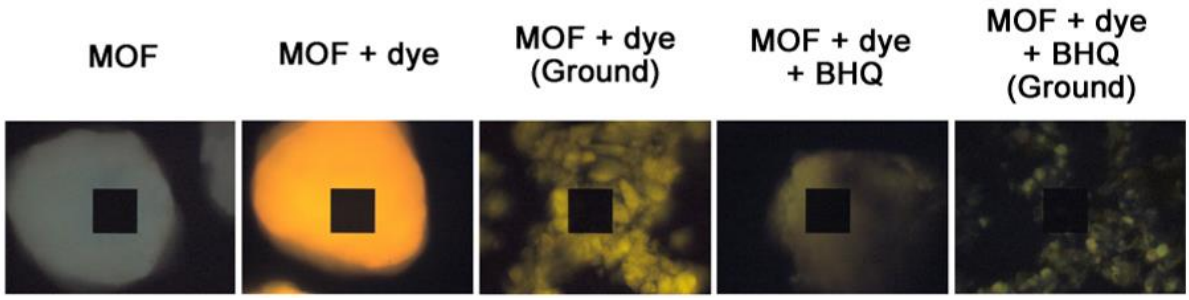

Figure 82. Microscopic images of the materials. The black squares represent the 31 × 31 μm^2 sampling area for spectroscopy.

4.0 ESTABLISHING POROSITY GRADIENTS WITHIN METAL-ORGANIC FRAMEWORKS USING POSTSYNTHETIC LIGAND EXCHANGE

This work, written in collaboration with Chenjie Zeng, Tian-Yi Luo, Andrea D. Merg, Rongchao Jin and Nathaniel L. Rosi*, has been submitted for publication.

Chenjie Zeng prepared the Au nanoclusters and assisted with characterization of the Au nanoclusters (UV-Vis, MALDI). Tian-Yi Luo assisted with synthesis of one ligand and PXRD characterization of MOF samples. Andrea D. Merg performed TEM imaging of Au nanocluster-embedded MOF samples.

4.1 INTRODUCTION

The properties and functions of some of the most fascinating natural systems derive from a collection of cooperative structural and functional domains/units precisely organized with respect to one another. These systems provide inspiration to chemists and materials scientists aiming to construct complex functional materials comprising multiple different functional domains or building blocks.

MOFs are attractive scaffold materials for organizing complex molecules and functional nanomaterials in 3-D space. First, MOFs are 3-D periodic crystalline materials, so the position of their component building blocks is known. Second, multiple strategies exist for modifying MOF

scaffolds with either small functional groups or even with large, complex molecules. Third, numerous methods have been reported for introducing structural and functional heterogeneity into otherwise homogeneous MOF crystals.[122] These approaches include mixed-ligand solvothermal synthesis, postsynthetic modification, ligand exchange and removal/corrosion, and crystal overgrowth to obtain core-shell or stratified MOFs.[22,26-27,29,129] Challenges remain to predict and identify the patterns of achievable structural and functional heterogeneity.[116,123-126]

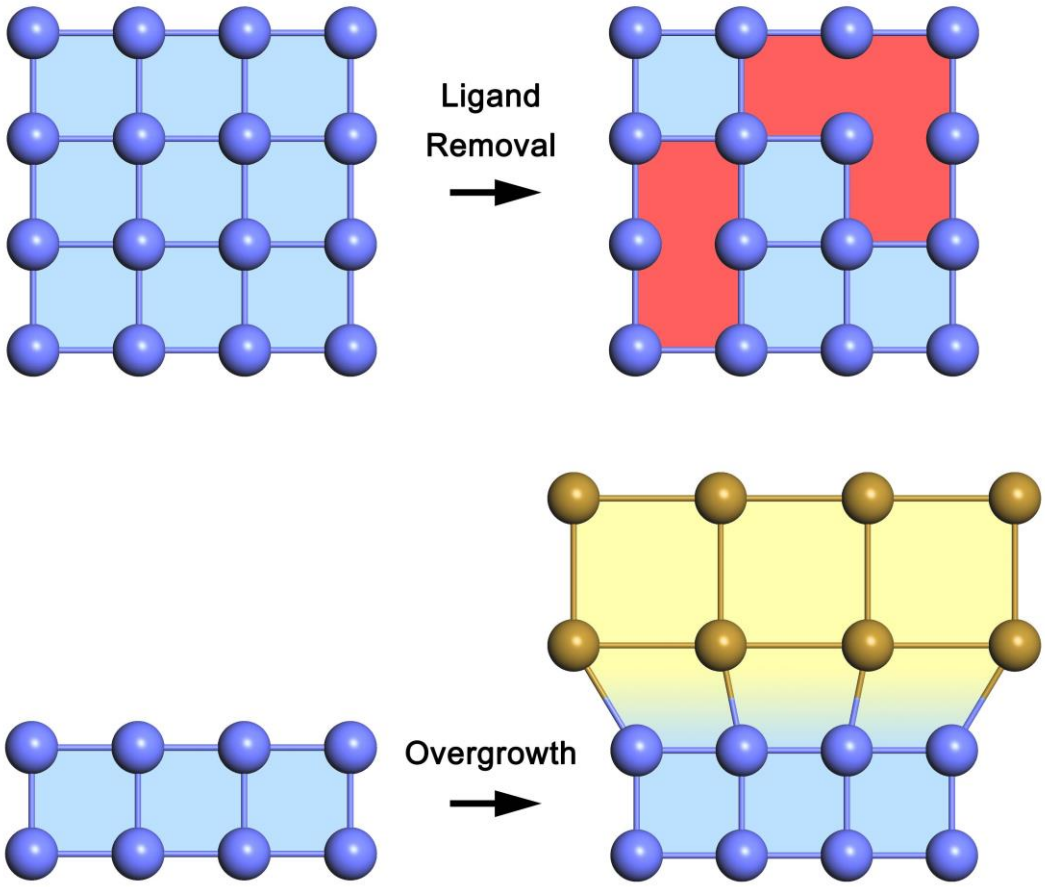

Figure 83. Achieving heterogeneity in MOFs via ligand removal and crystal overgrowth.

With the exception of crystal overgrowth, established methods usually lack spatial and compositional control over the heterogeneous components in MOFs. For example, partial ligand removal can disrupt local structures and merge neighboring pores (Figure 83, top).[57,130-132] Hence

hierarchical heterogeneity in porosity was often realized by overgrowth on thin-film or monolithic MOF crystals.[133] The process can be epitaxial growth of lattice-matched MOFs or combining completely different MOFs with the involvement of surfactants (Figure 83, bottom).[123,134-140] Constructing MOFs with organized domains or strata of differential porosity is a significant challenge. Controlled placement of pores of different sizes may ultimately allow for controllable flow of analytes or reagents from domain to domain within a MOF crystal. Further, it may enable selective placement of molecules within the crystal based on geometrical parameters such as kinetic diameter. Here, it is presented that pore size expansion within mesoporous bMOF-100 series MOF crystals via ligand exchange occurred not randomly but rather regionally and directionally in an "outside→in" fashion. This phenomenon was exploited to create discrete MOF crystals with identifiable domains of differential porosity and directional pore size gradients.

It was previously demonstrated by our group that stepwise ligand exchange could be used to incrementally increase the pore size of mesoporous bMOF-100 crystals by replacing the original ligands with longer ligands.[53] This study was the first example of using ligand exchange to increase MOF pore dimensions. The observed pore expansion phenomenon was fundamentally interesting because bMOF-100 is a cubic crystal, therefore ligand exchange and pore expansion must simultaneously occur in three dimensions. Other ligand exchange based pore expansion studies have since been reported for pillared MOFs, wherein the MOF was expanded in only a single dimension.[52] Given the unique aspects of the bMOF-100 system, study of the ligand exchange based pore expansion process in greater detail is meaningful in order to push the dimension limits of pore expansion and gain an understanding of the process.

4.2 RESULTS AND DISCUSSION

4.2.1 Sequential pore expansion from bMOF-100 to bMOF-107

The following sequential pore expansion process has been realized: bMOF-100→bMOF-102→bMOF-106→bMOF-107 (Figure 84). It is noteworthy that bMOF-106 and bMOF-107 represent new additions to this isoreticular series. In this series, bMOF-100 crystals were converted to bMOF-102 crystals via exchanging BPDC with ABDC; the as produced bMOF-102 crystals were converted to bMOF-106 crystals through exchange of ABDC with 2'-nitro-1,1':4',1''-terphenyl-4,4''-dicarboxylate (NO_2-TPDC); and finally the as produced bMOF-106 crystals were converted to bMOF-107 through exchange of NO_2-TPDC with 4-(3'-nitro-4'-(4''-carboxylphenylethynyl)phenyl)benzoate (NO_2-eTPDC). Unit cell parameters for the product MOFs were collected and model structures were constructed using these data (Experimental Section 4.4.4.5). Complete structural conversion via ligand exchange was confirmed by comparing the experimental powder X-ray diffraction (PXRD) patterns of the product materials to simulated PXRD patterns generated from the model structures (Figure 85). The composition of the product materials, after copious washing to remove unbound ligands, was determined via ^{1}H NMR of dissolved samples (Figure 86). In each case, ligand exchange was virtually complete (> 97% exchange). The mechanism of exchange (e.g., associative/dissociative) was yet to be unraveled, but it was known that the coordination capabilities of incoming ligands had a direct impact on the rate and extent of ligand exchange.[52] The structural conversion from bMOF-102 to bMOF-106 was similar to the previously reported expansion from bMOF-102 to bMOF-103;[53] however, conversion from 102 to 106 was significantly faster and more complete than the conversion from 102 to 103. The only difference between the two reactions was the functional

group on the terphenyldicarboxylic acid: an electron donating amino group for 103 and an electron withdrawing nitro for 106. This difference highlighted the importance of ligand acidity (i.e., concentration of coordination sites) for ligand exchange in this system, where more acidic ligands accelerated the process. It was therefore surmised that the reaction was kinetically controlled.

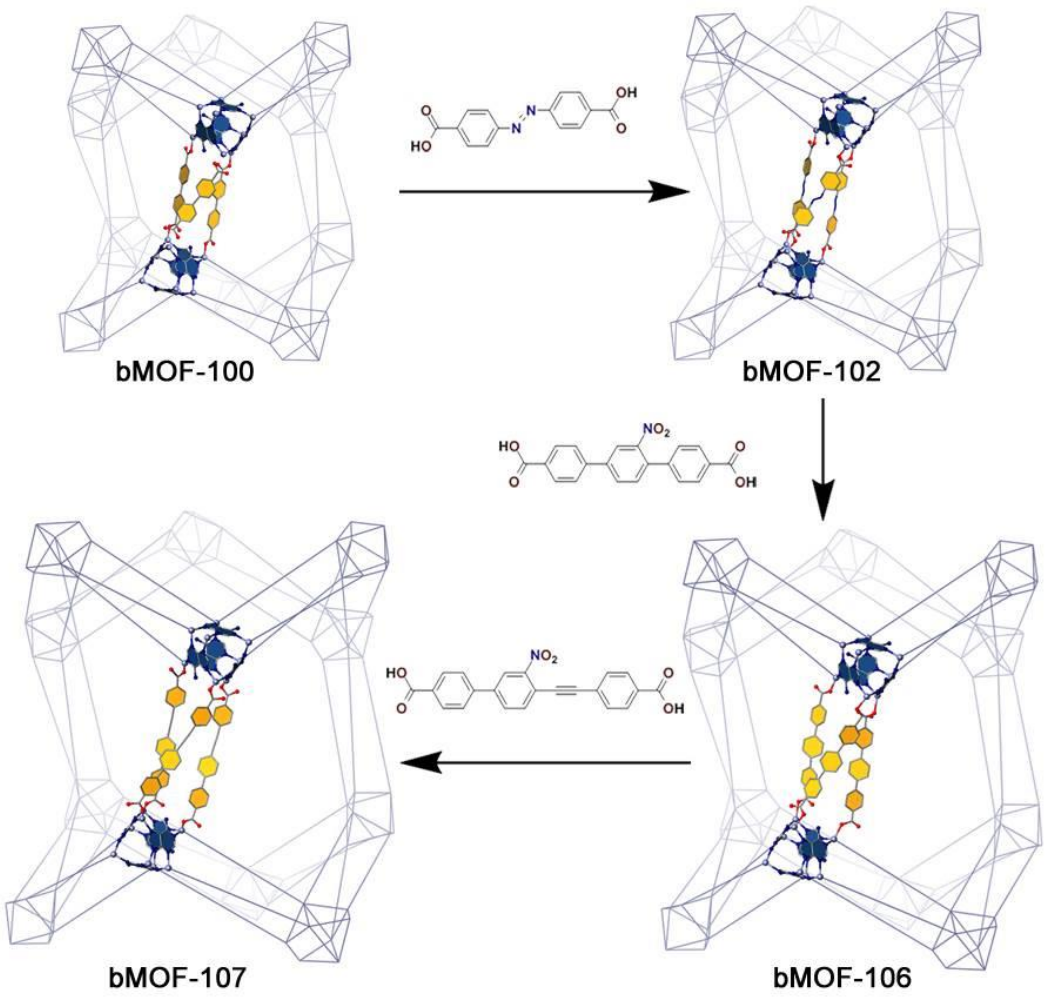

Figure 84. Schematic representation of sequential pore expansion from bMOF-100 to bMOF-102 to bMOF-106 to bMOF-107 via postsynthetic ligand exchange.

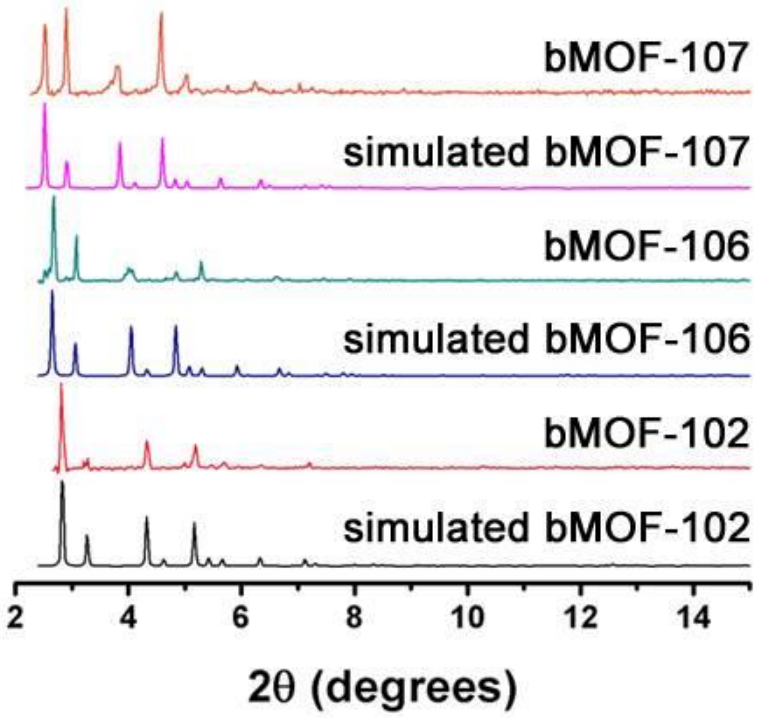

Figure 85. PXRD comparing MOFs prepared from ligand exchange with simulated patterns.

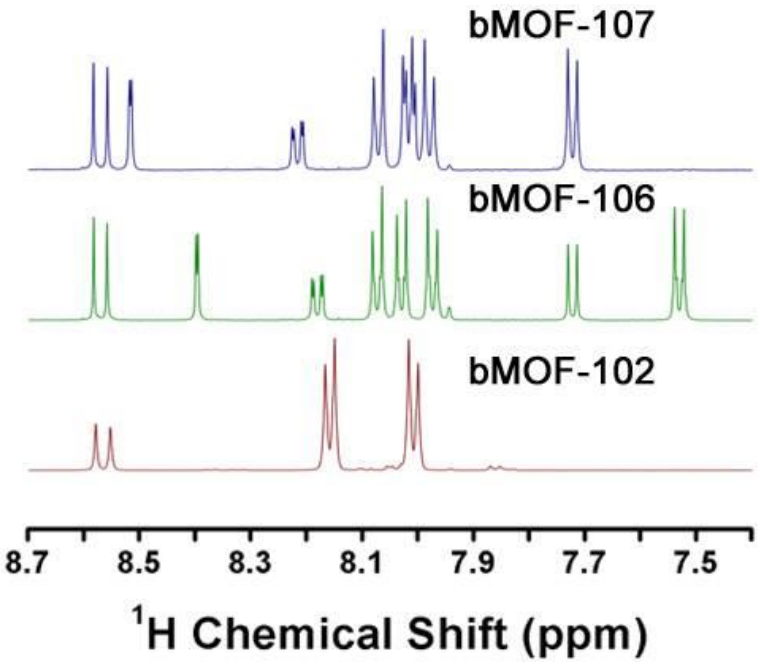

Figure 86. ^{1}H NMR spectra revealing the composition of MOFs made from ligand exchange.

For crystals with the same average size, close monitoring of the reaction with ^{1}H NMR revealed that ligand replacement proceeded gradually, as indicated by the gradually increasing presence of the longer linker in the product material (Figure 87). Based on this observation, it was proposed that there were two possible mechanisms for the ligand exchange-based MOF pore expansion: it could be a dissolution-recrystallization process; or it could be a solid state crystal-to-crystal transformation (Figure 88).

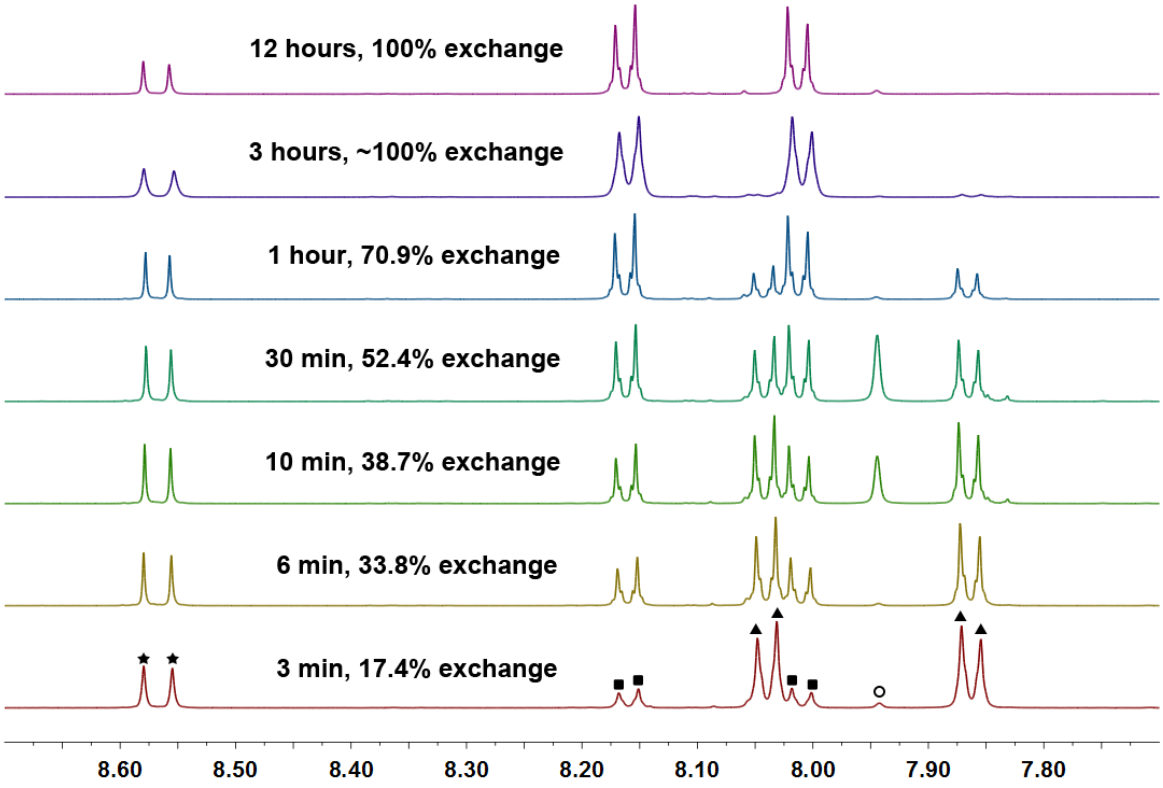

Figure 87. ^{1}H NMR spectra of dissolved crystals at different time points of the reaction between bMOF-100 and H_2-ABDC.*

* Peak assignment: star-adenine, square-ABDC, triangle-BPDC, circle-DMF. Exchange percentage was calculated by comparing ABDC and BPDC.

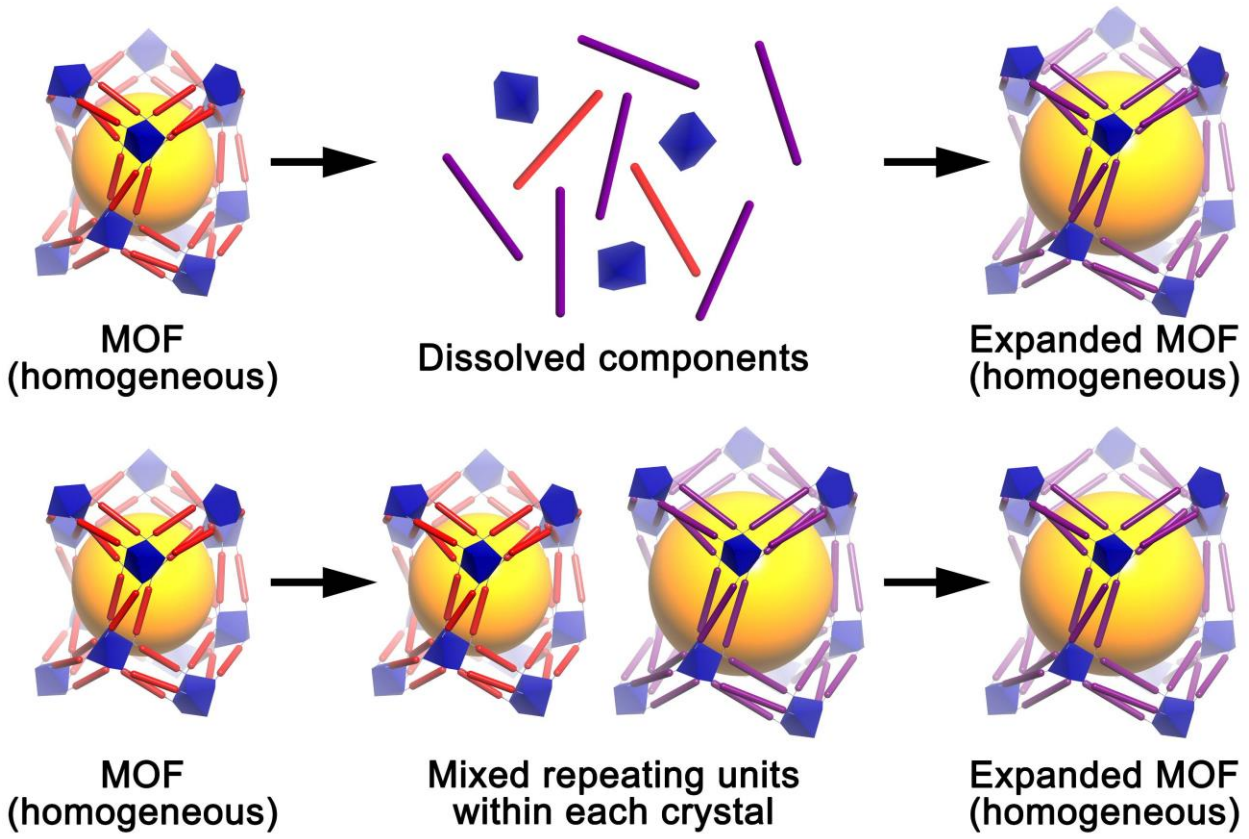

Figure 88. Possible mechanisms for MOF pore expansion (top: dissolution-recrystallization; bottom: solid state crystal-to-crystal transformation).

As illustrated in Figure 89, all attempts to directly convert bMOF-100 to 106 or 102 to 107 failed. In these cases, the framework remained unexpanded and did not contain the longer ligands, as evidenced by PXRD (Figure 90) and ^{1}H NMR (Figures 91), respectively. Therefore it was concluded that, for this system, MOF pore expansion via ligand exchange was only successful if the ligand length was incrementally increased (< ~0.3 nm length change). It was then deduced from these results that structure conversion occurred through ligand exchange in the solid state material rather than through a dissolution/recrystallization process, because the

latter process would presumably accommodate any ligand length provided that the ligand could form an isoreticular MOF. Additionally, the pores in this series are sufficiently large (> 2 nm) and continuous, so ligand diffusion should not be an issue.

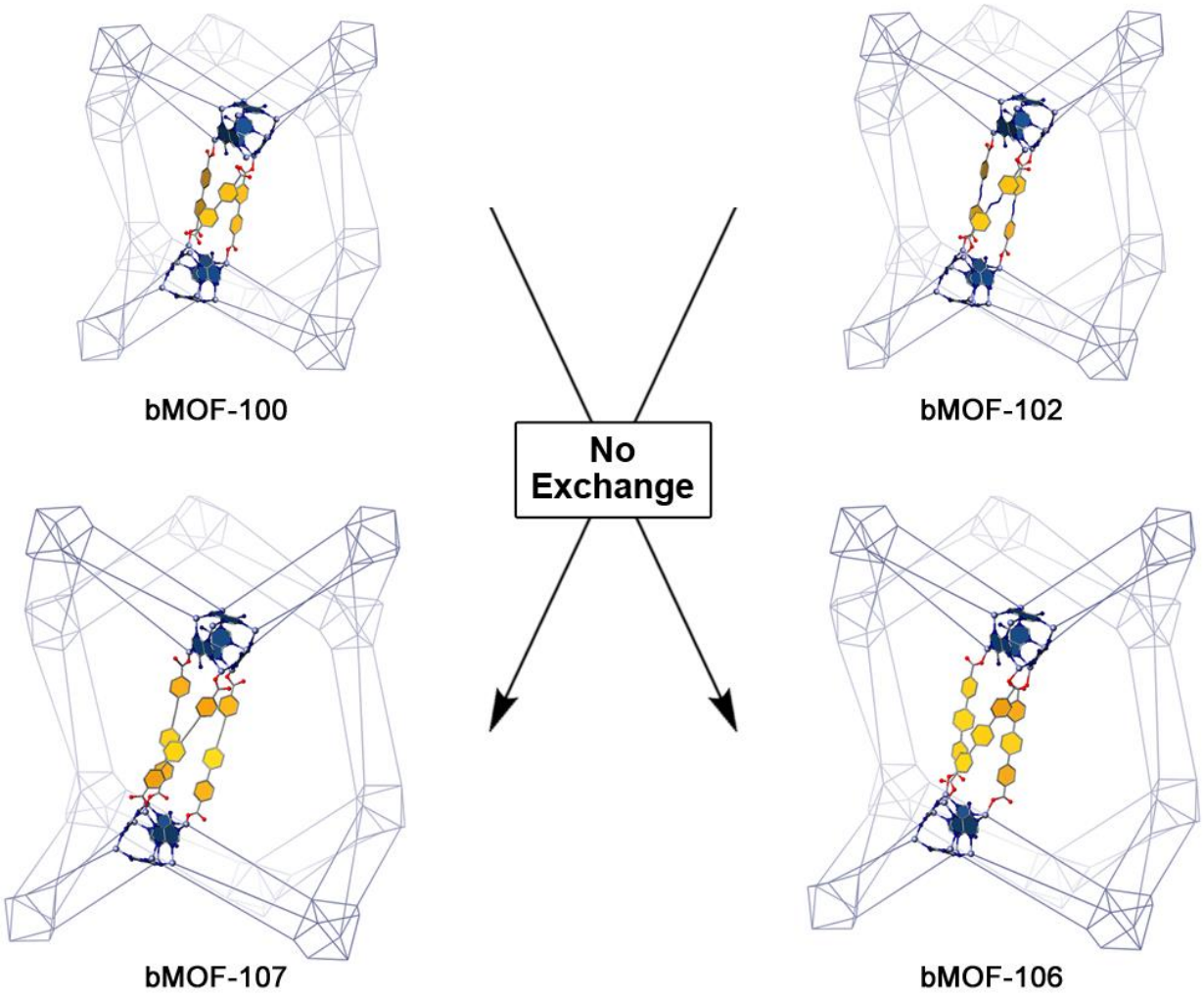

Figure 89. Inaccessible pore expansion from bMOF-100 to bMOF-106 and bMOF-102 to bMOF-107, as a result of inappropriate step sizes.

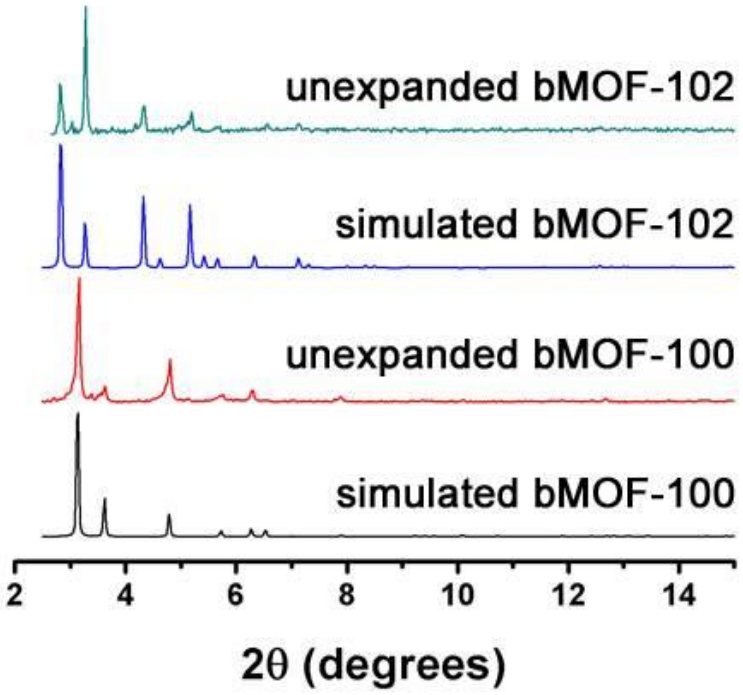

Figure 90. PXRD comparing MOFs after treatment of inappropriate ligands, proving unchanged structure and porosity.

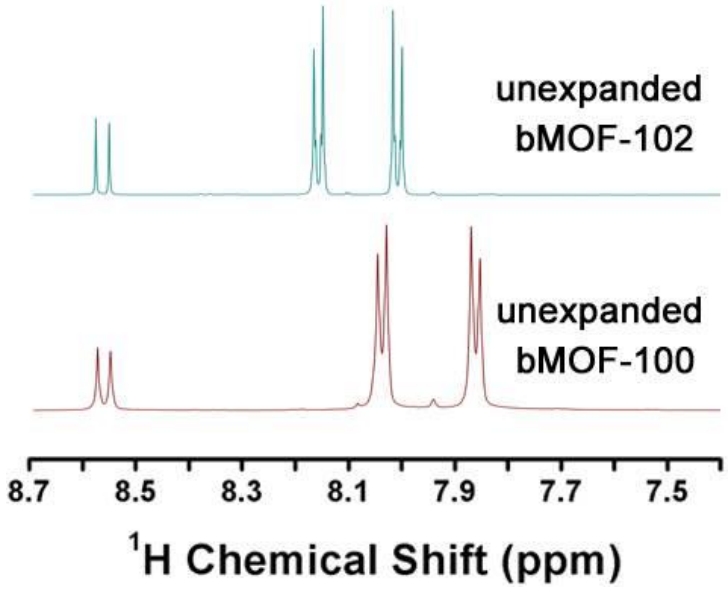

Figure 91. ^{1}H NMR spectra revealing the unchanged composition of MOFs after treatment of inappropriate ligands.

4.2.2 Intermediate MOFs during pore expansion

As described in 4.2.1, incremental stepwise pore expansion for the bMOF-100 series was established, to study the mechanism in greater detail, it was necessary to determine whether the ligand exchange process occurred homogeneously throughout the crystal (i.e., simultaneously in all regions of crystal) or heterogeneously (i.e., gradually from domain to domain). Large bMOF-100 crystals were synthesized under modulated solvothermal conditions (Experimental Section 4.4.3) and the ligand exchange reaction to produce bMOF-102 was allowed to proceed for 10 min. before it was terminated (Figure 92A). The composition and structure of the product crystals were analyzed. Based on ^{1}H NMR analysis, 38.7% of the BPDC ligands were exchanged with ABDC (Figure 87). A large crystal was carefully fractured. It was clear from light microscopy images (Figure 92B) that the crystal periphery bore the orange color characteristic of the ABDC ligand and the crystal core remained colorless. Inspired by studies of the transformation of MOFs using single crystal X-ray diffraction,[141] unit cell data were collected for the orange periphery fraction and the colorless core (Table 1). The data suggested that the ligands were distributed in a gradient fashion from ABDC to BPDC from the periphery to the core, respectively; that is, the periphery contained more bMOF-102 character (larger unit cell) and the core contained more bMOF-100 character (smaller unit cell).

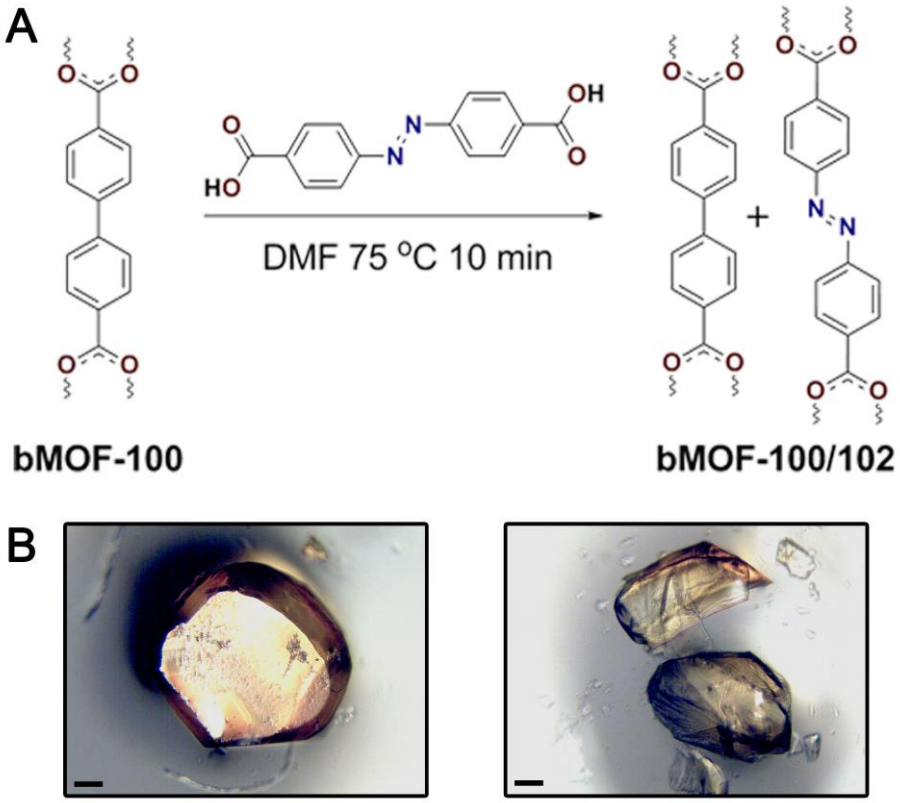

Figure 92. (A) Fast ligand exchange reaction to yield intermediate bMOF-100/102. (B) Optical images showing an intact crystal (left) and manually separated "core" and "shell" (right).*

Table 1. Comparison of crystallographic parameters in bMOF-100/102 system.

Sample	Space Group	$a = b = c$ (Å)	Reported $a = b = c$ (Å)
bMOF-100	*Ia-3d*	69.129(2)	69.12
bMOF-100 "unexchanged" core	*Ia-3d*	69.504(3)	N/A
bMOF-100 partially exchanged shell	*Ia-3d*	71.881(2)	N/A
bMOF-100 to bMOF-102 intermediate intact crystal	*Ia-3d*	70.554(18)	N/A
bMOF-102 "fully" exchanged	*Ia-3d*	75.235(1)	75.24

* For images on Figure 92B, scale bar = 50 μm

Similar experiments were performed on the bMOF-102/106 intermediate sample and the data also suggested that ligand exchange began at the periphery and proceeded toward the core (Figure 93 and Table 2). ^{1}H NMR was used to further study the composition (Figure 94). From these results, it was concluded that pore expansion via ligand exchange proceeded in an "outside→in" fashion. Here it is proposed that the "outside→in" mechanism is the only reasonable explanation for the gradual replacement of shorter ligands with longer ligands (e.g., ^{1}H NMR results in Figure 87). During the solid state crystal-to-crystal transformation, at the intermediate stages, structural units of different sizes (as shown in Figure 88) co-exist in the same crystal, which should generate mechanical strain. The 3-D structures of these MOFs are somewhat flexible and can tolerate the strain. To keep the crystals intact, apparently they must expand gradually and uniformly, starting from the outermost structural units, because otherwise a confined expansion would definitely lead to crystal decomposition. Therefore, the larger structural units are present to a higher extent in the periphery. Accordingly, the distribution of longer ligands occurs in a gradient fashion from the crystal periphery to the crystal core, indicating that the ligand exchange proceeds in an "outside→in" fashion. The interesting implication of these findings is that this process can be used to produce MOFs with porosity gradients or "core-shell" MOFs having large pores in the shell and small pores in the core. Two gradient MOFs bMOF-100/102 and bMOF-102/106, simplified as core-shell structures, are abstracted in Figure 95, illustrating the hierarchical distribution of different pore sizes.

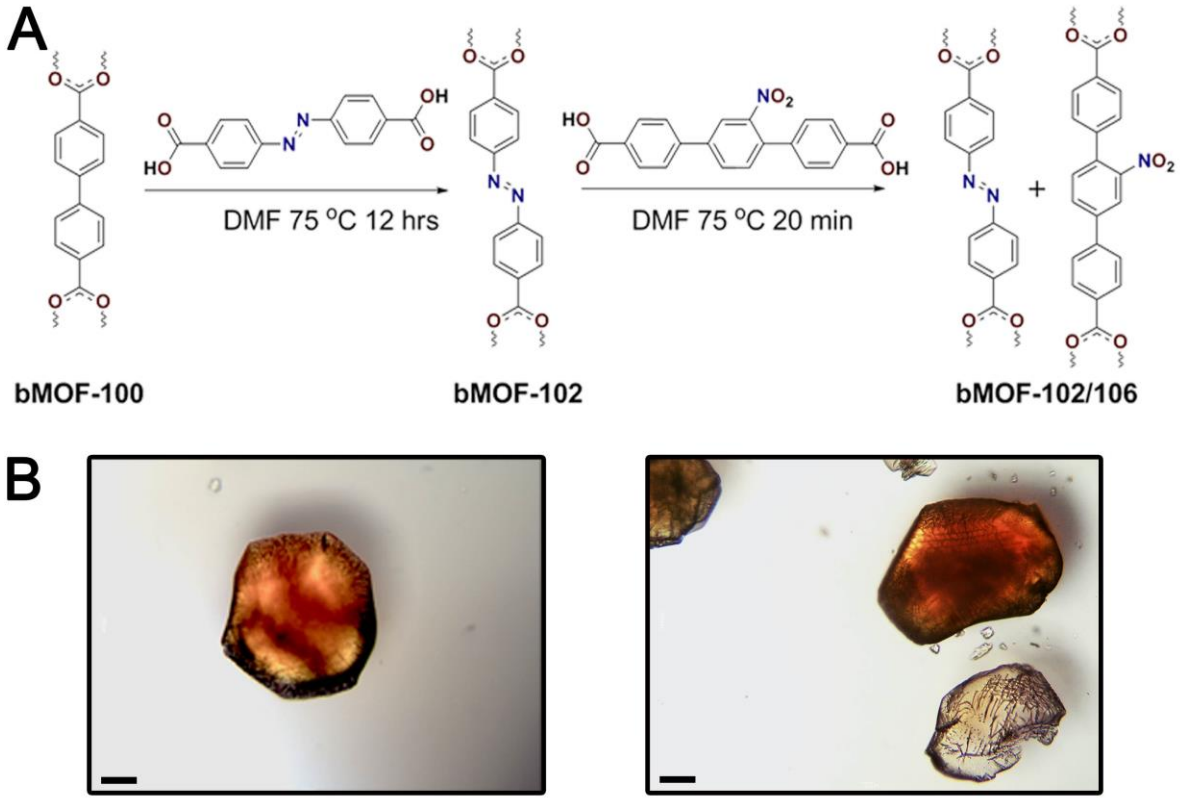

Figure 93. (A) Fast ligand exchange reaction to yield intermediate bMOF-102/106. (B) Optical images showing an intact crystal (left) and manually separated "core" and "shell" (right).*

Table 2. Comparison of crystallographic parameters for bMOF-102/106 system.

Sample	Space Group	$a = b = c$ (Å)	Reported $a = b = c$ (Å)
bMOF-102	*Ia-3d*	75.2350(10)	75.24
bMOF-102 "unexchanged" core	*Ia-3d*	75.7847(25)	75.24
bMOF-106 partially exchanged shell	*Ia-3d*	81.3147(322)	N/A
bMOF-102 to bMOF-106 intermediate intact crystal	*Ia-3d*	77.4103(78)	N/A
bMOF-106 "fully" exchanged	*Ia-3d*	81.7060(32)	N/A

* For images on Figure 93B, scale bar = 100 μm

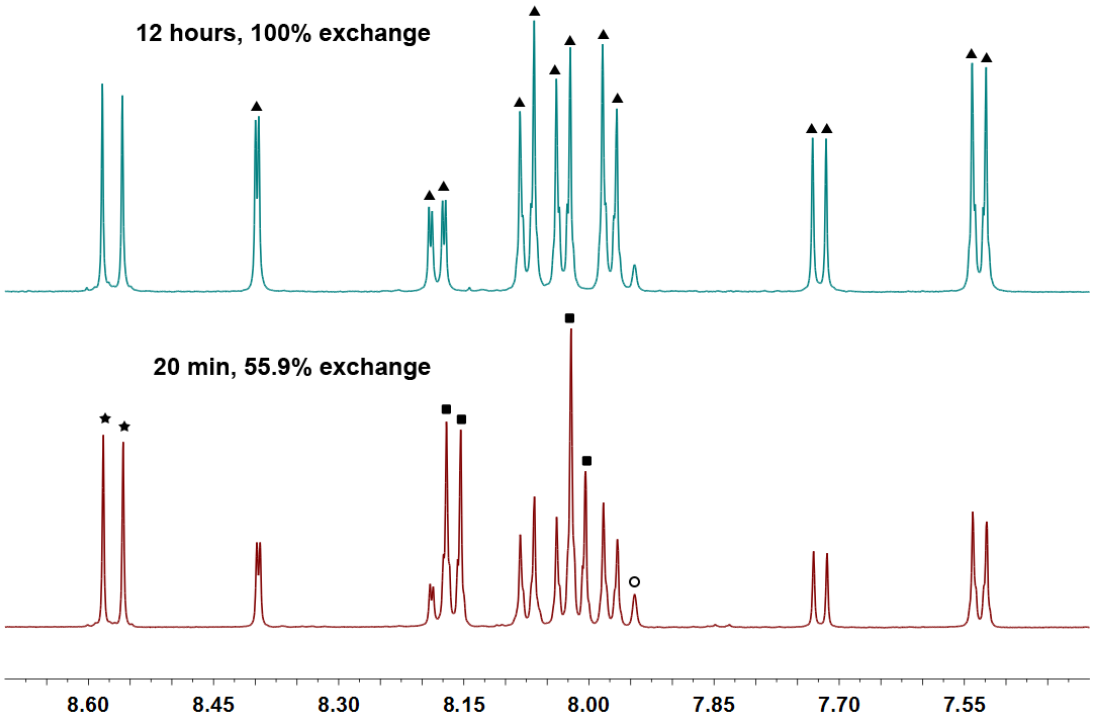

Figure 94. ^{1}H-NMR spectra of dissolved crystals at different time points of the reaction between bMOF-102 and H_2-NO_2-TPDC.*

* Peak assignment: star-adenine, square-ABDC, triangle-H_2-NO_2-TPDC, circle-DMF. Exchange percentage was calculated by comparing H_2-NO_2-TPDC and ABDC.

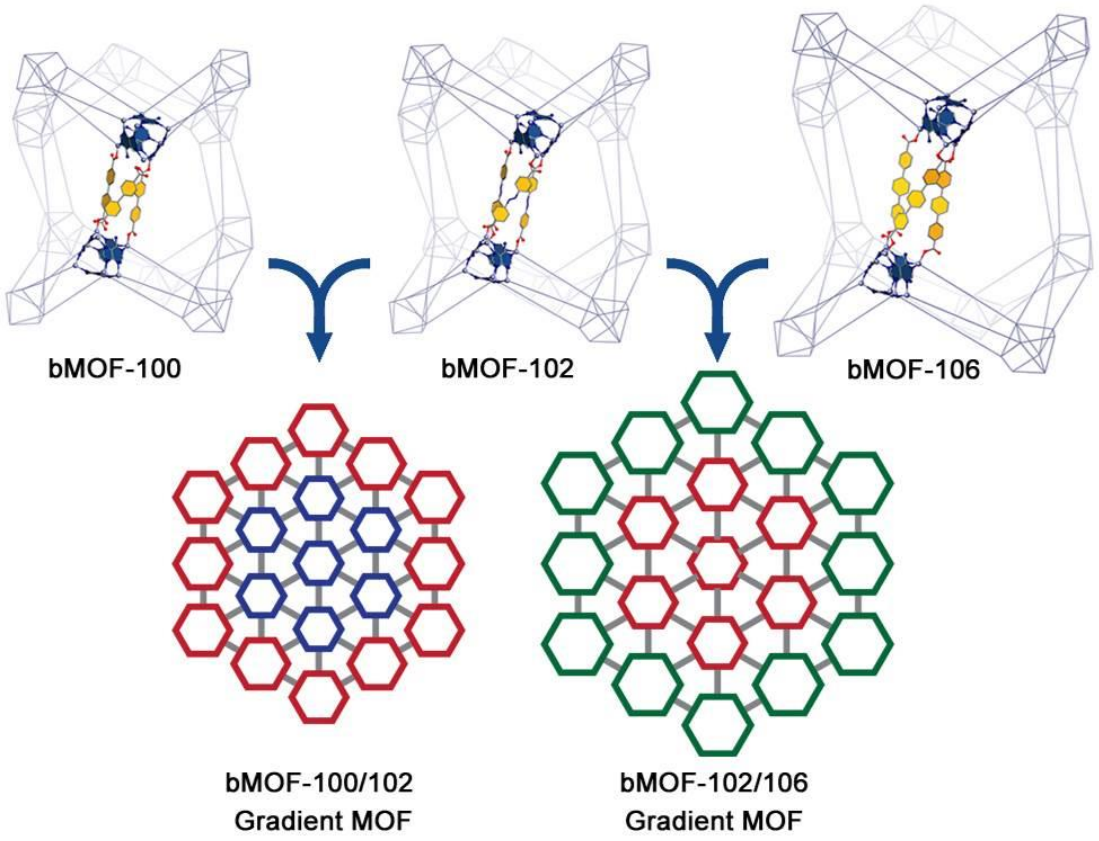

Figure 95. Simplified schematic representation of the constitution of gradient bMOF-100/102 and bMOF-102/106.

4.2.3 Heterogeneous organization of Au nanoclusters in MOFs

Porous crystals exhibiting domains with different pore dimensions present the opportunity of organizing molecules or nanomaterials in a hierarchical fashion based on size. It is anticipated that in MOF crystals with a 3-D porosity gradient, a guest species with carefully chosen size should only penetrate to a certain depth, resulting in a heterogeneous distribution. Gold-thiolate nanoclusters were chosen as guest species because of their precise dimensions and structures and interesting physical properties.[142-143] Further, their UV-Vis spectra are discernible from those of the MOF, which should enable determination of their relative positions within the 3-D crystal via

spectral microscopy. Thus, they are ideal nanoscale species that can serve as surrogate probe molecules for interrogating the dimensions of the gradient MOF pore space.[144-153]

Two pairs of gradient MOF/gold-thiolate cluster were used as host and guest respectively for proof-of-principle studies: the 102/106 gradient MOF and $Au_{133}(SR)_{52}$,[152-153] icosahedral cluster with a diameter of 3 nm; the 100/102 gradient MOF and $Au_{25}(SR)_{18}$,[154-155] another icosahedral cluster with a diameter of 2.4 nm. Based on their respective sizes, it is predicted that in bMOF-102/106, $Au_{133}(SR)_{52}$ should locate exclusively in the periphery or shell with bMOF-106 character (Figure 96A). Similarly, in bMOF-100/102, $Au_{25}(SR)_{18}$ should be found mostly in the periphery with more bMOF-102 character (Figure 96B).

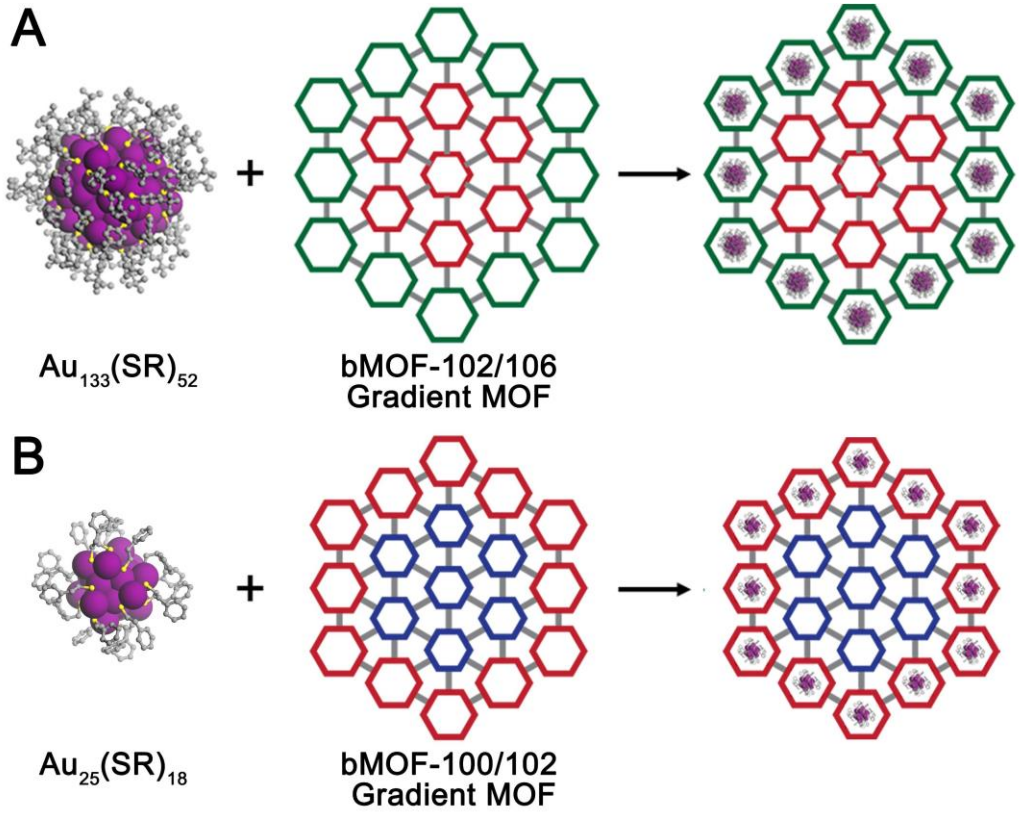

Figure 96. Schematic representation of ideal situations of (A) $Au_{133}(SR)_{52}$ residing exclusively in the periphery of gradient bMOF-102/106 and (B) $Au_{25}(SR)_{18}$ residing exclusively in the periphery of gradient bMOF-100/102.

All members of the bMOF-100 series are anionic, and dimethylammonium cations reside in the pores. Thus, cation exchange can be an effective means of introducing new guest species to the pore space. To enable cation exchange-driven diffusion, the nanoclusters were oxidized with H_2O_2 (Experimental Section 4.4.5.1).[156-159] Control experiments were performed using bMOF-102 and bMOF-106 single crystals, respectively. MOF samples were treated with identical DCM solutions of cationic $Au_{133}(SR)_{52}$ cluster for the same period of time. The absorbance spectra of the supernatants were monitored (Figure 97) to determine the extent of cluster uptake into the MOF samples. It was clear from these data that $Au_{133}(SR)_{52}^{+}$ diffused more readily into bMOF-106 than into bMOF-102, which has a pore diameter (~2.9 nm) slightly smaller than the cluster diameter. Microspectrophotometric results (Figure 98) showed that $Au_{133}(SR)_{52}^{+}$ penetrated to all regions of the bMOF-106 crystals, indicating that the crystals were sufficiently porous to allow for diffusion throughout the material and, importantly, revealing that the nanoclusters did not clog the pores and prevent further diffusion. $Au_{133}(SR)_{52}^{+}$-charged bMOF-106 was then dissolved to extract the nanoclusters. UV-Vis spectroscopy (Figure 99) and MALDI-TOF mass spectrometry (Figure 100) confirmed that $Au_{133}(SR)_{52}^{+}$ remained unchanged throughout the uptake/release process.

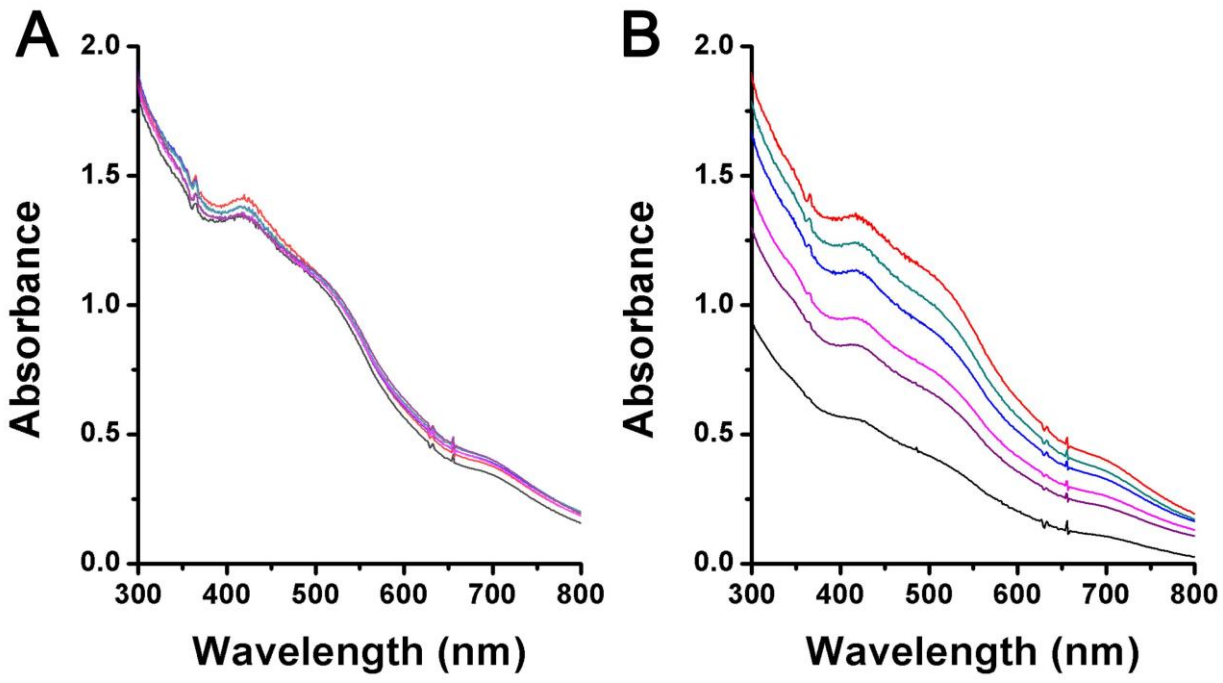

Figure 97. UV-Vis spectroscopy monitoring the $Au_{133}(SR)_{52}^{+}$ supernatant in the presence of (A) bMOF-102 or (B) bMOF-106 crystals.[*]

[*] Red: 0 hour (before addition of MOF); dark cyan: 30 min; blue: 90 min; magenta: 5 hours; violet: 8 hours; black: 24 hours.

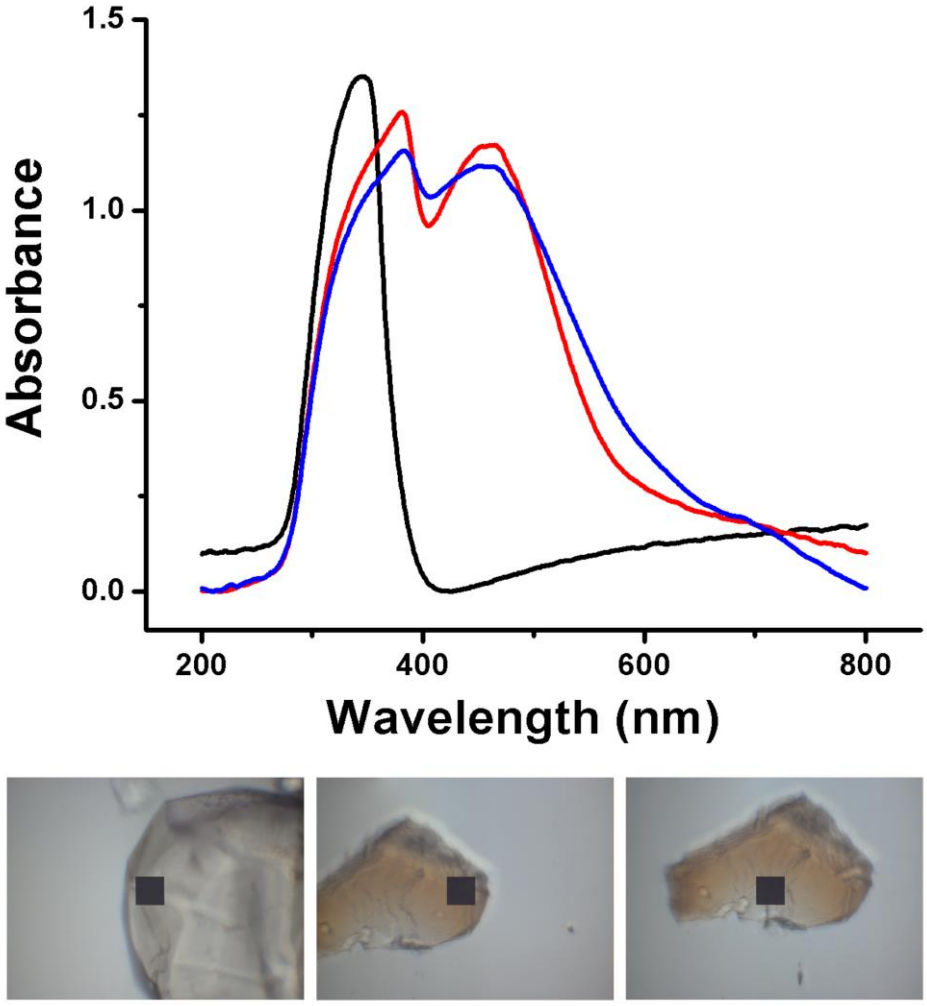

Figure 98. Absorbance spectra comparing unloaded bMOF-106 (black curve, bottom left image), periphery region of $Au_{133}(SR)_{52}^{+}$-charged bMOF-106 (red curve, bottom middle image), and core region of the same MOF crystal (blue curve, bottom right image).*

* Black boxes: sampling area for absorbance, 37 × 37 μm^2

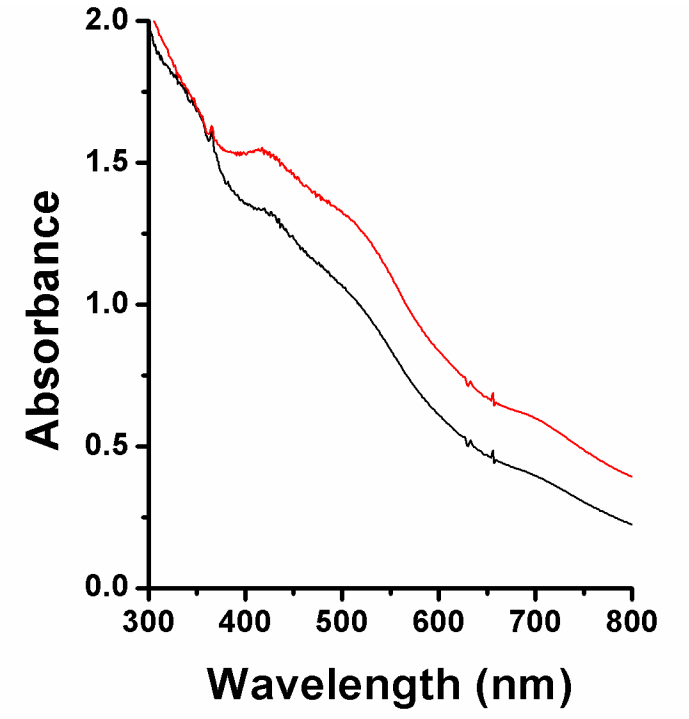

Figure 99. UV-Vis spectroscopy comparing the absorbance of $Au_{133}(SR)_{52}^{+}$ before addition into (red curve) and after extraction from (black curve) bMOF-106.

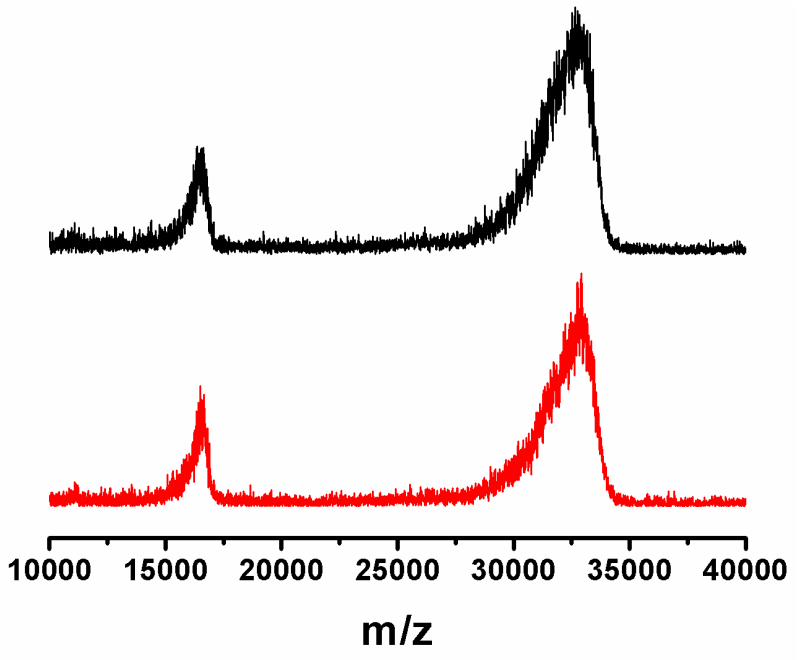

Figure 100. MALDI-TOF mass spectra comparing $Au_{133}(SR)_{52}^{+}$ before addition into (red curve) and after extraction from (black curve) bMOF-106.

Having determined that $Au_{133}(SR)_{52}^{+}$ can enter bMOF-106 but not bMOF-102 and remained intact throughout the course of the uptake experiments, the 102/106 gradient MOF was then treated with $Au_{133}(SR)_{52}^{+}$ in the same fashion as described above. The absorbance spectrum recorded for the gradient crystals after treatment with $Au_{133}(SR)_{52}^{+}$ showed new features characteristic of $Au_{133}(SR)_{52}^{+}$ (Figure 101). A microspectrophotometric study of fractured gradient crystals loaded with $Au_{133}(SR)_{52}^{+}$ revealed that the clusters resided in the crystal periphery (Figure 102).

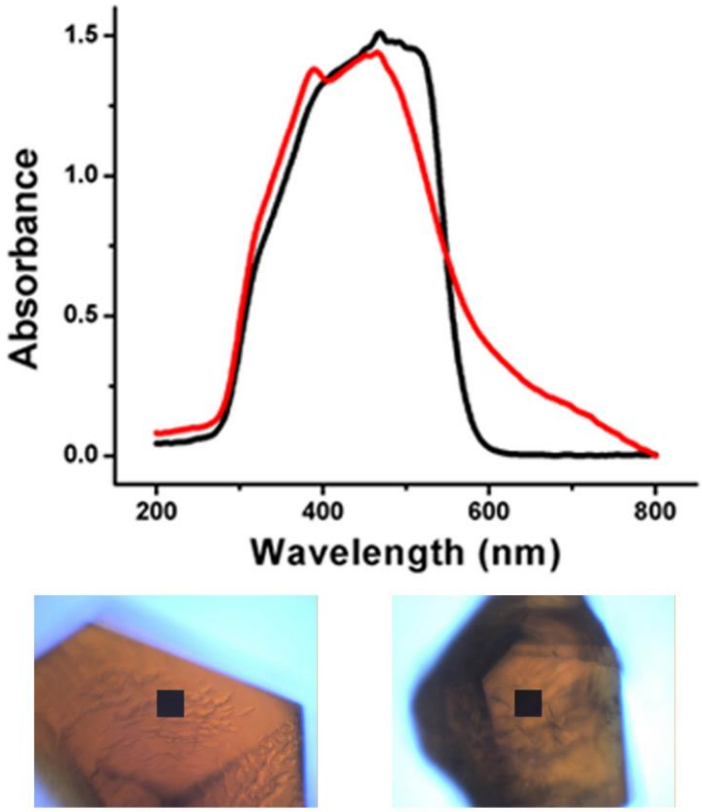

Figure 101. Absorbance spectra of bMOF-102/106 before (black) and after (red) encapsulation of $Au_{133}(SR)_{52}^{+}$ and corresponding optical images (before encapsulation: bottom left, after encapsulation: bottom right).*

* Black boxes: sampling area for absorbance, 37 × 37 μm^2

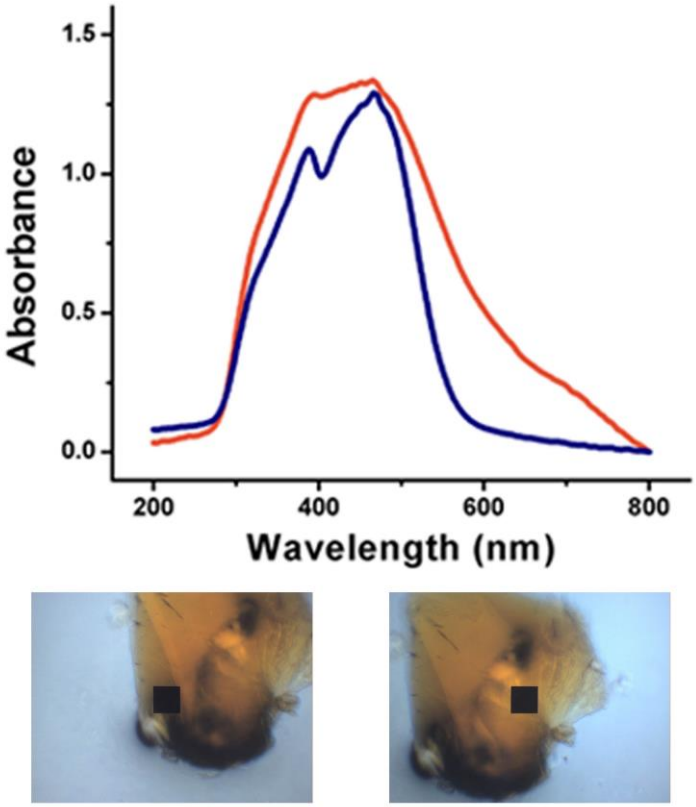

Figure 102. Absorbance spectra of different regions in a fractured bMOF-102/106 crystal showing the presence of $Au_{133}(SR)_{52}^{+}$ in the periphery (orange) but not core (blue) and corresponding optical images (periphery: bottom left, core: bottom right).*

The same series of experiments were performed on the bMOF-100/102 system. First, bMOF-100 and bMOF-102 single crystals were treated with identical DCM solutions of $Au_{25}(SR)_{18}^{+}$ for the same period of time, and the supernatants were monitored by UV-Vis spectroscopy. As shown in Figure 103, $Au_{25}(SR)_{18}^{+}$ could diffuse into bMOF-102 more readily than into bMOF-100, which has a pore diameter (~2.5 nm) too close to the cluster diameter.

* Black boxes: sampling area for absorbance, 37 × 37 μm^2

These results also indicated that $Au_{25}(SR)_{18}^{+}$ was fairly unstable during the process as it quickly lost its feature peaks, which suggested the majority of the $Au_{25}(SR)_{18}^{+}$ in the supernatant had changed. The experiments were stopped at 90 min. on account of the instability of $Au_{25}(SR)_{18}^{+}$. Microspectrophotometry revealed that $Au_{25}(SR)_{18}^{+}$ can penetrate to all regions of bMOF-102 crystals, indicating a uniform distribution (Figure 104). The results indicated that bMOF-102 was porous enough for the $Au_{25}(SR)_{18}^{+}$ cluster to move freely throughout the crystal, and that the nanoclusters did not clog the peripheral pores and prevent diffusion. Afterwards, the extracted Au clusters from $Au_{25}(SR)_{18}^{+}$–charged bMOF-102 were characterized with UV-Vis spectroscopy (Figure 105) and MALDI-TOF (Figure 106) to confirm their identity.

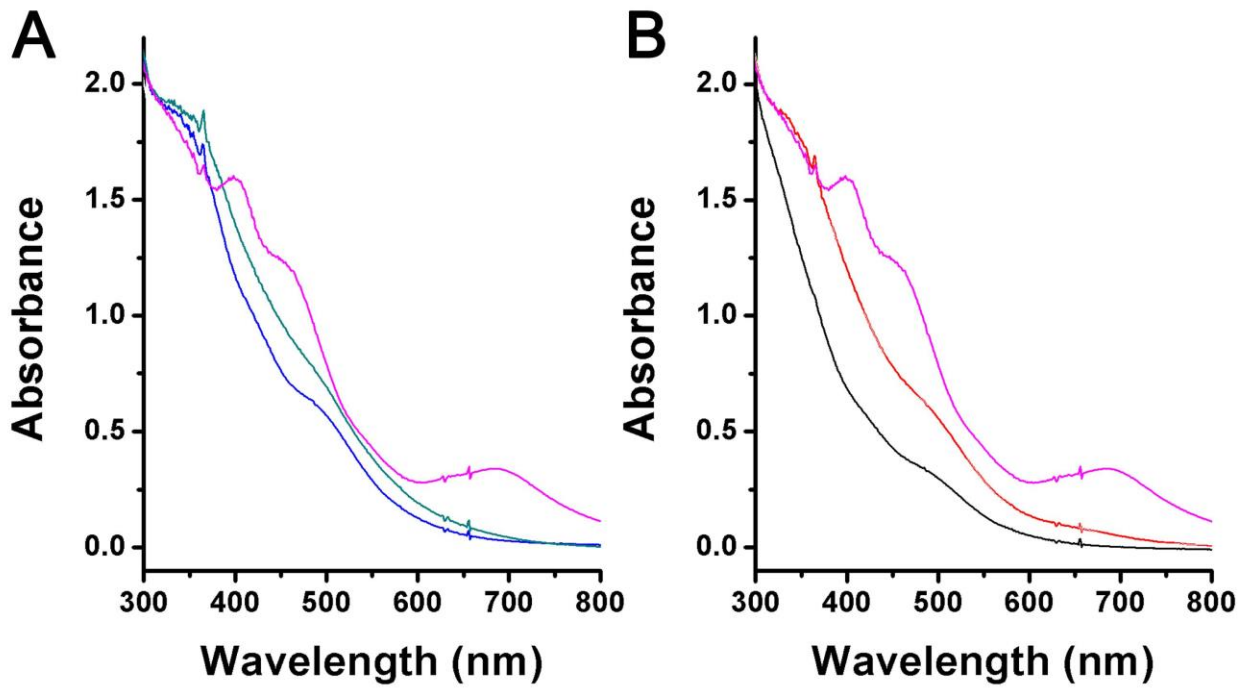

Figure 103. UV-Vis spectroscopy monitoring the $Au_{25}(SR)_{18}^{+}$ supernatant in the presence of (A) bMOF-100 or (B) bMOF-102 crystals.*

* Magenta: 0 hour (before addition of MOF); dark cyan: with bMOF-100, 30 min; blue: with bMOF-100, 90 min; red: with bMOF-102, 30 min; black: with bMOF-102, 90 min.

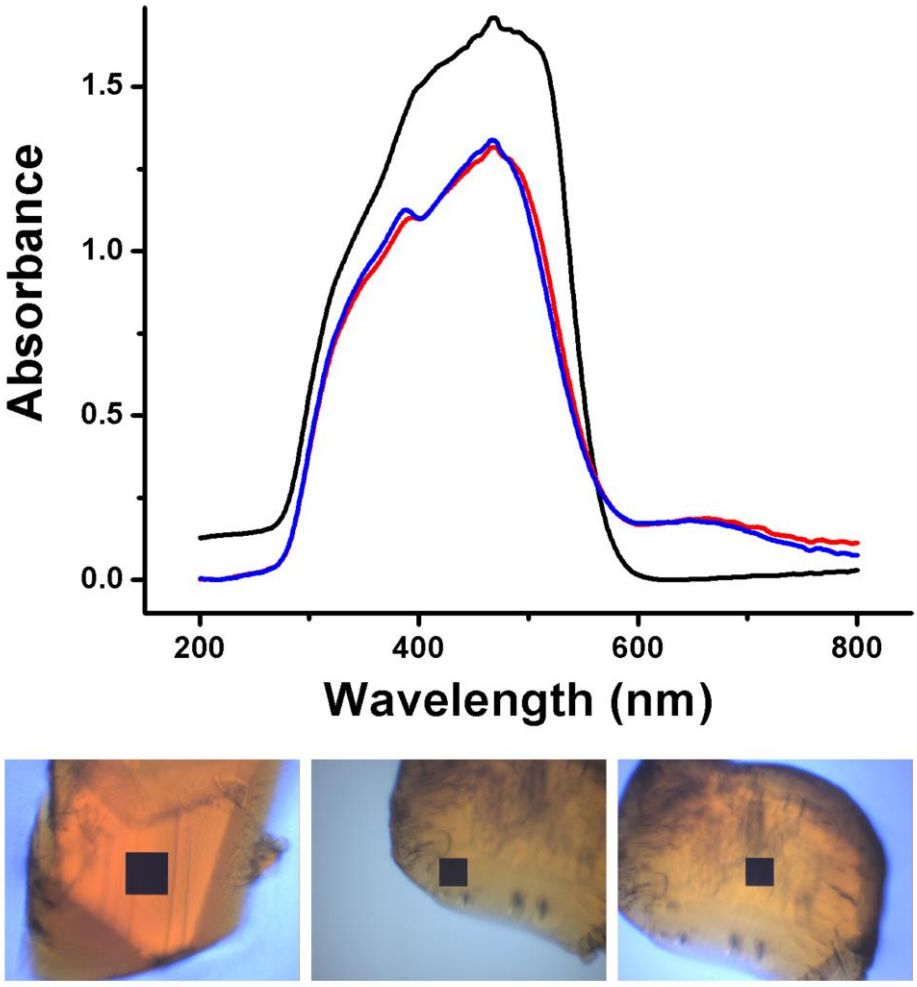

Figure 104. Absorbance spectra comparing unloaded bMOF-102 (black curve, bottom left image), periphery region of $Au_{25}(SR)_{18}^{+}$-charged bMOF-102 (red curve, bottom middle image), and core region of the same MOF crystal (blue curve, bottom right image).*

* Black boxes: sampling area for absorbance, 56 × 56 μm^2 for unloaded bMOF-102, 37 × 37 μm^2 for $Au_{25}(SR)_{18}^{+}$-charged bMOF-102.

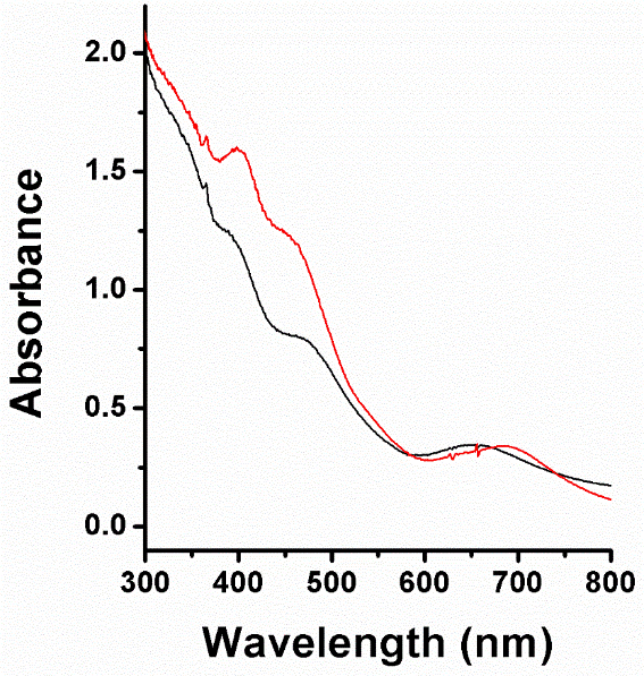

Figure 105. UV-Vis spectroscopy comparing absorbance of $Au_{25}(SR)_{18}^{+}$ before addition into (red curve) and after extraction from (black curve) bMOF-102.

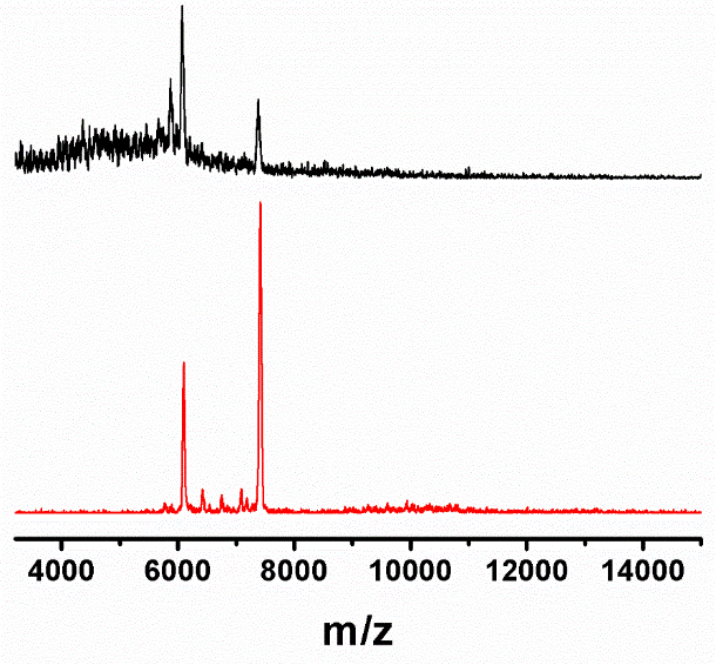

Figure 106. MALDI-TOF mass spectra comparing $Au_{25}(SR)_{18}^{+}$ before addition into (red curve) and after extraction from (black curve) bMOF-102.

Having shown that $Au_{25}(SR)_{18}^{+}$ can diffuse into bMOF-102 more readily than into bMOF-100, bMOF-100/102 gradient MOF was then treated with $Au_{25}(SR)_{18}^{+}$ in the same fashion. The absorbance spectrum collected for the gradient MOF crystals after treatment with $Au_{25}(SR)_{18}^{+}$ clearly showed spectral feature characteristic of the Au nanocluster, indicating successful encapsulation of $Au_{25}(SR)_{18}^{+}$ (Figure 107). A microspectrophotometric study of fractured bMOF-100/102 gradient MOF crystal loaded with $Au_{25}(SR)_{18}^{+}$ also revealed that the clusters resided selectively in the periphery (Figure 108).

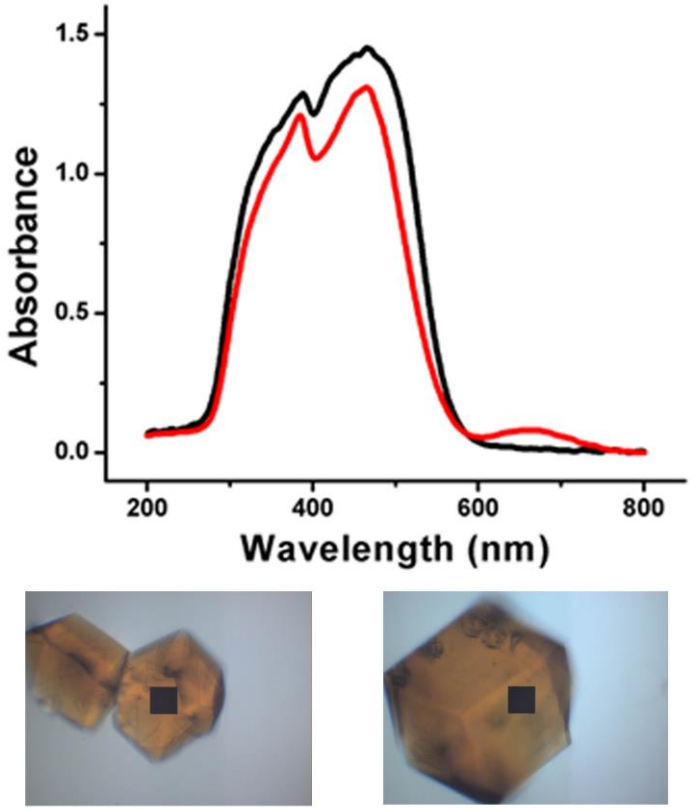

Figure 107. Absorbance spectra of bMOF-100/102 before (black) and after (red) encapsulation of $Au_{25}(SR)_{18}^{+}$ and corresponding optical images (before encapsulation: bottom left, after encapsulation: bottom right).*

* Black boxes: sampling area for absorbance, 37 × 37 μm^2

.

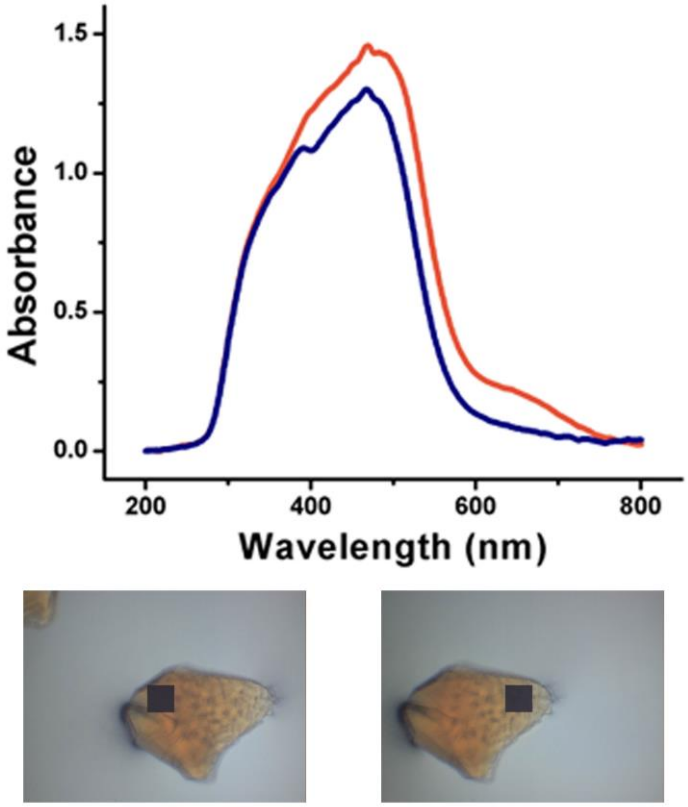

Figure 108. Absorbance spectra of different regions in a fractured bMOF-100/102 crystal showing the presence of $Au_{25}(SR)_{18}^{+}$ in the periphery (orange) but not core (blue) and corresponding optical images (periphery: bottom left, core: bottom right).*

* Black boxes: sampling area for absorbance, 37 × 37 μm^2

4.3 CONCLUSION

In summary, ligand exchange-facilitated pore expansion of 3-D bMOF-100 and its analogues was a gradual process that proceeded via ligand replacement from the crystal periphery to the crystal core. Increased acidity of the incoming carboxylic acid ligand accelerated the process. Halting the ligand exchange reaction enabled generation of new heterogeneously porous MOFs with internal pore gradients. The hierarchical distribution of porosity was used for heterogeneous organization of Au nanoclusters. It was demonstrated here for the first time that postsynthetic ligand exchange can be used to create structurally heterogeneous MOFs with internal directional porosity gradients. The realization of porosity gradients now permits size-selective spatial organization of molecular and nanoscale entities within MOF scaffolds and presents a new design strategy for potentially controlling the distribution and flow of matter throughout 3-D ordered molecular space.

4.4 EXPERIMENTAL SECTION

4.4.1 General procedure

All purchased chemicals were used without further purification except where otherwise stated. All DMF used for washing crystals was pre-dried over 4Å molecular sieves. Powder X-ray diffraction patterns were collected using a Bruker AXS D8 Discover powder diffractometer at 40 kV, 40 mA for Cu Kα, (λ = 1.5406 Å) with a scan speed of 0.10 sec/step from 2.2 to 20 º at a step size of 0.02 º. The data were analyzed using the EVA program from the Bruker Powder

Analysis Software package. The simulated powder patterns were calculated using Materials Studio based on single crystal data of corresponding MOFs. Single crystal X-ray diffraction experiments were performed on a Bruker X8 Prospector Ultra diffractometer equipped with an Apex II CCD detector and an IμS micro-focus CuKα X-ray source (λ = 1.54178 Å). MOF crystals were loaded into capillary tubes which were then flame sealed before mounting. Data were collected at room temperature and processed using Bruker APEX II software package. ^{1}H and ^{13}C NMR spectra were obtained using Bruker Avance III 300/400/500 MHz spectrometers. Chemical shifts are in parts per million using the residual solvent peaks (chloroform-*d*, DMSO-d_6, dichloromethane-d_2) as references. Microspectrophotometric experiments were performed on a CRAIC QDI 2010 microspectrophotometer. The sampling area was fixed at 37 × 37 μm^2 unless stated otherwise. The integration time was fixed at 8 ms for all acquired absorbance spectra. Light microscopic images were obtained using an Olympus BH-2 microscope. LC-MS analyses were performed on a Shimadzu LCMS-2020 instrument. The LC method used was 6 minute running time with a constant ratio of 1:1 acetonitrile:water at a constant flow rate of 0.2 mL/min. In this method the samples do not pass through a chromatographic column; therefore, there is virtually no separation of the components. The ionization interface was simultaneous ESI & APCI. UV-Vis spectroscopy was performed on an Agilent 8453 spectrophotometer. MALDI-TOF mass spectrometry was performed on an Applied Biosystems Voyager DE super-STR time-of-flight (TOF) mass spectrometer. Trans-2-[3-(4-tert-butylphenyl)-2-methyl-2-propenyldidene] malononitrile (DCTB) was used as the matrix. Transmission electron microscopy (TEM) samples were prepared by drop casting EtOH containing MOF crystals onto a 3 mm diameter copper grid. TEM images were collected with a FEI Morgagni 268 (80 kV) equipped with an AMT side mount CCD camera system.

4.4.2 Syntheses of ligands

The synthetic routes for the ligands of bMOF-106 (Compound **4**) and bMOF-107 (Compound **5**) are shown in Figure 109.

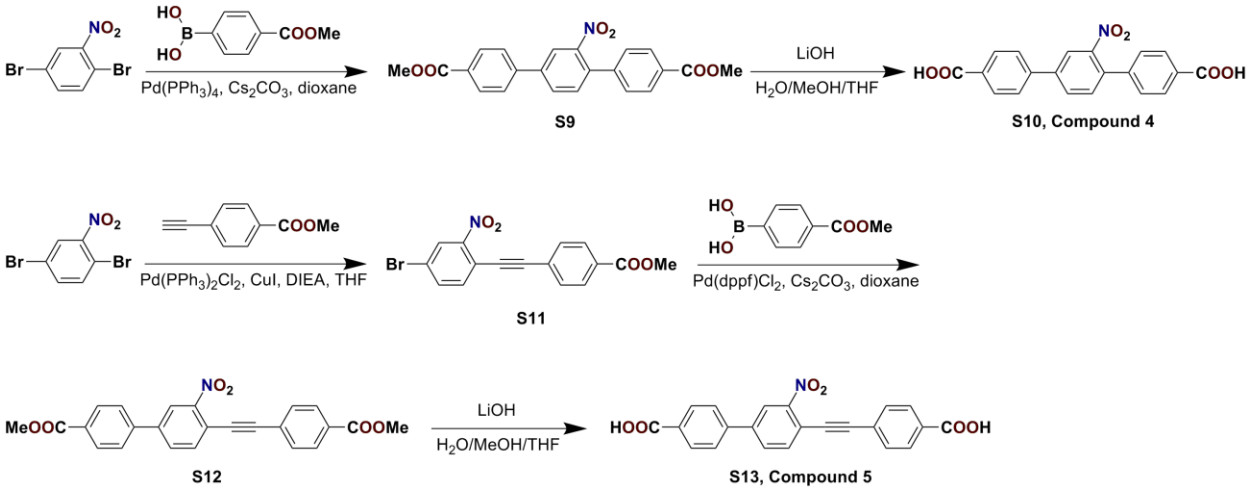

Figure 109. Synthetic routes for ligands of bMOF-106 and bMOF-107.

4.4.2.1 Synthesis of dimethyl 2'-nitro-1,1':4',1''-terphenyl-4,4''-dicarboxylate (S9)

1,4-Dibromo-2-nitrobenzene (500 mg, 1.78 mmol), 4-methoxycarbonylphenylboronic acid (1280 mg, 7.11 mmol), Cs_2CO_3 (2320 mg, 7.12 mmol), and $Pd(PPh_3)_4$ (102.8 mg, 0.0890 mmol) were mixed in degassed 1,4-dioxane (45 mL). The mixture was heated and stirred at 66 ^oC for 24 hours. The reaction progress was monitored by TLC. After complete conversion, the mixture was mixed with DI H_2O (400 mL) and extracted with DCM (50 mL, 2X). The combined organic phase was washed with DI H_2O (5X), dried over $MgSO_4$, filtered and concentrated. The crude product was purified via column chromatography (DCM:hexanes = 2:1 to 4:1) to yield **S9** (554 mg, 1.42 mmol, 79.8%). ^1H NMR (400 MHz, $CDCl_3$) δ 8.21-8.15 (m, 3H), 8.15-8.10 (m, 2H), 7.90 (dd, J = 8.0, 1.9 Hz, 1H), 7.76-7.70 (m, 2H), 7.55 (d, J = 8.0 Hz, 1H), 7.46-7.41 (m, 2H), 3.97 (s, 3H), 3.95 (s, 3H). ^{13}C NMR (101 MHz, $CDCl_3$) δ 166.71, 166.69, 149.50, 142.42,

141.72, 141.16, 135.02, 132.54, 131.09, 130.62, 130.42, 130.20, 130.13, 128.13, 127.20, 123.10, 52.46, 52.42.

4.4.2.2 Synthesis of 2'-nitro-1,1':4',1''-terphenyl-4,4''-dicarboxylic acid (S10, Compound 4)

S9 (545 mg, 1.39 mmol) was dissolved in THF (30 mL) and MeOH (10 mL). The resulting solution was mixed with a solution of $LiOH \cdot H_2O$ (175 mg, 4.16 mmol) in DI H_2O (10 mL). The reaction mixture was heated and stirred at 50 ^oC overnight. LC-MS was used to determine the completion of the hydrolysis. After all the volatiles were removed *in vacuo*, it was diluted with DI H_2O and acidified with 20% HCl solution until pH = 1. The precipitates were collected via filtration, washed with DI H_2O, and dried *in vacuo*. Compound **4** was collected as a faint yellow solid (492 mg, 1.36 mmol, 97.4 %). ^1H NMR (400 MHz, DMSO-d_6) δ 13.11 (s, 2H), 8.40 (d, J = 1.9 Hz, 1H), 8.18 (dd, J = 8.1, 1.9 Hz, 1H), 8.11-8.06 (m, 2H), 8.06-8.01 (m, 2H), 8.00-7.95 (m, 2H), 7.72 (d, J = 8.1 Hz, 1H), 7.56-7.51 (m, 2H). ^{13}C NMR (101 MHz, DMSO-d_6) δ 166.93, 166.89, 149.31, 141.25, 140.86, 139.96, 133.70, 132.46, 131.11, 130.77, 130.62, 130.11, 129.70, 128.13, 127.21, 122.49.

4.4.2.3 Synthesis of methyl 4-(4'-bromo-2'-nitrophenylethynyl)benzoate (S11)

A mixture of 1,4-dibromo-2-nitrobenzene (5080 mg, 18.2 mmol), CuI (142.5 mg, 0.751 mmol), $Pd(PPh_3)_2Cl_2$ (525 mg, 0.748 mmol) in THF (15 mL) and DIEA (15 mL) was degassed and charged with Ar (3X). After stirring at room temperature for 5 min, methyl 4-ethynylbenzoate (1200 mg, 7.50 mmol) was added. The reaction was monitored with TLC. After 24 h, DI H_2O (50 mL) was added to the reaction mixture and stirred for 20 min. Volatiles were removed *in vacuo* before more DI H_2O (250 mL) was added; then the mixture was extracted with DCM (50 mL, 3X). The combined organic phase was washed with DI H_2O (100 mL, 2X),

saturated $NaHCO_3$ solution (100 mL), saturated NaCl solution (100 mL), dried over $MgSO_4$, filtered and concentrated. The crude product was purified via column chromatography (DCM:hexanes = 1:1) to yield **S11** as an off-white solid (1.4738 g, 4.09 mmol, 54.6%). Single crystal X-ray diffraction was used to determine the structure of **S11** in order to confirm that the nitro group is at the 2'-position, not the 3'-position. Single crystals were prepared by vapor diffusion of pentane into a DCM solution of **S11**, X-ray diffraction experimental details and crystallographic tables are included in Appendix E. ^{1}H NMR (400 MHz, CD_2Cl_2) δ 8.27 (d, J = 1.6 Hz, 1H), 8.04 (d, J = 8.3 Hz, 2H), 7.79 (dd, J = 8.3, 1.7 Hz, 1H), 7.66 (d, J = 8.3 Hz, 2H), 7.63 (d, J = 8.4 Hz, 1H), 3.91 (s, 3H). ^{13}C NMR (101 MHz, CD_2Cl_2) δ 166.70, 150.42, 136.81, 136.30, 132.44, 131.35, 130.10, 128.51, 127.13, 123.10, 117.60, 97.39, 87.03, 52.77.

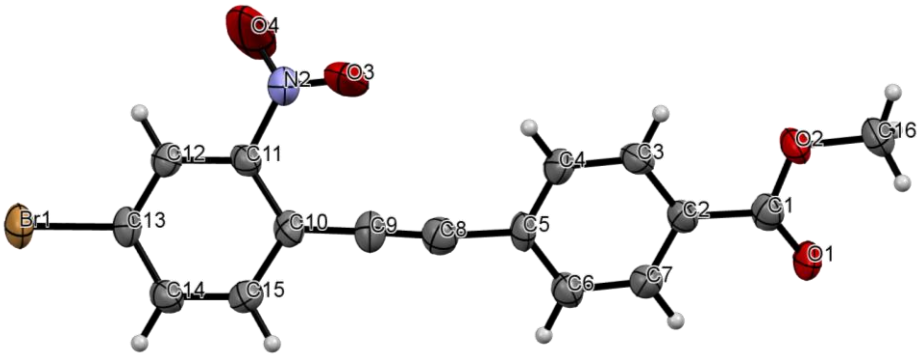

Figure 110. ORTEP diagram of **S11** (50% probability factor for the thermal ellipsoids), generated via Mercury 3.6, H labels are omitted for clarity.

4.4.2.4 Synthesis of methyl 4-(3'-nitro-4'-(4''-methylcarboxylphenylethynyl)phenyl) benzoate (S12)

S11 (720 mg, 2.00 mmol), 4-methoxycarbonylphenylboronic acid (1080 mg, 6.00 mmol), Cs_2CO_3 (1956 mg, 6.00 mmol), and $Pd(dppf)Cl_2$ (146 mg, 0.200 mmol) were mixed in 1,4-dioxane (50 mL), heated and stirred at 75 °C under Ar for 22 h. Then the mixture was diluted

with DI H_2O (150 mL) and extracted with DCM (50 mL, 3X). The combined organic phase was washed with DI H_2O (100 mL, 5X), dried over $MgSO_4$, filtered and concentrated. The crude product was re-dissolved in DCM and purified via column chromatography (DCM:hexanes = 10:1) to yield **S12** as a yellow solid (369 mg, 0.888 mmol, 44.4%). Single crystal X-ray diffraction was used to determine the structure of **S12** to have an accurate model of ligand compound **5** for bMOF-107 structure modelling. Single crystals were prepared by vapor diffusion of pentane into a DCM solution of **S12**, X-ray diffraction experimental details and crystallographic tables are included in Appendix F. ^{1}H NMR (500 MHz, $CDCl_3$) δ 8.38 (d, J = 1.5 Hz, 1H), 8.18 (d, J = 8.2 Hz, 2H), 8.07 (d, J = 8.1 Hz, 2H), 7.89 (dd, J = 7.9, 1.5 Hz, 1H), 7.83 (d, J = 8.1 Hz, 1H), 7.72 (d, J = 8.2 Hz, 2H), 7.68 (d, J = 8.1 Hz, 2H), 3.97 (s, 3H), 3.95 (s, 3H). ^{13}C NMR (101 MHz, CD_2Cl_2) δ 166.91, 166.74, 150.69, 142.56, 141.71, 135.88, 132.46, 131.95, 131.23, 131.15, 130.89, 130.10, 127.66, 127.38, 123.88, 117.89, 97.17, 87.77, 52.76.

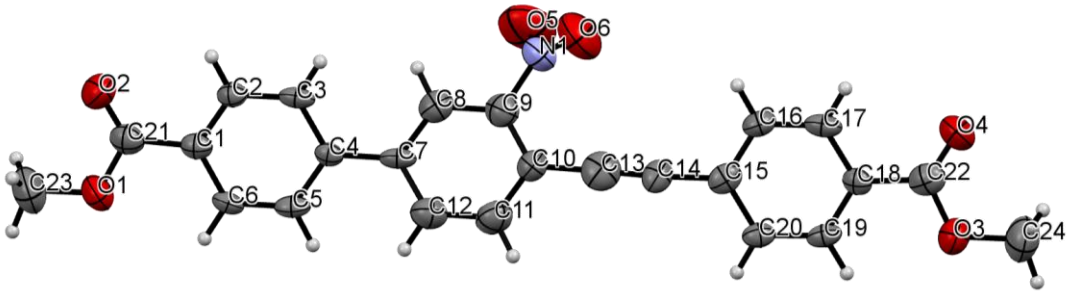

Figure 111. ORTEP diagram of **S12** (50% probability factor for the thermal ellipsoids), generated via Mercury 3.6, H labels are omitted for clarity.

4.4.2.5 Synthesis of 4-(3'-nitro-4'-(4''-carboxylphenylethynyl)phenyl)benzoic acid (S13, Compound 5)

S12 (369 mg, 0.888 mmol) was dissolved in THF (10 mL) and MeOH (10 mL). The resulting solution was mixed with a solution of $LiOH{\cdot}H_2O$ (186 mg, 4.44 mmol) in DI H_2O (12

mL). The reaction mixture was stirred at room temperature for 24 h. LC-MS was used to determine the completion of the hydrolysis. After all the volatiles were removed *in vacuo*, it was diluted with DI H_2O and stirred for 30 min with 6M HCl solution (pH < 1). The precipitates were collected via filtration, washed with DI H_2O, and dried in vacuo. Compound **5** was collected as a bright yellow solid (327 mg, 0.845 mmol, 95.2 %). ^{1}H NMR (300 MHz, DMSO-d_6) δ 13.41 (s, br, 2H), 8.51 (d, J = 1.9 Hz, 1H), 8.20 (dd, J = 8.2, 1.7 Hz, 1H), 8.06 (d, J = 8.4 Hz, 2H), 8.01-7.92 (m, 5H), 7.66 (d, J = 8.2 Hz, 2H). ^{13}C NMR (126 MHz, DMSO-d_6) δ 167.51, 167.27, 150.55, 135.62, 132.91, 132.00, 131.98, 131.46, 130.54, 130.53, 130.42, 130.11, 130.05, 128.36, 127.48, 127.45, 123.23, 116.31.

4.4.3 Modulated solvothermal synthesis of large bMOF-100 crystals

DMF solutions of $Zn(NO_3)_2 \cdot 6H_2O$ (0.05 M, 7.5 mL), adenine (0.05 M, 2.5 mL), H_2-BPDC (0.1 M, 2 mL), H_3-BTB (1,3,5-Tris(4-carboxyphenyl)benzene, 0.1 M, 0.5 mL), HNO_3 (1 M, 1.25 mL) and H_2O (1 mL) were mixed well in a 20 mL vial and heated in a 130 ^oC oven for 12 hours. Then the liquid was decanted and replaced with fresh DMF. The as-synthesized materials were washed as described in the following sections. The mass of MOFs used for subsequent experiments was determined after the DMF-washed crystals were dried under Ar flow to the point that they became free-flowing solids.

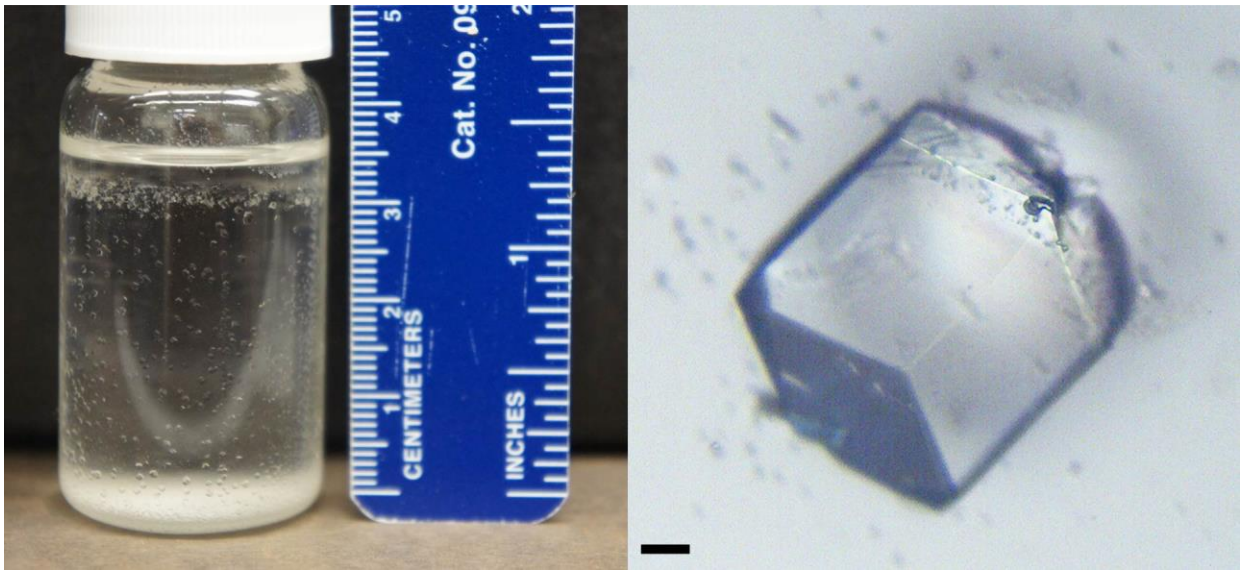

Figure 112. Optical images of synthesized bMOF-100 crystals in a 20 mL vial (left) and under microscope (right, scale bar: 100 μm).

4.4.4 Ligand exchange experiments

4.4.4.1 Ligand exchange of bMOF-100 to bMOF-102

As-synthesized bMOF-100 (6 mg) was washed with DMF (3X) in a 1.5 mL centrifuge tube. After removing most of the solvent while keeping the crystals wet, a DMF solution of azobenzene-4,4'-dicarboxylic acid (H_2-ABDC, 0.025 M, 0.5 mL) was added. The centrifuge tube was placed in a 75 °C oven for various time periods. For ^{1}H NMR analysis, after ligand exchange, the crystals were washed with DMF (3X), soaked in DMF at 75 °C for 30 minutes, washed with DMF (3X). Then the crystals were washed with DCM (3X), soaked in DCM at room temperature for at least 1 hour, washed with DCM (3X), and then dried under Ar flow. Then, the crystals were dissolved in DMSO-d_6 (0.7 mL) and DCl in D_2O (37%, 0.006 mL) for ^{1}H NMR analysis to determine the composition and exchange percentage (Figure 87). Based on the results, the conversion from bMOF-100 to bMOF-102 was almost complete after 3 hours of

reaction, and the composition remained the same after 12 hours of reaction. For convenience, 12-hour reaction time was chosen to be the standard synthetic procedure to prepare bMOF-102. PXRD experiment was also performed on the 12-hour sample. A 10-minute reaction time procedure was used to prepare intermediate samples for single crystal X-ray diffraction experiments.

4.4.4.2 Ligand exchange of bMOF-102 to bMOF-106

bMOF-102 was prepared according to the procedure described in 4.4.4.1, after removing most of the solvent while keeping the crystals wet, a DMF solution of compound **4** (0.025 M, 0.5 mL) was added. The centrifuge tube was heated in a 75 °C oven for various time periods. For ^{1}H NMR analysis, the crystals were treated the same way as described in 4.4.4.1 and dissolved in DMSO-d_6 (0.7 mL) and DCl in D_2O (37%, 0.006 mL) to determine the ligand composition and exchange percentage (Figure 94). Based on the results, the conversion from bMOF-102 to bMOF-106 was complete after 12 hours of reaction, so it was chosen to be the standard synthetic procedure to prepare bMOF-106. PXRD experiment was performed on this sample. A 20-minute reaction time procedure was used to prepare intermediate samples for single crystal X-ray diffraction experiments.

4.4.4.3 Ligand exchange of bMOF-106 to bMOF-107

bMOF-106 was prepared according to the procedure described in 4.4.4.2, after removing most of the solvent while keeping the crystals wet, a DMF suspension/solution of compound **5** (0.025 M, 0.5 mL) was added. The centrifuge tube was heated in a 75 °C oven for 24 hours. The crystals were treated the same way as described in 4.4.4.1 and 4.4.4.2 for PXRD analysis, then

dissolved in DMSO-d_6 (0.7 mL) and DCl in D_2O (37%, 0.006 mL) to determine the ligand composition and exchange percentage (Figure 113).

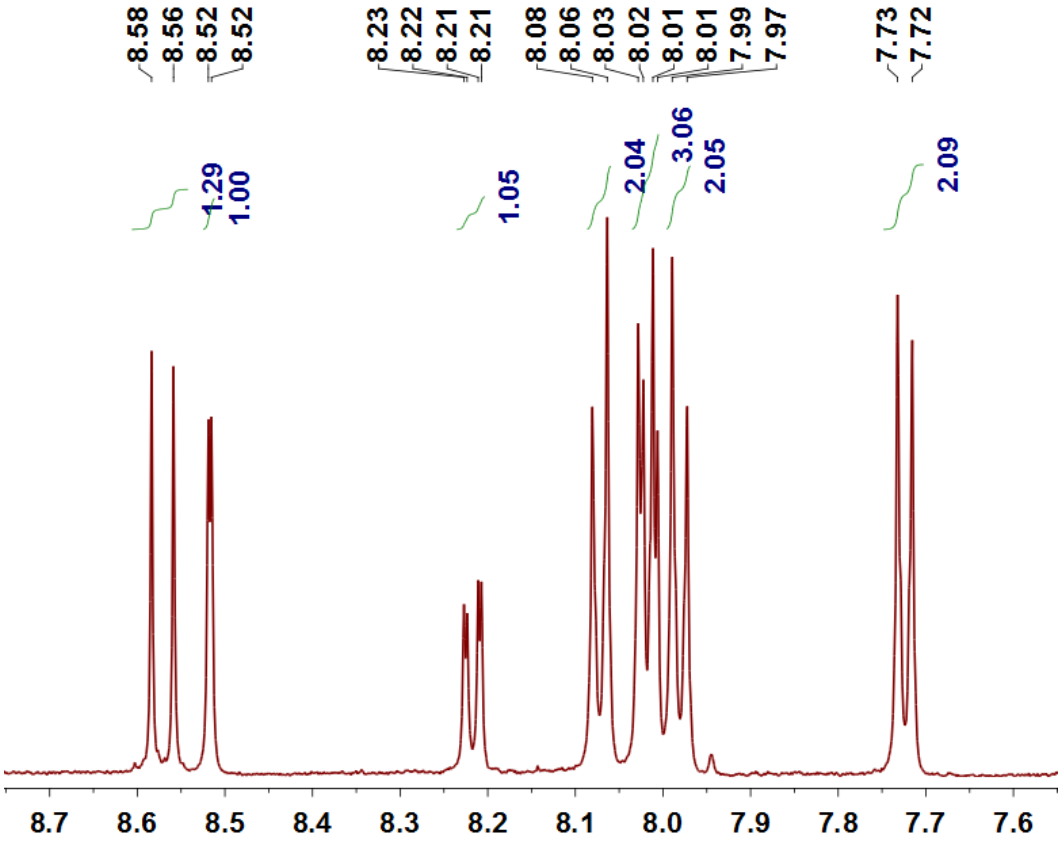

Figure 113. ^{1}H-NMR spectrum of dissolved crystals after bMOF-106 ligand exchange with compound **5**.

4.4.4.4 bMOF-100→106 and bMOF-102→107 exchange reactions

bMOF-100 was prepared according to the procedure described in 4.4.3, after removing most of the solvent while keeping the crystals wet, a DMF solution of compound **4** (0.025 M, 0.5 mL) was added. The centrifuge tube was heated in a 75 °C oven for 12 hours. The crystals were washed for PXRD analysis (Figure 90), and they were then dissolved in DMSO-d_6 (0.7 mL) and DCl in D_2O (37%, 0.006 mL) to determine the composition via ^{1}H NMR (Figure 91). bMOF-102

was prepared according to the procedure described in 4.4.4.1, after removing most of the solvent while keeping the crystals wet, a DMF suspension/solution of compound **5** (0.025 M, 0.5 mL) was added. The centrifuge tube was heated in a 75 °C oven for 12 hours. The crystals were washed for PXRD analysis (Figure 90), and they were then dissolved in DMSO-d_6 (0.7 mL) and DCl in D_2O (37%, 0.006 mL) to determine the composition via ^{1}H NMR (Figure 91).

4.4.4.5 Gradient MOFs and single crystal X-ray diffraction experiments

As mentioned previously in 4.4.4.1, bMOF-100 exchange reaction with H_2-ABDC was halted after 10 min and bMOF-102 exchange with compound **4** was halted after 20 min, yielding two intermediate MOFs whose composition was revealed previously (Figures 87 and 94, respectively). Sample crystals from these reactions were thoroughly washed with DMF prior to selection for single crystal X-ray diffraction experiments to determine unit cell parameters. Suitable crystals were loaded into capillary tubes that were then flame sealed. These crystals were denoted as "intermediate intact crystal" in Table 1 and Table 2. Under the light microscope, suitable crystals were cut with a razor blade, to carefully separate the crystal periphery (shell) from the core. The shell and core crystal samples were also loaded into capillary tubes that were then flame sealed prior to mounting for determination of unit cell parameters. These crystals were denoted as "partially exchanged shell" and "unexchanged core" respectively in Table 1 and Table 2. Single crystal X-ray diffraction data were also collected to determine the unit cell parameters of a solvothermally prepared bMOF-100 crystal (4.4.3), a fully exchanged bMOF-102 crystal (4.4.4.1) and a fully exchanged bMOF-106 crystal (4.4.4.2); these results were also included in Table 1 and Table 2. Fully exchanged bMOF-107 (4.4.4.3) was also loaded into a capillary that was then flame sealed prior to mounting for single crystal X-ray diffraction analysis. All crystals diffracted weakly, but a reliable space group (*Ia-3d*) and the *a* values of the

unit cells were accurately determined, as summarized in Table 1 and Table 2, except for bMOF-107 (a = 85.929(3) Å). Model crystal structures for bMOF-102, bMOF-106, and bMOF-107 were constructed in Materials Studio in the same manner as previously reported[54], based on their corresponding unit cell parameters. Atomic coordinates of Zn^{2+} and adeninate atoms were converted from those in bMOF-100. Then linear ligands were fitted manually into the crystal structures: for bMOF-102 and bMOF-106, ligand fragments were taken from the Cambridge Crystallographic Data Centre (CCDC); for bMOF-107, the fragment was taken from the structure of compound **S12** which was determined experimentally in this study (4.4.2.4 and Appendix F). Modelled structures are shown in Figure 114. These model structures were used to generate simulated PXRD patterns.

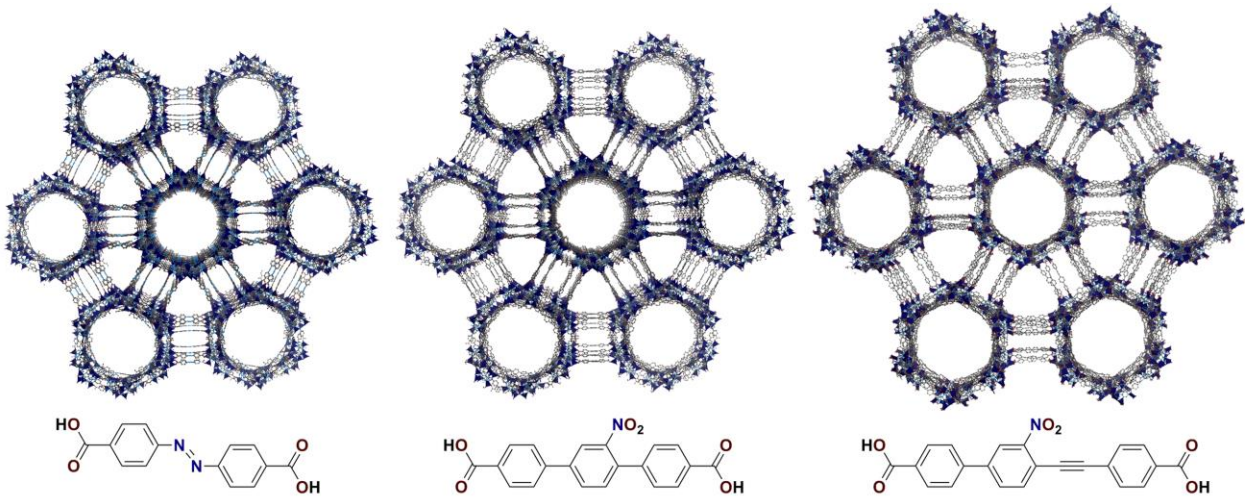

Figure 114. Modelled structures and corresponding linear ligands for bMOF-102 (left), bMOF-106 (middle), and bMOF-107 (right).

4.4.5 Au nanocluster syntheses and MOF encapsulation

4.4.5.1 Oxidation of $Au_{25}(SR)_{18}$ and $Au_{133}(SR)_{52}$

$Au_{25}(SR)_{18}$ and $Au_{133}(SR)_{52}$ were synthesized according to the literature protocols[152,160] and oxidized according to established procedure[156]. A Au nanocluster solution in DCM (1 mL, ~0.03 mg/mL) was mixed with H_2O_2/H_2O (10 μL, 50 wt. %) and stirred. Oxidation progress was monitored with UV-Vis spectroscopy. The $Au_{25}(SR)_{18}$ oxidation process is shown in Figure 115, spectral changes were consistent with literature and after oxidation, $Au_{25}(SR)_{18}^{+}$ solution turned green, which was also consistent with reported observation.[159] As shown in Figure 116, after oxidation of $Au_{133}(SR)_{52}$, the absorbance bands at 421, 503, and 712 nm did not show significant changes, and no visible change in color was observed, indicating retention of structural integrity.

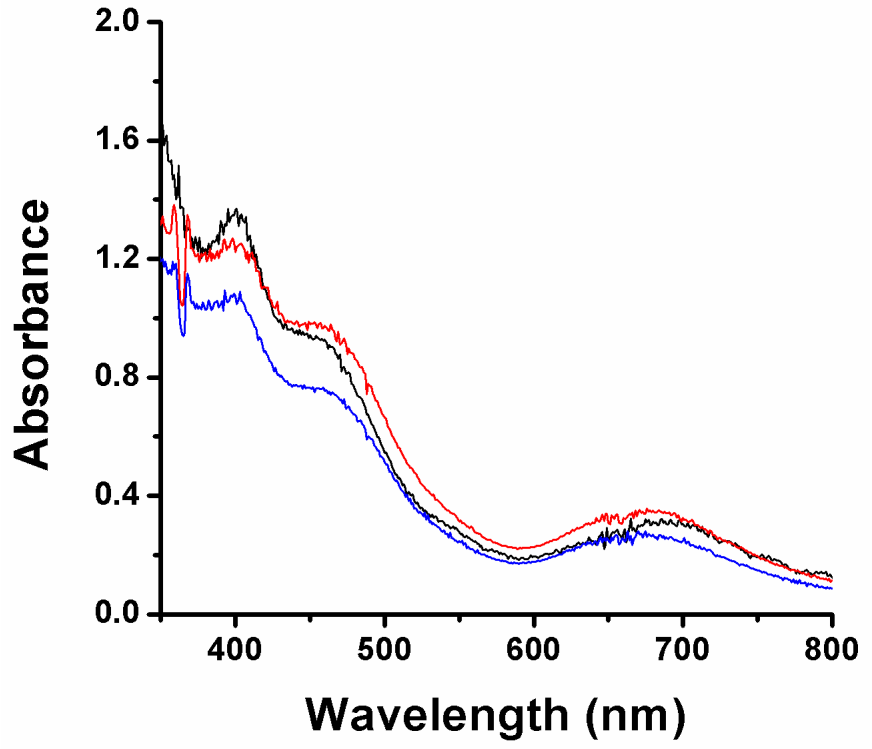

Figure 115. UV-Vis spectroscopy monitoring the oxidation progress of $Au_{25}(SR)_{18}$. Black: 0 hour (before addition of H_2O_2); red: 1 hour; blue: 1.5 hours.

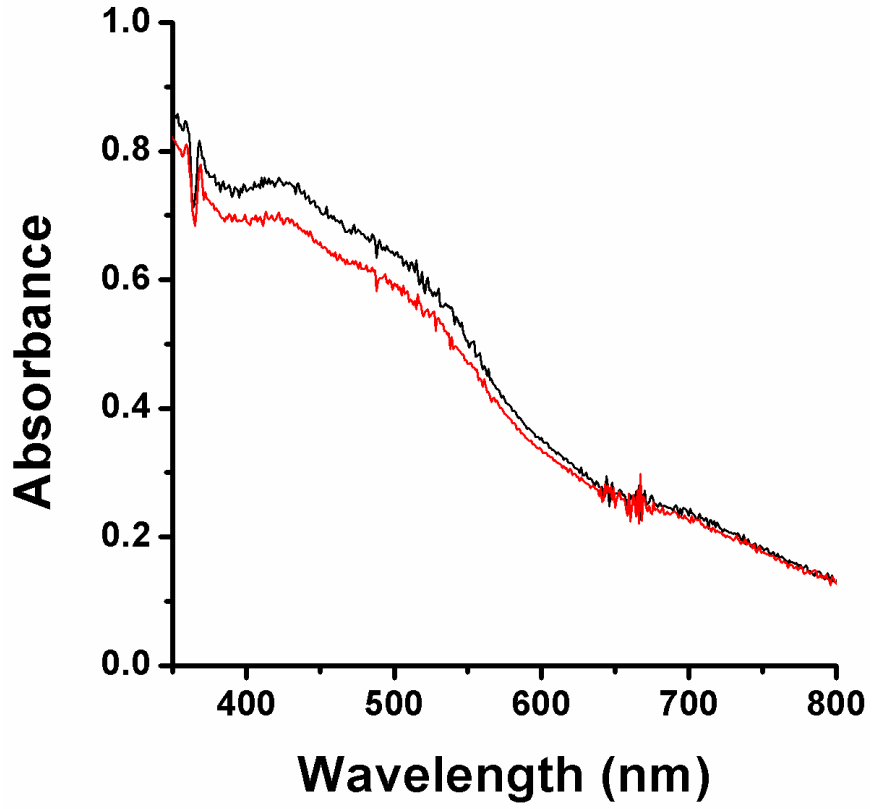

Figure 116. UV-Vis spectroscopy monitoring the oxidation progress of $Au_{133}(SR)_{52}$. Black: 0 hour (before addition of H_2O_2); red: 2 hours.

4.4.5.2 $Au_{133}(SR)_{52}^{+}$ encapsulation in bMOF-102 and bMOF-106 and bMOF-102/106 gradient MOF

After synthesis, bMOF-102 and bMOF-106 were washed with DMF and DCM as previously described. Identical $Au_{133}(SR)_{52}^{+}$/DCM solutions (2 mL, 0.05 mg/mL) were added to bMOF-102 and bMOF-106 crystals, respectively. The supernatant was monitored with UV-Vis spectroscopy (Figure 97) to determine the extent of $Au_{133}(SR)_{52}^{+}$ uptake into the MOF crystals. From the UV-Vis data, it was clear that bMOF-106 more effectively removed $Au_{133}(SR)_{52}^{+}$ clusters from solution compared to bMOF-102, which did not significantly decrease the

concentration of the cluster in the supernatant. To determine the spatial distribution of $Au_{133}(SR)_{52}^{+}$ clusters in different regions of a bMOF-106 crystal, absorbance spectra of the crystal periphery and core were compared, along with unloaded bMOF-106 (Figure 98). After 24 hours, bMOF-106 crystals were separated from the gold cluster solution and washed with DCM (5X). The crystals were then digested with a mixture of DCM (1 mL) and acetic acid (0.1 mL). The product was centrifuged at 10k rpm for 5 minutes and the supernatant was analyzed by UV-Vis spectroscopy (Figure 99) and MALDI-TOF (Figure 100). These data confirmed that the $Au_{133}(SR)_{52}^{+}$ clusters remained intact throughout the uptake experiment. The bMOF-102/106 gradient MOF was prepared as described in 4.4.4.2. The crystals were washed with DMF and DCM as described previously, and then mixed with $Au_{133}(SR)_{52}^{+}$/DCM solution (1 mL, 0.05 mg/mL) for 24 hours. Thereafter, the MOF crystals were separated and washed with DCM (5X) and DMF (5X) for microspectrophotometric studies.

4.4.5.3 $Au_{25}(SR)_{18}^{+}$ encapsulation in bMOF-100 and bMOF-102 and bMOF-100/102 gradient MOF

After synthesis, bMOF-100 and bMOF-102 were washed with DMF and DCM as previously described. Identical $Au_{25}(SR)_{18}^{+}$/DCM solutions (2 mL, 0.05 mg/mL) were added to bMOF-100 and bMOF-102 crystals, respectively. The supernatant was monitored with UV-Vis spectroscopy (Figure 103) to determine the extent of $Au_{25}(SR)_{18}^{+}$ uptake into the MOF crystals. UV-Vis results clearly indicated that bMOF-102 can remove $Au_{25}(SR)_{18}^{+}$ clusters from solution more effectively compared to bMOF-100. To determine the spatial distribution of $Au_{25}(SR)_{18}^{+}$ clusters in different regions of a bMOF-102 crystal, absorbance spectra of the crystal periphery and crystal core were compared, along with unloaded bMOF-102 (Figure 104). After 1.5 hours, bMOF-102 crystals were separated from the gold cluster solution and washed with DCM (5X).

The crystals were then digested with a mixture of DCM (1 mL) and acetic acid (0.1 mL). The product was centrifuged at 10k rpm for 5 minutes and the supernatant was analyzed by UV-Vis spectroscopy (Figure 105) and MALDI-TOF (106). These data confirmed that most of the $Au_{25}(SR)_{18}^{+}$ clusters remained intact after the uptake experiment. The bMOF-100/102 gradient MOF was prepared as described in 4.4.4.1. The crystals were washed with DMF and DCM as described previously, and then mixed with $Au_{25}(SR)_{18}^{+}$/DCM solution (1 mL, 0.05 mg/mL) for 1.5 hours. Thereafter, the MOF crystals were separated and washed with DCM (5X) and DMF (5X) for microspectrophotometric studies.

4.4.5.4 TEM imaging of $Au_{133}(SR)_{52}^{+}$ in bMOF-102/106 gradient MOF

As described in 4.4.5.2, bMOF-102/106 gradient MOF was treated with a $Au_{133}(SR)_{52}^{+}$/DCM solution (1 mL, 0.05 mg/mL) for 24 hours. Thereafter, the MOF crystals were separated from the gold cluster solution and washed with DCM (5X), and then some crystals were deposited onto TEM grid for characterization. As shown in Figure 117 and Figure 118, many small particles as well as some significantly larger particles were observed. It is inevitable that some clusters aggregate or fuse together under TEM conditions of high vacuum and strong electron beam, accounting for the large particles. Nevertheless, based on the single crystal structure, the Au core of $Au_{133}(SR)_{52}$ nanocluster is approximately 2 nm in diameter, which matches the average size (1.99 nm, 100 counts) of the observed small particles, indicating successful encapsulation.

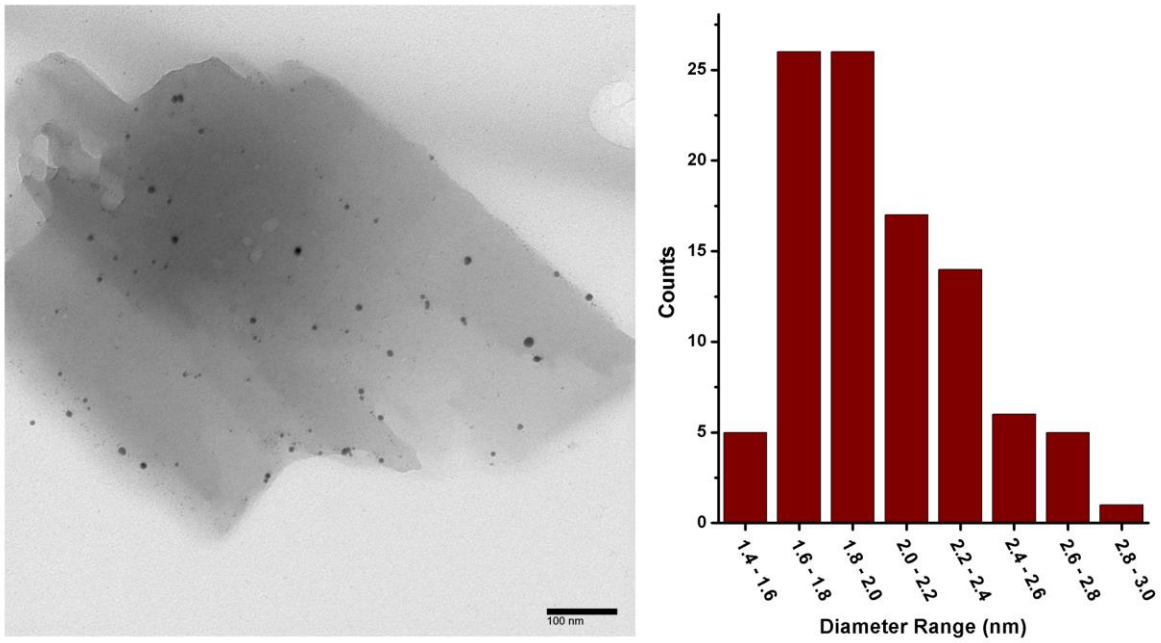

Figure 117. Left: TEM image of bMOF-102/106 with $Au_{133}(SR)_{52}^{+}$. Right: size distribution of the Au nanoclusters (100 counts).

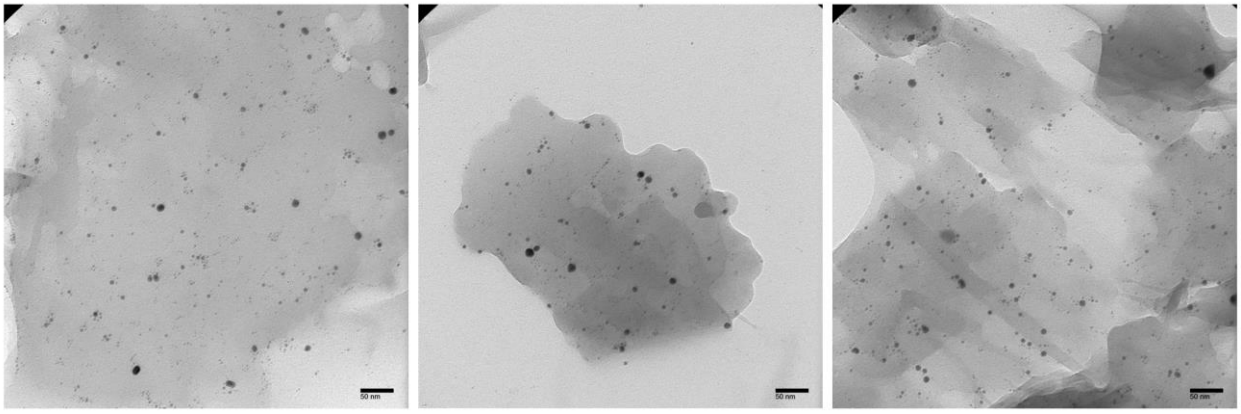

Figure 118. Additional TEM images of bMOF-102/106 with $Au_{133}(SR)_{52}^{+}$.

5.0 SYNTHESIS AND CHARACTERIZATION OF ISORETICULAR RARE EARTH METAL-ORGANIC FRAMEWORKS WITH FCU TOPOLOGY

This work, in collaboration with Svetlana V. Eliseeva, Tian-Yi Luo, Patrick Muldoon, Stéphane Petoud and Nathaniel L. Rosi*, is in preparation for publication.

Svetlana V. Eliseeva and Patrick Muldoon assisted with spectroscopic study of the materials, Tian-Yi Luo assisted with optimization of synthesis and characterization with EA, PXRD, and SEM.

5.1 INTRODUCTION

In the trivalent ions of the lanthanide series (Ln^{3+}), electrons gradually fill the 4f orbitals, from $4f^0$ (La^{3+}) to $4f^{14}$ (Lu^{3+}). The [Xe]$4f^n$ electronic configuration can theoretically generate $14!/n!(14-n)!$ electronic levels, which translates to 3432 electronic levels for Gd^{3+}, for instance. Because the 4f orbitals are well shielded from the chemical environment by the closed $5s^2$ and $5p^6$ sub-shells, the ligands in the first and second coordination spheres have very limited effect on the electronic configurations of Ln^{3+}. As a corollary, the Ln^{3+} 4f-4f transitions exhibit narrowband emissions (sharp peaks) and excitation states with long lifetimes.[161-163] Ln^{3+} are known for their signature luminescence properties. For example, Eu^{3+} emits red light, Tb^{3+} green light, Sm^{3+} orange light, and Tm^{3+} blue light. In addition, Yb^{3+}, Nd^{3+}, and Er^{3+} are well-known

for their near-infrared (NIR) luminescence (Figure 119).[164-165] Ln^{3+} photoluminescence is of great research importance and has been applied in numerous fields including sensing, tissue and cell imaging, and display technology.

NIR Ln^{3+} photoluminescence is especially important and desirable for biological imaging. Biological tissues exhibit low auto-fluorescence in the NIR region of the spectrum; therefore, NIR reporters can easily be distinguished from background, giving rise to enhanced signal-to-noise ratios and more sensitive detection.[166] Additionally, light scatters less in the NIR compared to the visible, which results in improved optical resolution for imaging purposes.[167-168] Finally, photons in the NIR energy range do not interact with biological tissues as strongly as visible photons, thus reducing the risk of disturbing or damaging the observed biological systems.[169]

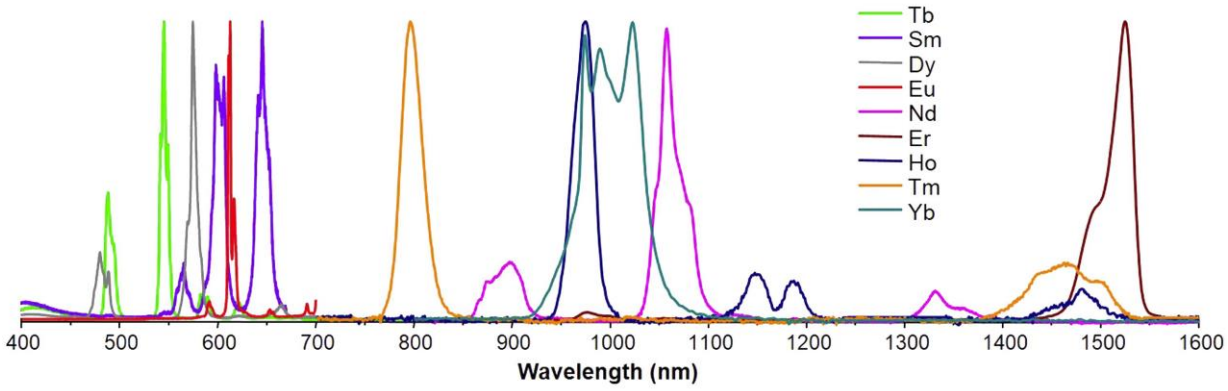

Figure 119. Normalized emission spectra for selected Ln^{3+}.[164-165]

There are some challenges associated with Ln^{3+} luminescence. Because the f-f LaPorte transitions are parity-forbidden, most of these transitions have molar absorption coefficients smaller than 10 $L \cdot mol^{-1}cm^{-1}$. Consequently, it is very difficult to observe strong luminescence through direct excitation of the Ln^{3+}, even if the intrinsic quantum yield of the Ln^{3+} is large, unless high-power laser excitation is used. The inherent weak light absorption of Ln^{3+} can be

overcome by attaching ligands to Ln^{3+} that can sensitize luminescence via the so-called antenna effect (Figure 120). Here, excitation radiation is centered on an absorption band of the ligand and energy is transferred to the Ln^{3+} which leads to f-f transitions and ultimately luminescence.[170]

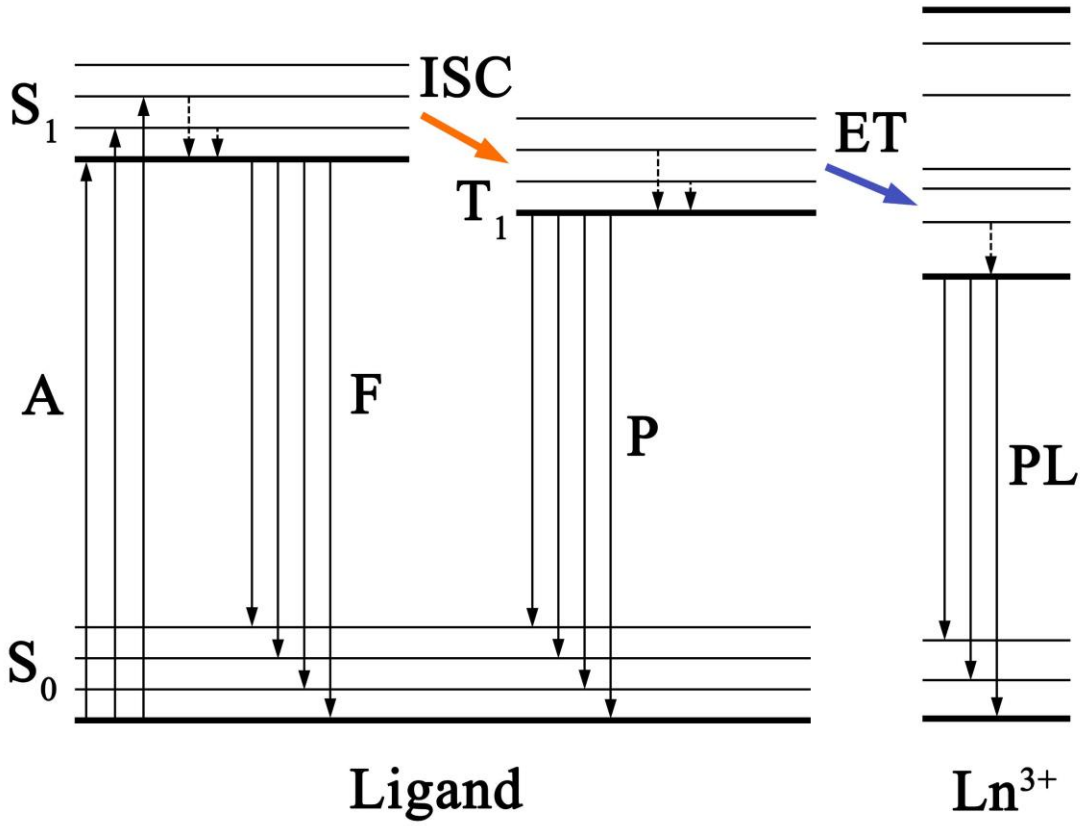

Figure 120. Schematic representation of the photophysical processes involved in the antenna effect (Ln^{3+} sensitization)[161*].

For Ln^{3+} complexes, the overall luminescence yield is determined by both the intrinsic quantum yield and the ligand sensitization efficiency. Intrinsic quantum yield is the quantum

[*] Abbreviations: A = absorption; F = fluorescence; P = phosphorescence; PL = lanthanide photoluminescence; ISC = intersystem crossing; ET = energy transfer; S = singlet state; T = triplet state. Solid vertical arrows indicate radiative transitions; dotted vertical arrows indicate non-radiative transitions.

yield of direct excitation in the Ln^{3+} 4f levels, which is dependent on the energy gap between the emissive state of Ln^{3+} and ground state or receiving multiplet state. Luminescence quenching can decrease the quantum yield. Non-radiative transition processes such as O-H, N-H, and C-H vibrations in the nearby environment can quench the luminescence, especially in cases where there is a small energy gap between the f levels.[163] Compared to Eu^{3+} and Tb^{3+} ions, NIR light-emitting Yb^{3+}, Nd^{3+} and Er^{3+} naturally have smaller energy gaps between the ground states and emissive states. As a result, the luminescence from NIR Ln^{3+} is easily quenched by oscillators in the ligands and nearby solvents.

Three general strategies have been proposed and developed to overcome these drawbacks that limit the use of Ln^{3+} photoluminescence: i) design of new ligands with matching energy levels to Ln^{3+} to increase the efficiency of ligand-to-Ln^{3+} energy transfer; ii) design complexes that can provide coordination environments that protect the Ln^{3+} luminescent centers from solvent molecules to minimize quenching; and iii) design complexes that have a high density of Ln^{3+} photoluminescence centers and sensitizing ligands.

It is proposed that MOFs are ideal platform materials to explore and optimize Ln^{3+} luminescence properties.[171-174] First, the diversity of MOFs provides many ligands and chemical environments to test in order to achieve satisfactory energy transfer efficiency. As described extensively in this dissertation, MOFs can be modified in several ways to fine-tune the interaction between ligands and Ln^{3+}. Second, MOFs are crystalline materials in which the positions of ligands and Ln^{3+} can be unambiguously identified, enabling correlation of structure and luminescence properties. Third, MOFs typically have rigid structures with thermodynamically stable coordinative spheres in which the ligands and Ln^{3+} are spatially constrained and well-organized, and macroscopic MOF crystals are heterogeneous entities in the

medium of study. Both of these features should serve to protect the Ln^{3+} from quenching to some extent. Finally, although they cannot compare to materials like Eu_2O_3 in terms of Ln^{3+} density, MOFs, especially microporous MOFs, commonly contain SBUs constructed from multiple Ln^{3+} ions and large numbers of organic ligands. As a result, MOFs have a much higher density of luminescence centers and sensitizers compared to discrete complexes, which naturally should result in brighter emitters. Consider, for example, two Ln^{3+}-based reporter tags used to track a biological process. One tag is a molecular complex and one is a 20 nm diameter Ln^{3+}-based nanoMOF crystal. The nanoMOF crystal will have orders of magnitude more Ln^{3+} and sensitizers compared to the molecular complex and should therefore be significantly brighter and easier to track because it would be emitting more photons.

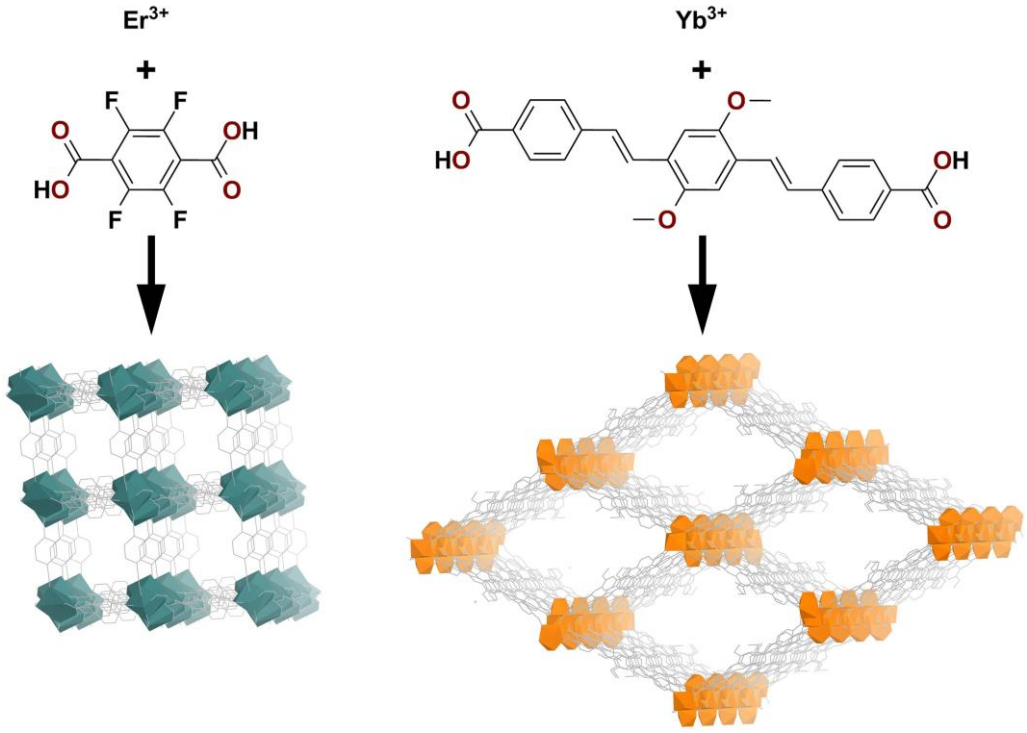

Figure 121. Two examples of NIR-emissive Ln^{3+}-MOFs.[169,175-177]

Synthesis and study of luminescence in Ln^{3+}-MOFs is well-documented.[171-174,178] However, there are few NIR-emissive Ln^{3+}-MOFs reported as compared to the visible emissive Ln^{3+}-MOFs; two examples are shown in Figure 121.[169,175-177] Due to the rich coordination chemistry of Ln^{3+}, there are usually high degrees of flexibility and variability in Ln^{3+}-MOF structures. Most Ln^{3+}-MOFs are defined by high coordination numbers and infinite chain-like Ln^{3+}-carboxylate SBUs. In general, it is difficult to predict MOF topology since the structures are sensitive to conditions, and it is difficult to target specific topologies because the Ln^{3+} coordination sphere is difficult to control. To systematically study structure-property relationships in luminescent Ln^{3+}-MOF materials, it would be ideal to have a single platform Ln^{3+}-MOF structure that could be systematically varied and modified without changing the MOF topology.

Eddaoudi and coworkers recently developed synthetic protocols for constructing a new isoreticular series of Ln^{3+}-MOFs that represents an attractive platform for studying and tuning Ln^{3+} luminescence in MOFs.[179-183] Their syntheses included a modulator/structural directing agent, 2-fluorobenzoic acid, which assisted in the formation of a discrete rare earth metal SBU. It was suggested that the modulator led to the formation of a discrete complex that then acted as a precursor species for the final MOF structure (Figure 122). In the presence of bridging ligands of different geometry, MOFs with different topology can be made based on the aforementioned SBU (Figure 123). The 2-fluorine atom adjacent to the carboxylate group was critical to facilitate the formation of the discrete rare earth SBU with high symmetry, as well as the *fcu* and *ftw* MOFs.[179,182]

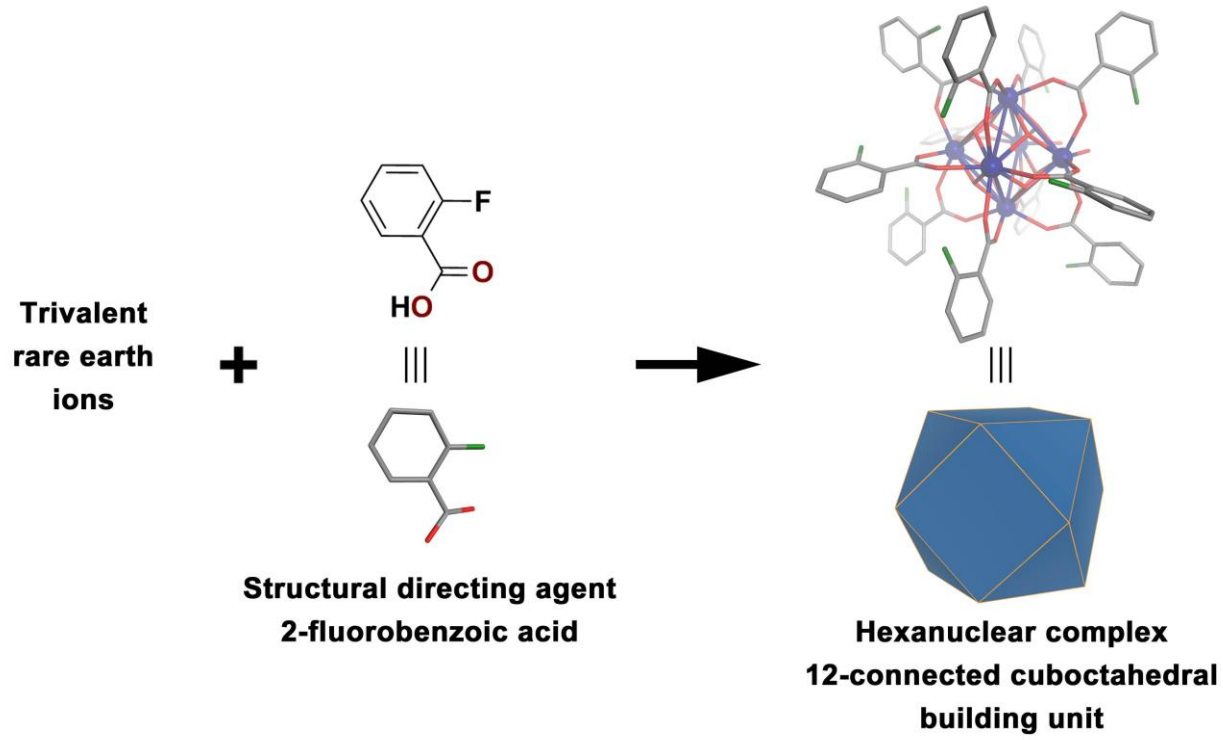

Figure 122. Formation of discrete rare earth SBU with structural directing agent.[180]

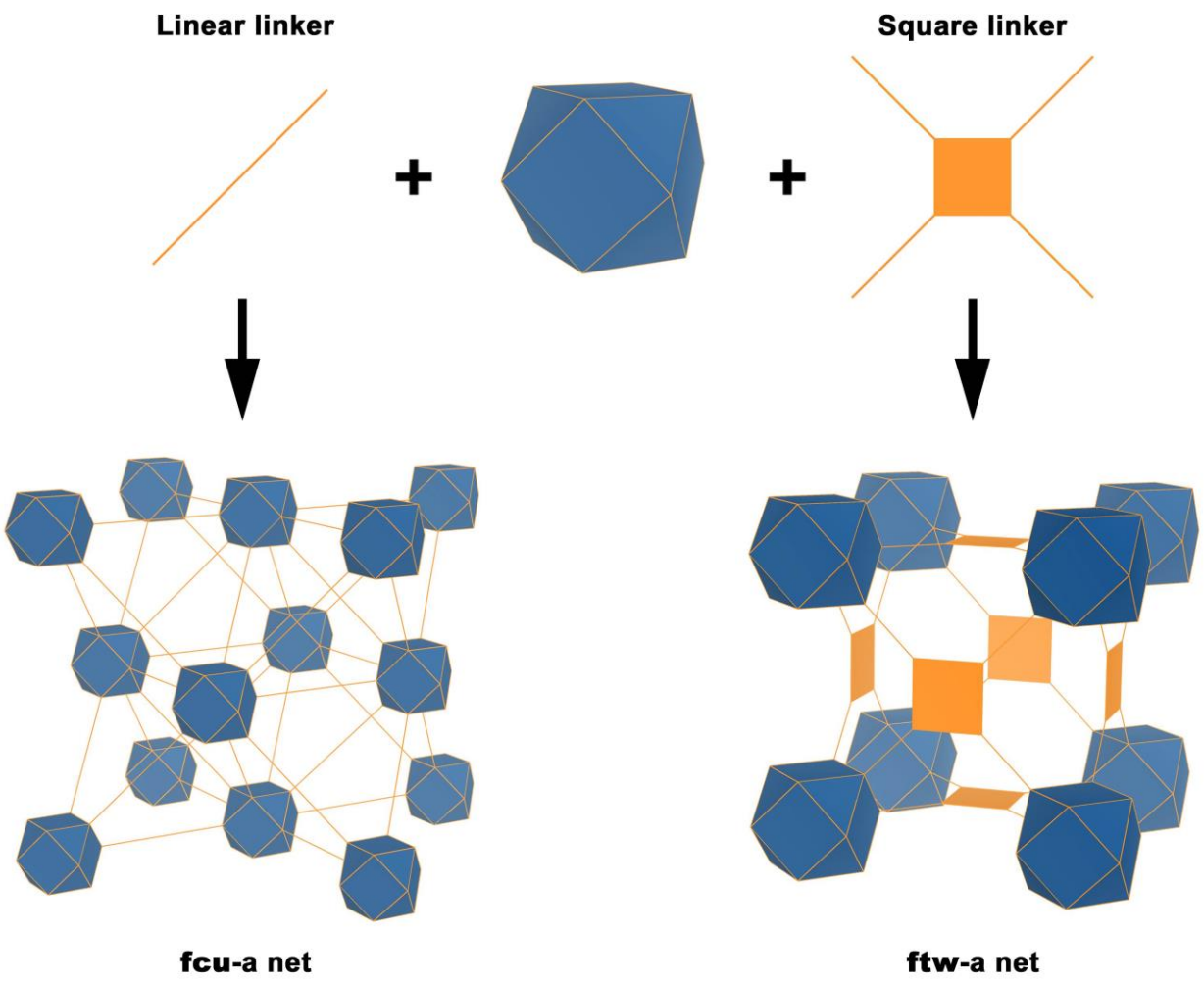

Figure 123. Coupling of cuboctahedral SBU with linear and square ligands to form augmented *fcu* and *ftw* topology MOFs.[179,182]

MOFs with *fcu* topology are usually made with group 4 metal ions. They have stable structures and are a well-studied class of MOFs.[184-185] The *fcu* Zr^{4+}-MOFs are among a few that have attracted the most attention in MOF chemistry, due to their highly connected and stable structures, excellent compatibility with functionalization, and tunable porosity.[186-191] The *fcu* Zr^{4+}-MOFs are charge-neutral. Group 3 *fcu*-MOFs are anionic and charge balancing cations

reside in their pores. Cation exchange can be used to introduce new functional cations to their pores, providing another dimension of MOF tunability.[179]

To explore the rich potential that lies within the rare earth class of *fcu* MOFs, further synthetic optimization and exploration of applications are necessary. After noting that, in several cases, ligands fluorinated at the 2 position were used to prepare Ln^{3+}-MOFs with the *fcu* topology,[179] it is reasoned that introducing modulators into the synthesis that bear multiple F atoms may allow for access to *fcu* Ln^{3+}-MOFs using common non-fluorinated ligands, especially ones that are commercially available. Such a synthetic advance would lead to greater utility and accessibility of this important new class of MOFs. Here, it is proposed to i) introduce methods to expand the rare earth *fcu*-MOF platform; ii) begin exploration of their intrinsic luminescence properties; and iii) perform cation-exchange experiments to incorporate low-energy cationic chromophoric sensitizers into the pores to optimize the luminescence properties for future biological imaging applications.

5.2 RESULTS AND DISCUSSION

5.2.1 Isoreticular *fcu* rare earth MOFs

First, benzoic acid derivatives with multiple fluorine atoms, including 2,6-difluorobenzoic acid, 2,4,6-trifluorobenzoic acid, 2,3,5,6-tetrafluorobenzoic acid, and 2,3,4,5,6-pentafluorobenzoic acid, were tested as modulators for the synthesis of *fcu* rare earth MOFs (Figure 124). Among these candidate molecules, 2,6-difluorobenzoic acid (DFBA) was found to be most effective in facilitating the exclusive formation of *fcu* rare earth MOFs. As described in detail in the

Experimental Section 5.4.2, usage of DFBA in large quantities helped yield three *fcu* rare earth MOFs with $DyCl_3 \cdot 6H_2O$ and commercially available ligands 2,6-naphthalenedicarboxylic acid (2,6-NDC), 4,4'-biphenyldicarboxylic acid (BPDC) and 4,4'-azobenzenedicarboxylic acid (ABDC) (Figure 125). The structures were successfully determined via single crystal X-ray diffraction experiments. The crystallographic data and structure refinement are summarized in Table 3, while X-ray diffraction experimental details and crystallographic tables are included in appendices A, B, and C.

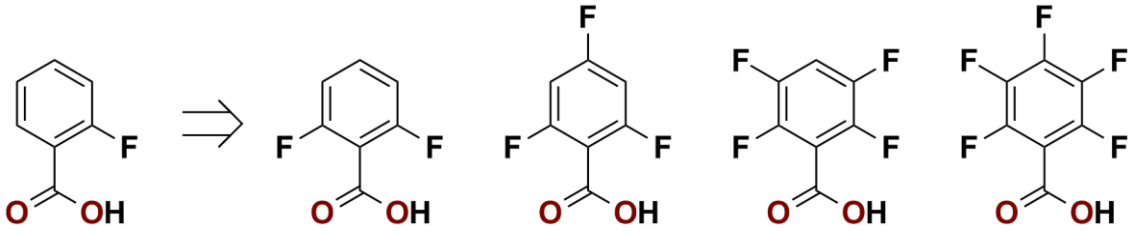

Figure 124. Different fluorinated benzoic acid tested as modulators in MOF synthesis.

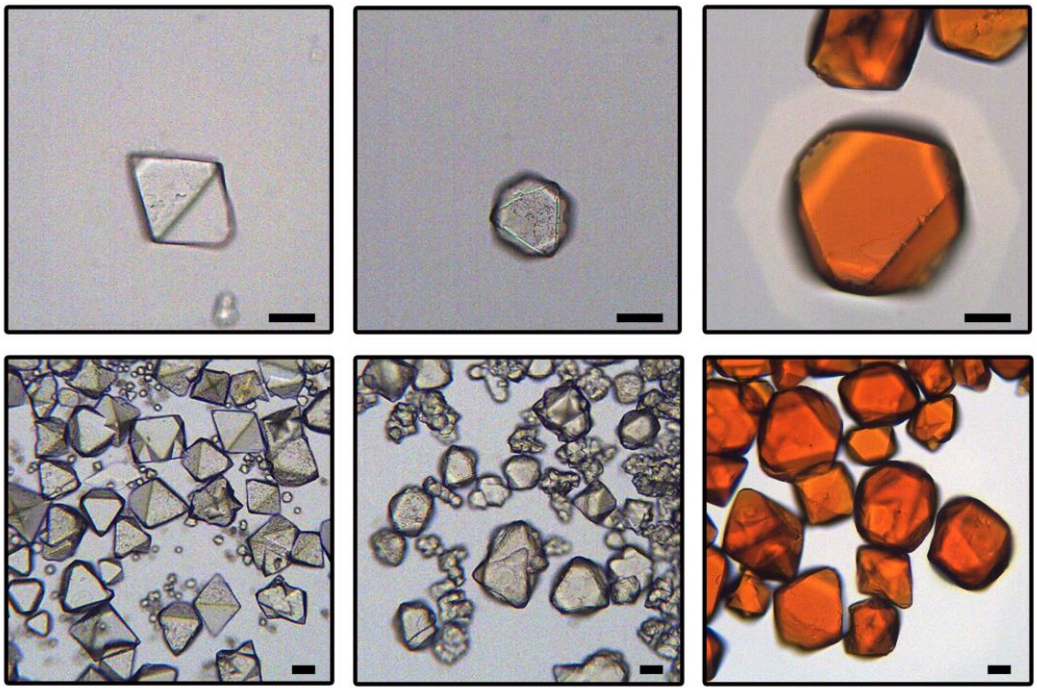

Figure 125. Optical images of Dy^{3+}-NDC (left), Dy^{3+}-BPDC (middle), and Dy^{3+}-ABDC (right) (scale bar: 50 μm).

Table 3. Crystal data and structure refinement of Dy^{3+}-NDC, Dy^{3+}-BPDC, and Dy^{3+}-ABDC.

Identification code	**Dy^{3+}-NDC**	**Dy^{3+}-BPDC**	**Dy^{3+}-ABDC**
Empirical formula	C_{144} Dy_{12} O_{64}	C_{42} H_{24} Dy_3 O_{20}	C_{42} H_{24} Dy_3 N_6 O_{16}
Formula weight	4703.44	1336.11	1356.17
Crystal system	Cubic	Cubic	Cubic
Space group	*Fm-3m*	*Fm-3m*	*Fm-3m*
***a* (Å)**	24.8328(3)	27.5659(2)	29.9107(6)
Volume (Å^3)	15313.6(3)	20946.7(3)	26759.6(9)
Z	2	8	8
Crystal size (mm^3)	0.08 × 0.08 × 0.06	0.10 × 0.06 × 0.06	0.12 × 0.12 × 0.08
θ_{max} (°)	68.31	66.54	68.54
Completeness	99.1%	99.9 %	99.9%
R_{int}	0.0671	0.0785	0.1647
R_1 ($I > 2\sigma(I_0)$)	0.1562	0.0562	0.0529
wR_2 (all data)	0.5450	0.1926	0.1606

The three isoreticular MOFs share the same underlying connectivity (Figure 126). 8 μ_3-OH groups occupy the triangular faces of the core Dy_6 octahedron and serve to bridge three Dy^{3+} together. Along the edges of the octahedron, the Dy^{3+} are further bridged by 12 μ_2-COO^- groups from the ligands, which serve to link the clusters together into a periodic extended structure. As evidenced by PXRD, the *fcu* MOFs were made in pure phases using this synthetic strategy (Figure 127). Their respective purity and composition were further confirmed by ^{1}H NMR and CHN elemental analysis (Experimental Section 5.4.3). Further, this protocol was fully compatible with multiple rare earth elements for all three ligands, including Y^{3+}, Eu^{3+}, Gd^{3+}, Tb^{3+}, Dy^{3+}, Ho^{3+}, Er^{3+}, Tm^{3+}, Yb^{3+}, and Lu^{3+}, as confirmed by PXRD (Figures 128-130).

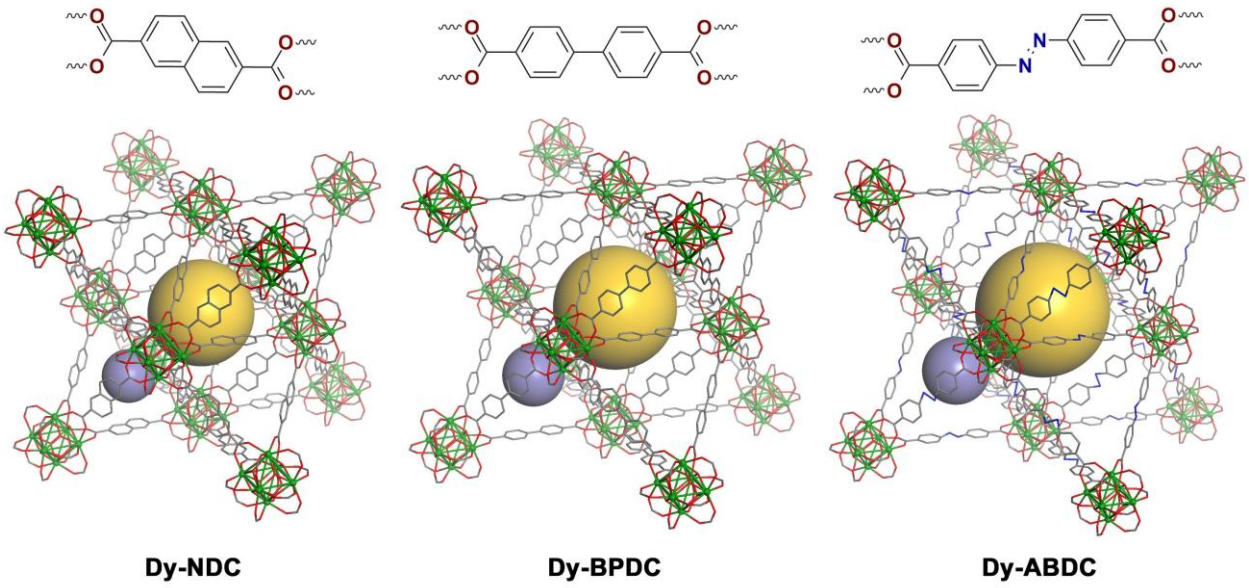

Figure 126. Structure illustration of Dy^{3+}-NDC, Dy^{3+}-BPDC, Dy^{3+}-ABDC *fcu* MOFs.*

* In all schemes, Dy: green balls; C: grey sticks; O: red sticks; N: blue sticks. H atoms are omitted for clarity. Two types of pores are indicated by gold and purple spheres, respectively.

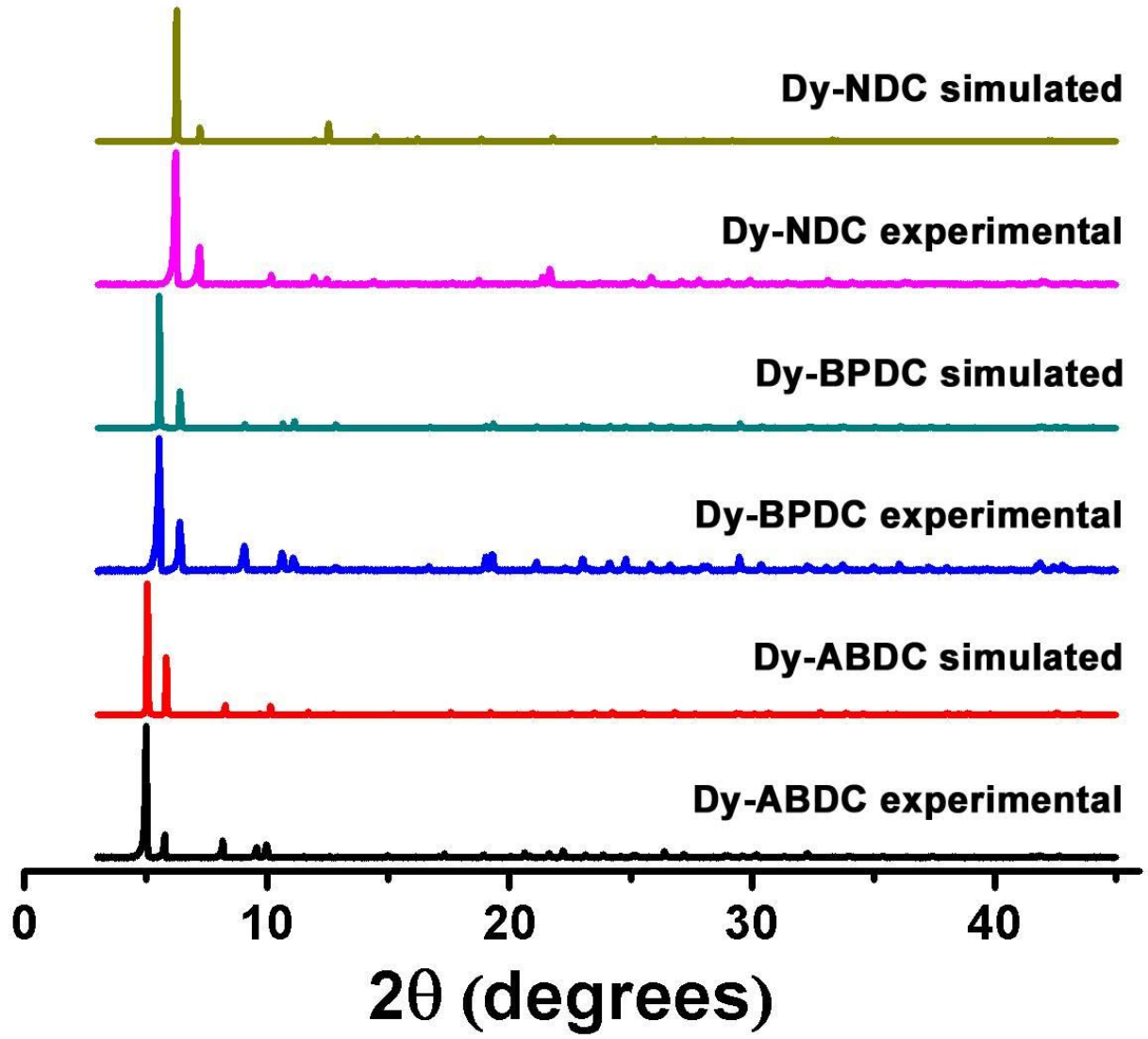

Figure 127. Comparison of simulated and experimental PXRD patterns of three *fcu* Dy^{3+}-MOFs.

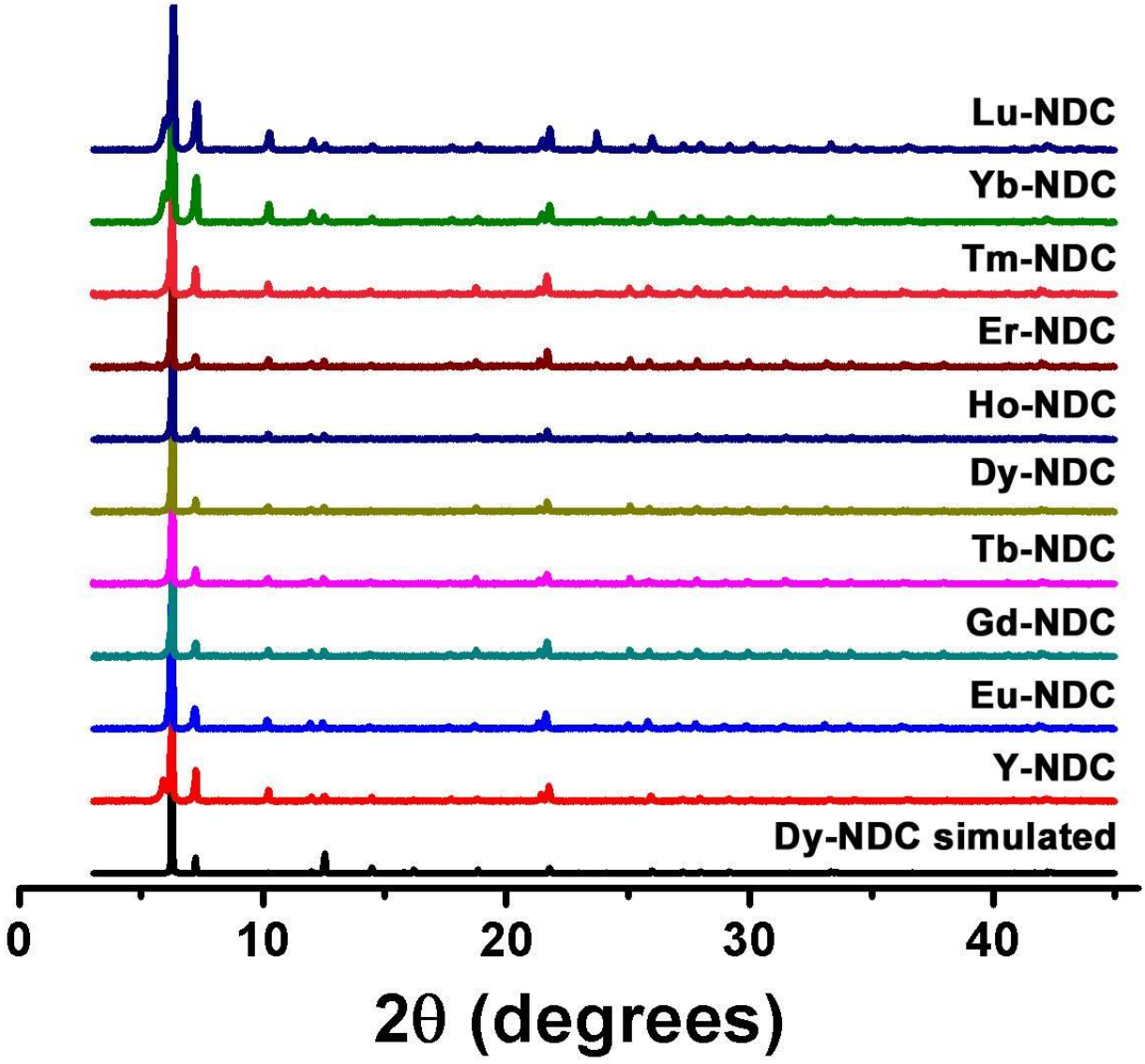

Figure 128. PXRD patterns of rare earth NDC MOFs.

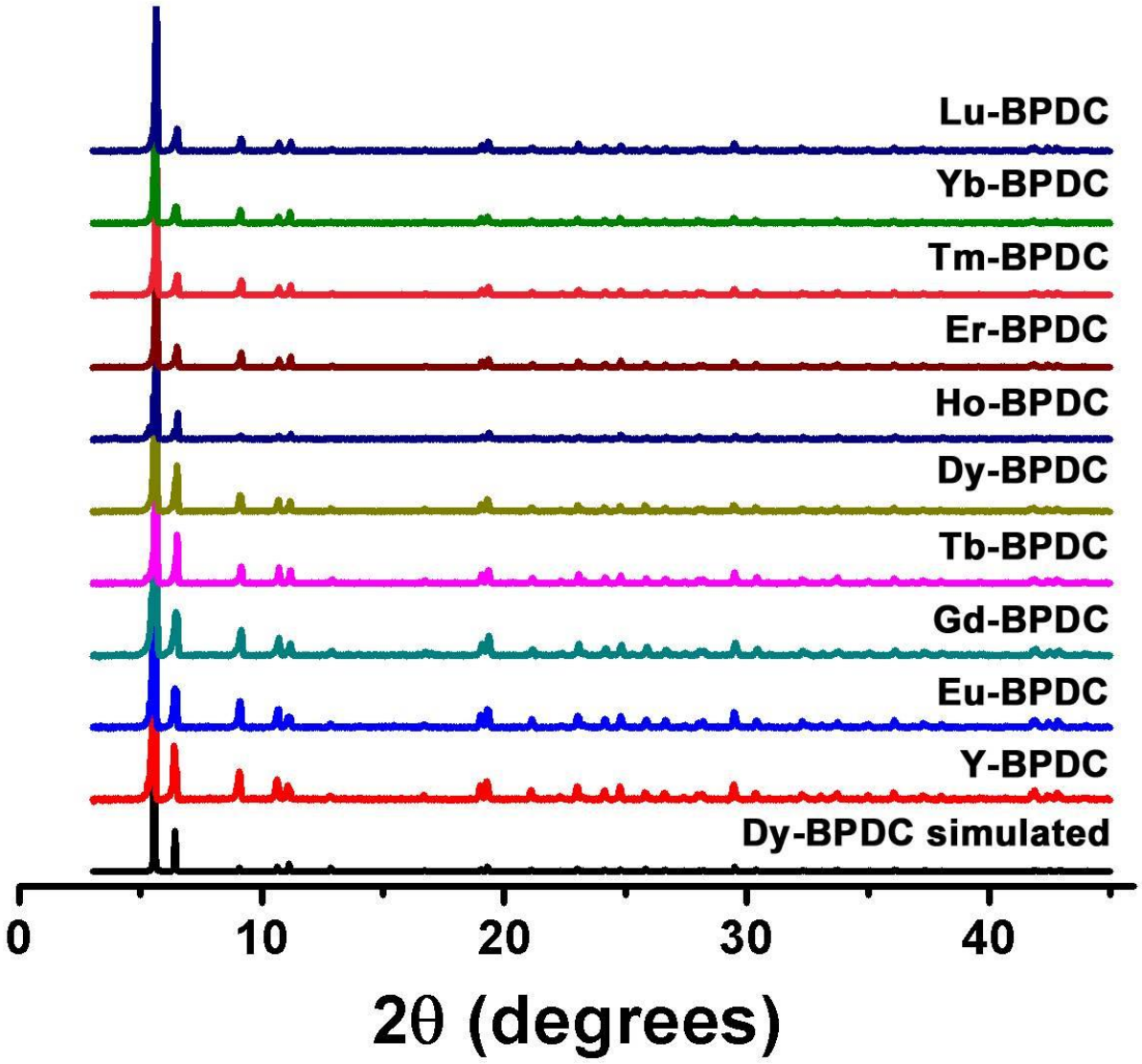

Figure 129. PXRD patterns of rare earth BPDC MOFs.

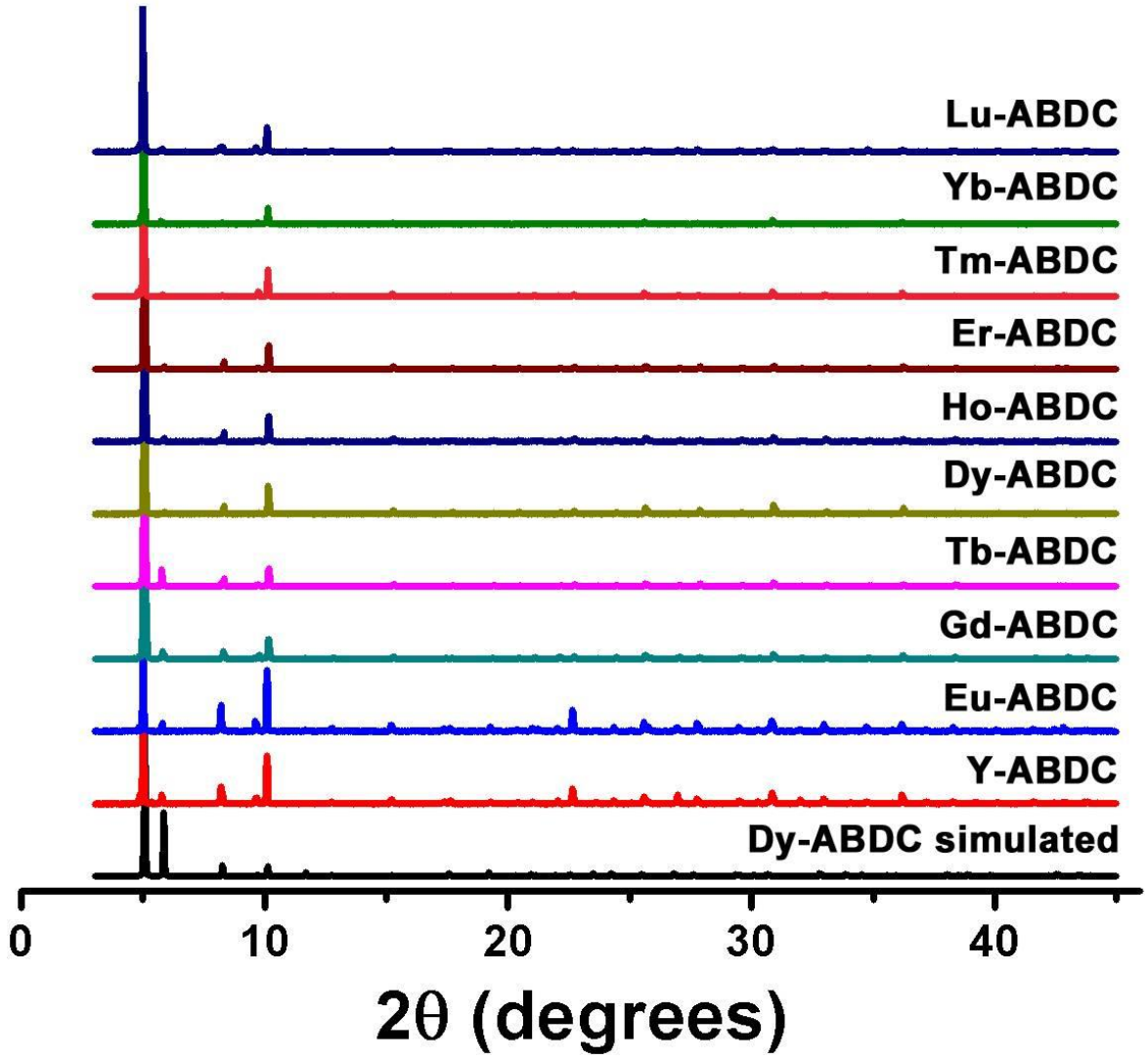

Figure 130. PXRD patterns of rare earth ABDC MOFs.

Considering many mixed-Ln^{3+} MOFs have demonstrated potential to serve as ratiometric sensors, spectroscopic barcodes, and white-light emitters,[174,177,192-193] it was next attempted to obtain *fcu* MOFs with multiple rare earth elements within individual crystals. First, PXRD was used to confirm the crystallinity and phase purity of NDC MOFs prepared using 2 or 3 different rare earth metal ions (Figure 131). Scanning electron microscopy (SEM) coupled with energy dispersive X-ray spectroscopy (EDX) was then used to analyze the composition of the mixed-

metal MOFs (Table 4, Figure 132). As described in Experimental Section 5.4.2.5, different rare earth salts were added in equal quantity to the synthesis. EDX results indicated that different rare earth elements were indeed present in approximately equal abundance in the product MOF crystals, especially when only Ln^{3+} were mixed, re-affirming the versatility of the synthetic strategy.

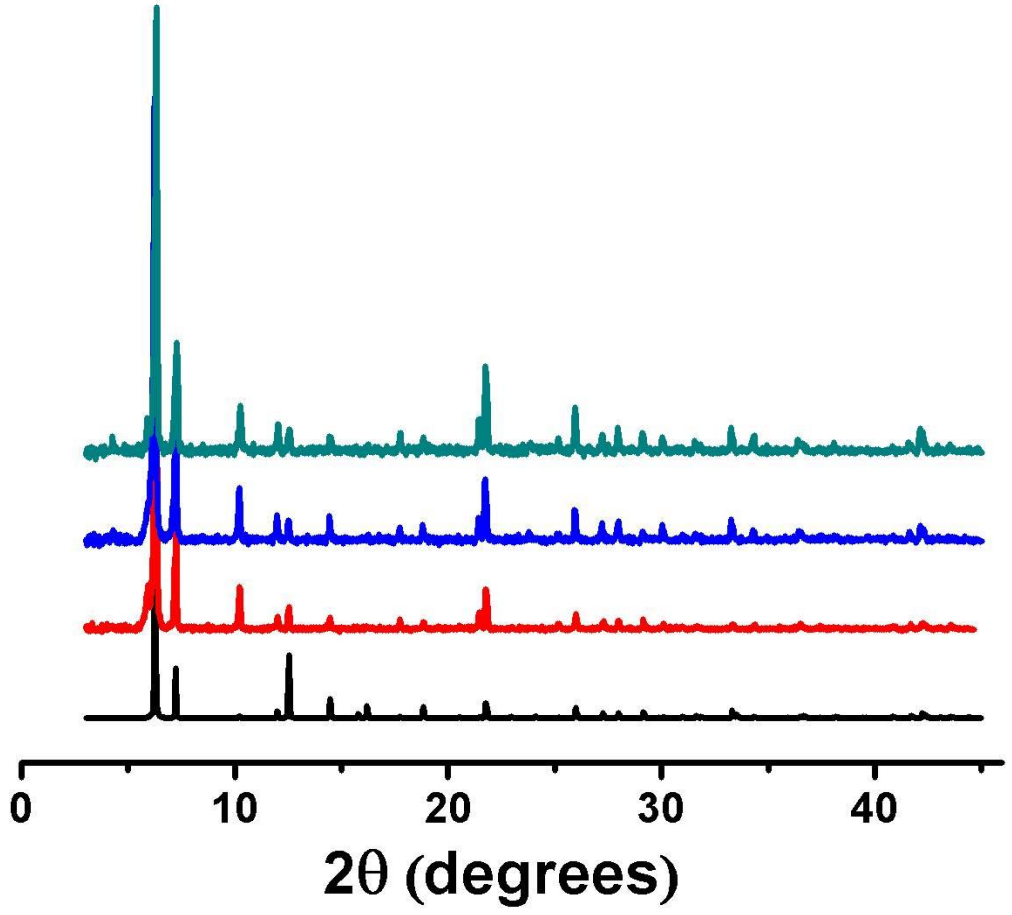

Figure 131. PXRD comparing Eu^{3+}/Tb^{3+}, Tb^{3+}/Ho^{3+}, $Y^{3+}/Gd^{3+}/Tm^{3+}$ mixed-metal NDC MOFs with simulated pattern.*

* Black: simulated Dy^{3+}-NDC; red: Eu^{3+}/Tb^{3+}-NDC; blue: Tb^{3+}/Ho^{3+}-NDC; dark cyan: $Y^{3+}/Gd^{3+}/Tm^{3+}$-NDC

Table 4. EDX analyzing the ratios of different elements in mixed-metal NDC MOFs

Sample	Eu^{3+}/Tb^{3+}-NDC	Tb^{3+}/Ho^{3+}-NDC	$Y^{3+}/Gd^{3+}/Tm^{3+}$-NDC
Ratio (from Atom%)	1 : 1.022	1 : 1.020	1 : 0.9363 : 0.8717

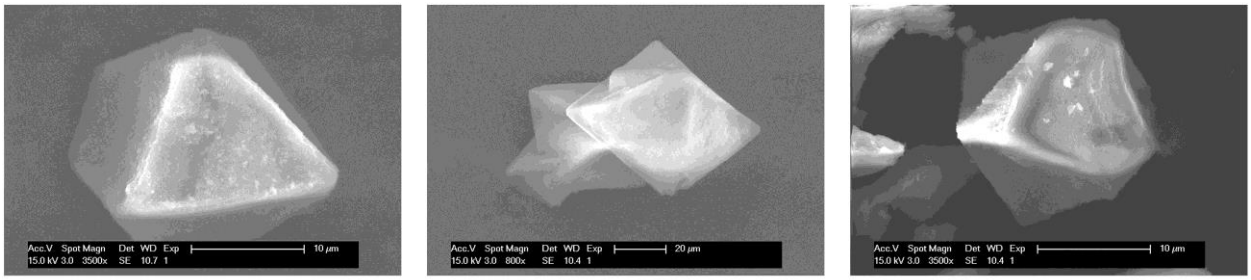

Figure 132. SEM images of mixed-metal NDC MOFs.

5.2.2 Photoluminescence of *fcu* Yb^{3+}-NDC/BPDC/ABDC MOFs.

As discussed in 5.1, NIR-emissive Ln^{3+}-MOFs are potential candidate materials for biological imaging applications. Therefore, the luminescence properties of the *fcu* Yb^{3+}-MOFs were explored, because Yb^{3+} has characteristic NIR emission at 980 nm. Excitation/emission contour maps were collected for the solid MOF samples. Yb^{3+}-NDC showed very intense emission (Figures 133-134). A cross-section of the contour map at maximum emission revealed Yb^{3+} characteristic emission (Figure 135). Similarly, Yb^{3+}-BPDC also exhibited very strong Yb^{3+} emission (Figures 136-138). However, in marked contrast, Yb^{3+}-ABDC exhibited almost no Yb^{3+} emission (Figure 139), especially when excited in the absorption wavelength range of the ABDC ligand. To determine whether this result was due to increased framework flexibility imparted by the longer ABDC linker, an analogous MOF was prepared using 4,4'-stilbenedicarboxylic acid (H_2-SBDC) as the ligand.

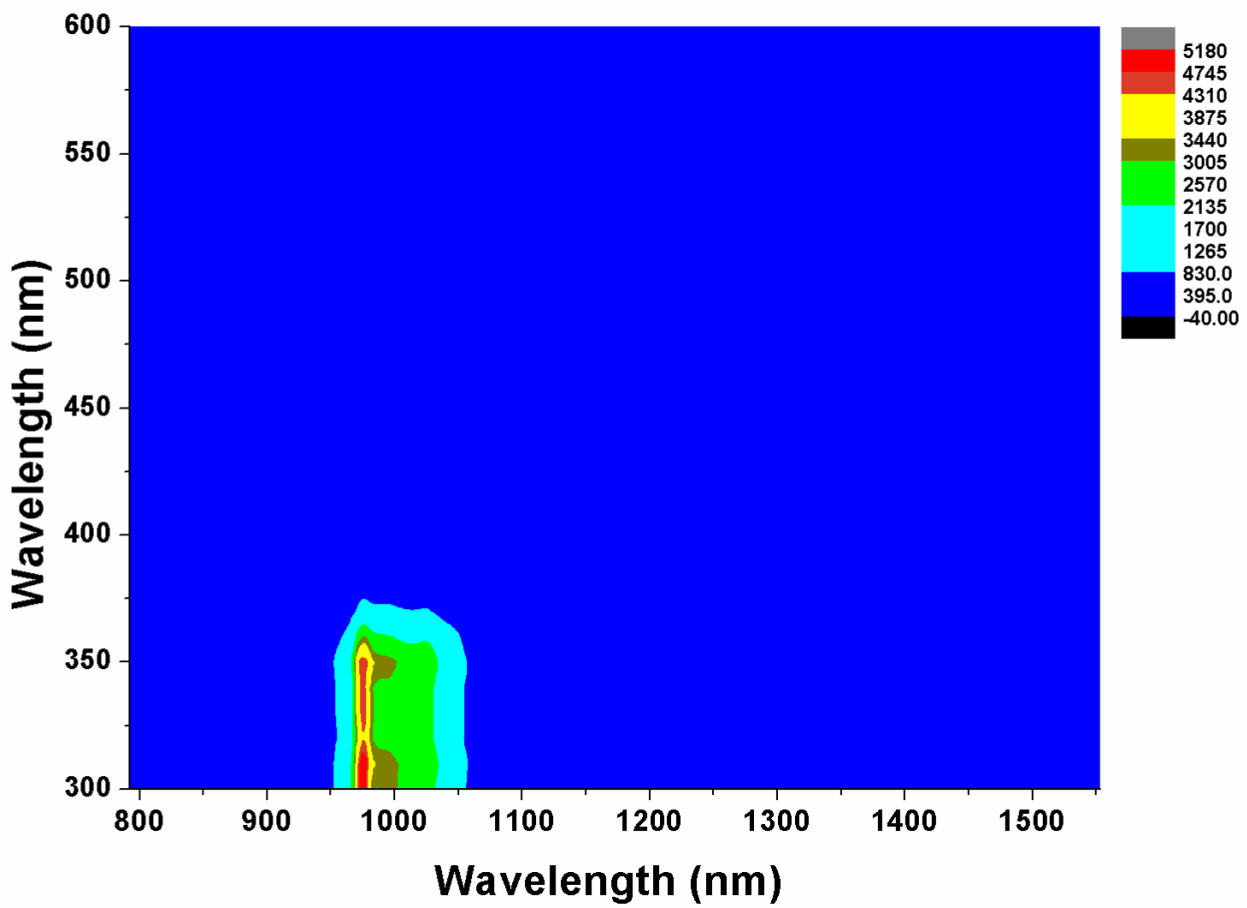

Figure 133. Excitation/emission contour map of Yb^{3+}-NDC.

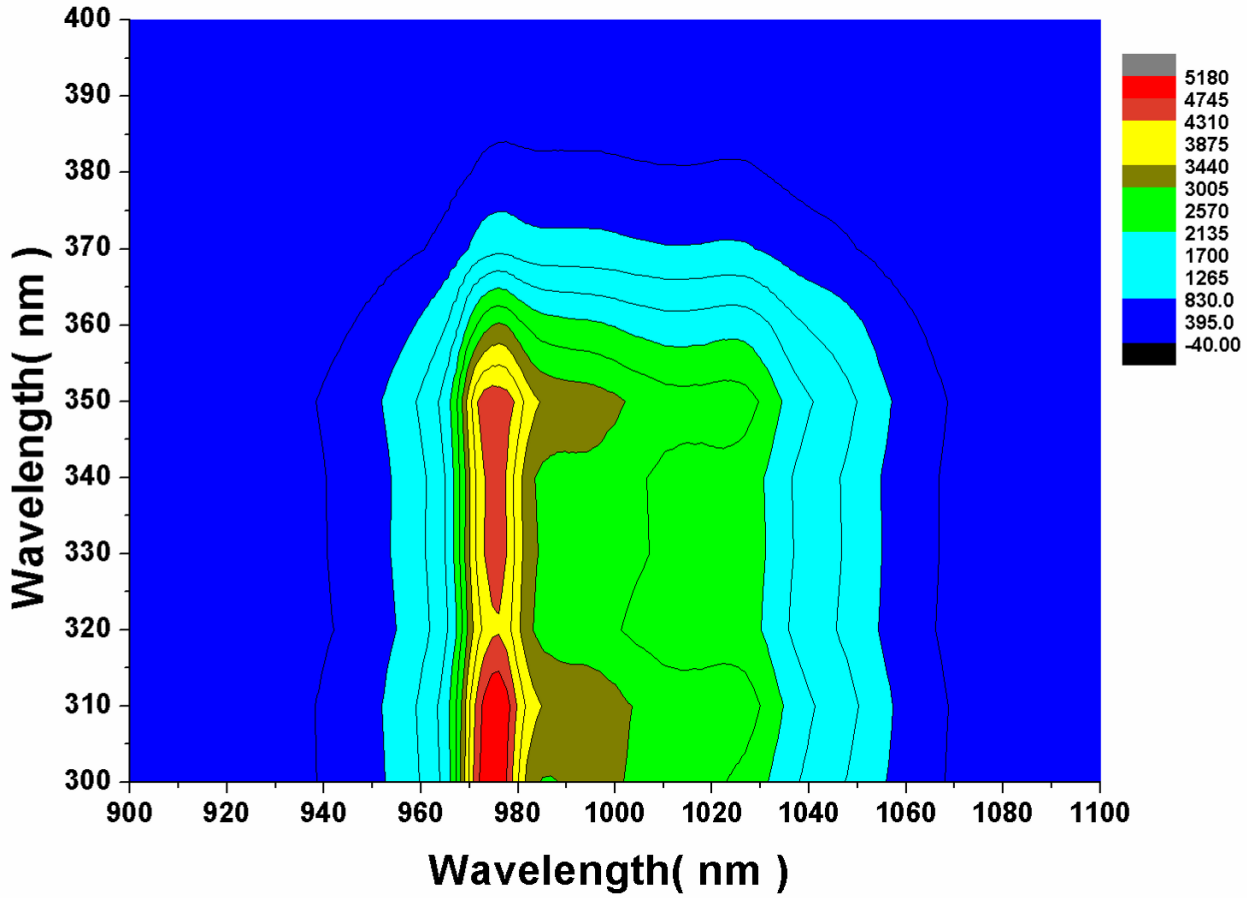

Figure 134. Enlarged excitation/emission contour map of Yb^{3+}-NDC.

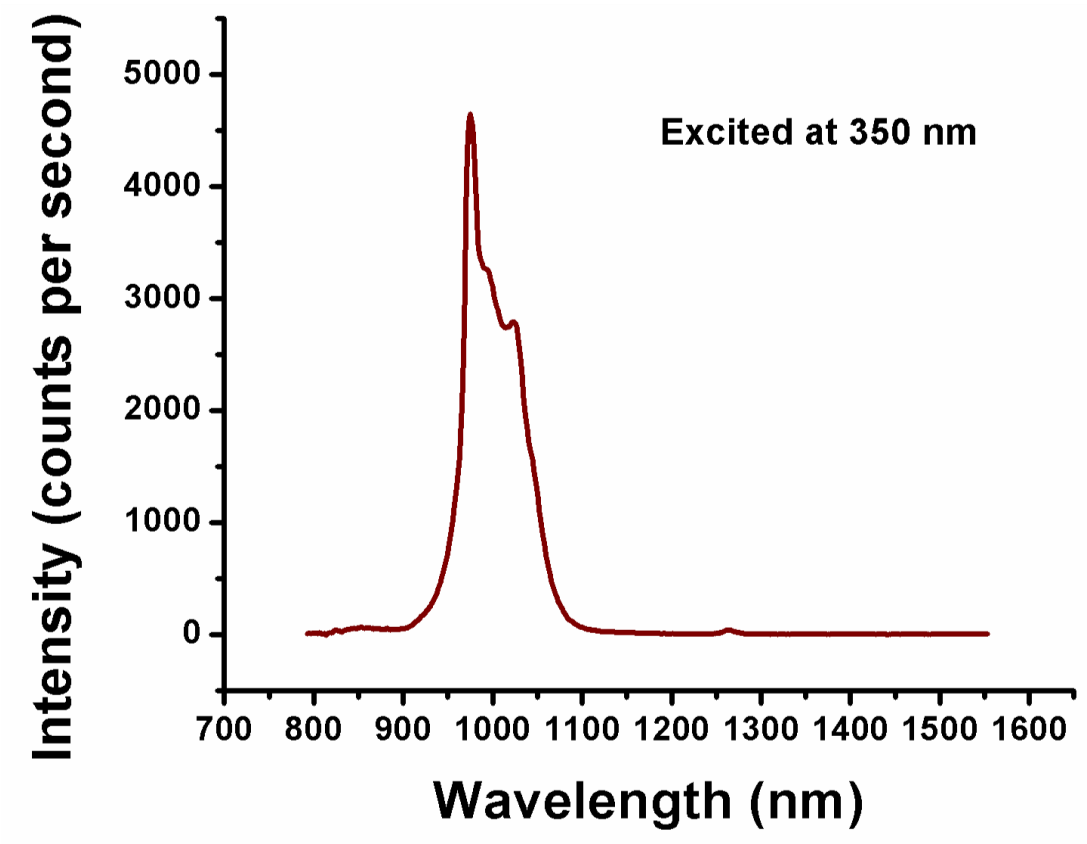

Figure 135. Photoluminescence spectrum of Yb^{3+}-NDC excited at 350 nm.

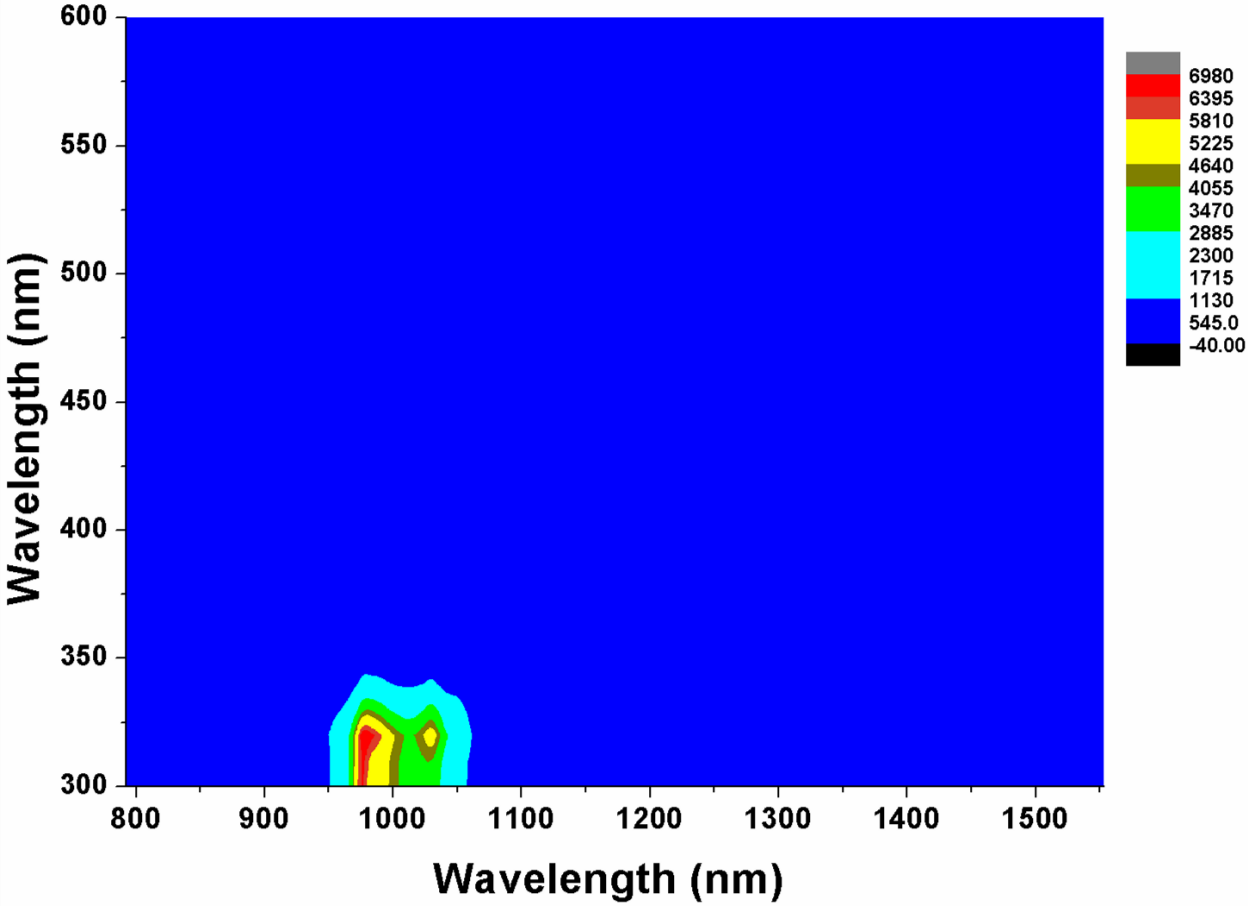

Figure 136. Excitation/emission contour map of Yb^{3+}-BPDC.

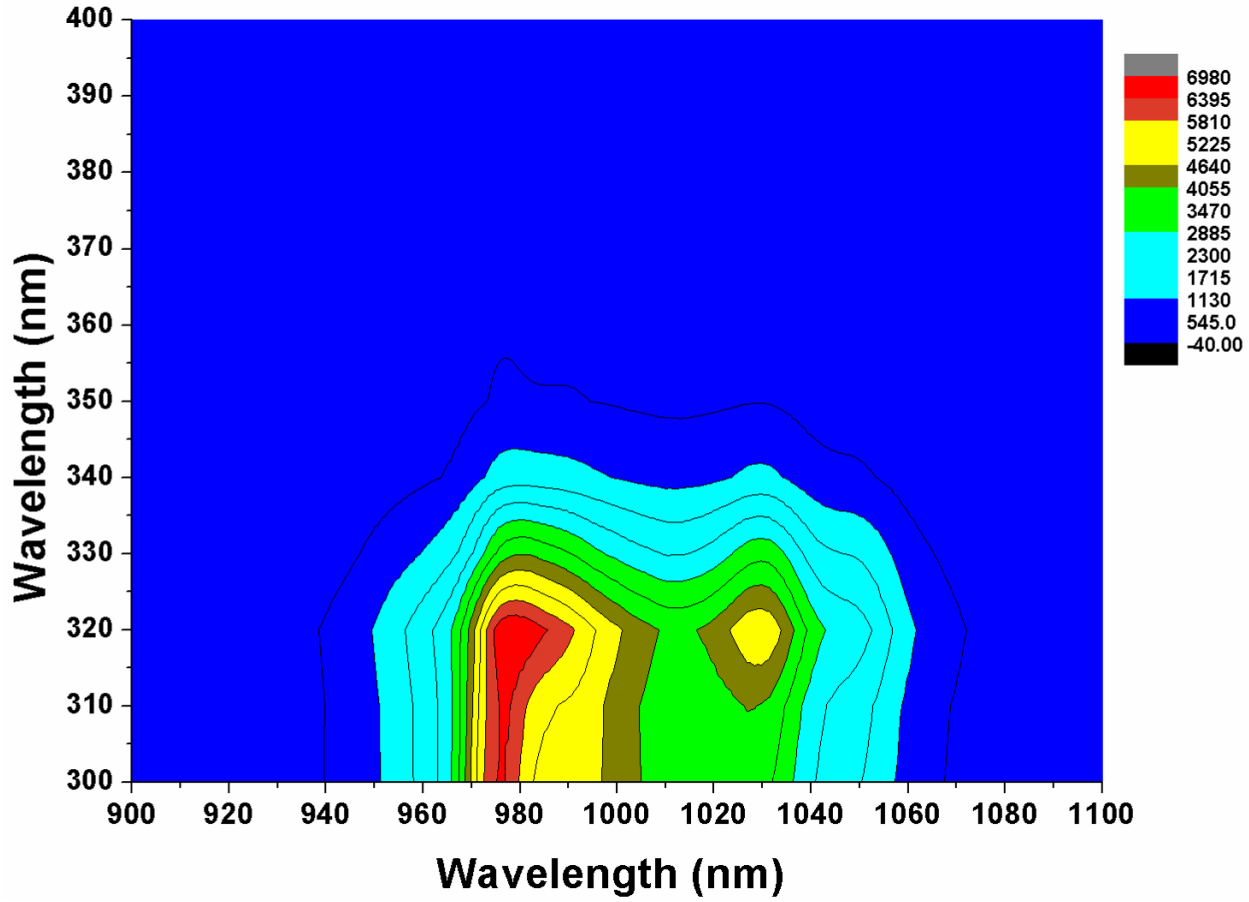

Figure 137. Enlarged excitation/emission contour map of Yb^{3+}-BPDC.

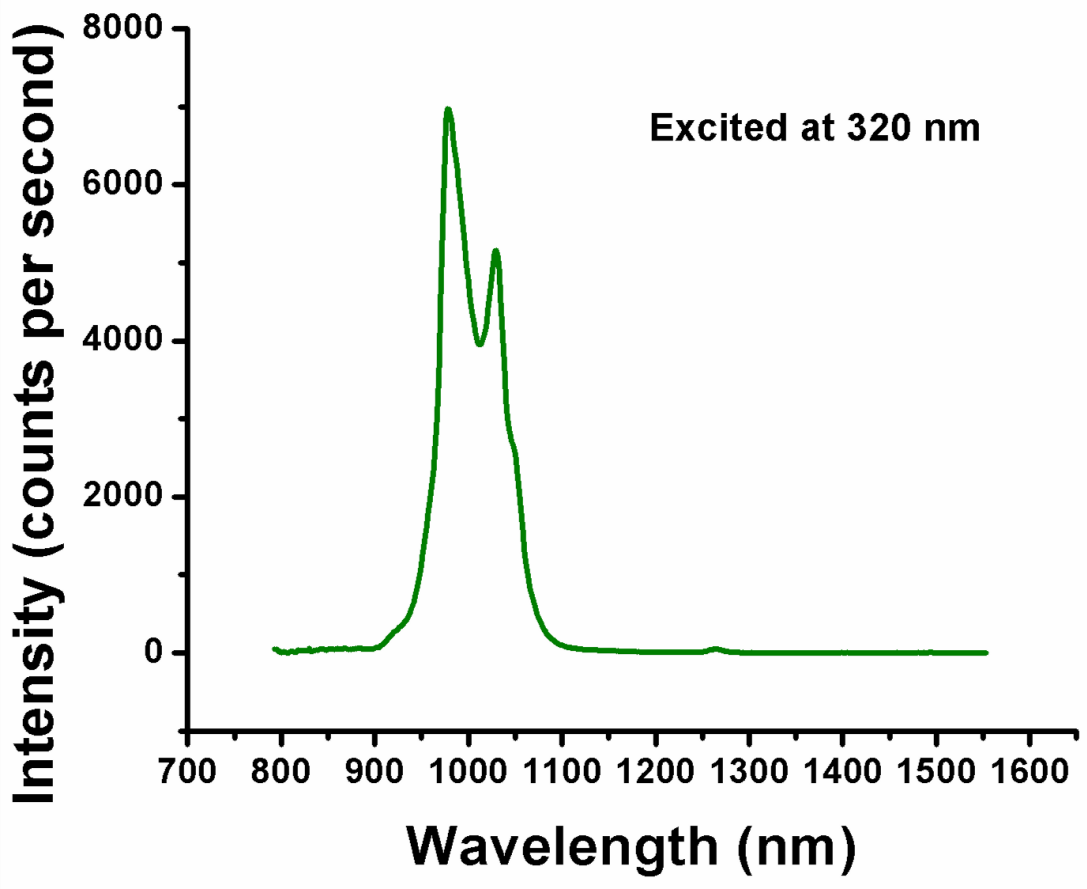

Figure 138. Photoluminescence spectrum of Yb^{3+}-BPDC excited at 320 nm.

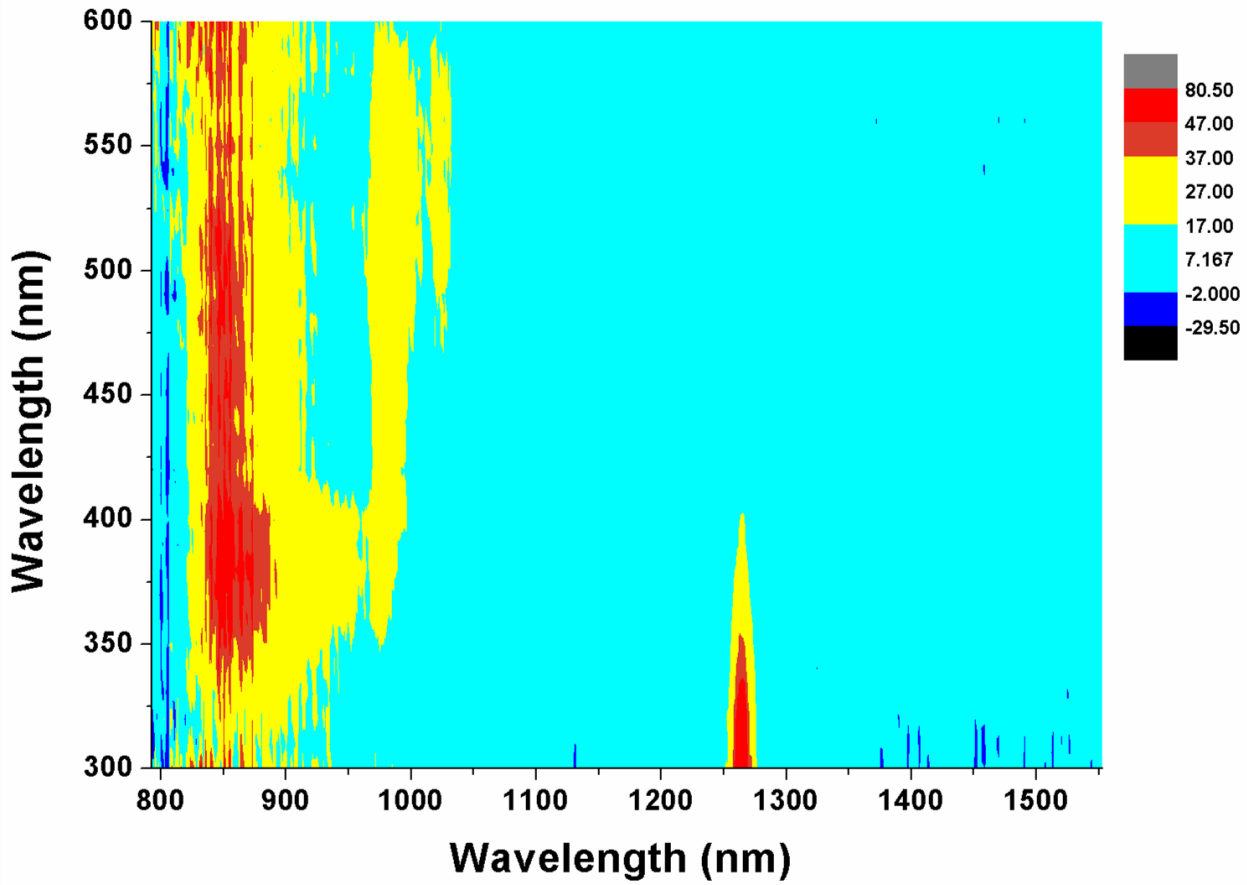

Figure 139. Excitation/emission contour map of Yb^{3+}-ABDC.

Crystallographic data and tables for Dy^{3+}-SBDC are listed in Table 5 and Appendix D. Dy^{3+}-SBDC is structurally similar to Dy^{3+}-ABDC (Figure 140). The composition of Dy^{3+}-SBDC was further studied via ^{1}H NMR and CHN elemental analysis (Experimental Section 5.4.3). An isostructural MOF with Yb^{3+} was synthesized using the same condition. The experimental PXRD patterns for Dy^{3+}-SBDC and Yb^{3+}-SBDC were compared to the simulated pattern to verify phase purity (Figure 141). Despite the structural similarity to Yb^{3+}-ABDC, Yb^{3+}-SBDC demonstrated very different photoluminescence behavior (Figure 142 and enlarged Figure 143). The photoluminescence spectrum (Figure 144) of Yb^{3+}-SBDC clearly showed the characteristic Yb^{3+} emission peaks, which were not observed for Yb^{3+}-ABDC. Based on these results, it was concluded that poor Yb^{3+} sensitization in Yb^{3+}-ABDC was not likely the result of larger pore size or more flexible structure. Since ABDC and similar ligands have been shown to successfully sensitize Ln^{3+} photoluminescence in MOFs,[194-195] the poor Yb^{3+} sensitization in Yb^{3+}-ABDC was more likely due to some intrinsic electronic properties of this MOF that are not fully understood at this stage.

Table 5. Crystal data and structure refinement of Dy^{3+}-SBDC.

Identification code	**Dy^{3+}-SBDC**
Empirical formula	C_{54} H_{24} Dy_3 O_{28}
Formula weight	1608.23
Crystal system	Cubic
Space group	*Fm-3m*
***a* (Å)**	30.7854(3)
Volume (Å^3)	29176.6(5)
Z	8
Crystal size (mm^3)	0.16 × 0.14 × 0.12
θ_{max} (°)	68.26
Completeness	99.4%
R_{int}	0.1175
R_1 (I > 2σ(I$_0$))	0.0945
wR_2 (all data)	0.3012

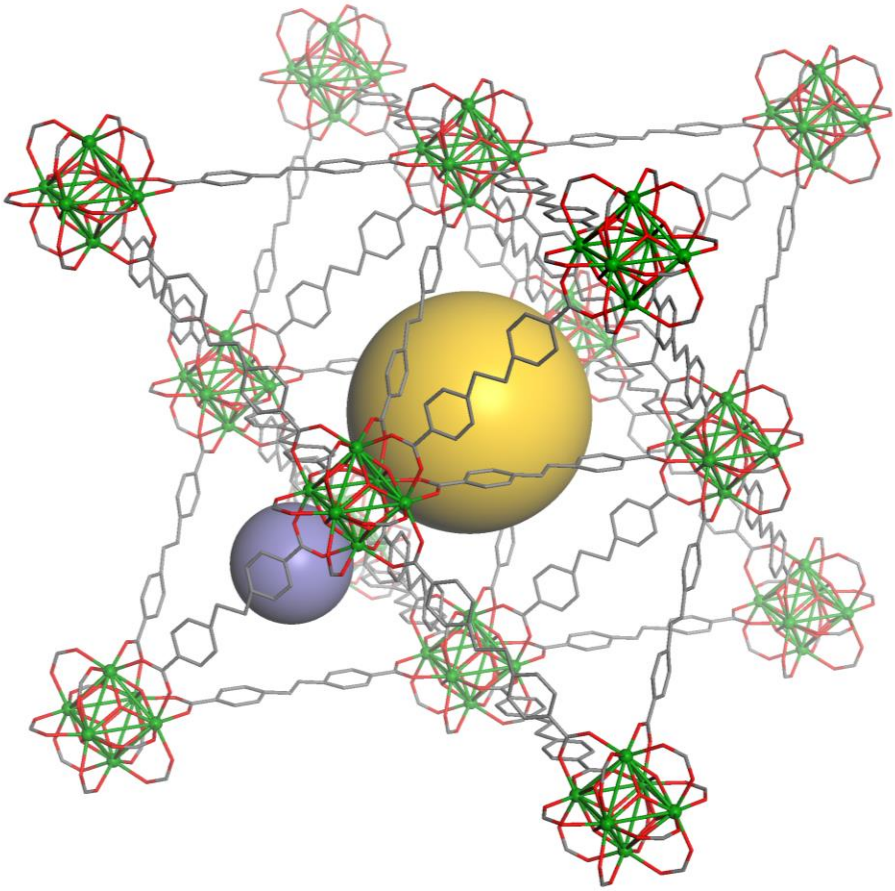

Figure 140. Structural illustration of Dy^{3+}-SBDC *fcu* MOF.*

* Dy: green balls; C: grey sticks; O: red sticks. H atoms are omitted for clarity. Two types of pores are indicated by gold and purple spheres, respectively.

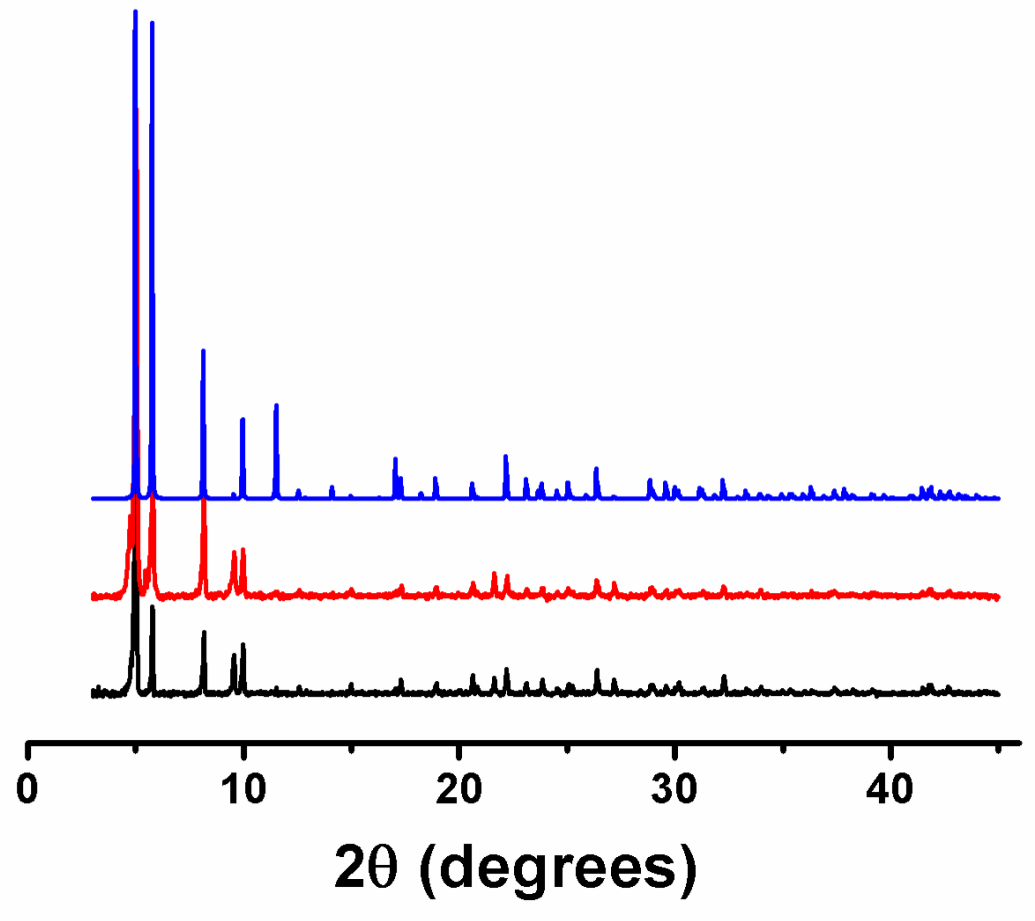

Figure 141. PXRD comparing Dy^{3+}-SBDC, Yb^{3+}-SBDC and simulated patterns.*

* Black: Dy^{3+}-SBDC; red: Yb^{3+}-SBDC; blue: simulated from single crystal X-ray diffraction data of Dy^{3+}-SBDC

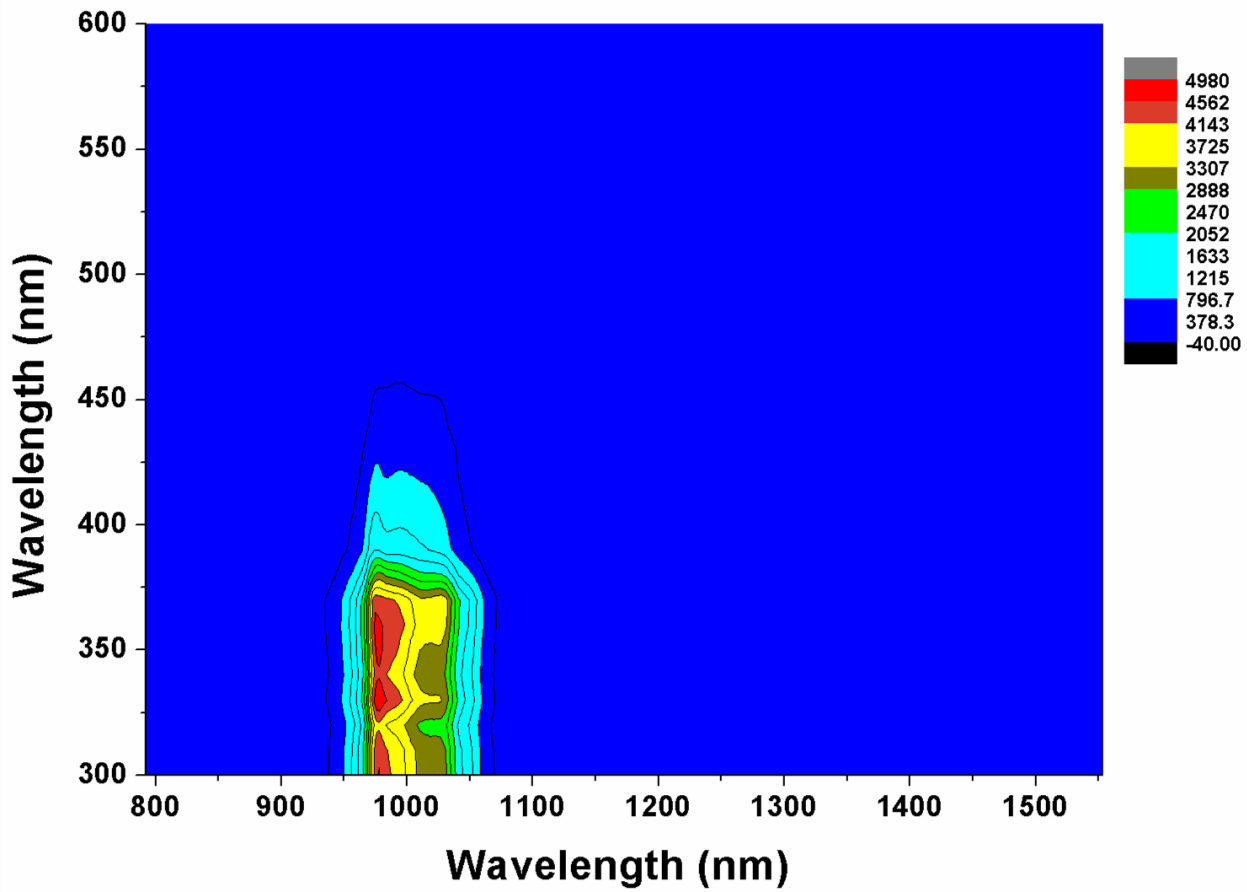

Figure 142. Excitation/emission contour map of Yb^{3+}-SBDC.

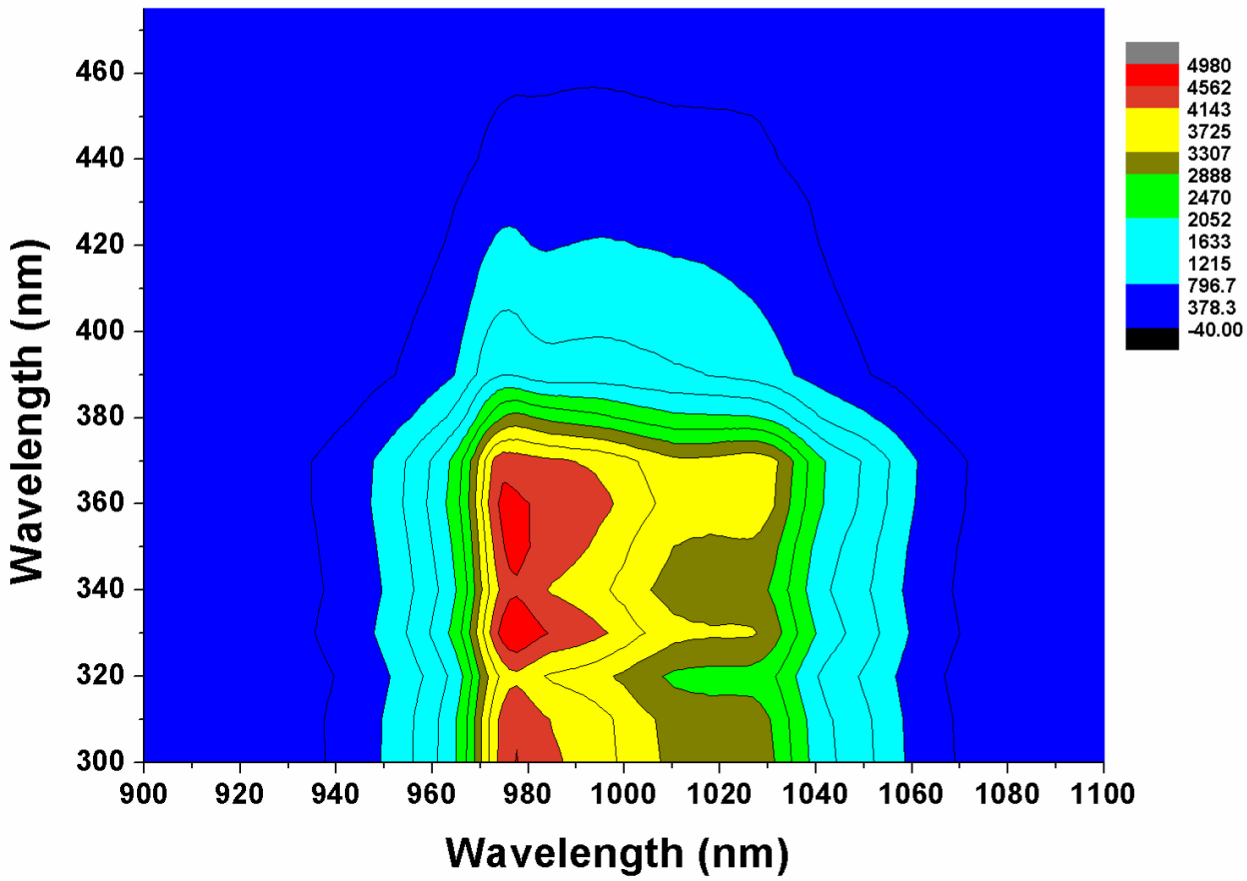

Figure 143. Enlarged excitation/emission contour map of Yb^{3+}-SBDC.

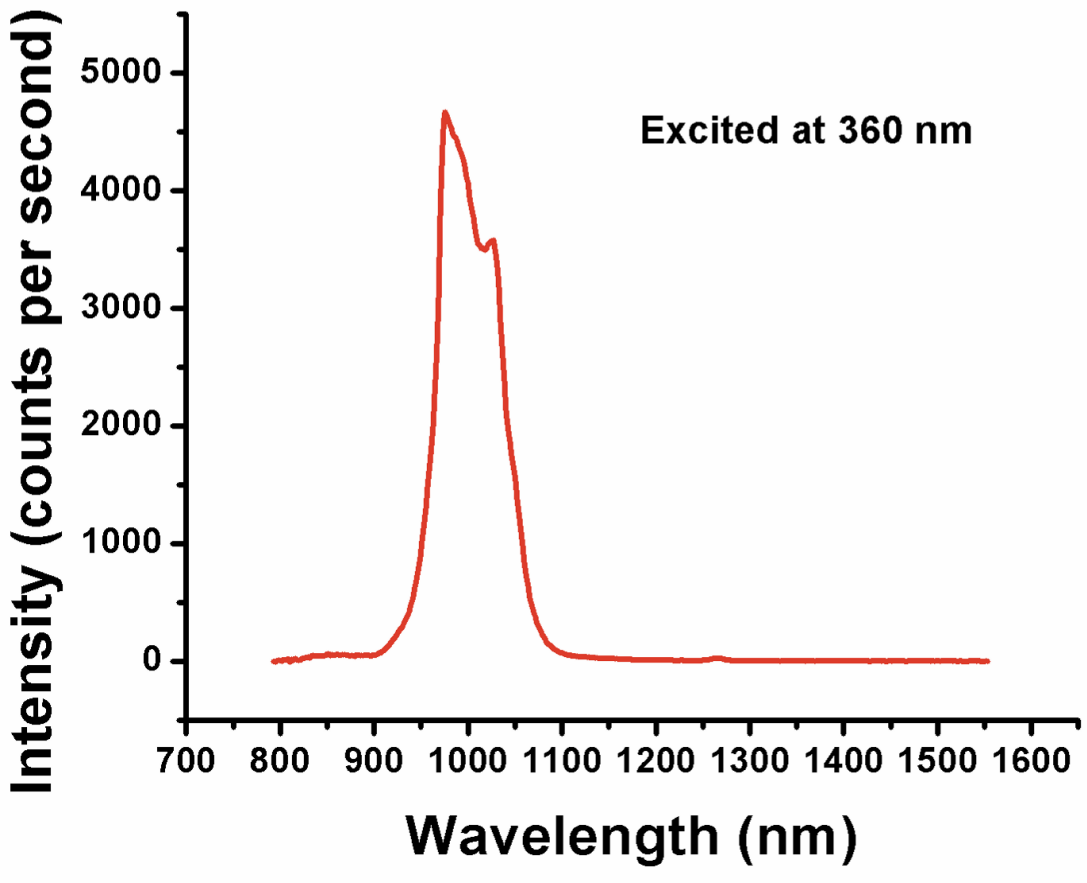

Figure 144. Photoluminescence spectrum of Yb^{3+}-SBDC excited at 360 nm.

5.2.3 Cationic guest incorporation in *fcu* Yb^{3+}-MOFs.

NIR emission of Yb^{3+} was successfully sensitized in isoreticular Yb^{3+}-NDC, Yb^{3+}-BPDC, and Yb^{3+}-SBDC MOFs. In each case, however, the MOFs were excited in the ultraviolet (UV). To realize NIR imaging, the excitation wavelength of the Ln^{3+}-MOF agent should ideally be red-shifted to the low energy visible or into the NIR to prevent tissue damage and for greater depth penetration due to low tissue absorptivity in this region. In order to shift the excitation wavelength, modifications to the MOFs were required. As previously determined, the *fcu* Ln^{3+}-

MOFs are anionic, so cationic guest compounds should be easily introduced into their cavities. Sensitization of NIR Ln^{3+} emission can be accomplished by placing organic dyes in proximity to the Ln^{3+} centers.[196] Therefore, it was proposed that sensitizing dye molecules be introduced into MOF cavities via cation exchange.

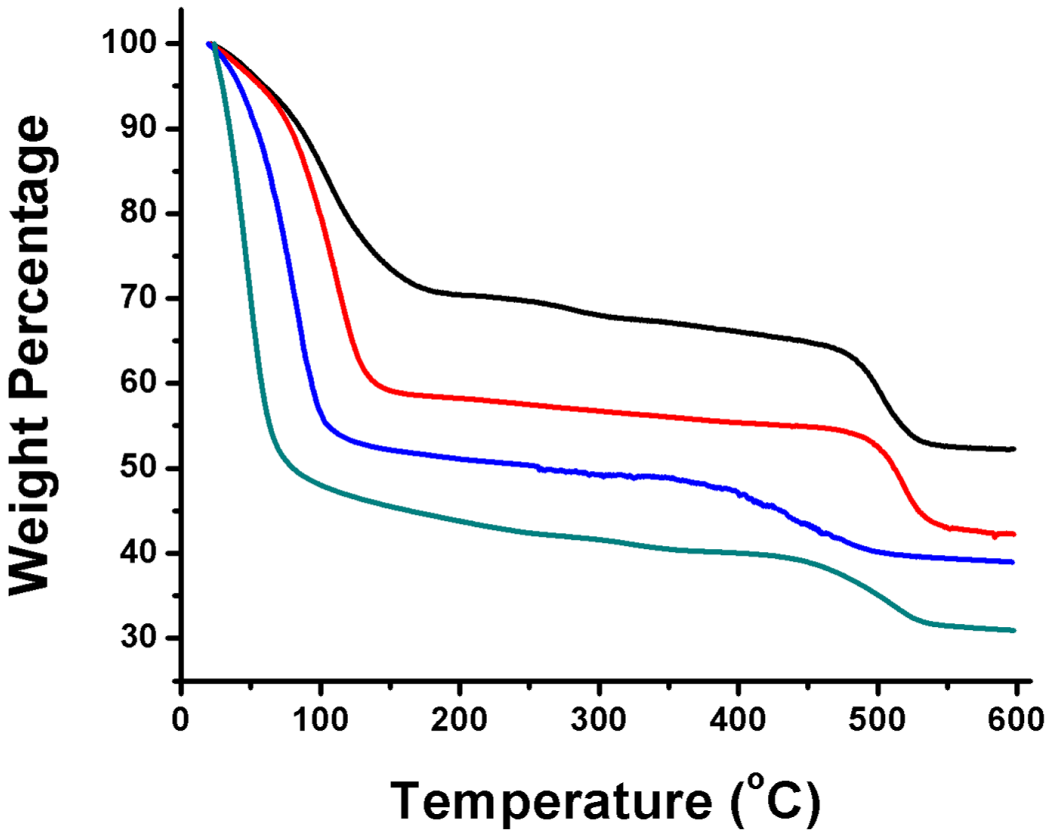

Figure 145. TGA profile of Dy^{3+}-NDC/BPDC/ABDC/SBDC MOFs.*

To assess MOFs' capabilities to accommodate large dye molecules, TGA was first used to study the thermal stability and porosity of these materials (Figure 145). All four isoreticular MOFs had significant porosity, as indicated by the significant loss of entrapped solvent during the TGA measurement. Dy^{3+}-NDC and Dy^{3+}-BPDC MOFs had excellent thermal stability

* Black: Dy^{3+}-NDC; red: Dy^{3+}-BPDC; blue: Dy^{3+}-ABDC; dark cyan: Dy^{3+}-SBDC

exceeding 450 °C. The more porous Dy^{3+}-ABDC and Dy^{3+}-SBDC MOFs were less stable, but the decomposition temperatures were still above 350 °C. The thermal stability of these MOFs was attributed to the highly connected and rigid *fcu* topology (Figure 146). Upon examining the crystal structure, one can identify two types of cavities; the pore apertures are relatively small and triangular in shape. The porosity in different *fcu* MOFs was also estimated in PLATON[197] using the CALC SOLV function.

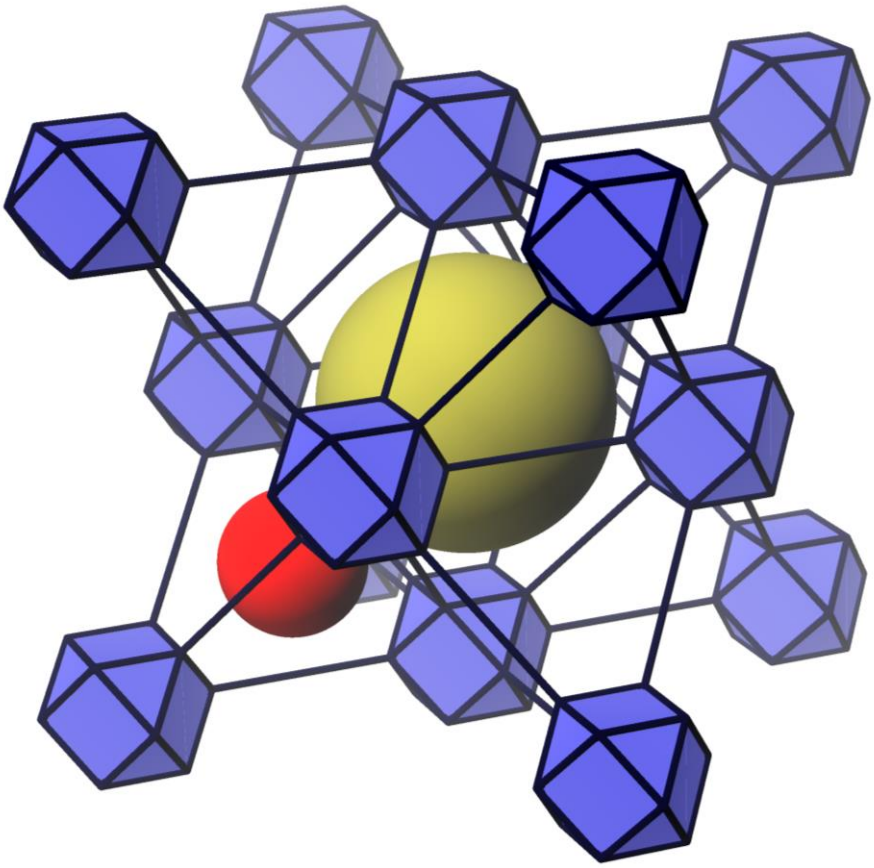

Figure 146. Schematic structure illustration of *fcu* Ln^{3+}-MOFs, featuring two different cavities and uniform triangular apertures.

With the porosity revealed by SC-XRD and TGA and the anionic nature of the framework confirmed by CHN elemental analysis, guest molecules could be incorporated into

MOFs via cation exchange as long as they fit into the internal MOF cavities. Additionally, cationic dye molecules that were known to sensitize Ln^{3+} photoluminescence should be selected as candidates.[198-199] Based on the these criteria, five common dyes, including Rhodamine 590, Rhodamine 610, Rhodamine 640, LDS 698, and LDS 750 were chosen as candidates for cationic exchange into the *fcu* MOFs (Figure 147). Their respective size and geometry were estimated (Experimental Section 5.4.5.1). Treatment of Dy^{3+}-NDC, Dy^{3+}-BPDC and Dy^{3+}-ABDC with identical solutions of each dye compound yielded different loading percentages, as confirmed via ^{1}H NMR (Experimental Section 5.4.5.2; Table 6). As previously shown, the three different *fcu* MOFs have significantly different pore aperture dimensions and porosity, which are responsible for the different dye loading behavior.

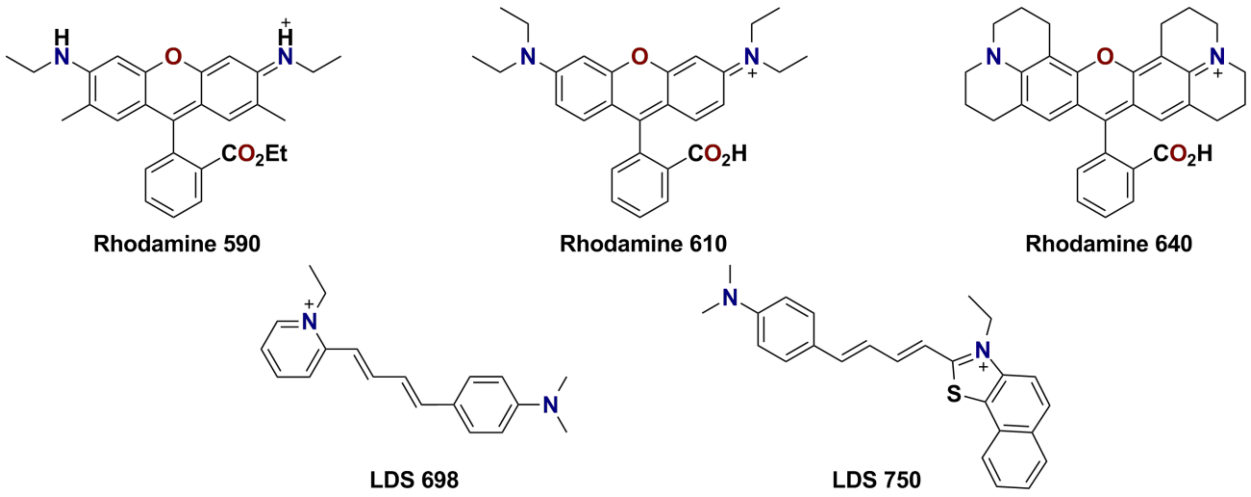

Figure 147. Five dyes to test guest incorporation in isoreticular *fcu* Dy^{3+}-MOFs via cation exchange

Table 6. Loading profile of different dyes in Dy^{3+}-NDC, Dy^{3+}-BPDC, and Dy^{3+}-ABDC.*

MOFs / Dyes	Dy^{3+}-NDC		Dy^{3+}-BPDC		Dy^{3+}-ABDC	
	Ligand : Dye	Efficiency	Ligand : Dye	Efficiency	Ligand : Dye	Efficiency
Rhodamine 590	-	-	1 : 0.087	26.11%	1 : 0.107	32.13%
Rhodamine 610	1 : 0.018	5.45%	1 : 0.062	18.63%	1 : 0.090	27.03%
Rhodamine 640	-	-	1 : 0.030	9.09%	1 : 0.075	22.52%
LDS 698	-	-	1 : 0.019	5.72%	1 : 0.105	31.53%
LDS 750	-	-	1 : 0.031	9.50%	1 : 0.080	24.02%

The BPDC MOF was chosen for continued studies because: i) it showed significant loading capacity for all dyes and ii) the dye loading capacity was expected to be tunable by adjusting dye concentration and cation exchange time. Among all five dyes, LDS 750 compound was chosen for subsequent loading control and spectroscopic studies. LDS 750 was selected because, of the dyes studied, it had one of the lowest energy absorption bands (572 nm). For the Yb^{3+}-BPDC MOF, ^{1}H NMR revealed that LDS 750 loading was tunable based on different dye solution concentrations and soaking time (Figure 148 and Table 7). From these results, it was also clear that the cation exchange process was very rapid.

* The ligand-to-dye ratios were directly observed on the ^{1}H NMR spectra. The loading efficiency percentages were calculated based on the MOFs' formula $M_6(OH)_8L_6(cation)_2$, maximum ligand-to-dye ratio would be 1 : 0.333.

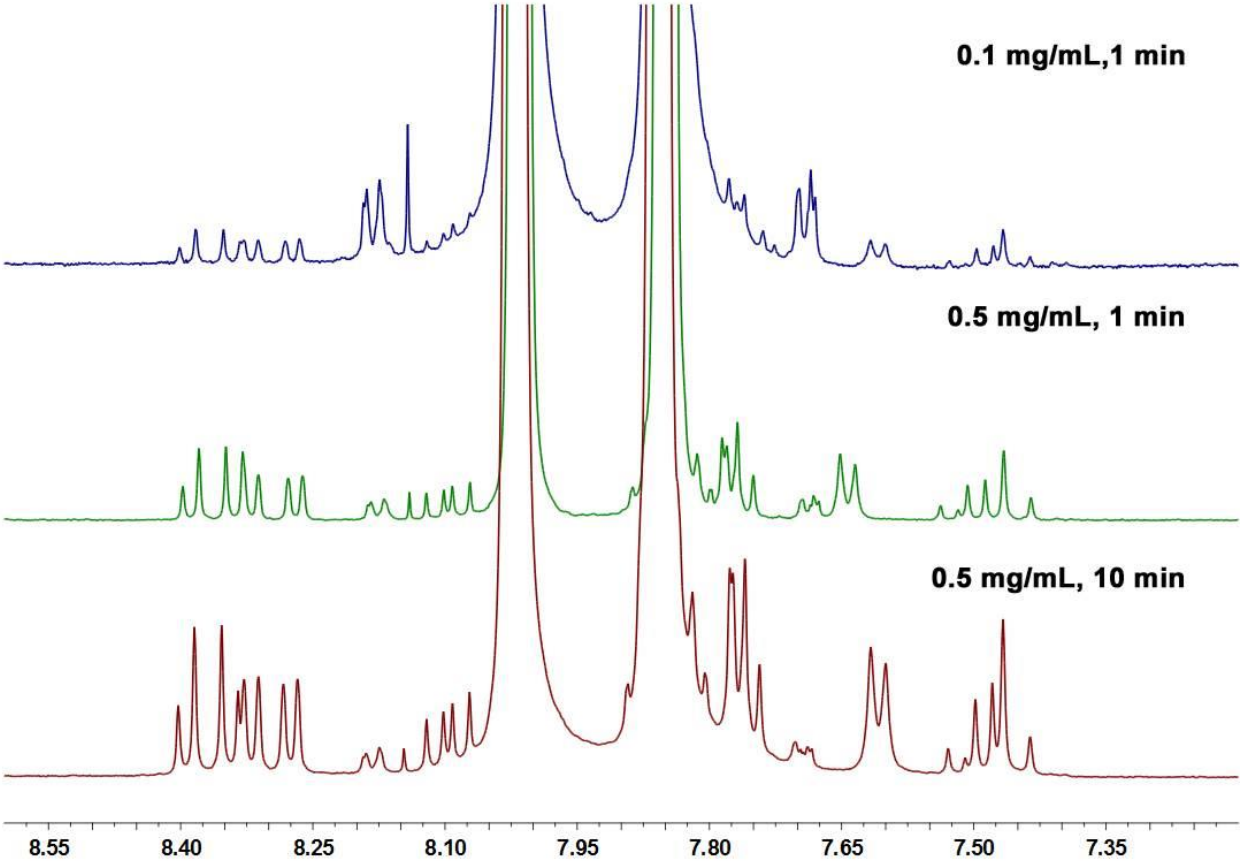

Figure 148. ^{1}H NMR spectra of dissolved Yb^{3+}-BPDC loaded with different amounts of LDS 750.*

* The peaks at the leftmost which correspond to one of the LDS 750 alkenyl groups were used to compare with the highest peak which is from BPDC.

Table 7. Loading profile of LDS 750 in Yb^{3+}-BPDC.*

MOF / Condition	Yb^{3+}-BPDC	
	Ligand : Dye	Efficiency
0.1 mg/mL, 1 min	1 : 0.003	1.02%
0.5 mg/mL, 1 min	1 : 0.03	9.27%
0.5 mg/mL, 10 min	1 : 0.06	18.8%

Yb^{3+}-BPDC loaded with the least amount of LDS 750 was tested for Yb^{3+} sensitization. Successful energy transfer from non-covalently incorporated LDS 750 to Yb^{3+} was observed, as revealed by the excitation spectrum (Figure 149) and photoluminescence spectrum (Figure 150). The excitation wavelength range of the Yb^{3+}-BPDC-LDS 750 composite was much broader (Figure 149). Indeed the Yb^{3+} photoluminesce can now be sensitized at a much longer wavelength, close to the NIR. However, possibly due to low transfer efficiency and high fluorescence efficiency of LDS750, emission of the dye itself was very high. Additionally, the relatively isolated coordinative environment of the Ln^{3+} centers in the *fcu* MOF could prevent association between the dyes and the Ln^{3+} centers, which may contribute to inadequate sensitization.[200] Nonetheless, the successful sensitization of Yb^{3+} indicated that the strategy worked; future studies will focus on optimizing dye loading and the interaction between the Yb^{3+} and the loaded dyes.

* The ligand-to-dye ratios were directly observed on the ^1H NMR spectra. The loading efficiency percentages were calculated based on the MOFs' formula $M_6(OH)_8L_6(cation)_2$, maximum ligand-to-dye ratio would be 1 : 0.333.

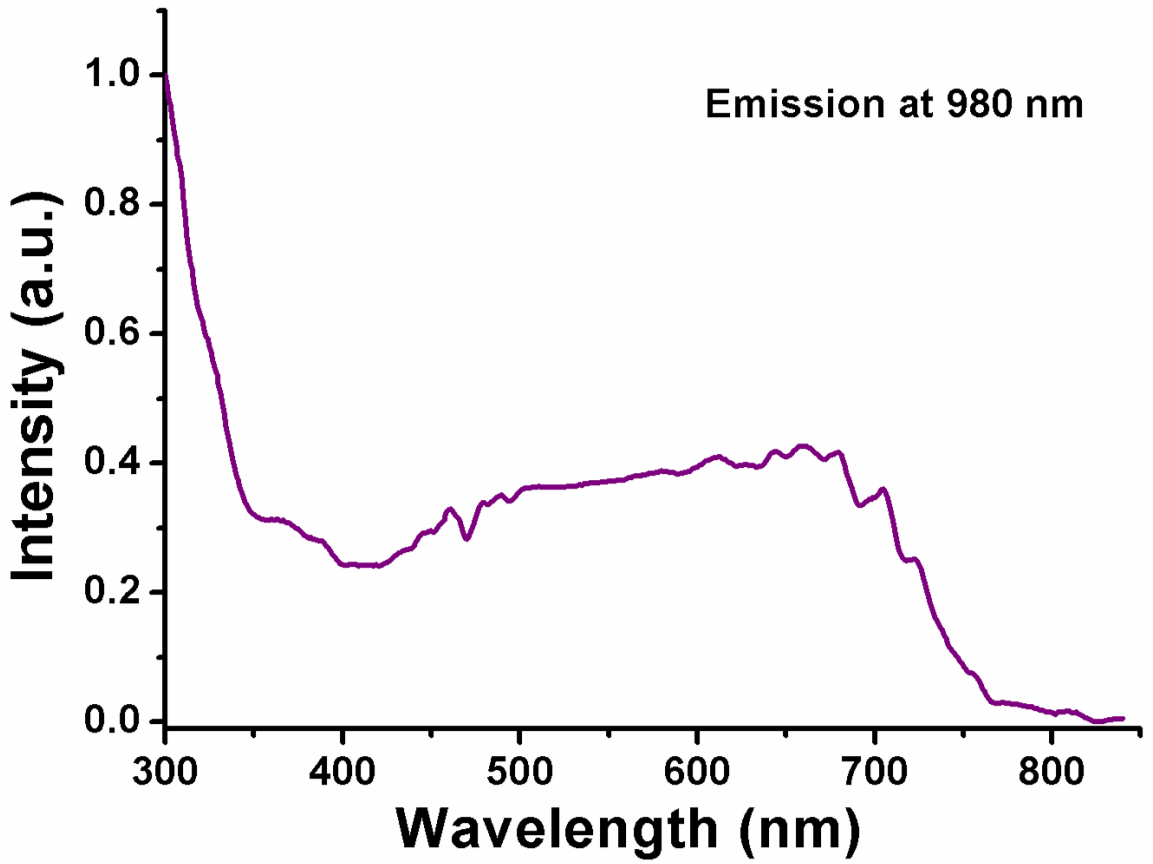

Figure 149. Absorption spectrum of Yb^{3+}-BPDC loaded with LDS 750.

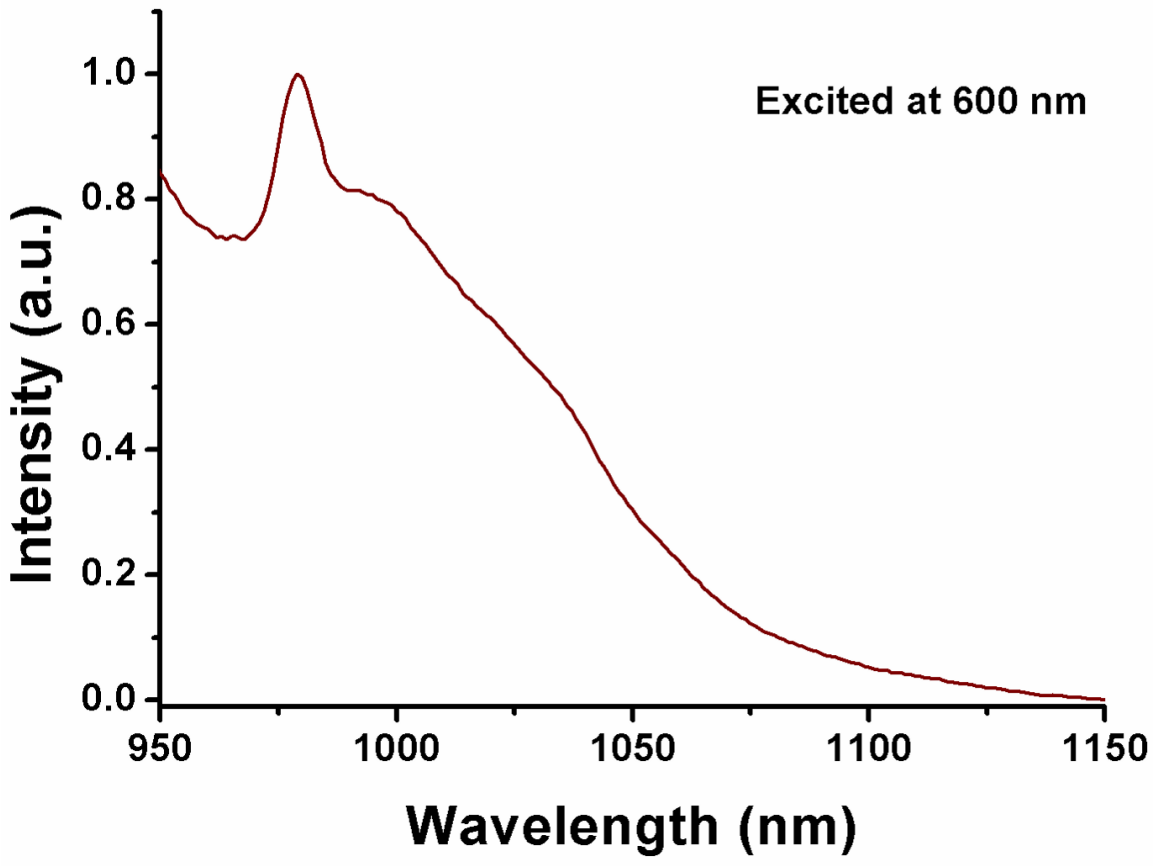

Figure 150. Photoluminescence spectrum of Yb^{3+}-BPDC loaded with LDS 750.

5.3 CONCLUSION

Employing a novel structural directing agent 2,6-difluorobenzoic acid, an isoreticular series of four rare earth MOFs with *fcu* topology were successfully synthesized from commercially available ligands (H_2-NDC, H_2-BPDC, H_2-ABDC, H_2-SBDC). The structures were determined via single crystal X-ray diffraction. The synthetic condition was highly efficient and yielded pure phase products. The versatility of the strategy was demonstrated by successful application to 10 different rare earth metal ions as well as binary or ternary mixtures of different metal ions.

Three of the four MOFs showed excellent antenna effect in sensitizing Yb^{3+} NIR photoluminescence. Due to the anionic nature of the MOFs, cationic dyes were loaded via simple cation exchange procedure. The loading efficiency was dependent on MOF pore size and accessibility as well as dye concentration and exchange time. A non-covalently incorporated LDS 750 dye was able to sensitize Yb^{3+} NIR photoluminescence, greatly expanding the excitation range of the Yb^{3+}-MOF.

5.4 EXPERIMENTAL SECTION

5.4.1 General procedure

All purchased chemicals were used without further purification unless stated otherwise. The term "dry DMF" means DMF dried over pre-activated 4 Å molecular sieves for at least 24 hours prior to use. Single crystal X-ray diffraction experiments were performed on a Bruker X8 Prospector Ultra diffractometer equipped with an Apex II CCD detector and an IμS micro-focus CuKα X-ray source (λ = 1.54178 Å). Samples were mounted using two different methods: i) MOF crystals were loaded into capillary tubes which were then flame sealed before mounting. Data were collected at ambient temperature; ii) MOF crystals were placed onto MiTeGen MicroMesh using Fluorolube and data were collected under cold N_2 stream at specified temperature. SC-XRD data were processed using Bruker APEX II software package. Powder X-ray powder diffraction patterns were collected using a Bruker AXS D8 Discover powder diffractometer at 40 kV, 40 mA for Cu Kα, (λ = 1.5406 Å) with a scan speed of 0.10 sec/step from 3.0 to 45 º at a step size of 0.02 º. The data were analyzed using the EVA program from the Bruker Powder

Analysis Software package. The simulated powder pattern was calculated using Materials Studio from single crystal data of corresponding Dy^{3+}-MOFs. ^{1}H NMR spectra were obtained using a Bruker Avance III 500 MHz spectrometers. Chemical shifts are in parts per million using the residual solvent peak (DMSO-d_6) as the reference value. SEM/EDX experiments were performed on a Philips XL 30 scanning electron microscope (SEM) with EDX capability. Double-sided adhesive carbon tape on a SEM specimen mount was used to hold the sample crystals. SEM images of the sample were then taken under SE mode with 10 mm working distance and 10 kV beam. EDX was performed on the same SEM with an EDAX CDU leap detector with 10 mm working distance and under 15 kV beam. Light microscopic images of crystals were collected using an Olympus BH-2 microscope. Thermogravimetric analyses (TGA) were performed using a TGA Q500 thermal analysis system. All TGA experiments were performed under a N_2 atmosphere from about 20 °C to 600 °C at a rate of 5 °C /min. Data were analyzed using the TA Universal Analysis software package. The CHN elemental analyses (EA) were performed by the University of Illinois, Department of Chemistry Microanalysis Laboratory using an Exeter Analytical CE440. The Yb^{3+}-MOFs' photoluminescence properties were measured using a Horiba Jobin-Yvon NanoLog spectrofluorometer with a 450 W xenon source and a Symphony II InGaAs array detector. Excitation gratings were blazed at 330 nm with 1200 grooves/mm and emission gratings were blazed at 780 nm with 100 grooves/mm. All spectra were corrected for gratings, lamp, and detector response. An integration sphere utilizing quartz tubes as sample holders was used. The MOF crystals under dry DMF were loaded into quartz tubes before being placed in the center of the integration sphere. For the excitation/emission contour maps, the excitation measurements range from 300 nm to 600 nm, the emission measurements range from 800 nm to 1550 nm, both with 10 nm slit widths, 7 s integration times, in 10 nm increments.

Emission, excitation spectra for the LDS 750-incorporated Yb^{3+}-BPDC MOF were performed in the integration sphere using samples (solids under DMF) placed into quartz tubes on the FluoroLog 3 spectrofluorimeter (Horiba Scientific) equipped with a visible photomultiplier tube (PMT) (220-800 nm, R928P; Hamamatsu), and a NIR PMT (950-1650 nm, H10330-75; Hamamatsu). All spectra were corrected for the instrumental functions. Emission signal was selected using iHR-320 monochromator, detected using NIR PMT, fed into a 500 MHz bandpass digital oscilloscope (TDS 754C; Tektronix), transferred to a PC where the data were processed with the Origin 8® program.

5.4.2 Solvothermal syntheses of *fcu* MOFs

The protocols in the following sub-sections to synthesize corresponding MOFs were optimized to balance crystal size, yield, quality and time. Generally, 40 equivalents of the structural directing agent (DFBA) was used. When less DFBA was used, the product crystallized more quickly, however with impurities of other unidentified MOFs; when more DFBA was used, the product crystallized more slowly, with increased sizes. When the reaction mixture was heated at 120 ^{o}C for too long, crystals that initially formed would "deteriorate" which can be easily observed under light microscope. DMF was the sole solvent for NDC and BPDC MOFs. A mixture of DMF/DMA (DMA = *N*,*N*-dimethylacetamide) was used for synthesizing ABDC and SBDC MOFs, different ratios of the two solvents were tested. Generally more DMA would yield larger crystals in less amounts (slower crystallization). When other salts (such as $M(NO_3)_3 \cdot xH_2O$, $M(OAc)_3 \cdot xH_2O$) were attempted under the same condition to replace $MCl_3 \cdot 6H_2O$, in the presence of DFBA, they did not yield pure phase *fcu* MOFs, but the preparation involving those salts was not fully optimized.

5.4.2.1 Synthesis of rare earth-NDC MOFs

Clear stock solutions of H_2-NDC (0.05 M) and $MCl_3 \cdot 6H_2O$ (0.1 M, M = Y^{3+}, Eu^{3+}, Gd^{3+}, Tb^{3+}, Dy^{3+}, Ho^{3+}, Er^{3+}, Tm^{3+}, Yb^{3+}, Lu^{3+}) were made by dissolving corresponding compounds in DMF with the aid of ultrasonication. In a 20-mL glass vial, H_2-NDC (0.05 M, 4 mL, 2×10^{-4} mol), $MCl_3 \cdot 6H_2O$ (0.1 M, 1 mL, 1×10^{-4} mol), and DFBA (632 mg, 4×10^{-3} mol) were mixed and briefly sonicated to dissolve DFBA. The vial was tightly capped and heated in a 120 ^oC isothermal oven for 24 hours. After cooling to room temperature, the crystals were collected and washed with dry DMF via centrifugation, hereafter denoted as "as-synthesized" MOFs.

5.4.2.2 Synthesis of rare earth-BPDC MOFs

Clear stock solutions of $MCl_3 \cdot 6H_2O$ (0.1 M, M = Y^{3+}, Eu^{3+}, Gd^{3+}, Tb^{3+}, Dy^{3+}, Ho^{3+}, Er^{3+}, Tm^{3+}, Yb^{3+}, Lu^{3+}) were made by dissolving corresponding compounds in DMF with the aid of ultrasonication. Stock suspension of H_2-BPDC (0.05 M) was made by mixing the ligand with DMF and sonicated for 5 min. In a 20-mL glass vial, H_2-BPDC (0.05 M, 4 mL, 2×10^{-4} mol), $MCl_3 \cdot 6H_2O$ (0.1 M, 0.5 mL, 5×10^{-5} mol), and DFBA (316 mg, 2×10^{-3} mol) were mixed and briefly sonicated to dissolve DFBA. The vial was tightly capped and heated in a 120 ^oC isothermal oven for 24 hours. After cooling to room temperature, the crystals were collected and washed with dry DMF via centrifugation, hereafter denoted as "as-synthesized" MOFs.

5.4.2.3 Synthesis of rare earth-ABDC MOFs

Clear stock solutions of $MCl_3 \cdot 6H_2O$ (0.1 M, M = Y^{3+}, Eu^{3+}, Gd^{3+}, Tb^{3+}, Dy^{3+}, Ho^{3+}, Er^{3+}, Tm^{3+}, Yb^{3+}, Lu^{3+}) were made by dissolving corresponding compounds in a mixture of DMA and DMF (v/v = 4:1) with the aid of ultrasonication. Stock suspension of H_2-ABDC (0.05 M) was made by adding the ligand into a mixture of DMA and DMF (v/v = 4:1) and sonicated for 5 min.

In a 20-mL glass vial, H_2-ABDC (0.05 M, 6 mL, 3×10^{-4} mol), $MCl_3\cdot6H_2O$ (0.1 M, 0.5 mL, 5×10^{-5} mol), and DFBA (316 mg, 2×10^{-3} mol) were mixed and briefly sonicated to dissolve DFBA. The vial was tightly capped and heated in a 120 °C isothermal oven for 48 hours. After cooling to room temperature, the crystals were collected and washed with dry DMF via centrifugation, hereafter denoted as "as-synthesized" MOFs.

5.4.2.4 Synthesis of rare earth-SBDC MOFs

Clear stock solutions of $MCl_3\cdot6H_2O$ (0.1 M, M = Dy^{3+}, Yb^{3+}) were made by dissolving corresponding compounds in a mixture of DMA and DMF (v/v = 1:1) with the aid of ultrasonication. Stock suspension of H_2-SBDC (0.05 M) was made by adding the ligand into a mixture of DMA and DMF (v/v = 1:1) and sonicated for 5 min. In a 20-mL glass vial, H_2-SBDC (0.05 M, 6 mL, 3×10^{-4} mol), $MCl_3\cdot6H_2O$ (0.1 M, 0.5 mL, 5×10^{-5} mol), and DFBA (316 mg, 2×10^{-3} mol) were mixed and briefly sonicated to dissolve DFBA. The vial was tightly capped and heated in a 120 °C isothermal oven for 48 to 72 hours. After cooling to room temperature, the crystals were collected and washed with dry DMF via centrifugation, hereafter denoted as "as-synthesized" MOFs.

5.4.2.5 Synthesis of mixed rare earth-NDC MOFs

Clear stock solutions of H_2-NDC (0.05 M) and $MCl_3\cdot6H_2O$ (0.1 M, M = Y^{3+}, Eu^{3+}, Gd^{3+}, Tb^{3+}, Ho^{3+}, Tm^{3+}) were made by dissolving corresponding compounds in DMF with the aid of ultrasonication. In a 20-mL glass vial, H_2-NDC (0.05 M, 4 mL, 2×10^{-4} mol), $MCl_3\cdot6H_2O$ (0.1 M, Eu/Tb 0.5 mL/0.5 mL or Tb/Ho 0.5 mL/0.5 mL or Y/Gd/Tm 0.333 mL/0.333 mL/0.333 mL, total 1×10^{-4} mol), and DFBA (632 mg, 4×10^{-3} mol) were mixed and briefly sonicated to dissolve DFBA. The vial was tightly capped and heated in a 120 °C isothermal oven for 24 hours. After

cooling to room temperature, the crystals were collected and washed with dry DMF via centrifugation.

5.4.3 Characterization of *fcu* MOFs

5.4.3.1 XRD of *fcu* MOFs

The as-synthesized MOFs were washed with dry DMF, then screened under light microscope for single-crystal X-ray diffraction experiments. ORTEP diagrams for the asymmetric units of all 4 MOFs are shown in Figure 151 to Figure 154. Detailed experimental information, structural solution and refinement, crystallographic tables are listed as appendices. For PXRD, the as-synthesized MOFs were washed with dry DMF (3X), soaked at 75 ^{o}C for 10 min, washed with dry DMF (3X), soaked at 75 ^{o}C for another 10 min, washed and stored under dry DMF. PXRD experiments were run on wet crystals which were placed on glass slides with excess DMF removed. Based on the SC-XRD data, PLATON (CALC SOLV function) was used to estimate the porosity of each MOF, in which voxels more than 1.2 Å away from the frameworks were summed up. The solvent-accessible void percentages were determined to be 62.9%, 64.1%, 75.3%, and 67.2% for Dy^{3+}-NDC, Dy^{3+}-BPDC, Dy^{3+}-ABDC, Dy^{3+}-SBDC, respectively.

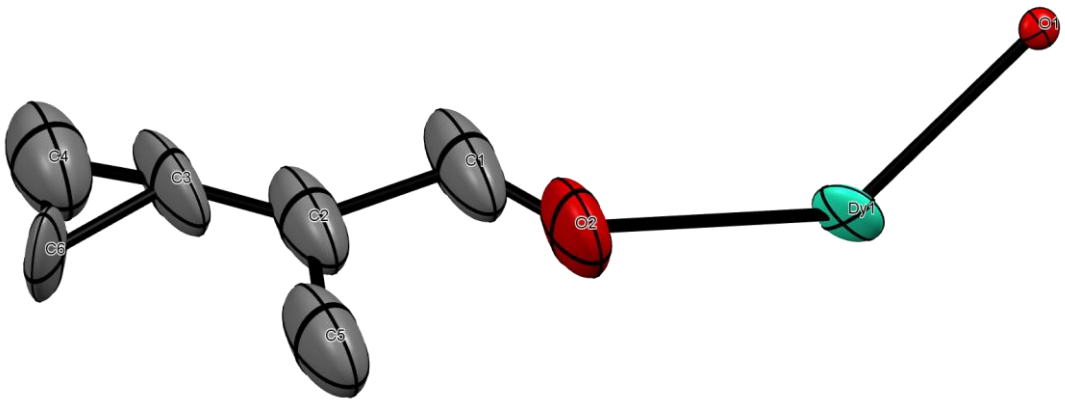

Figure 151. ORTEP diagram of the asymmetric unit of Dy^{3+}-NDC (50% probability factor for the thermal ellipsoids), generated via Mercury 3.6.

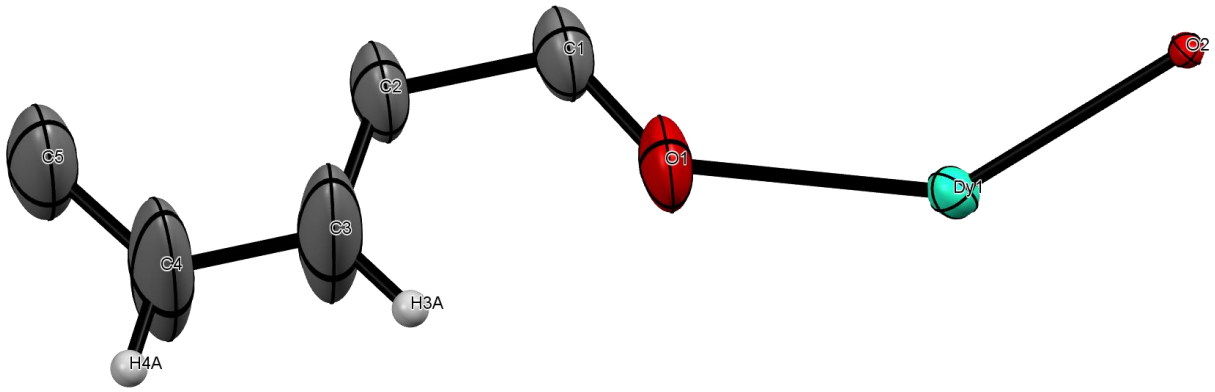

Figure 152. ORTEP diagram of the asymmetric unit of Dy^{3+}-BPDC (50% probability factor for the thermal ellipsoids), generated via Mercury 3.6.

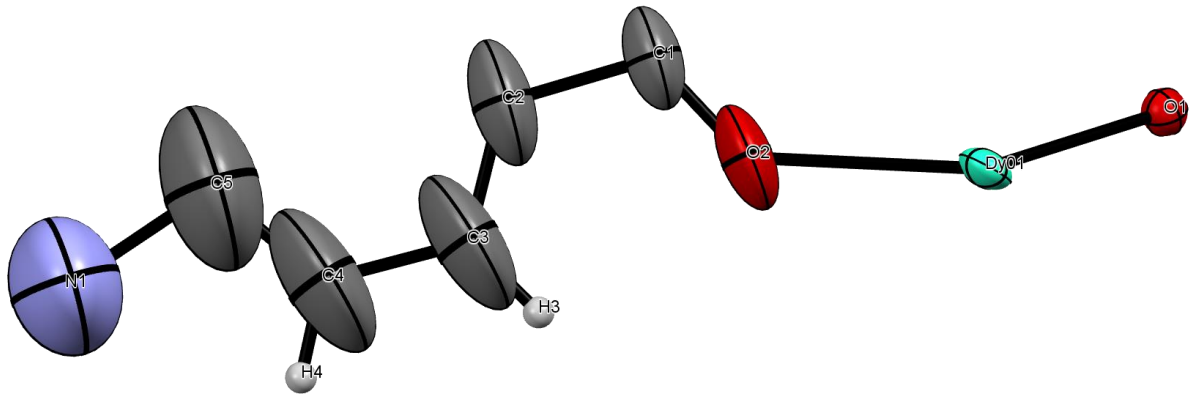

Figure 153. ORTEP diagram of the asymmetric unit of Dy^{3+}-ABDC (50% probability factor for the thermal ellipsoids), generated via Mercury 3.6.

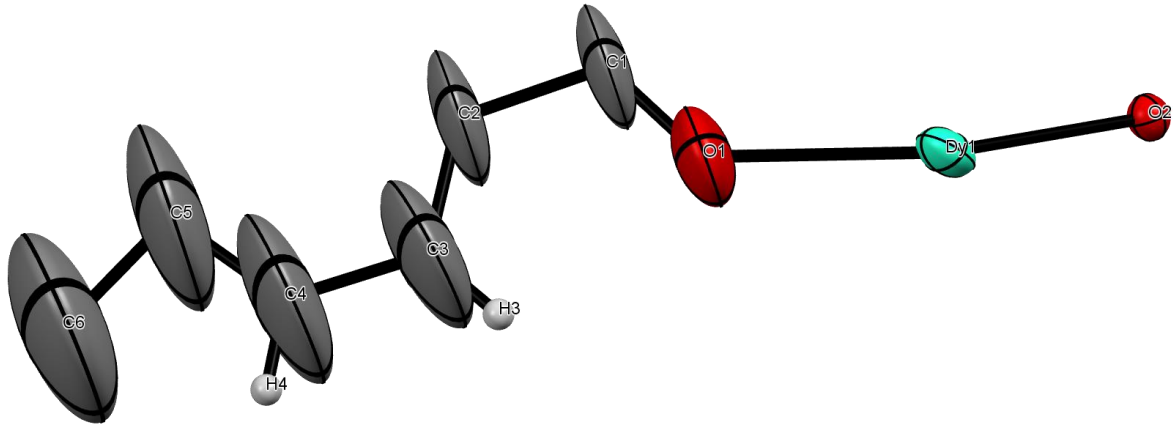

Figure 154. ORTEP diagram of the asymmetric unit of Dy^{3+}-SBDC (50% probability factor for the thermal ellipsoids), generated via Mercury 3.6.

5.4.3.2 ^{1}H NMR of *fcu* MOFs

MOF crystals were washed with dry DMF as previously described in 5.4.3.1, and washed with DCM (3X), soaked in DCM at room temperature for 1 hour, washed again with DCM (3X), and dried with Ar flow. Dried MOF samples were dissolved in DMSO-d_6 (0.7 mL) and DCl in D_2O (37%, 0.01 mL) for ^{1}H NMR. As shown in Figure 155, the product MOFs are free of DFBA.

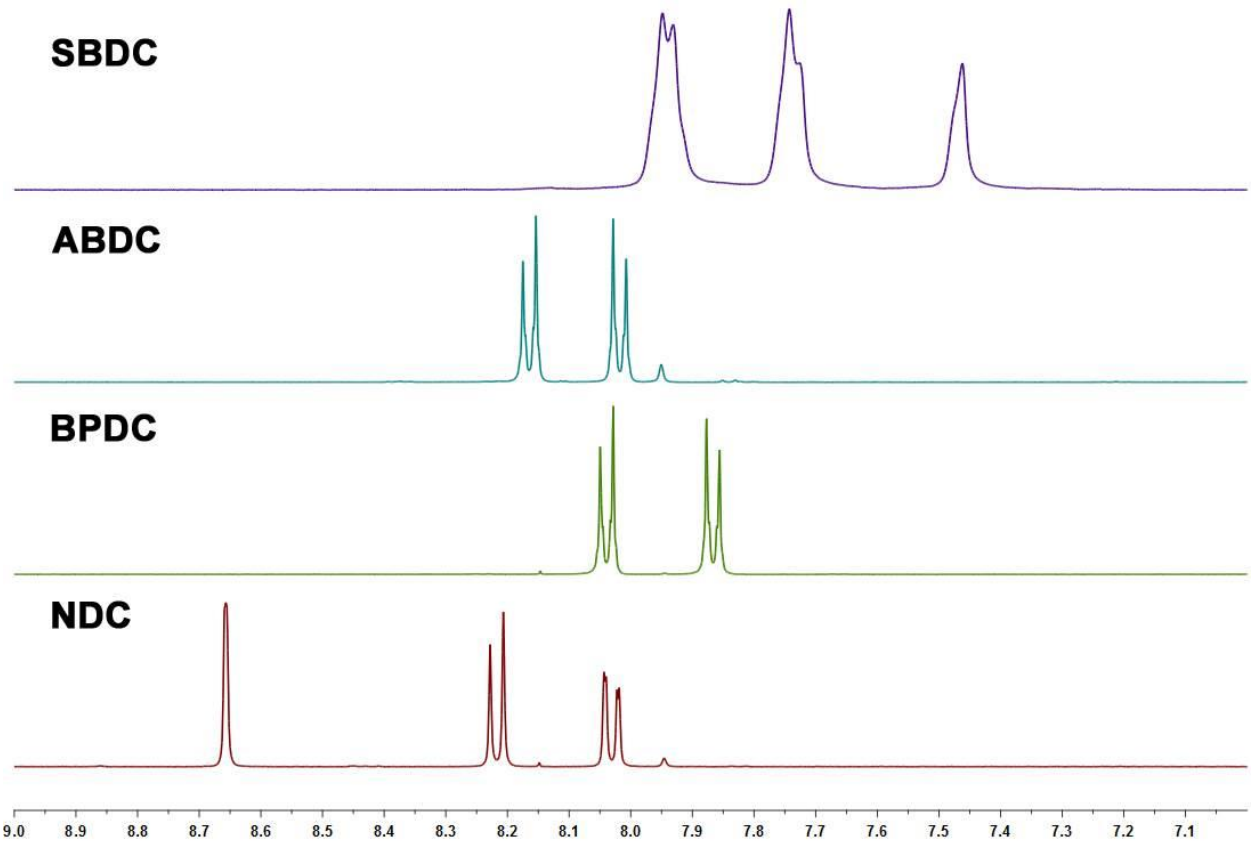

Figure 155. ^{1}H NMR spectra of dissolved Dy^{3+}-NDC, Dy^{3+}-BPDC, Dy^{3+}-ABDC, and Dy^{3+}-SBDC.

5.4.3.3 CHN elemental analysis of *fcu* MOFs

MOF crystals were washed with dry DMF as previously described in 5.4.3.1, and dried with Ar flow until they became free-flowing solids. The CHN elemental analysis (EA) results for 4 *fcu* MOFs are listed here. Dy^{3+}-NDC, EA calculated % for $Dy_6(OH)_8(C_{12}H_6O_4)_6(C_2H_8N)_2 \cdot (DMF)_{10}(H_2O)_6$: C, 38.26; H, 4.3; N, 5.05. Found (%): C, 37.68; H, 3.8; N, 5.79. Dy^{3+}-BPDC, EA calculated % for $Dy_6(OH)_8(C_{14}H_8O_4)_6(C_2H_8N)_2 \cdot (DMF)_{18}(H_2O)_1$: C, 42.83; H, 5.06; N, 7.03. Found (%): C, 46.05; H, 4.64; N, 6.36. Dy^{3+}-ABDC, EA calculated % for $Dy_6(OH)_8(C_{14}H_8N_2O_4)_6(C_2H_8N)_2 \cdot (DMF)_{18}(H_2O)_{10}$: C, 39.59; H, 5.1; N, 10.4. Found (%): C, 38.48; H, 5.00; N, 11.2. Dy^{3+}-SBDC, EA calculated % for $Dy_6(OH)_8(C_{16}H_{10}O_4)_6(C_2H_8N)_2 \cdot (DMF)_{18}(H_2O)_4$: C, 44.15; H, 5.25; N, 6.69. Found (%): C, 39.52; H, 4.65; N, 7.24.

5.4.3.4 SEM/EDX of *fcu* NDC MOFs

The as-synthesized MOFs were washed with dry DMF and DCM as previously described in 5.4.3.1 and 5.4.3.2 to obtain dry powders. The powders were placed on double-sided adhesive carbon tapes (without Pd deposition) for imaging and EDX analysis.

5.4.3.5 TGA of *fcu* MOFs

The as-synthesized MOF crystals were washed with dry DMF as previously described in 5.4.3.1, and dried with Ar flow until they became free-flowing solids, then loaded into a tared Pt pan for TGA.

5.4.4 Photoluminescence study of Yb^{3+}-MOFs

The as-synthesized MOF crystals were washed with dry DMF as previously described in 5.4.3.1 and kept under dry DMF. Approximately 5 mg of the MOF samples were loaded into quartz tubes for photoluminescence measurements. Dry DMF was used as reference.

5.4.5 Cation exchange with dyes

5.4.5.1 Size estimation of the dyes

Models of the 5 dye compounds were created in ChemBio3D Ultra 11.0 and imported into Scigress as c3xml files. Geometry optimization was done using B88LYP DFT functional and DGauss double zeta double valence polarization (DZVP) basis set. Then, the molecule was fitted into an orthorhombic box, with consideration of the atoms' van der Waals radii. The dimensions of the orthorhombic box were used to estimate the molecules' sizes (Figure 156).

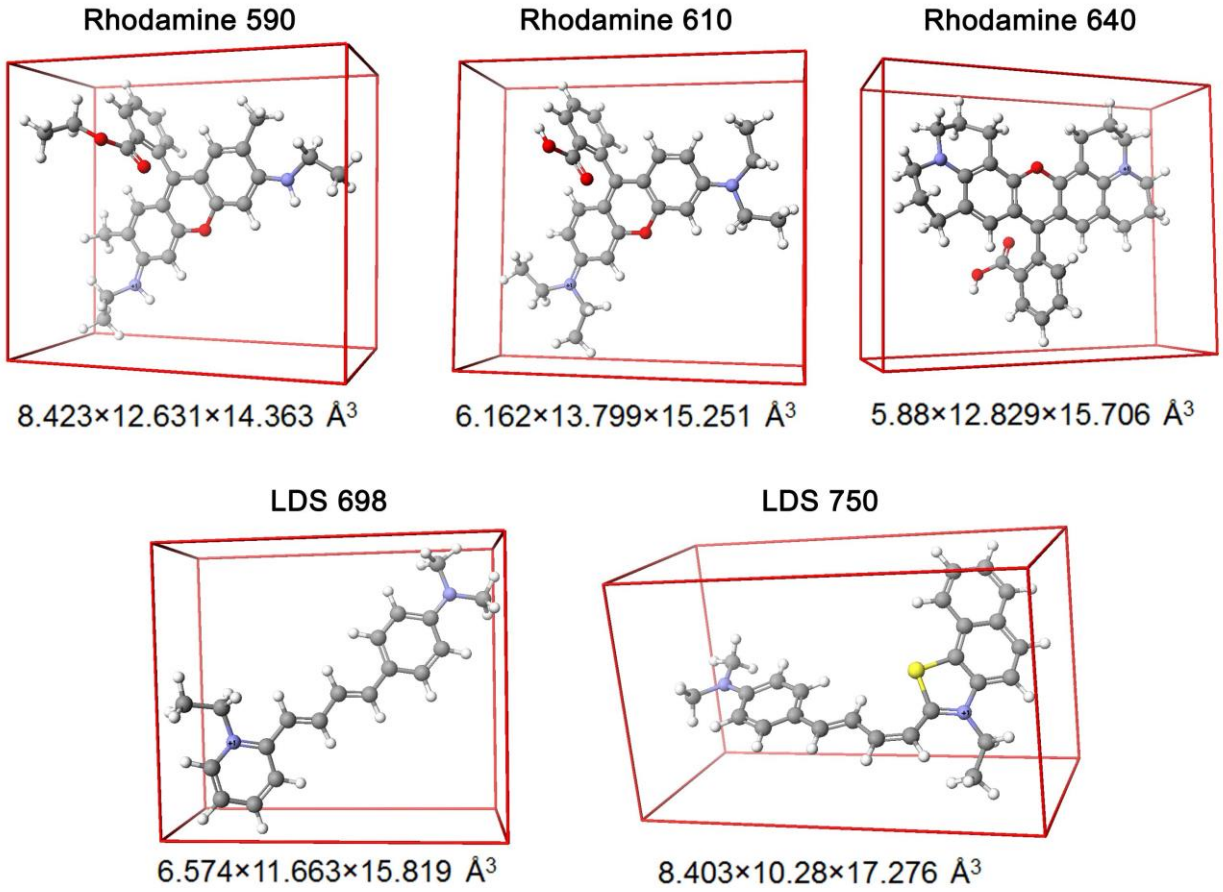

Figure 156. Size estimation of dye compounds.

5.4.5.2 Cation exchange dye incorporation and ^{1}H NMR analysis

The as-synthesized MOF crystals were washed with dry DMF as previously described in 5.4.3.1, then washed with DMSO (3X, pre-dried over 4Å molecular sieves), soaked in DMSO for 1 hour, washed again with DMSO (3X) and kept under DMSO. Dye compounds were dissolved in DMSO with the aid of ultrasonication to achieve pre-determined concentrations. For Dy^{3+}-MOF incorporation, approximately 5 mg of DMSO-exchanged MOF crystals were mixed with corresponding dye/DMSO solutions (0.5 mL, 10 mg/mL) and soaked at room temperature for 24 hours. The MOF crystals were then separated from the dye solutions via centrifugation and copiously washed with DMSO until the supernatant appeared colorless. As shown in Figure 171,

at this point the MOFs appeared to be loaded with dyes. The MOFs were then washed with DCM (5X), soaked in DCM for 1 hour, washed again with DCM (5X) and dried with Ar flow. The dried MOF samples were dissolved in DMSO-d_6 (0.7 mL) and DCl in D_2O (37%, 0.012 mL) for ^1H NMR. For comparison, pure dye compounds were also acidified and dissolved in DMSO-d_6 (0.7 mL) and DCl in D_2O (37%, 0.024 mL) for ^1H NMR. ^1H NMR spectra are shown from Figure 157 to Figure 170. Specifically, ^1H NMR spectra for Dy^{3+}-NDC treated with various dyes are shown in Figure 157, to identify the additional peaks on the spectra, comparison with pure LDS 698 is shown in Figure 158. Similarly, ^1H NMR spectra for Dy^{3+}-BPDC after dye exchange reactions are shown in Figure 159. And a comparison of different Dy^{3+}-BPDC-dye samples with corresponding pure dye molecules is shown in Figure 160 to Figure 164. ^1H NMR spectra for various Dy^{3+}-ABDC-dye samples are shown in Figure 165, and Figure 166 to Figure 170 can be used to help identify the presence and abundance of the dyes.

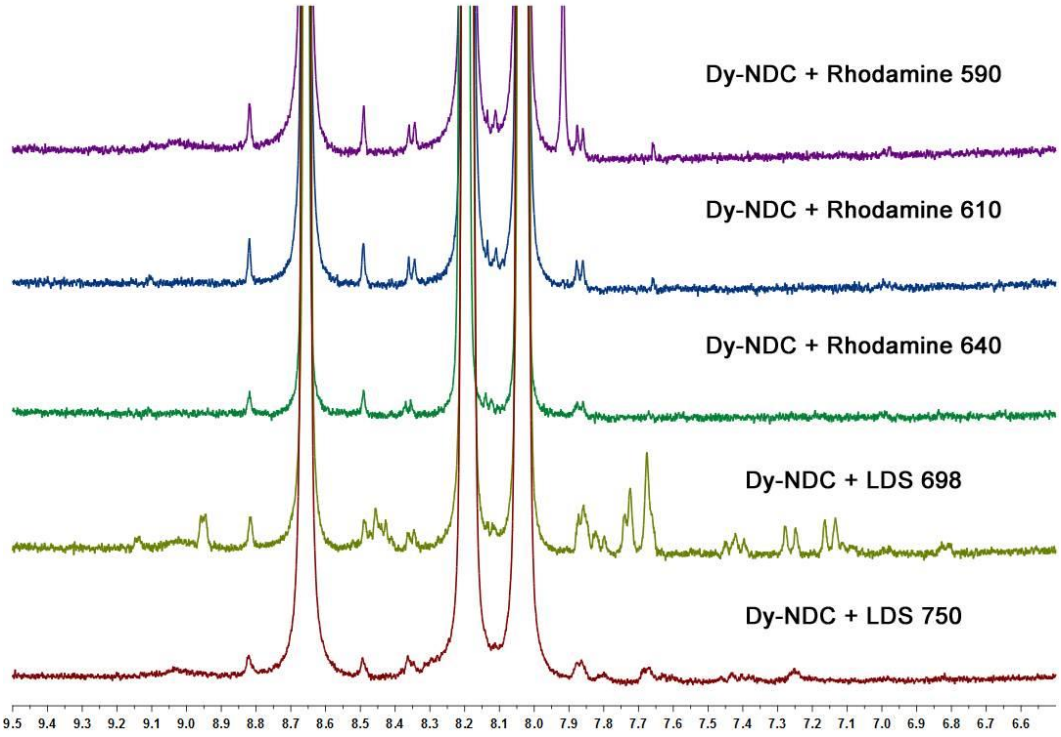

Figure 157. ^1H NMR spectra of dissolved Dy^{3+}-NDC after treatments of various dyes.

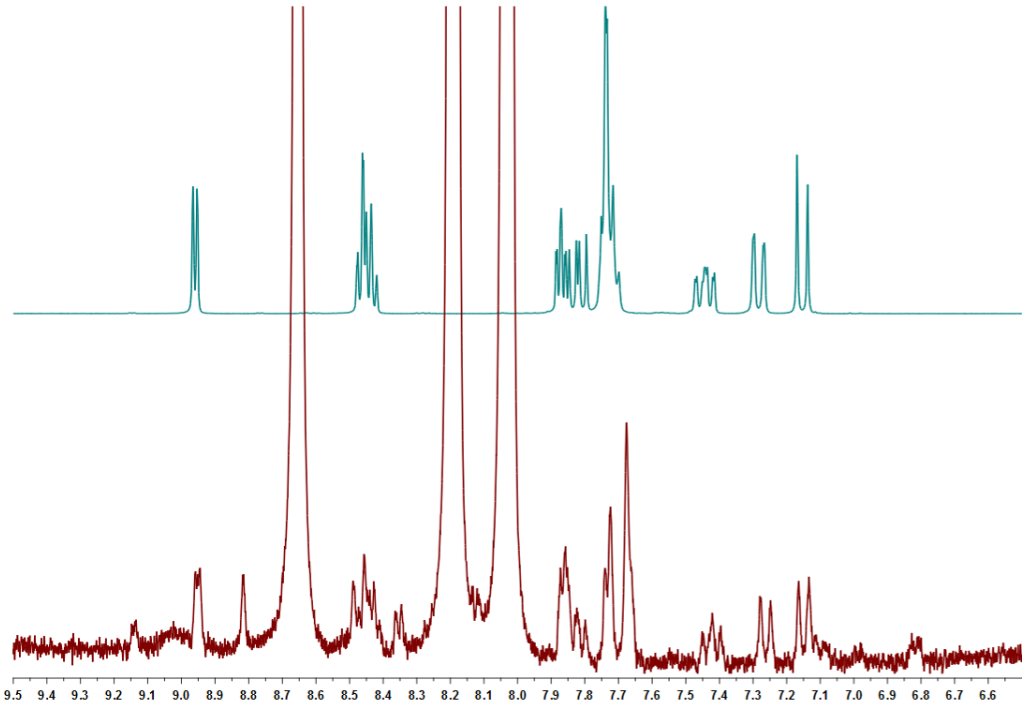

Figure 158. ^{1}H NMR spectra of LDS 698 (top) and Dy^{3+}-NDC + LDS 698 (bottom).

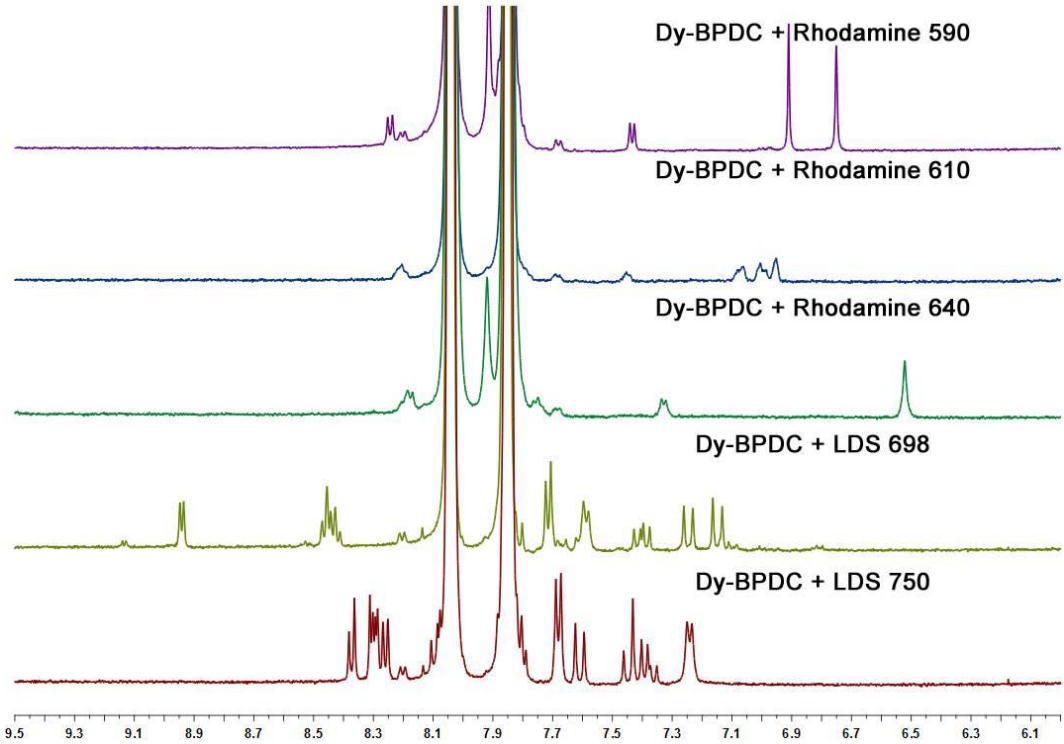

Figure 159. ^{1}H NMR spectra of dissolved Dy^{3+}-BPDC after treatments of various dyes.

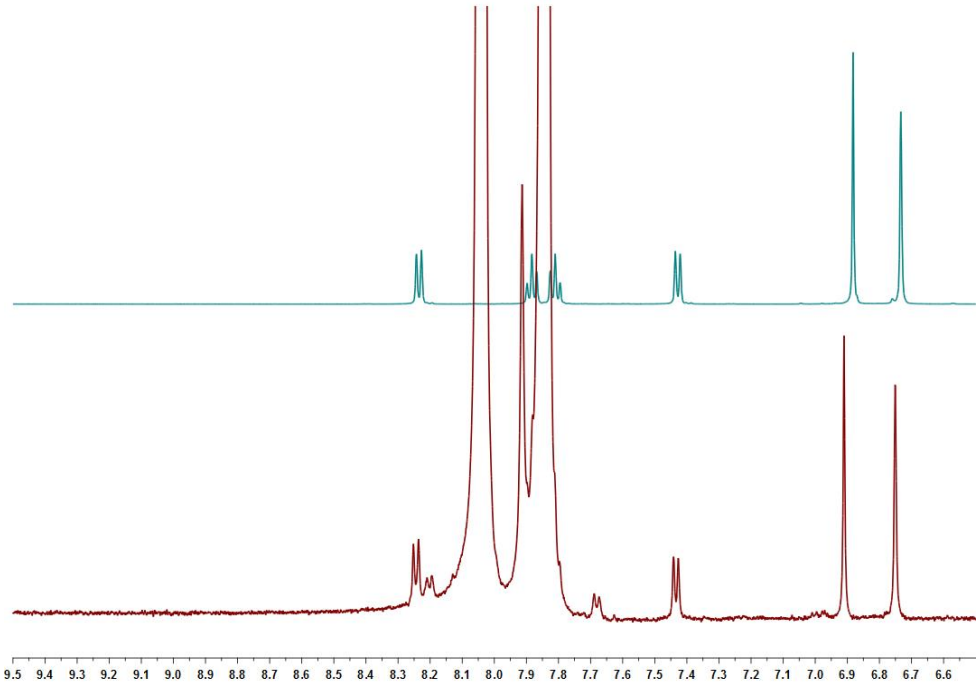

Figure 160. ^{1}H NMR spectra of Rhodamine 590 (top) and Dy^{3+}-BPDC + Rhodamine 590 (bottom).

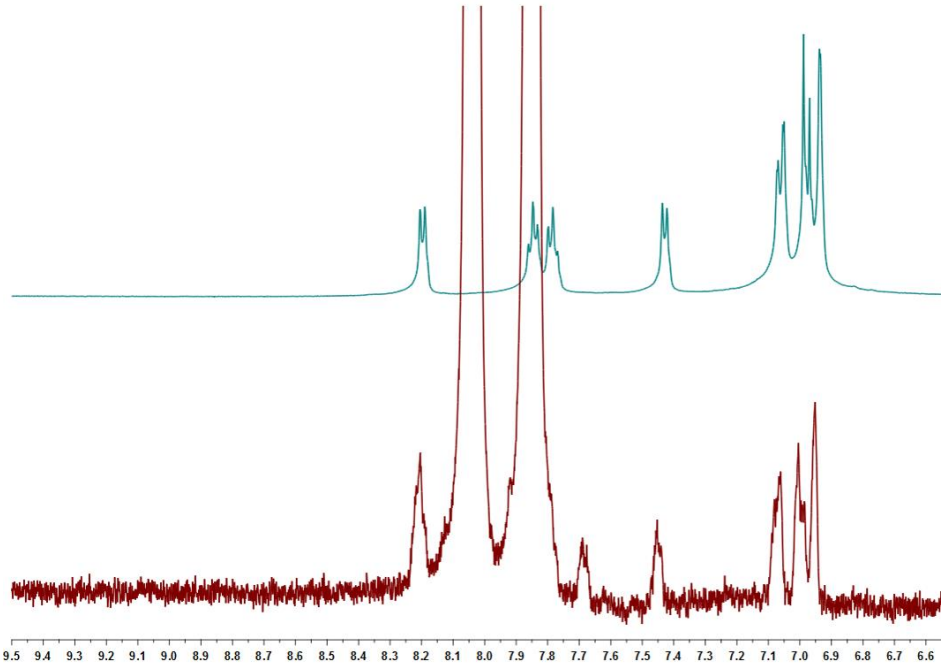

Figure 161. ^{1}H NMR spectra of Rhodamine 610 (top) and Dy^{3+}-BPDC + Rhodamine 610 (bottom).

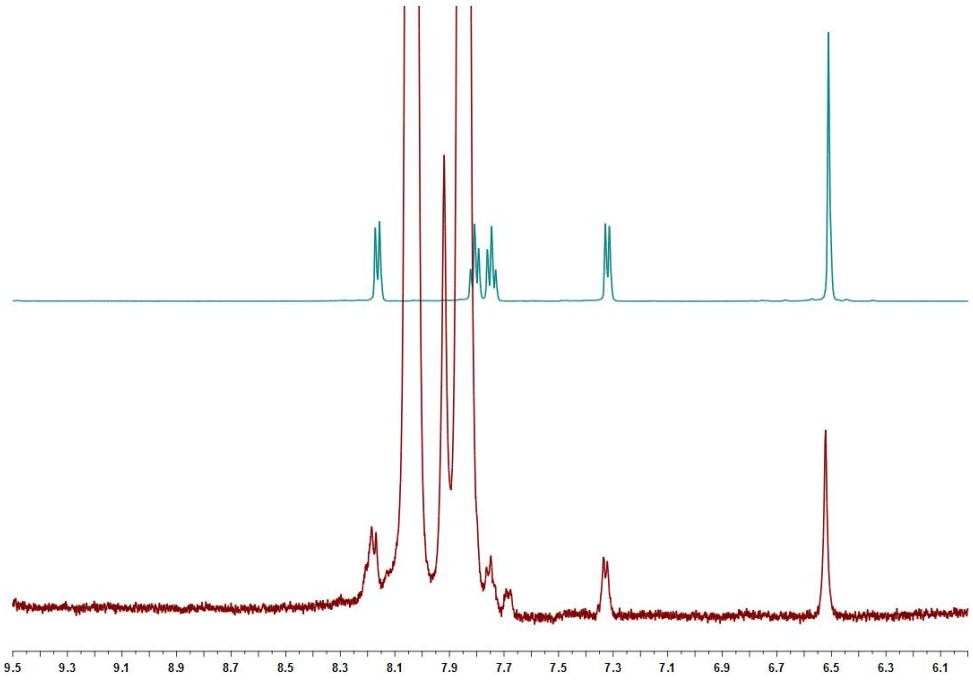

Figure 162. ^{1}H NMR spectra of Rhodamine 640 (top) and Dy^{3+}-BPDC + Rhodamine 640 (bottom).

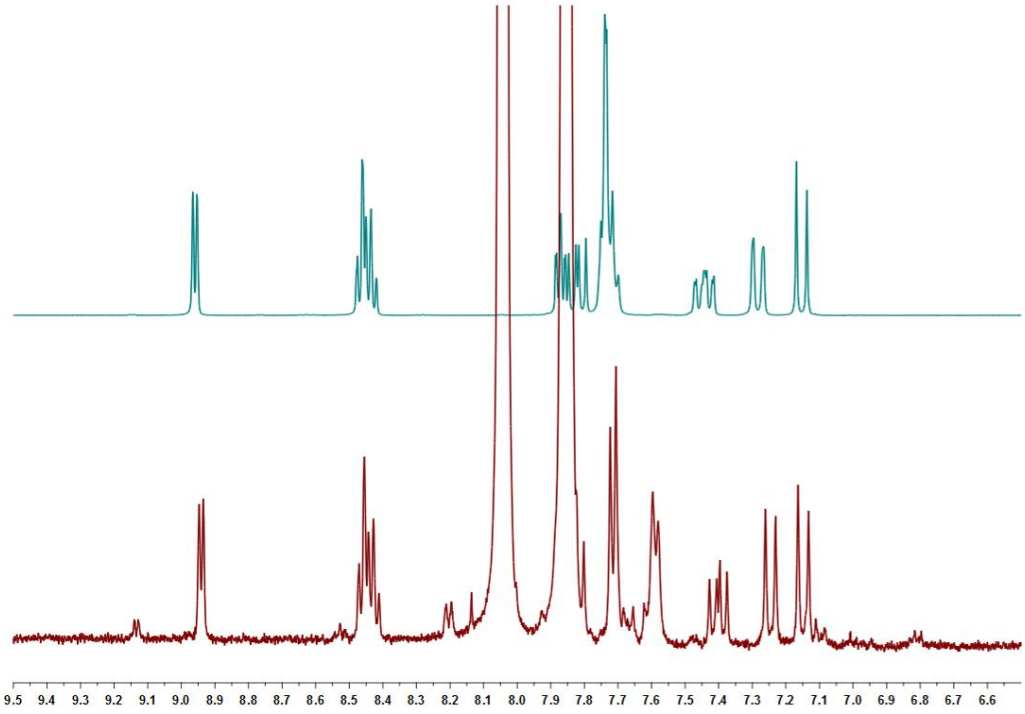

Figure 163. ^{1}H NMR spectra of LDS 698 (top) and Dy^{3+}-BPDC + LDS 698 (bottom).

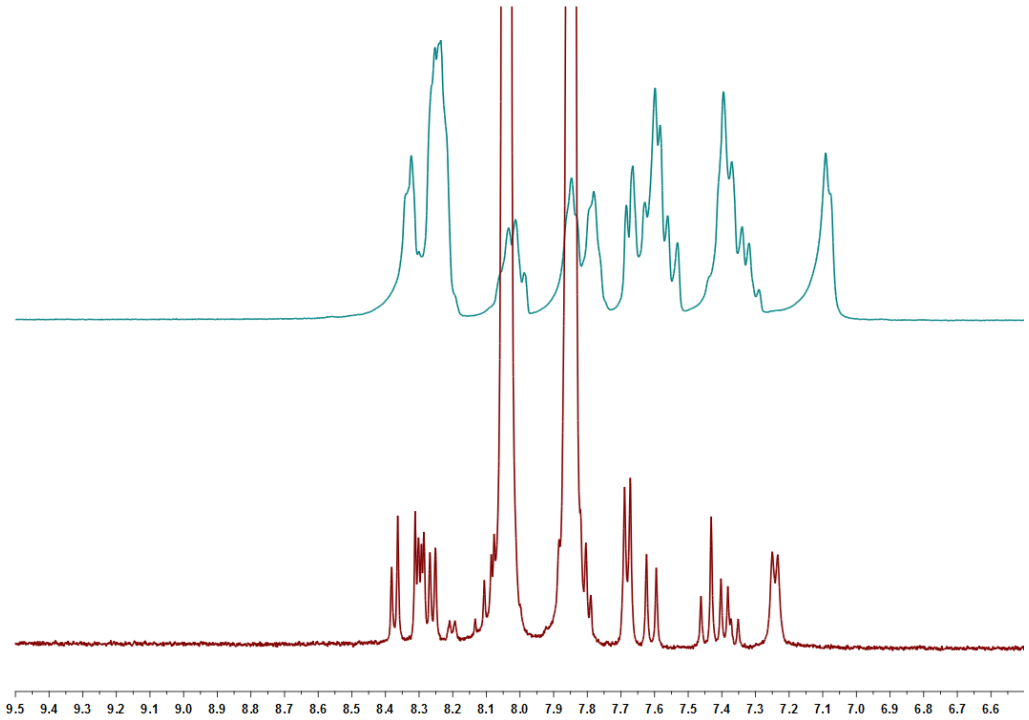

Figure 164. ^{1}H NMR spectra of LDS 750 (top) and Dy^{3+}-BPDC + LDS 750 (bottom).

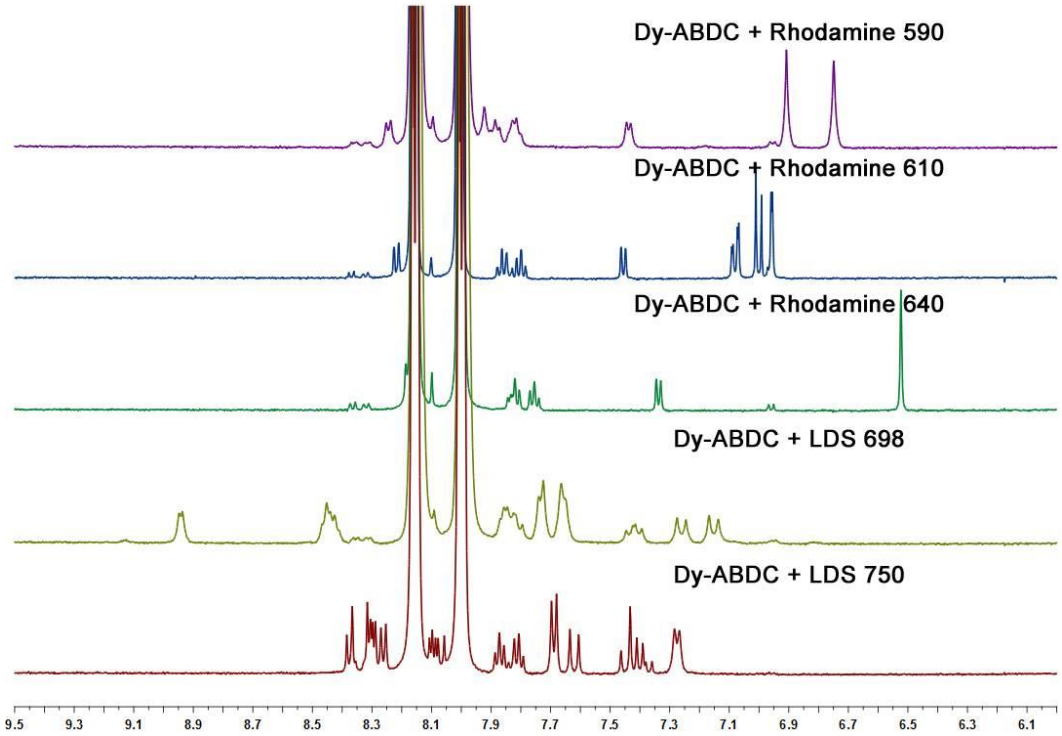

Figure 165. ^{1}H NMR spectra of dissolved Dy^{3+}-ABDC after treatments of various dyes

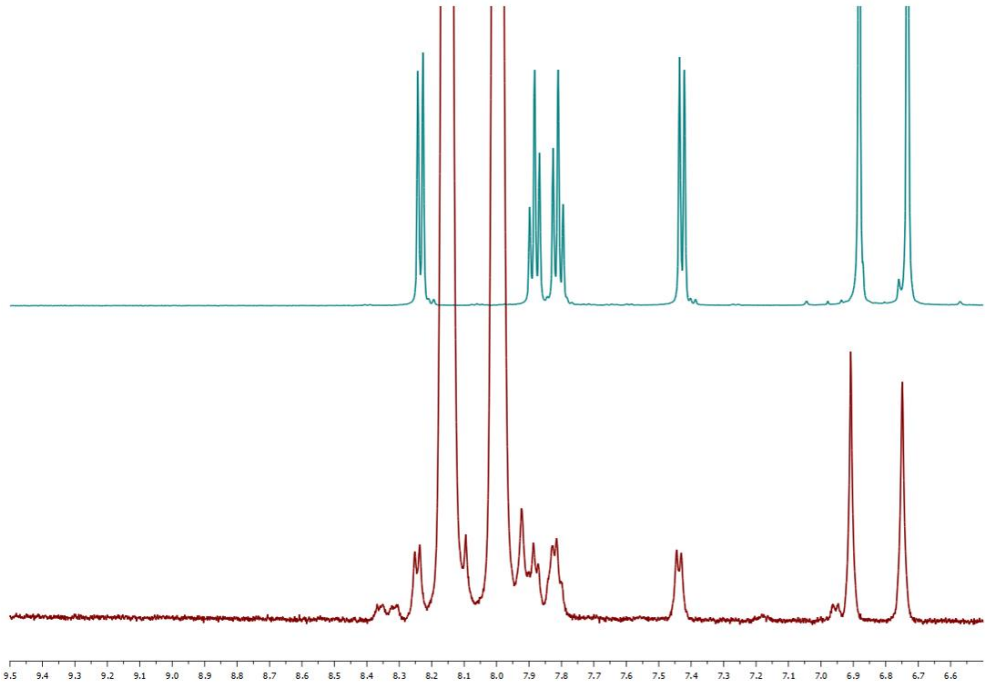

Figure 166. ^{1}H NMR spectra of Rhodamine 590 (top) and Dy^{3+}-ABDC +Rhodamine 590 (bottom).

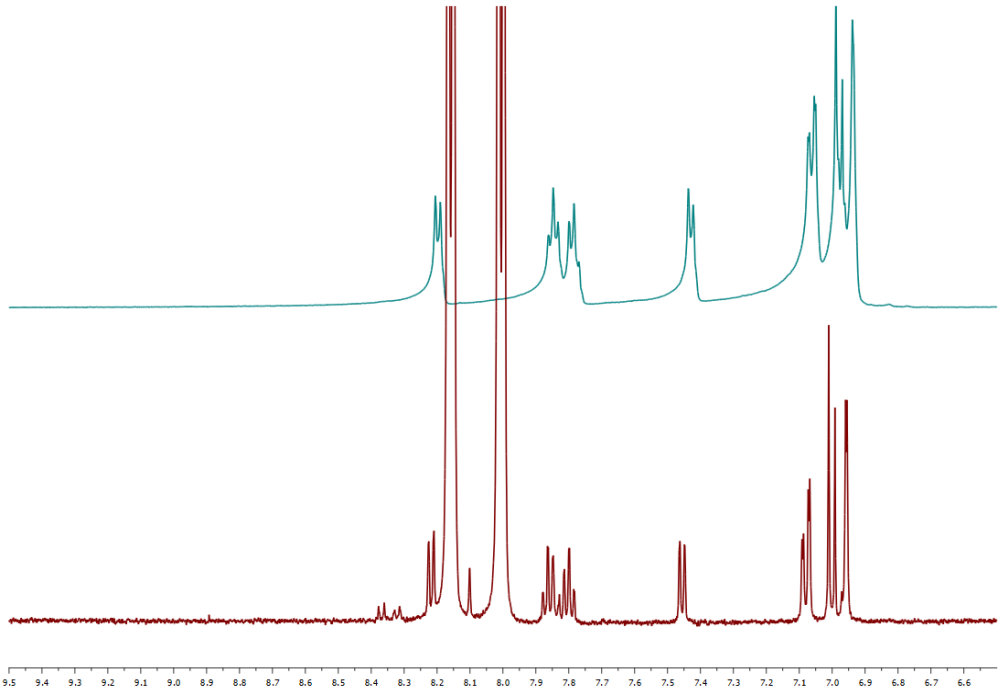

Figure 167. ^{1}H NMR spectra of Rhodamine 610 (top) and Dy^{3+}-ABDC +Rhodamine 610 (bottom).

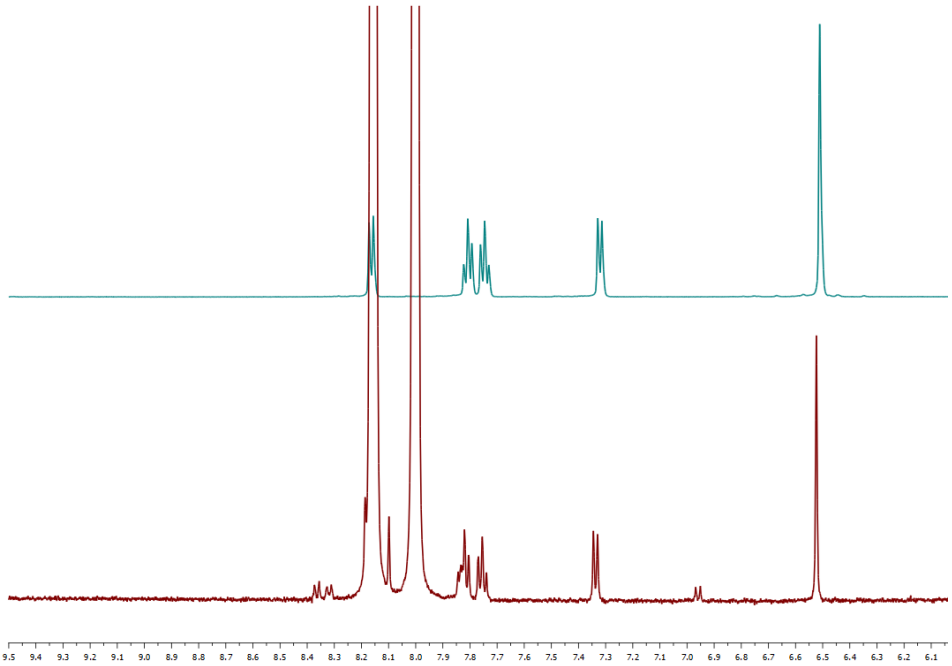

Figure 168. ^{1}H NMR spectra of Rhodamine 640 (top) and Dy^{3+}-ABDC +Rhodamine 640 (bottom).

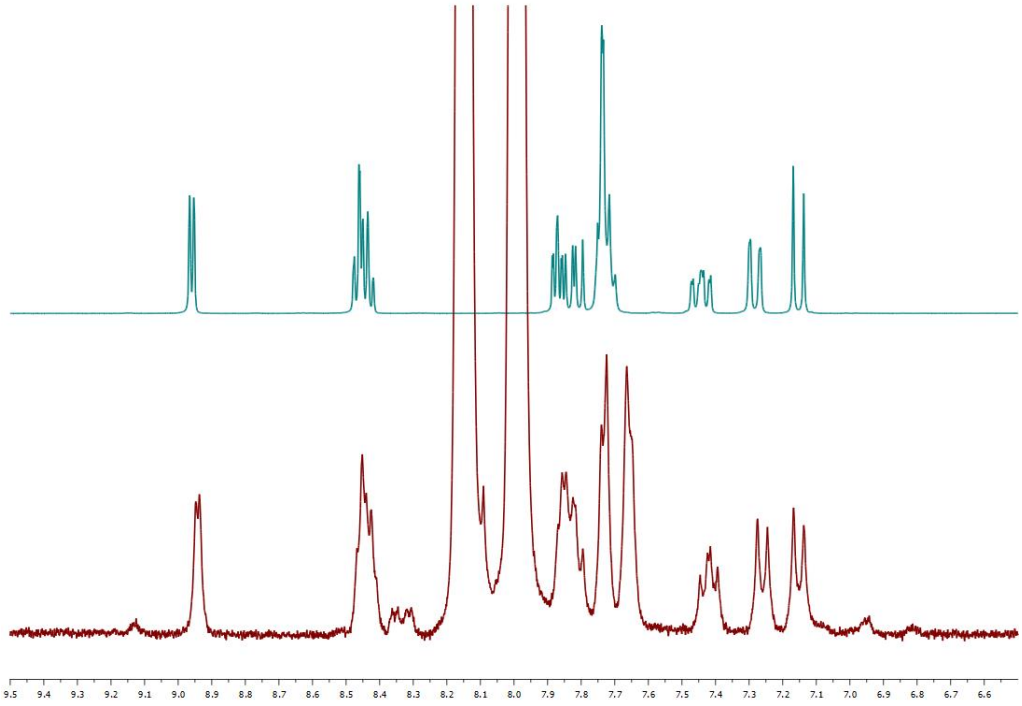

Figure 169. ^{1}H NMR spectra of LDS 698 (top) and Dy^{3+}-ABDC + LDS 698 (bottom).

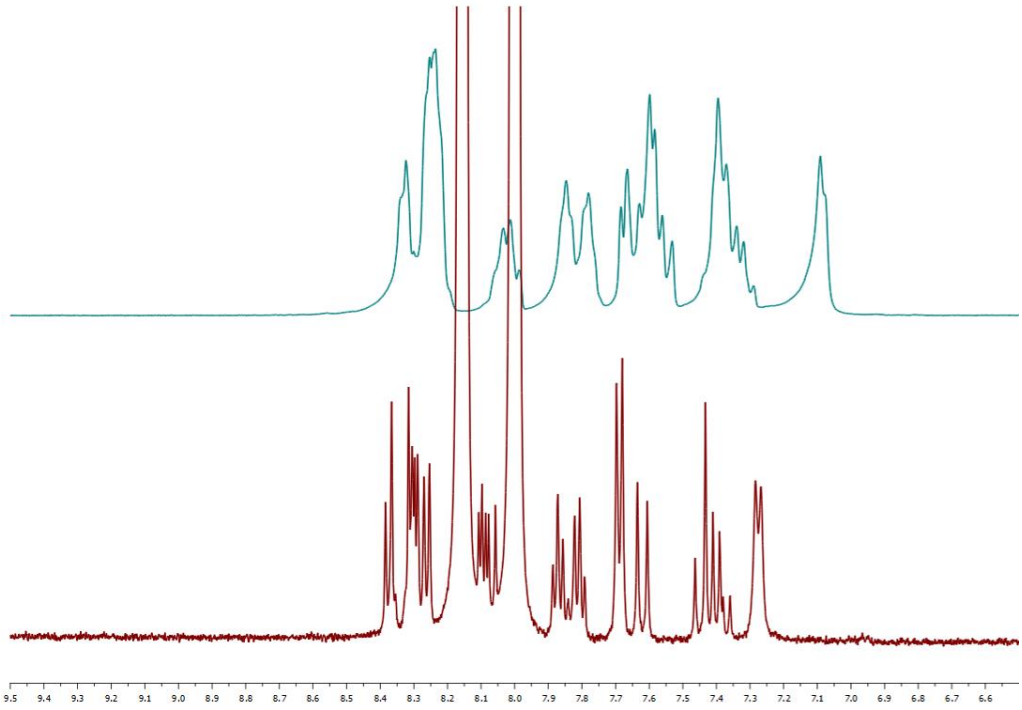

Figure 170. ^{1}H NMR spectra of LDS 750 (top) and Dy^{3+}-ABDC + LDS 750 (bottom).

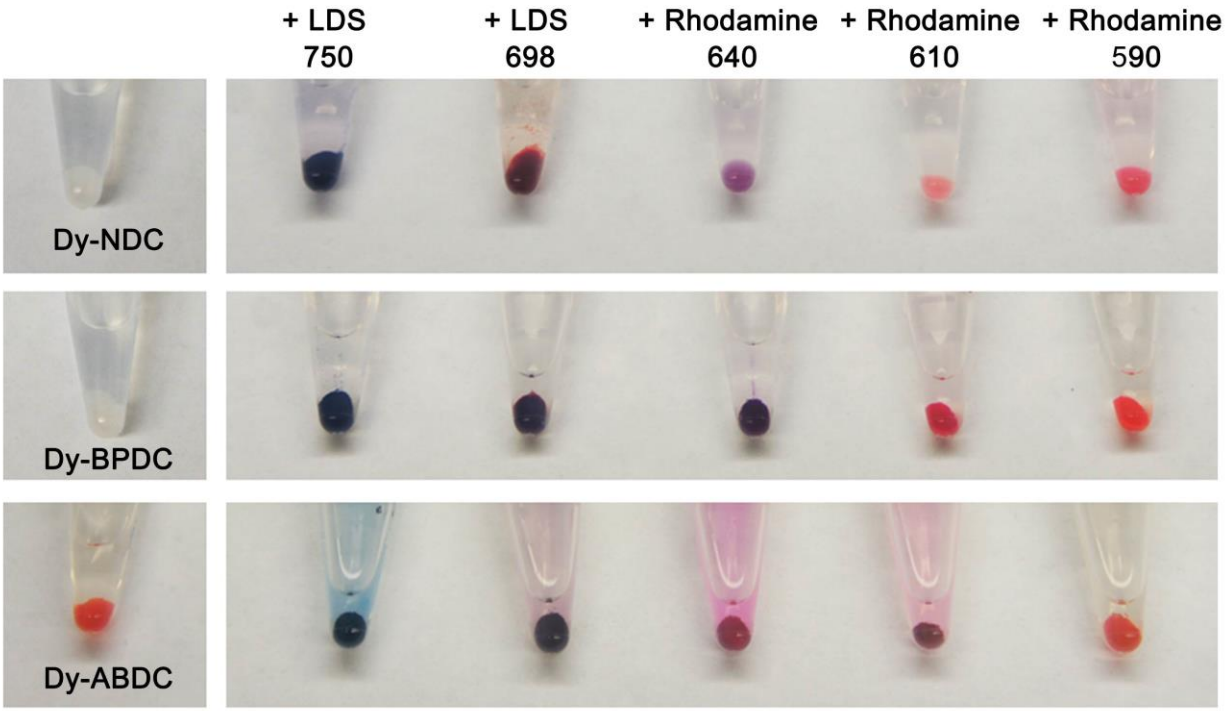

Figure 171. Visible changes before and after loading various dyes into Dy^{3+}-MOFs.

For LDS 750 incorporation in the Yb^{3+}-BPDC MOF, approximately 5 mg of DMSO-exchanged MOF crystals were mixed with LDS 750/DMSO solution (0.5 mL, 0.1 mg/mL or 0.5 mg/mL) and soaked at room temperature for specified periods of time. The MOF crystals were then separated from the dye solutions via centrifugation and copiously washed with DMSO until the supernatant appeared colorless. The MOFs were then washed with DCM (5X), soaked in DCM for 1 hour, washed again with DCM (5X) and dried with Ar flow. The dried MOF samples were dissolved in DMSO-d_6 (0.7 mL) and DCl in D_2O (37%, 0.01 mL) for ^1H NMR (Figure 148).

5.4.6 Photoluminescence study of Yb^{3+}-BPDC with LDS 750

Photoluminescence measurements of LDS 750-incorporated Yb^{3+}-BPDC were performed at solid state. The as-synthesized Yb^{3+}-BPDC MOFs were treated with DMF, DMSO, LDS 750 solution, DMSO and DCM, as previously described in 5.4.5.2, then dried with Ar flow. The dried samples were mixed and ground with MgO before loaded into quartz tubes for spectroscopic study. To ensure the LDS 750@Yb^{3+}-BPDC in the MgO/MOF mixture was still crystalline, PXRD was used to compare (Figure 172).

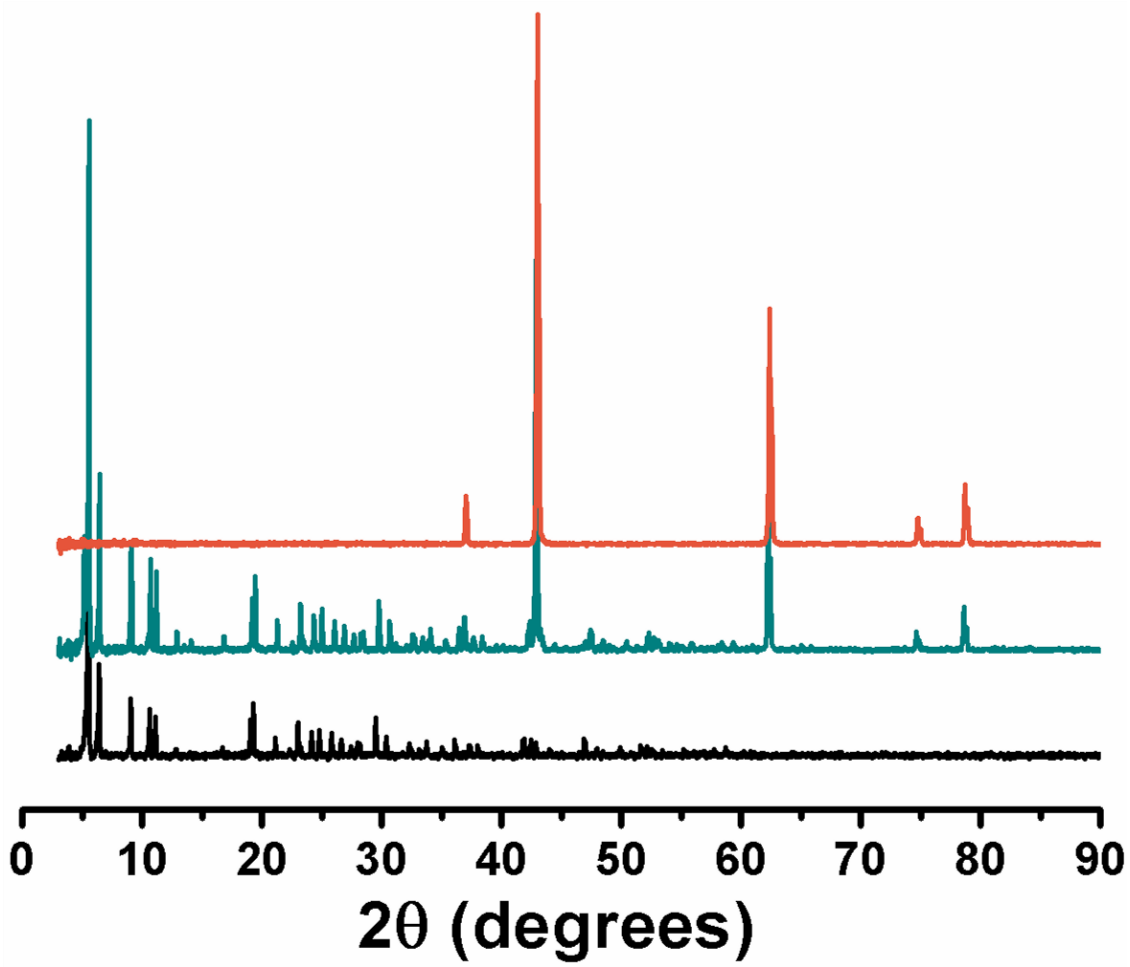

Figure 172. PXRD comparing dye@Yb^{3+}-BPDC (black), dye@Yb^{3+}-BPDC+MgO (dark cyan), and MgO (orange).

APPENDIX A

DY^{3+}-NDC CRYSTALLOGRAPHIC DATA

X-ray diffraction data of Dy^{3+}-NDC were collected on a Bruker X8 Prospector Ultra equipped with an Apex II CCD detector and an IμS micro-focus CuK\α source (λ = 1.54178 Å). An octahedron-shaped colorless crystal with dimensions 0.08 × 0.08 × 0.06 mm^3 was sealed in a 0.5 mm OD glass number 50 (borosilicate glass) capillary tube with MiTeGen MicroTools before mounted onto a goniometer head. The data were collected under ambient temperature.

A cubic unit cell with dimensions $a = b = c = 24.8328(3)$ Å, $\alpha = \beta = \gamma = 90$ °, was derived from the least-square refinement of 9016 reflections in the range of $3.083 < \theta < 68.080$. Centrosymmetric space group Fm-3 was initially assigned using XPREP[201] based on intensity statistics and the systematic absences.

The data were collected to 0.81 Å, and truncated to 0.83 Å for integration by Bruker program SAINT[202], empirical absorption correction was applied using program SADABS[202]. The structure was solved with direct method using SHELXS[203] and refined by full-matrix least-squares on F^2 using SHELXL[204] in Olex2[205]. All the Dy, O atoms and some C atoms were located easily, the rest of the C atoms were generated via subsequent difference Fourier syntheses.

All the non-H atoms were refined anisotropically. SIMU and DELU were applied to the C atoms. ISOR was applied to O1 and C3 atoms. DFIX was applied to some carbon-carbon bonds. After initial refinements, ADDSYM operation in PLATON[197] was used to convert the structure to a higher symmetry (Fm-3m), and transformation matrix [0 1 0 1 0 0 0 0 -1] was applied. The structure was finally refined and converged in the new space group.

Responses to checkCIF alerts:

RFACR01_ALERT_3_A The value of the weighted R factor is > 0.45

Weighted R factor given 0.545

PLAT084_ALERT_3_A High wR2 Value (i.e., > 0.25) ..... 0.55 Report

Response: wR2 is too large because the quality of the diffraction data is sub-optimal. However, the refinements converge well and yield a completely reasonable structure, comparable with previously reported similar structure involving Zr^{IV}.[206]

PLAT601_ALERT_2_A Structure Contains Solvent Accessible VOIDS of 9635 Ang3

Response: The sample is a porous metal-organic framework material and the volume of the void is reasonable. There are severely disordered solvent molecules that cannot be crystallographically located residing in the void(s).

Table 8. Crystal data and structure refinement for LC70521rt_0m

Identification code	lc70521rt_0m	
Empirical formula	C144 Dy12 O64	
Formula weight	4703.44	
Temperature	280(2) K	
Wavelength	1.54178 Å	
Crystal system	Cubic	
Space group	Fm-3m	
Unit cell dimensions	a = 24.8328(3) Å	$\alpha = 90°$
	b = 24.8328(3) Å	$\beta = 90°$
	c = 24.8328(3) Å	$\gamma = 90°$
Volume	15313.6(3) $Å^3$	
Z	2	
Density (calculated)	1.020 mg/m^3	
Absorption coefficient	15.735 mm^{-1}	
F(000)	4335	
Crystal size	0.08 × 0.08 × 0.06 mm^3	
Theta range for data collection	3.08 to 68.31°.	
Index ranges	-27<=h<=29, -29<=k<=26, -29<=l<=29	
Reflections collected	23178	
Independent reflections	758 [R(int) = 0.0671]	
Completeness to theta = 68.31°	99.1 %	
Absorption correction	Semi-empirical from equivalents	
Max. and min. transmission	0.4520 and 0.3658	
Refinement method	Full-matrix least-squares on F^2	
Data / restraints / parameters	758 / 58 / 45	
Goodness-of-fit on F^2	2.986	
Final R indices [I>2sigma(I)]	R1 = 0.1562, wR2 = 0.5328	
R indices (all data)	R1 = 0.1623, wR2 = 0.5450	
Largest diff. peak and hole	2.276 and -6.265 e.$Å^{-3}$	

Table 9. Atomic coordinates ($\times 10^4$) and equivalent isotropic displacement parameters ($Å^2 \times 10^3$) for LC70521rt_0m. U(eq) is defined as one third of the trace of the orthogonalized U^{ij} tensor.

	x	y	z	U(eq)
Dy(1)	1131(1)	0	5000	33(2)
O(1)	500(5)	-500(5)	5500(5)	11(3)
O(2)	1516(9)	0	4112(10)	70(6)
C(6)	2747(4)	0	2621(5)	58(16)
C(3)	1786(6)	0	2682(6)	75(13)
C(5)	2317(6)	0	3463(7)	89(15)
C(4)	1831(6)	0	2234(7)	95(17)

Table 10. Bond lengths [Å] and angles [°] for LC70521rt_0m.

Dy(1)-O(1)#1	2.354(5)
Dy(1)-O(1)#2	2.354(5)
Dy(1)-O(1)#3	2.354(5)
Dy(1)-O(1)	2.354(5)
Dy(1)-O(2)#1	2.40(2)
Dy(1)-O(2)#4	2.40(2)
Dy(1)-O(2)#5	2.40(2)
Dy(1)-O(2)	2.40(2)
Dy(1)-Dy(1)#6	3.972(3)
Dy(1)-Dy(1)#7	3.972(3)
Dy(1)-Dy(1)#3	3.972(3)
Dy(1)-Dy(1)#8	3.972(3)
O(1)-Dy(1)#7	2.354(5)
O(1)-Dy(1)#8	2.354(5)
O(2)-C(1)	1.24(3)
C(6)-C(4)#9	1.107(19)
C(6)-C(6)#10	1.295(19)
C(6)-C(4)#10	1.361(18)
C(6)-C(6)#11	1.368(18)
C(6)-C(3)#9	1.383(17)
C(6)-C(3)#10	1.82(2)
C(3)-C(5)#10	0.62(3)
C(3)-C(4)	1.12(2)
C(3)-C(2)	1.300(16)
C(3)-C(6)#11	1.383(17)
C(3)-C(6)#10	1.82(2)
C(5)-C(3)#10	0.62(3)
C(5)-C(4)#10	1.332(17)
C(5)-C(2)	1.445(15)
C(4)-C(6)#11	1.107(19)
C(4)-C(5)#10	1.332(17)
C(4)-C(6)#10	1.361(18)
C(4)-C(4)#12	1.42(4)

C(1)-O(2)#10	1.24(3)
C(1)-C(2)	1.51(2)
C(2)-C(3)#10	1.300(16)
C(2)-C(5)#10	1.445(15)
O(1)#1-Dy(1)-O(1)#2	63.7(6)
O(1)#1-Dy(1)-O(1)#3	96.6(10)
O(1)#2-Dy(1)-O(1)#3	63.7(6)
O(1)#1-Dy(1)-O(1)	63.7(5)
O(1)#2-Dy(1)-O(1)	96.6(10)
O(1)#3-Dy(1)-O(1)	63.7(5)
O(1)#1-Dy(1)-O(2)#1	138.5(4)
O(1)#2-Dy(1)-O(2)#1	138.5(4)
O(1)#3-Dy(1)-O(2)#1	77.3(6)
O(1)-Dy(1)-O(2)#1	77.3(6)
O(1)#1-Dy(1)-O(2)#4	138.5(4)
O(1)#2-Dy(1)-O(2)#4	77.3(6)
O(1)#3-Dy(1)-O(2)#4	77.3(6)
O(1)-Dy(1)-O(2)#4	138.5(4)
O(2)#1-Dy(1)-O(2)#4	80.9(5)
O(1)#1-Dy(1)-O(2)#5	77.3(6)
O(1)#2-Dy(1)-O(2)#5	138.5(4)
O(1)#3-Dy(1)-O(2)#5	138.5(4)
O(1)-Dy(1)-O(2)#5	77.3(6)
O(2)#1-Dy(1)-O(2)#5	80.9(5)
O(2)#4-Dy(1)-O(2)#5	133.1(12)
O(1)#1-Dy(1)-O(2)	77.3(6)
O(1)#2-Dy(1)-O(2)	77.3(6)
O(1)#3-Dy(1)-O(2)	138.5(4)
O(1)-Dy(1)-O(2)	138.5(4)
O(2)#1-Dy(1)-O(2)	133.1(12)
O(2)#4-Dy(1)-O(2)	80.9(5)
O(2)#5-Dy(1)-O(2)	80.9(5)
O(1)#1-Dy(1)-Dy(1)#6	32.46(18)
O(1)#2-Dy(1)-Dy(1)#6	32.46(18)
O(1)#3-Dy(1)-Dy(1)#6	84.4(4)

O(1)-Dy(1)-Dy(1)#6	84.4(4)
O(2)#1-Dy(1)-Dy(1)#6	158.4(6)
O(2)#4-Dy(1)-Dy(1)#6	106.3(4)
O(2)#5-Dy(1)-Dy(1)#6	106.3(4)
O(2)-Dy(1)-Dy(1)#6	68.5(6)
O(1)#1-Dy(1)-Dy(1)#7	32.46(18)
O(1)#2-Dy(1)-Dy(1)#7	84.4(4)
O(1)#3-Dy(1)-Dy(1)#7	84.4(4)
O(1)-Dy(1)-Dy(1)#7	32.46(18)
O(2)#1-Dy(1)-Dy(1)#7	106.3(4)
O(2)#4-Dy(1)-Dy(1)#7	158.4(6)
O(2)#5-Dy(1)-Dy(1)#7	68.4(6)
O(2)-Dy(1)-Dy(1)#7	106.3(4)
Dy(1)#6-Dy(1)-Dy(1)#7	60.0
O(1)#1-Dy(1)-Dy(1)#3	84.4(4)
O(1)#2-Dy(1)-Dy(1)#3	32.46(18)
O(1)#3-Dy(1)-Dy(1)#3	32.46(18)
O(1)-Dy(1)-Dy(1)#3	84.4(4)
O(2)#1-Dy(1)-Dy(1)#3	106.3(4)
O(2)#4-Dy(1)-Dy(1)#3	68.4(6)
O(2)#5-Dy(1)-Dy(1)#3	158.4(6)
O(2)-Dy(1)-Dy(1)#3	106.3(4)
Dy(1)#6-Dy(1)-Dy(1)#3	60.0
Dy(1)#7-Dy(1)-Dy(1)#3	90.0
O(1)#1-Dy(1)-Dy(1)#8	84.4(4)
O(1)#2-Dy(1)-Dy(1)#8	84.4(4)
O(1)#3-Dy(1)-Dy(1)#8	32.46(18)
O(1)-Dy(1)-Dy(1)#8	32.46(18)
O(2)#1-Dy(1)-Dy(1)#8	68.4(6)
O(2)#4-Dy(1)-Dy(1)#8	106.3(4)
O(2)#5-Dy(1)-Dy(1)#8	106.3(4)
O(2)-Dy(1)-Dy(1)#8	158.5(6)
Dy(1)#6-Dy(1)-Dy(1)#8	90.0
Dy(1)#7-Dy(1)-Dy(1)#8	60.0
Dy(1)#3-Dy(1)-Dy(1)#8	60.0

Dy(1)#7-O(1)-Dy(1)#8	115.1(4)
Dy(1)#7-O(1)-Dy(1)	115.1(4)
Dy(1)#8-O(1)-Dy(1)	115.1(4)
C(1)-O(2)-Dy(1)	138.8(16)
C(4)#9-C(6)-C(6)#10	153.9(12)
C(4)#9-C(6)-C(4)#10	69.2(19)
C(6)#10-C(6)-C(4)#10	136.9(9)
C(4)#9-C(6)-C(6)#11	173(2)
C(6)#10-C(6)-C(6)#11	18.8(11)
C(4)#10-C(6)-C(6)#11	118.1(15)
C(4)#9-C(6)-C(3)#9	51.9(12)
C(6)#10-C(6)-C(3)#9	102.0(9)
C(4)#10-C(6)-C(3)#9	121.1(14)
C(6)#11-C(6)-C(3)#9	120.8(15)
C(4)#9-C(6)-C(3)#10	107.0(15)
C(6)#10-C(6)-C(3)#10	99.1(7)
C(4)#10-C(6)-C(3)#10	37.9(9)
C(6)#11-C(6)-C(3)#10	80.2(12)
C(3)#9-C(6)-C(3)#10	158.9(15)
C(5)#10-C(3)-C(4)	96(2)
C(5)#10-C(3)-C(2)	90.7(19)
C(4)-C(3)-C(2)	173.3(18)
C(5)#10-C(3)-C(6)#11	147(3)
C(4)-C(3)-C(6)#11	51.2(10)
C(2)-C(3)-C(6)#11	122.1(16)
C(5)#10-C(3)-C(6)#10	144(2)
C(4)-C(3)-C(6)#10	48.3(10)
C(2)-C(3)-C(6)#10	125.0(14)
C(6)#11-C(3)-C(6)#10	2.9(3)
C(3)#10-C(5)-C(4)#10	56.5(18)
C(3)#10-C(5)-C(2)	64(2)
C(4)#10-C(5)-C(2)	120.6(15)
C(6)#11-C(4)-C(3)	76.8(14)
C(6)#11-C(4)-C(5)#10	104.3(18)
C(3)-C(4)-C(5)#10	27.4(14)

C(6)#11-C(4)-C(6)#10	17.0(10)
C(3)-C(4)-C(6)#10	93.8(14)
C(5)#10-C(4)-C(6)#10	121.2(16)
C(6)#11-C(4)-C(4)#12	63.9(12)
C(3)-C(4)-C(4)#12	140.7(11)
C(5)#10-C(4)-C(4)#12	168.2(10)
C(6)#10-C(4)-C(4)#12	46.9(9)
O(2)-C(1)-O(2)#10	126(2)
O(2)-C(1)-C(2)	117.2(12)
O(2)#10-C(1)-C(2)	117.2(12)
C(3)#10-C(2)-C(3)	91.9(17)
C(3)#10-C(2)-C(5)	25.3(11)
C(3)-C(2)-C(5)	117.2(14)
C(3)#10-C(2)-C(5)#10	117.2(14)
C(3)-C(2)-C(5)#10	25.3(11)
C(5)-C(2)-C(5)#10	142.5(18)
C(3)#10-C(2)-C(1)	134.0(9)
C(3)-C(2)-C(1)	134.0(9)
C(5)-C(2)-C(1)	108.8(9)
C(5)#10-C(2)-C(1)	108.8(9)

Symmetry transformations used to generate equivalent atoms:

#1 x,y,-z+1

#2 -y,x,-z+1

#3 -y,x,z

#4 x,-z+1/2,-y+1/2

#5 x,z-1/2,-y+1/2

#6 -y,-z+1/2,-x+1/2

#7 y,-x,-z+1

#8 y,z-1/2,x+1/2

#9 -x+1/2,-y,-z+1/2

#10 -z+1/2,-y,-x+1/2

#11 -x+1/2,y,-z+1/2

#12 z,y,x

Table 11. Anisotropic displacement parameters ($Å^2 \times 10^3$) for LC70521rt_0m. The anisotropic displacement factor exponent takes the form: $-2\pi^2[h^2 a^{*2} U^{11} + ... + 2 h k a^* b^* U^{12}]$

	U^{11}	U^{22}	U^{33}	U^{23}	U^{13}	U^{12}
Dy(1)	7(2)	46(2)	46(2)	0	0	0
O(1)	11(3)	11(3)	11(3)	3(2)	-3(2)	3(2)
O(2)	54(12)	91(18)	64(14)	0	34(11)	0
C(6)	50(40)	110(40)	10(20)	0	0(30)	0
C(3)	70(20)	70(20)	92(15)	0	64(18)	0
C(5)	92(17)	80(30)	100(30)	0	60(20)	0
C(4)	110(40)	90(40)	90(16)	0	50(30)	0
C(1)	100(20)	60(20)	100(20)	0	70(30)	0
C(2)	90(14)	60(20)	90(14)	0	60(19)	0

APPENDIX B

DY^{3+}-BPDC CRYSTALLOGRAPHIC DATA

X-ray diffraction data of Dy^{3+}-BPDC were collected on a Bruker X8 Prospector Ultra equipped with an Apex II CCD detector and an IμS micro-focus CuK\α source (λ = 1.54178 Å). An octahedron-shaped colorless crystal with dimensions 0.10 × 0.06 × 0.06 mm^3 was mounted on a goniometer head using MiTeGen MicroMesh. The data were collected under N_2 stream at 240K.

A cubic unit cell with dimensions $a = b = c = 27.5659$ (2) Å, $\alpha = \beta = \gamma = 90$ °, was derived from the least-square refinement of 9965 reflections in the range of $2.777 < \theta < 66.544$. Centrosymmetric space group Fm-3m was determined based on intensity statistics and the systematic absences.

The data were collected and integrated to 0.84 Å by Bruker program SAINT[202], empirical absorption correction was applied using program SADABS[202]. The structure was solved with direct method using SHELXT[207] and refined by full-matrix least-squares on F^2 using SHELXL[204] in Olex2[205]. All the Dy, O atoms and some C atoms were located easily, the rest of the C atoms were generated via subsequent difference Fourier syntheses. Idealized atom positions were calculated for H atoms (d-(C-H) = 0.950 Å).

All the non-H atoms were refined anisotropically. All the H atoms were refined isotropically.

Response to checkCIF alert:

PLAT601_ALERT_2_A Structure Contains Solvent Accessible VOIDS of 13424 Ang3

Response: The sample is a porous metal-organic framework material and the volume of the void is reasonable. There are severely disordered solvent molecules that cannot be crystallographically located residing in the void(s).

Table 12. Crystal data and structure refinement for LC61245_0m

Identification code	lc61245_0m	
Empirical formula	C42 H24 Dy3 O20	
Formula weight	1336.11	
Temperature	240(2) K	
Wavelength	1.54178 Å	
Crystal system	Cubic	
Space group	Fm-3m	
Unit cell dimensions	a = 27.5659(2) Å	α = 90°
	b = 27.5659(2) Å	β = 90°
	c = 27.5659(2) Å	γ = 90°
Volume	20946.7(3) $Å^3$	
Z	8	
Density (calculated)	0.847 mg/m^3	
Absorption coefficient	11.571 mm^{-1}	
F(000)	5072	
Crystal size	0.10 × 0.06 × 0.06 mm^3	
Theta range for data collection	2.78 to 66.54°.	
Index ranges	-23<=h<=32, -31<=k<=31, -32<=l<=32	
Reflections collected	21680	
Independent reflections	990 [R(int) = 0.0785]	
Completeness to theta = 66.54°	99.9 %	
Absorption correction	Semi-empirical from equivalents	
Max. and min. transmission	0.5436 and 0.3908	
Refinement method	Full-matrix least-squares on F^2	
Data / restraints / parameters	990 / 0 / 40	
Goodness-of-fit on F^2	1.357	
Final R indices [I>2sigma(I)]	R1 = 0.0562, wR2 = 0.1854	
R indices (all data)	R1 = 0.0633, wR2 = 0.1926	
Largest diff. peak and hole	1.922 and -0.668 e.$Å^{-3}$	

Table 13. Atomic coordinates ($\times 10^4$) and equivalent isotropic displacement parameters ($Å^2 \times 10^3$) for LC61245_0m. U(eq) is defined as one third of the trace of the orthogonalized U^{ij} tensor.

	x	y	z	U(eq)
Dy(1)	5000	6000(1)	5000	19(1)
C(1)	5000	6204(4)	6204(4)	51(4)
C(2)	5000	6593(4)	6593(4)	61(5)
C(3)	5000	7069(6)	6472(5)	144(11)
C(4)	5000	7428(6)	6828(6)	156(12)
C(5)	5000	7307(4)	7307(4)	92(8)
O(1)	5000	6359(3)	5761(2)	47(2)
O(2)	4542(2)	5458(2)	4542(2)	10(2)
O(3)	3619(13)	6381(13)	6381(13)	290(30)

Table 14. Bond lengths [Å] and angles [°] for LC61245_0m.

Dy(1)-O(1)#1	2.321(6)
Dy(1)-O(1)#2	2.321(6)
Dy(1)-O(1)#3	2.321(6)
Dy(1)-O(1)	2.321(6)
Dy(1)-O(2)	2.329(2)
Dy(1)-O(2)#4	2.329(2)
Dy(1)-O(2)#3	2.329(2)
Dy(1)-O(2)#5	2.329(2)
Dy(1)-Dy(1)#6	3.8986(11)
Dy(1)-Dy(1)#7	3.8986(11)
Dy(1)-Dy(1)#8	3.8986(11)
Dy(1)-Dy(1)#9	3.8986(11)
C(1)-O(1)	1.293(9)
C(1)-O(1)#10	1.293(9)
C(1)-C(2)	1.517(19)
C(2)-C(3)	1.352(17)
C(2)-C(3)#10	1.352(17)
C(3)-C(4)	1.394(19)
C(3)-H(3A)	0.9400
C(4)-C(5)	1.363(19)
C(4)-H(4A)	0.9400
C(5)-C(4)#10	1.363(19)
C(5)-C(5)#11	1.50(3)
O(2)-Dy(1)#6	2.329(2)
O(2)-Dy(1)#7	2.329(2)
O(1)#1-Dy(1)-O(1)#2	129.5(4)
O(1)#1-Dy(1)-O(1)#3	79.52(15)
O(1)#2-Dy(1)-O(1)#3	79.52(15)
O(1)#1-Dy(1)-O(1)	79.52(15)
O(1)#2-Dy(1)-O(1)	79.52(15)
O(1)#3-Dy(1)-O(1)	129.5(4)
O(1)#1-Dy(1)-O(2)	139.84(10)
O(1)#2-Dy(1)-O(2)	77.4(2)

O(1)#3-Dy(1)-O(2)	77.4(2)
O(1)-Dy(1)-O(2)	139.84(10)
O(1)#1-Dy(1)-O(2)#4	77.4(2)
O(1)#2-Dy(1)-O(2)#4	139.84(10)
O(1)#3-Dy(1)-O(2)#4	77.4(2)
O(1)-Dy(1)-O(2)#4	139.84(10)
O(2)-Dy(1)-O(2)#4	65.7(2)
O(1)#1-Dy(1)-O(2)#3	139.84(10)
O(1)#2-Dy(1)-O(2)#3	77.4(2)
O(1)#3-Dy(1)-O(2)#3	139.84(10)
O(1)-Dy(1)-O(2)#3	77.4(2)
O(2)-Dy(1)-O(2)#3	65.7(2)
O(2)#4-Dy(1)-O(2)#3	100.3(4)
O(1)#1-Dy(1)-O(2)#5	77.4(2)
O(1)#2-Dy(1)-O(2)#5	139.84(10)
O(1)#3-Dy(1)-O(2)#5	139.84(10)
O(1)-Dy(1)-O(2)#5	77.4(2)
O(2)-Dy(1)-O(2)#5	100.3(4)
O(2)#4-Dy(1)-O(2)#5	65.7(2)
O(2)#3-Dy(1)-O(2)#5	65.7(2)
O(1)#1-Dy(1)-Dy(1)#6	107.56(12)
O(1)#2-Dy(1)-Dy(1)#6	107.56(13)
O(1)#3-Dy(1)-Dy(1)#6	70.25(19)
O(1)-Dy(1)-Dy(1)#6	160.25(19)
O(2)-Dy(1)-Dy(1)#6	33.17(7)
O(2)#4-Dy(1)-Dy(1)#6	33.17(7)
O(2)#3-Dy(1)-Dy(1)#6	86.01(16)
O(2)#5-Dy(1)-Dy(1)#6	86.01(16)
O(1)#1-Dy(1)-Dy(1)#7	160.25(19)
O(1)#2-Dy(1)-Dy(1)#7	70.25(19)
O(1)#3-Dy(1)-Dy(1)#7	107.56(13)
O(1)-Dy(1)-Dy(1)#7	107.56(13)
O(2)-Dy(1)-Dy(1)#7	33.17(7)
O(2)#4-Dy(1)-Dy(1)#7	86.01(16)
O(2)#3-Dy(1)-Dy(1)#7	33.17(7)

O(2)#5-Dy(1)-Dy(1)#7	86.01(16)
Dy(1)#6-Dy(1)-Dy(1)#7	60.0
O(1)#1-Dy(1)-Dy(1)#8	70.25(19)
O(1)#2-Dy(1)-Dy(1)#8	160.25(19)
O(1)#3-Dy(1)-Dy(1)#8	107.56(13)
O(1)-Dy(1)-Dy(1)#8	107.56(13)
O(2)-Dy(1)-Dy(1)#8	86.01(16)
O(2)#4-Dy(1)-Dy(1)#8	33.17(7)
O(2)#3-Dy(1)-Dy(1)#8	86.01(16)
O(2)#5-Dy(1)-Dy(1)#8	33.17(7)
Dy(1)#6-Dy(1)-Dy(1)#8	60.0
Dy(1)#7-Dy(1)-Dy(1)#8	90.0
O(1)#1-Dy(1)-Dy(1)#9	107.56(12)
O(1)#2-Dy(1)-Dy(1)#9	107.56(12)
O(1)#3-Dy(1)-Dy(1)#9	160.25(19)
O(1)-Dy(1)-Dy(1)#9	70.25(19)
O(2)-Dy(1)-Dy(1)#9	86.01(16)
O(2)#4-Dy(1)-Dy(1)#9	86.01(16)
O(2)#3-Dy(1)-Dy(1)#9	33.17(7)
O(2)#5-Dy(1)-Dy(1)#9	33.17(7)
Dy(1)#6-Dy(1)-Dy(1)#9	90.0
Dy(1)#7-Dy(1)-Dy(1)#9	60.0
Dy(1)#8-Dy(1)-Dy(1)#9	60.0
O(1)-C(1)-O(1)#10	128.6(12)
O(1)-C(1)-C(2)	115.7(6)
O(1)#10-C(1)-C(2)	115.7(6)
C(3)-C(2)-C(3)#10	118.7(16)
C(3)-C(2)-C(1)	120.7(8)
C(3)#10-C(2)-C(1)	120.7(8)
C(2)-C(3)-C(4)	121.0(15)
C(2)-C(3)-H(3A)	119.5
C(4)-C(3)-H(3A)	119.5
C(5)-C(4)-C(3)	120.5(15)
C(5)-C(4)-H(4A)	119.7
C(3)-C(4)-H(4A)	119.7

C(4)-C(5)-C(4)#10	118.3(18)
C(4)-C(5)-C(5)#11	120.8(9)
C(4)#10-C(5)-C(5)#11	120.8(9)
C(1)-O(1)-Dy(1)	135.5(7)
Dy(1)-O(2)-Dy(1)#6	113.66(15)
Dy(1)-O(2)-Dy(1)#7	113.66(15)
Dy(1)#6-O(2)-Dy(1)#7	113.66(15)

Symmetry transformations used to generate equivalent atoms:

#1 z,y,-x+1

#2 -z+1,y,-x+1

#3 x,y,-z+1

#4 -x+1,y,z

#5 -x+1,y,-z+1

#6 -z+1,-x+1,-y+1

#7 -y+1,-z+1,-x+1

#8 y,z,x

#9 z,x,y

#10 -x+1,z,y

#11 -x+1,-y+3/2,-z+3/2

Table 15. Anisotropic displacement parameters ($Å^2 \times 10^3$) for LC61245_0m. The anisotropic displacement factor exponent takes the form: $-2\pi^2[h^2 a^{*2} U^{11} + ... + 2 h k a^* b^* U^{12}]$

	U^{11}	U^{22}	U^{33}	U^{23}	U^{13}	U^{12}
Dy(1)	21(1)	15(1)	21(1)	0	0	0
C(1)	69(11)	41(6)	41(6)	-19(7)	0	0
C(2)	99(14)	41(6)	41(6)	-21(7)	0	0
C(3)	330(30)	56(9)	42(8)	-21(7)	0	0
C(4)	370(40)	47(9)	52(9)	-25(7)	0	0
C(5)	180(30)	48(7)	48(7)	-17(9)	0	0
O(1)	57(4)	46(4)	38(4)	-24(3)	0	0
O(2)	10(2)	10(2)	10(2)	-2(2)	2(2)	-2(2)
O(3)	290(30)	290(30)	290(30)	50(30)	-50(30)	-50(30)

Table 16. Hydrogen coordinates ($\times 10^4$) and isotropic displacement parameters ($Å^2 \times 10^3$) for LC61245_0m.

	x	y	z	U(eq)
H(3A)	5000	7158	6143	173
H(4A)	5000	7757	6736	187

APPENDIX C

DY^{3+}-ABDC CRYSTALLOGRAPHIC DATA

X-ray diffraction data of Dy^{3+}-ABDC were collected on a Bruker X8 Prospector Ultra equipped with an Apex II CCD detector and an IμS micro-focus CuK\α source (λ = 1.54178 Å). An octahedron-shaped orange-colored crystal with dimensions 0.12 × 0.12 × 0.08 mm^3 was mounted on a goniometer head using MiTeGen MicroMesh. The data were collected under N_2 stream at 240K.

A cubic unit cell with dimensions $a = b = c = 29.9107(6)$ Å, $\alpha = \beta = \gamma = 90$ °, was derived from the least-square refinement of 9865 reflections in the range of $4.174 < \theta < 68.296$. Centrosymmetric space group Fm-3m was determined based on intensity statistics and the systematic absences.

The data were collected to 0.81 Å and truncated to 0.83 Å for integration by Bruker program SAINT[202], empirical absorption correction was applied using program SADABS[202]. The structure was solved with direct method using SHELXT[207] and refined by full-matrix least-squares on F^2 using SHELXL[204] in Olex2[205]. All the Dy, O atoms and some C atoms were located easily, the rest of the non-H atoms were generated via subsequent difference Fourier syntheses. Idealized atom positions were calculated for H atoms (d-(C-H) = 0.950 Å).

All the non-H atoms were refined anisotropically. All the H atoms were refined isotropically. ADP and rigid bond restraints were applied to the C and N atoms using SIMU and DELU commands. DFIX was also used to restrain some of the bond lengths.

Responses to checkCIF alerts:

PLAT430_ALERT_2_A Short Inter D...A Contact O1 .. O1 .. 2.49 Ang.

Response: The $Dy_6(OH)_8$ is a reasonable SBU structure which is also present in many other MOF structures reported in this dissertation as well as published literature, and the 2.49 Å inter-atomic distance is consistent with those values.

PLAT602_ALERT_2_A VERY LARGE Solvent Accessible VOID(S) in Structure

Response: The sample is a porous metal-organic framework material and the very large void is reasonable. There are severely disordered solvent molecules that cannot be crystallographically located residing in the void(s).

Table 17. Crystal data and structure refinement for LC70513_0m

Identification code	lc70513_0m	
Empirical formula	C42 H24 Dy3 N6 O16	
Formula weight	1356.17	
Temperature	240(2) K	
Wavelength	1.54178 Å	
Crystal system	Cubic	
Space group	Fm-3m	
Unit cell dimensions	a = 29.9107(6) Å	α = 90°
	b = 29.9107(6) Å	β = 90°
	c = 29.9107(6) Å	γ = 90°
Volume	26759.6(9) $Å^3$	
Z	8	
Density (calculated)	0.673 mg/m^3	
Absorption coefficient	9.052 mm^{-1}	
F(000)	5152	
Crystal size	0.12 × 0.12 × 0.08 mm^3	
Theta range for data collection	2.56 to 68.54°.	
Index ranges	-36<=h<=35, -36<=k<=31, -23<=l<=36	
Reflections collected	43329	
Independent reflections	1293 [R(int) = 0.1647]	
Completeness to theta = 68.54°	99.9 %	
Absorption correction	Semi-empirical from equivalents	
Max. and min. transmission	0.5312 and 0.4097	
Refinement method	Full-matrix least-squares on F^2	
Data / restraints / parameters	1293 / 48 / 41	
Goodness-of-fit on F^2	1.203	
Final R indices [I>2sigma(I)]	R1 = 0.0529, wR2 = 0.1535	
R indices (all data)	R1 = 0.0581, wR2 = 0.1606	
Largest diff. peak and hole	1.117 and -1.219 e.$Å^{-3}$	

Table 18. Atomic coordinates ($\times 10^4$) and equivalent isotropic displacement parameters ($Å^2 \times 10^3$) for LC70513_0m. U(eq) is defined as one third of the trace of the orthogonalized U^{ij} tensor.

	x	y	z	U(eq)
Dy(01)	5000	5000	5896(1)	25(1)
O(1)	4584(1)	4584(1)	5416(1)	21(1)
O(2)	5000	5681(2)	6226(2)	78(2)
C(1)	5000	6089(3)	6089(3)	78(4)
C(2)	5000	6442(2)	6442(2)	118(6)
C(3)	5000	6329(5)	6886(4)	183(8)
C(5)	5000	7123(3)	7123(3)	251(13)
C(4)	5000	6676(5)	7213(5)	222(9)
N(1)	5000	7382(6)	7618(6)	239(14)

Table 19. Bond lengths [Å] and angles [°] for LC70513_0m.

Dy(01)-O(2)#1	2.265(6)
Dy(01)-O(2)#2	2.265(6)
Dy(01)-O(2)	2.265(6)
Dy(01)-O(2)#3	2.265(6)
Dy(01)-O(1)	2.2709(17)
Dy(01)-O(1)#4	2.2709(17)
Dy(01)-O(1)#5	2.2709(17)
Dy(01)-O(1)#3	2.2709(17)
Dy(01)-Dy(01)#6	3.7895(8)
Dy(01)-Dy(01)#7	3.7895(8)
Dy(01)-Dy(01)#8	3.7895(8)
Dy(01)-Dy(01)#9	3.7895(8)
O(1)-Dy(01)#7	2.2709(17)
O(1)-Dy(01)#6	2.2709(17)
O(2)-C(1)	1.287(9)
C(1)-O(2)#10	1.287(9)
C(1)-C(2)	1.493(13)
C(2)-C(3)#10	1.370(13)
C(2)-C(3)	1.370(13)
C(3)-C(4)	1.427(13)
C(3)-H(3)	0.9400
C(5)-C(4)#10	1.364(15)
C(5)-C(4)	1.364(15)
C(5)-N(1)#11	1.672(14)
C(5)-N(1)	1.672(14)
C(4)-H(4)	0.9400
N(1)-N(1)#11	1.00(5)
N(1)-C(5)#11	1.672(14)
O(2)#1-Dy(01)-O(2)#2	128.2(4)
O(2)#1-Dy(01)-O(2)	79.01(16)
O(2)#2-Dy(01)-O(2)	79.01(16)
O(2)#1-Dy(01)-O(2)#3	79.01(16)
O(2)#2-Dy(01)-O(2)#3	79.01(16)

O(2)-Dy(01)-O(2)#3	128.2(4)
O(2)#1-Dy(01)-O(1)	140.26(10)
O(2)#2-Dy(01)-O(1)	77.5(2)
O(2)-Dy(01)-O(1)	140.26(11)
O(2)#3-Dy(01)-O(1)	77.5(2)
O(2)#1-Dy(01)-O(1)#4	77.5(2)
O(2)#2-Dy(01)-O(1)#4	140.26(11)
O(2)-Dy(01)-O(1)#4	140.26(11)
O(2)#3-Dy(01)-O(1)#4	77.5(2)
O(1)-Dy(01)-O(1)#4	66.47(16)
O(2)#1-Dy(01)-O(1)#5	140.26(11)
O(2)#2-Dy(01)-O(1)#5	77.5(2)
O(2)-Dy(01)-O(1)#5	77.5(2)
O(2)#3-Dy(01)-O(1)#5	140.26(11)
O(1)-Dy(01)-O(1)#5	66.47(16)
O(1)#4-Dy(01)-O(1)#5	101.6(3)
O(2)#1-Dy(01)-O(1)#3	77.5(2)
O(2)#2-Dy(01)-O(1)#3	140.26(11)
O(2)-Dy(01)-O(1)#3	77.5(2)
O(2)#3-Dy(01)-O(1)#3	140.26(11)
O(1)-Dy(01)-O(1)#3	101.6(3)
O(1)#4-Dy(01)-O(1)#3	66.47(16)
O(1)#5-Dy(01)-O(1)#3	66.47(16)
O(2)#1-Dy(01)-Dy(01)#6	160.9(2)
O(2)#2-Dy(01)-Dy(01)#6	70.9(2)
O(2)-Dy(01)-Dy(01)#6	107.98(14)
O(2)#3-Dy(01)-Dy(01)#6	107.98(14)
O(1)-Dy(01)-Dy(01)#6	33.45(6)
O(1)#4-Dy(01)-Dy(01)#6	86.60(13)
O(1)#5-Dy(01)-Dy(01)#6	33.45(6)
O(1)#3-Dy(01)-Dy(01)#6	86.60(13)
O(2)#1-Dy(01)-Dy(01)#7	107.98(13)
O(2)#2-Dy(01)-Dy(01)#7	107.98(14)
O(2)-Dy(01)-Dy(01)#7	160.9(2)
O(2)#3-Dy(01)-Dy(01)#7	70.9(2)

O(1)-Dy(01)-Dy(01)#7	33.45(6)
O(1)#4-Dy(01)-Dy(01)#7	33.45(6)
O(1)#5-Dy(01)-Dy(01)#7	86.60(13)
O(1)#3-Dy(01)-Dy(01)#7	86.60(13)
Dy(01)#6-Dy(01)-Dy(01)#7	60.0
O(2)#1-Dy(01)-Dy(01)#8	107.98(14)
O(2)#2-Dy(01)-Dy(01)#8	107.98(14)
O(2)-Dy(01)-Dy(01)#8	70.9(2)
O(2)#3-Dy(01)-Dy(01)#8	160.9(2)
O(1)-Dy(01)-Dy(01)#8	86.60(13)
O(1)#4-Dy(01)-Dy(01)#8	86.60(13)
O(1)#5-Dy(01)-Dy(01)#8	33.45(6)
O(1)#3-Dy(01)-Dy(01)#8	33.45(6)
Dy(01)#6-Dy(01)-Dy(01)#8	60.0
Dy(01)#7-Dy(01)-Dy(01)#8	90.0
O(2)#1-Dy(01)-Dy(01)#9	70.9(2)
O(2)#2-Dy(01)-Dy(01)#9	160.9(2)
O(2)-Dy(01)-Dy(01)#9	107.98(14)
O(2)#3-Dy(01)-Dy(01)#9	107.98(14)
O(1)-Dy(01)-Dy(01)#9	86.60(13)
O(1)#4-Dy(01)-Dy(01)#9	33.45(6)
O(1)#5-Dy(01)-Dy(01)#9	86.60(13)
O(1)#3-Dy(01)-Dy(01)#9	33.45(6)
Dy(01)#6-Dy(01)-Dy(01)#9	90.0
Dy(01)#7-Dy(01)-Dy(01)#9	60.0
Dy(01)#8-Dy(01)-Dy(01)#9	60.0
Dy(01)-O(1)-Dy(01)#7	113.10(12)
Dy(01)-O(1)-Dy(01)#6	113.10(12)
Dy(01)#7-O(1)-Dy(01)#6	113.10(12)
C(1)-O(2)-Dy(01)	135.5(6)
O(2)#10-C(1)-O(2)	127.2(10)
O(2)#10-C(1)-C(2)	116.4(5)
O(2)-C(1)-C(2)	116.4(5)
C(3)#10-C(2)-C(3)	118.6(13)
C(3)#10-C(2)-C(1)	120.7(7)

C(3)-C(2)-C(1)	120.7(7)
C(2)-C(3)-C(4)	119.0(13)
C(2)-C(3)-H(3)	120.5
C(4)-C(3)-H(3)	120.5
C(4)#10-C(5)-C(4)	112.9(14)
C(4)#10-C(5)-N(1)#11	106.1(10)
C(4)-C(5)-N(1)#11	140.9(12)
C(4)#10-C(5)-N(1)	140.9(12)
C(4)-C(5)-N(1)	106.1(10)
N(1)#11-C(5)-N(1)	34.8(17)
C(5)-C(4)-C(3)	125.2(14)
C(5)-C(4)-H(4)	117.4
C(3)-C(4)-H(4)	117.4
N(1)#11-N(1)-C(5)	72.6(9)
N(1)#11-N(1)-C(5)#11	72.6(8)
C(5)-N(1)-C(5)#11	145.2(17)

Symmetry transformations used to generate equivalent atoms:

#1 y,x,z

#2 -y+1,-x+1,z

#3 -x+1,-y+1,z

#4 -x+1,y,z

#5 x,-y+1,z

#6 -z+1,-x+1,-y+1

#7 -y+1,-z+1,-x+1

#8 y,z,x

#9 z,x,y

#10 -x+1,z,y

#11 -x+1,-y+3/2,-z+3/2

Table 20. Anisotropic displacement parameters ($Å^2 \times 10^3$) for LC70513_0m. The anisotropic displacement factor exponent takes the form: $-2\pi^2[h^2 a^{*2} U^{11} + ... + 2 h k a^* b^* U^{12}]$

	U^{11}	U^{22}	U^{33}	U^{23}	U^{13}	U^{12}
Dy(01)	31(1)	31(1)	12(1)	0	0	0
O(1)	21(1)	21(1)	21(1)	-1(1)	-1(1)	1(1)
O(2)	93(5)	79(5)	61(4)	-45(4)	0	0
C(1)	102(11)	67(6)	67(6)	-38(8)	0	0
C(2)	162(16)	96(7)	96(7)	-62(9)	0	0
C(3)	300(20)	171(12)	84(7)	-77(9)	0	0
C(5)	400(30)	177(13)	177(13)	-93(17)	0	0
C(4)	370(20)	199(15)	97(10)	-85(12)	0	0
N(1)	420(30)	150(16)	150(16)	-35(18)	0	0

Table 21. Hydrogen coordinates ($\times 10^4$) and isotropic displacement parameters ($Å^2 \times 10^3$) for LC70513_0m.

	x	y	z	U(eq)
H(3)	5000	6027	6974	220
H(4)	5000	6590	7516	266

APPENDIX D

DY^{3+}-SBDC CRYSTALLOGRAPHIC DATA

First paragraph. X-ray diffraction data of Dy^{3+}-SBDC were collected on a Bruker X8 Prospector Ultra equipped with an Apex II CCD detector and an IμS micro-focus CuK\α source (λ = 1.54178 Å). An octahedron-shaped colorless crystal with dimensions 0.16 × 0.14 × 0.12 mm^3 was sealed in a 0.5 mm OD glass number 50 (borosilicate glass) capillary tube with MiTeGen MicroTools before mounted onto a goniometer head. The data were collected at room temperature.

A cubic unit cell with dimensions $a = b = c = 30.7854(3)$ Å, $\alpha = \beta = \gamma = 90$ °, was derived from the least-square refinement of 9729 reflections in the range of $2.486 < \theta < 67.851$. Centrosymmetric space group Fm-3m was determined based on intensity statistics and the systematic absences.

The data were collected to 0.81 Å and truncated to 0.83 Å for integration by Bruker program SAINT[202], empirical absorption correction was applied using program SADABS[202]. The structure was solved with direct method using SHELXT[207] and refined by full-matrix least-squares on F^2 using SHELXL[204] in Olex2[205]. All the Dy, O atoms and some C atoms were located easily, the rest of the C atoms were generated via subsequent difference Fourier

syntheses. Idealized atom positions were calculated for H atoms (d-(C-H) = 0.950 Å). The H atoms on the alkene group were omitted.

All the non-H atoms were refined anisotropically. All the H atoms were refined isotropically. ADP restraints were applied to the C atoms using SIMU command. DFIX was also used to restrain some of the bond lengths.

Response to checkCIF alert:

PLAT602_ALERT_2_A VERY LARGE Solvent Accessible VOID(S) in Structure

Response: The sample is a porous metal-organic framework material and the very large void is reasonable. There are severely disordered solvent molecules that cannot be crystallographically located residing in the void(s).

Table 22. Crystal data and structure refinement for LC61371r_0m

Identification code	lc61371r_0m	
Empirical formula	C54 H24 Dy3 O28	
Formula weight	1608.23	
Temperature	296(2) K	
Wavelength	1.54178 Å	
Crystal system	Cubic	
Space group	Fm-3m	
Unit cell dimensions	a = 30.7854(3) Å	α = 90°
	b = 30.7854(3) Å	β = 90°
	c = 30.7854(3) Å	γ = 90°
Volume	29176.6(5) $Å^3$	
Z	8	
Density (calculated)	0.732 mg/m^3	
Absorption coefficient	8.404 mm^{-1}	
F(000)	6160	
Crystal size	0.16 × 0.14 × 0.12 mm^3	
Theta range for data collection	2.49 to 68.26°.	
Index ranges	-37<=h<=37, -36<=k<=37, -37<=l<=37	
Reflections collected	76998	
Independent reflections	1382 [R(int) = 0.1175]	
Completeness to theta = 68.26°	99.4 %	
Absorption correction	Semi-empirical from equivalents	
Max. and min. transmission	0.4321 and 0.3466	
Refinement method	Full-matrix least-squares on F^2	
Data / restraints / parameters	1382 / 33 / 49	
Goodness-of-fit on F^2	1.174	
Final R indices [I>2sigma(I)]	R1 = 0.0945, wR2 = 0.3000	
R indices (all data)	R1 = 0.0968, wR2 = 0.3012	
Largest diff. peak and hole	1.189 and -1.525 e.$Å^{-3}$	

Table 23. Atomic coordinates ($\times 10^4$) and equivalent isotropic displacement parameters ($Å^2 \times 10^3$) for LC61371r_0m. U(eq) is defined as one third of the trace of the orthogonalized U^{ij} tensor.

	x	y	z	U(eq)
Dy(1)	5896(1)	5000	5000	31(1)
C(1)	6080(6)	5000	6080(6)	118(13)
C(2)	6419(7)	5000	6419(7)	151(13)
C(3)	6860(11)	5000	6307(12)	205(14)
C(4)	7173(10)	5000	6640(8)	255(17)
C(5)	7081(8)	5000	7081(8)	290(20)
C(6)	7543(13)	5000	7221(15)	320(30)
O(1)	6220(4)	5000	5675(4)	79(4)
O(2)	5410(2)	4590(2)	4590(2)	19(3)
O(3)	8450(40)	5670(30)	6550(40)	960(140)

Table 24. Bond lengths [Å] and angles [°] for LC61371r_0m.

Dy(1)-O(1)#1	2.304(12)
Dy(1)-O(1)#2	2.304(12)
Dy(1)-O(1)	2.304(12)
Dy(1)-O(1)#3	2.304(12)
Dy(1)-O(2)	2.329(3)
Dy(1)-O(2)#4	2.329(3)
Dy(1)-O(2)#2	2.329(3)
Dy(1)-O(2)#5	2.329(3)
Dy(1)-Dy(1)#6	3.9022(18)
Dy(1)-Dy(1)#7	3.9022(18)
Dy(1)-Dy(1)#8	3.9022(18)
Dy(1)-Dy(1)#9	3.9022(18)
C(1)-O(1)#10	1.319(18)
C(1)-O(1)	1.319(18)
C(1)-C(2)	1.48(4)
C(2)-C(3)	1.40(4)
C(2)-C(3)#10	1.40(4)
C(3)-C(4)	1.406(18)
C(3)-H(3)	0.9300
C(4)-C(5)	1.386(19)
C(4)-H(4)	0.9300
C(5)-C(4)#10	1.386(19)
C(5)-C(6)	1.487(19)
C(5)-C(6)#10	1.487(19)
C(6)-C(6)#11	1.03(6)
C(6)-C(6)#10	1.40(10)
C(6)-C(6)#12	1.73(10)
O(2)-Dy(1)#7	2.329(3)
O(2)-Dy(1)#6	2.329(3)
O(1)#1-Dy(1)-O(1)#2	79.2(3)
O(1)#1-Dy(1)-O(1)	79.2(3)
O(1)#2-Dy(1)-O(1)	128.8(7)
O(1)#1-Dy(1)-O(1)#3	128.8(7)

O(1)#2-Dy(1)-O(1)#3	79.2(3)
O(1)-Dy(1)-O(1)#3	79.2(3)
O(1)#1-Dy(1)-O(2)	77.8(4)
O(1)#2-Dy(1)-O(2)	77.8(4)
O(1)-Dy(1)-O(2)	140.0(2)
O(1)#3-Dy(1)-O(2)	140.0(2)
O(1)#1-Dy(1)-O(2)#4	140.0(2)
O(1)#2-Dy(1)-O(2)#4	77.8(4)
O(1)-Dy(1)-O(2)#4	140.0(2)
O(1)#3-Dy(1)-O(2)#4	77.8(4)
O(2)-Dy(1)-O(2)#4	65.6(3)
O(1)#1-Dy(1)-O(2)#2	77.8(4)
O(1)#2-Dy(1)-O(2)#2	140.0(2)
O(1)-Dy(1)-O(2)#2	77.8(4)
O(1)#3-Dy(1)-O(2)#2	140.0(2)
O(2)-Dy(1)-O(2)#2	65.6(3)
O(2)#4-Dy(1)-O(2)#2	100.0(6)
O(1)#1-Dy(1)-O(2)#5	140.0(2)
O(1)#2-Dy(1)-O(2)#5	140.0(2)
O(1)-Dy(1)-O(2)#5	77.8(4)
O(1)#3-Dy(1)-O(2)#5	77.8(4)
O(2)-Dy(1)-O(2)#5	100.0(6)
O(2)#4-Dy(1)-O(2)#5	65.6(3)
O(2)#2-Dy(1)-O(2)#5	65.6(3)
O(1)#1-Dy(1)-Dy(1)#6	70.6(4)
O(1)#2-Dy(1)-Dy(1)#6	107.8(3)
O(1)-Dy(1)-Dy(1)#6	107.8(3)
O(1)#3-Dy(1)-Dy(1)#6	160.6(4)
O(2)-Dy(1)-Dy(1)#6	33.11(11)
O(2)#4-Dy(1)-Dy(1)#6	85.9(2)
O(2)#2-Dy(1)-Dy(1)#6	33.11(11)
O(2)#5-Dy(1)-Dy(1)#6	85.9(2)
O(1)#1-Dy(1)-Dy(1)#7	107.8(3)
O(1)#2-Dy(1)-Dy(1)#7	70.6(4)
O(1)-Dy(1)-Dy(1)#7	160.6(4)

O(1)#3-Dy(1)-Dy(1)#7	107.8(2)
O(2)-Dy(1)-Dy(1)#7	33.11(12)
O(2)#4-Dy(1)-Dy(1)#7	33.11(11)
O(2)#2-Dy(1)-Dy(1)#7	85.9(2)
O(2)#5-Dy(1)-Dy(1)#7	85.9(2)
Dy(1)#6-Dy(1)-Dy(1)#7	60.0
O(1)#1-Dy(1)-Dy(1)#8	160.6(4)
O(1)#2-Dy(1)-Dy(1)#8	107.8(2)
O(1)-Dy(1)-Dy(1)#8	107.8(2)
O(1)#3-Dy(1)-Dy(1)#8	70.6(4)
O(2)-Dy(1)-Dy(1)#8	85.9(2)
O(2)#4-Dy(1)-Dy(1)#8	33.11(12)
O(2)#2-Dy(1)-Dy(1)#8	85.9(2)
O(2)#5-Dy(1)-Dy(1)#8	33.11(12)
Dy(1)#6-Dy(1)-Dy(1)#8	90.0
Dy(1)#7-Dy(1)-Dy(1)#8	60.0
O(1)#1-Dy(1)-Dy(1)#9	107.8(3)
O(1)#2-Dy(1)-Dy(1)#9	160.6(4)
O(1)-Dy(1)-Dy(1)#9	70.6(4)
O(1)#3-Dy(1)-Dy(1)#9	107.8(3)
O(2)-Dy(1)-Dy(1)#9	85.9(2)
O(2)#4-Dy(1)-Dy(1)#9	85.9(2)
O(2)#2-Dy(1)-Dy(1)#9	33.11(12)
O(2)#5-Dy(1)-Dy(1)#9	33.11(12)
Dy(1)#6-Dy(1)-Dy(1)#9	60.0
Dy(1)#7-Dy(1)-Dy(1)#9	90.0
Dy(1)#8-Dy(1)-Dy(1)#9	60.0
O(1)#10-C(1)-O(1)	128(2)
O(1)#10-C(1)-C(2)	115.9(12)
O(1)-C(1)-C(2)	115.9(12)
C(3)-C(2)-C(3)#10	118(3)
C(3)-C(2)-C(1)	120.8(17)
C(3)#10-C(2)-C(1)	120.8(17)
C(2)-C(3)-C(4)	119(4)
C(2)-C(3)-H(3)	120.5

C(4)-C(3)-H(3)	120.5
C(5)-C(4)-C(3)	125(4)
C(5)-C(4)-H(4)	117.5
C(3)-C(4)-H(4)	117.5
C(4)-C(5)-C(4)#10	114(4)
C(4)-C(5)-C(6)	95(2)
C(4)#10-C(5)-C(6)	151(4)
C(4)-C(5)-C(6)#10	151(4)
C(4)#10-C(5)-C(6)#10	95(2)
C(6)-C(5)-C(6)#10	56(5)
C(6)#11-C(6)-C(6)#10	90.000(12)
C(6)#11-C(6)-C(5)	152(2)
C(6)#10-C(6)-C(5)	62(2)
C(6)#11-C(6)-C(6)#12	54(2)
C(6)#10-C(6)-C(6)#12	36(2)
C(5)-C(6)-C(6)#12	98(4)
C(1)-O(1)-Dy(1)	135.4(14)
Dy(1)-O(2)-Dy(1)#7	113.8(2)
Dy(1)-O(2)-Dy(1)#6	113.8(2)
Dy(1)#7-O(2)-Dy(1)#6	113.8(2)

Symmetry transformations used to generate equivalent atoms:

#1 x,-z+1,-y+1

#2 x,y,-z+1

#3 x,z,-y+1

#4 x,-y+1,z

#5 x,-y+1,-z+1

#6 -z+1,-x+1,-y+1

#7 -y+1,-z+1,-x+1

#8 z,x,y

#9 y,z,x

#10 z,-y+1,x

#11 -z+3/2,y,-x+3/2

#12 -x+3/2,-y+1,-z+3/2

Table 25. Anisotropic displacement parameters ($Å^2 \times 10^3$) for LC61371r_0m. The anisotropic displacement factor exponent takes the form: $-2\pi^2[h^2 a^{*2} U^{11} + ... + 2 h k a^* b^* U^{12}]$

	U^{11}	U^{22}	U^{33}	U^{23}	U^{13}	U^{12}
Dy(1)	17(1)	38(1)	38(1)	0	0	0
C(1)	88(16)	180(30)	88(16)	0	-70(20)	0
C(2)	100(15)	250(30)	100(15)	0	-81(19)	0
C(3)	101(19)	350(40)	170(20)	0	-97(19)	0
C(4)	140(20)	430(40)	200(30)	0	-130(20)	0
C(5)	190(30)	490(50)	190(30)	0	-150(30)	0
C(6)	190(40)	540(50)	240(40)	0	-150(30)	0
O(1)	66(8)	101(11)	69(9)	0	-38(7)	0
O(2)	19(3)	19(3)	19(3)	1(3)	-1(3)	-1(3)
O(3)	1200(200)	440(120)	1200(200)	370(120)	-400(200)	-370(120)

Table 26. Hydrogen coordinates ($\times 10^4$) and isotropic displacement parameters ($Å^2 \times 10^3$) for LC61371r_0m.

	x	y	z	U(eq)
H(3)	6945	5000	6017	246
H(4)	7464	5000	6558	306

APPENDIX E

COMPOUND S11 CRYSTALLOGRAPHIC DATA

X-ray diffraction data of S11 were collected on a Bruker X8 Prospector Ultra equipped with an Apex II CCD detector and an IμS micro-focus CuK\α source (λ = 1.54178 Å). A needle-shaped colorless crystal with dimensions 0.20 × 0.02 × 0.02 mm^3 was mounted on a goniometer head using MiTeGen MicroMesh. The data were collected under N_2 stream at 240K.

A triclinic unit cell with dimensions a = 3.9365(8) Å, b = 12.261(2) Å, c = 15.859(3) Å, α = 111.241(13)°, β = 91.027(15)°, γ = 91.753(15)°, was derived from the least-square refinement of 3947 reflections in the range of $2.991 < \theta < 50.608$. Centrosymmetric space group P-1 was determined based on intensity statistics and the lack of systematic absences.

The data were collected to 0.83 Å and truncated to 1.00 Å for integration by Bruker program SAINT[202], empirical absorption correction was applied using program SADABS[202]. The structure was solved with direct method using SHELXT[207] and refined by full-matrix least-squares on F^2 using SHELXL[204] in Olex2[205]. Most atoms were located easily, the rest of the non-H atoms were generated via subsequent difference Fourier syntheses. Idealized atom positions were calculated for H atoms (d-(C_{phenyl}-H) = 0.950 Å, d-(C_{methyl}-H) = 0.979 Å).

All the non-H atoms were refined anisotropically. All the H atoms were refined isotropically.

Response to checkCIF alert:

THETM01_ALERT_3_A The value of sine(theta_max)/wavelength is less than 0.550 Calculated sine(theta_max)/wavelength = 0.5020

Response: Data were collected to 0.83 Å but later truncated to 1 Å for integration due to weak diffraction. Nonetheless the solved molecular structure and composition are not in doubt.

Table 27. Crystal data and structure refinement for LC40871_0m

Identification code	lc40871_0m	
Empirical formula	C16 H10 Br N O4	
Formula weight	360.16	
Temperature	240(2) K	
Wavelength	1.54178 Å	
Crystal system	Triclinic	
Space group	P-1	
Unit cell dimensions	a = 3.9365(8) Å	α = 111.241(13)°
	b = 12.261(2) Å	β = 91.027(15)°
	c = 15.859(3) Å	γ = 91.753(15)°
Volume	712.8(2) $Å^3$	
Z	2	
Density (calculated)	1.678 mg/m^3	
Absorption coefficient	4.106 mm^{-1}	
F(000)	360	
Crystal size	0.20 × 0.02 × 0.02 mm^3	
Theta range for data collection	2.99 to 50.71°.	
Index ranges	-3<=h<=3, -12<=k<=12, -15<=l<=15	
Reflections collected	5089	
Independent reflections	1477 [R(int) = 0.0332]	
Completeness to theta = 50.71°	99.1 %	
Absorption correction	Semi-empirical from equivalents	
Max. and min. transmission	0.9224 and 0.4939	
Refinement method	Full-matrix least-squares on F^2	
Data / restraints / parameters	1477 / 0 / 200	
Goodness-of-fit on F^2	1.054	
Final R indices [I>2sigma(I)]	R1 = 0.0772, wR2 = 0.1923	
R indices (all data)	R1 = 0.0817, wR2 = 0.1986	
Largest diff. peak and hole	2.546 and -0.623 e.$Å^{-3}$	

Table 28. Atomic coordinates ($\times 10^4$) and equivalent isotropic displacement parameters ($Å^2 \times 10^3$) for LC40871_0m. U(eq) is defined as one third of the trace of the orthogonalized U^{ij} tensor.

	x	y	z	U(eq)
Br(1)	8716(2)	1137(1)	-580(1)	51(1)
O(2)	-3058(14)	10135(4)	6421(3)	47(2)
O(1)	-1464(17)	9261(5)	7383(4)	55(2)
N(2)	6720(20)	5487(7)	1417(5)	56(2)
C(2)	-620(18)	8302(6)	5819(5)	35(2)
C(1)	-1730(19)	9256(7)	6630(6)	40(2)
C(11)	6411(18)	4276(6)	1363(5)	34(2)
C(10)	5061(18)	3998(7)	2077(5)	34(2)
C(5)	1593(18)	6445(6)	4345(5)	36(2)
C(7)	788(19)	7332(7)	5929(5)	39(2)
C(6)	1845(19)	6407(7)	5205(5)	39(2)
C(15)	4907(19)	2802(7)	1944(5)	39(2)
C(12)	7522(18)	3437(6)	589(5)	34(2)
C(14)	6030(20)	1960(7)	1176(5)	40(2)
C(4)	160(20)	7404(7)	4226(5)	44(2)
C(3)	-870(20)	8323(7)	4953(5)	41(2)
C(8)	2790(20)	5519(8)	3565(6)	44(2)
C(13)	7347(19)	2290(7)	491(5)	37(2)
C(9)	3850(20)	4827(7)	2875(6)	42(2)
C(16)	-4190(20)	11107(7)	7181(6)	50(2)
O(3)	5750(50)	6216(9)	1979(9)	209(9)
O(4)	8040(50)	5744(8)	903(12)	272(13)

Table 29. Bond lengths [Å] and angles [°] for LC40871_0m.

Br(1)-C(13)	1.874(8)
O(2)-C(1)	1.354(10)
O(2)-C(16)	1.443(10)
O(1)-C(1)	1.194(9)
N(2)-O(3)	1.093(11)
N(2)-O(4)	1.106(11)
N(2)-C(11)	1.457(11)
C(2)-C(3)	1.384(11)
C(2)-C(7)	1.392(11)
C(2)-C(1)	1.475(11)
C(11)-C(12)	1.374(11)
C(11)-C(10)	1.404(11)
C(10)-C(15)	1.403(11)
C(10)-C(9)	1.408(12)
C(5)-C(6)	1.384(11)
C(5)-C(4)	1.390(11)
C(5)-C(8)	1.442(12)
C(7)-C(6)	1.371(11)
C(7)-H(7)	0.9400
C(6)-H(6)	0.9400
C(15)-C(14)	1.372(11)
C(15)-H(15)	0.9400
C(12)-C(13)	1.358(11)
C(12)-H(12)	0.9400
C(14)-C(13)	1.392(11)
C(14)-H(14)	0.9400
C(4)-C(3)	1.367(11)
C(4)-H(4)	0.9400
C(3)-H(3)	0.9400
C(8)-C(9)	1.206(12)
C(16)-H(16A)	0.9700
C(16)-H(16B)	0.9700
C(16)-H(16C)	0.9700

C(1)-O(2)-C(16)	115.2(6)
O(3)-N(2)-O(4)	114.7(9)
O(3)-N(2)-C(11)	122.8(8)
O(4)-N(2)-C(11)	122.5(9)
C(3)-C(2)-C(7)	118.1(7)
C(3)-C(2)-C(1)	123.5(7)
C(7)-C(2)-C(1)	118.3(7)
O(1)-C(1)-O(2)	123.8(7)
O(1)-C(1)-C(2)	124.3(7)
O(2)-C(1)-C(2)	111.9(7)
C(12)-C(11)-C(10)	122.5(7)
C(12)-C(11)-N(2)	116.7(7)
C(10)-C(11)-N(2)	120.8(7)
C(15)-C(10)-C(11)	115.3(7)
C(15)-C(10)-C(9)	120.3(7)
C(11)-C(10)-C(9)	124.3(7)
C(6)-C(5)-C(4)	119.3(7)
C(6)-C(5)-C(8)	121.8(7)
C(4)-C(5)-C(8)	118.8(7)
C(6)-C(7)-C(2)	121.6(7)
C(6)-C(7)-H(7)	119.2
C(2)-C(7)-H(7)	119.2
C(7)-C(6)-C(5)	119.5(7)
C(7)-C(6)-H(6)	120.2
C(5)-C(6)-H(6)	120.2
C(14)-C(15)-C(10)	122.6(7)
C(14)-C(15)-H(15)	118.7
C(10)-C(15)-H(15)	118.7
C(13)-C(12)-C(11)	120.3(7)
C(13)-C(12)-H(12)	119.9
C(11)-C(12)-H(12)	119.9
C(15)-C(14)-C(13)	119.4(7)
C(15)-C(14)-H(14)	120.3
C(13)-C(14)-H(14)	120.3

C(3)-C(4)-C(5)	120.6(7)
C(3)-C(4)-H(4)	119.7
C(5)-C(4)-H(4)	119.7
C(4)-C(3)-C(2)	120.8(7)
C(4)-C(3)-H(3)	119.6
C(2)-C(3)-H(3)	119.6
C(9)-C(8)-C(5)	173.6(9)
C(12)-C(13)-C(14)	119.9(7)
C(12)-C(13)-Br(1)	120.4(6)
C(14)-C(13)-Br(1)	119.6(6)
C(8)-C(9)-C(10)	178.7(9)
O(2)-C(16)-H(16A)	109.5
O(2)-C(16)-H(16B)	109.5
H(16A)-C(16)-H(16B)	109.5
O(2)-C(16)-H(16C)	109.5
H(16A)-C(16)-H(16C)	109.5
H(16B)-C(16)-H(16C)	109.5

Table 30. Anisotropic displacement parameters ($Å^2 \times 10^3$) for LC40871_0m. The anisotropic displacement factor exponent takes the form: $-2\pi^2[h^2 a^{*2} U^{11} + ... + 2 h k a^* b^* U^{12}]$

	U^{11}	U^{22}	U^{33}	U^{23}	U^{13}	U^{12}
Br(1)	64(1)	42(1)	36(1)	-2(1)	9(1)	9(1)
O(2)	74(4)	27(3)	35(3)	5(3)	1(3)	13(3)
O(1)	97(5)	38(4)	25(4)	3(3)	9(3)	14(3)
N(2)	86(6)	40(5)	41(5)	11(4)	21(4)	14(4)
C(2)	42(5)	27(5)	33(5)	6(4)	3(3)	-4(3)
C(1)	44(5)	34(5)	37(6)	5(4)	4(4)	-6(4)
C(11)	44(5)	23(5)	32(5)	6(4)	-3(3)	0(3)
C(10)	40(5)	33(5)	25(4)	4(4)	-8(3)	0(3)
C(5)	39(5)	28(5)	29(5)	-4(4)	5(3)	-1(3)
C(7)	47(5)	35(5)	35(5)	12(4)	7(4)	1(4)
C(6)	43(5)	29(5)	40(5)	7(4)	4(4)	2(3)
C(15)	46(5)	42(5)	33(5)	17(4)	4(4)	5(4)
C(12)	40(5)	35(5)	26(4)	8(4)	-2(3)	0(4)
C(14)	55(5)	27(5)	37(5)	9(4)	-3(4)	0(4)
C(4)	64(6)	37(5)	27(5)	7(4)	6(4)	0(4)
C(3)	60(5)	27(5)	37(5)	12(4)	-2(4)	2(4)
C(8)	46(5)	39(5)	44(6)	10(5)	3(4)	-5(4)
C(13)	38(5)	37(5)	29(5)	2(4)	0(3)	3(3)
C(9)	42(5)	43(5)	35(5)	6(5)	4(4)	8(4)
C(16)	66(6)	32(5)	48(5)	8(4)	8(4)	15(4)
O(3)	420(20)	60(6)	191(12)	79(8)	216(16)	90(10)
O(4)	470(30)	52(6)	310(20)	68(9)	310(20)	50(10)

Table 31. Hydrogen coordinates ($\times 10^4$) and isotropic displacement parameters ($Å^2 \times 10^3$) for LC40871_0m.

	x	y	z	U(eq)
H(7)	1019	7311	6513	47
H(6)	2736	5752	5293	47
H(15)	3995	2569	2399	47
H(12)	8407	3659	126	41
H(14)	5920	1168	1114	49
H(4)	-108	7419	3640	52
H(3)	-1762	8978	4865	50
H(16A)	-5405	11634	6962	76
H(16B)	-2241	11523	7554	76
H(16C)	-5693	10816	7538	76

APPENDIX F

COMPOUND S12 CRYSTALLOGRAPHIC DATA

X-ray diffraction data of S12 were collected on a Bruker X8 Prospector Ultra equipped with an Apex II CCD detector and an IμS micro-focus CuK\α source (λ = 1.54178 Å). A plate-shaped colorless crystal with dimensions 0.18 × 0.08 × 0.01 mm^3 was mounted on a goniometer head using MiTeGen MicroMesh. The data were collected under N_2 stream at 240K.

A monoclinic unit cell with dimensions a = 7.4170(4) Å, b = 10.5890(6) Å, c = 25.5745(16) Å, $\alpha = \gamma = 90°$, β = 93.439(5)° was derived from the least-square refinement of 4068 reflections in the range of 3.463 < θ < 52.680. Centrosymmetric space group P2(1)/c was determined based on intensity statistics and the systematic absences.

The data were collected and integrated to 0.97 Å by Bruker program SAINT[202] due to weak diffraction, empirical absorption correction was applied using program SADABS[202]. The structure was solved with direct method using SHELXT[207] and refined by full-matrix least-squares on F^2 using SHELXL[204] in Olex2[205]. Most atoms were located easily, the rest of the non-H atoms were generated via subsequent difference Fourier syntheses. Idealized atom positions were calculated for H atoms (d-(C_{phenyl}-H) = 0.950 Å, d-(C_{methyl}-H) = 0.979 Å).

All the non-H atoms were refined anisotropically. All the H atoms were refined isotropically.

Response to checkCIF alert:

THETM01_ALERT_3_A The value of sine(theta_max)/wavelength is less than 0.550 Calculated sin(theta_max)/wavelength = 0.5166

Response: Data were collected to 0.83 Å but later truncated to 0.97 Å for integration due to weak diffraction. Nonetheless the solved molecular structure and composition are not in doubt.

Table 32. Crystal data and structure refinement for LC6111_0m

Identification code	lc6111_0m	
Empirical formula	C24 H17 N O6	
Formula weight	415.39	
Temperature	240(2) K	
Wavelength	1.54178 Å	
Crystal system	Monoclinic	
Space group	P2(1)/c	
Unit cell dimensions	a = 7.4170(4) Å	α = 90°
	b = 10.5890(6) Å	β = 93.439(5)°
	c = 25.5745(16) Å	γ = 90°
Volume	2005.0(2) $Å^3$	
Z	4	
Density (calculated)	1.376 Mg/m^3	
Absorption coefficient	0.831 mm^{-1}	
F(000)	864	
Crystal size	0.18 x 0.08 x 0.01 mm^3	
Theta range for data collection	3.46 to 52.80°.	
Index ranges	-7<=h<=7, -10<=k<=10, -26<=l<=26	
Reflections collected	8883	
Independent reflections	2293 [R(int) = 0.0531]	
Completeness to theta = 52.80°	99.0 %	
Absorption correction	Semi-empirical from equivalents	
Max. and min. transmission	0.9917 and 0.8648	
Refinement method	Full-matrix least-squares on F^2	
Data / restraints / parameters	2293 / 0 / 280	
Goodness-of-fit on F^2	1.538	
Final R indices [I>2sigma(I)]	R1 = 0.0940, wR2 = 0.2302	
R indices (all data)	R1 = 0.1296, wR2 = 0.2448	
Largest diff. peak and hole	0.655 and -0.282 e.$Å^{-3}$	

Table 33. Atomic coordinates ($\times 10^4$) and equivalent isotropic displacement parameters ($Å^2 \times 10^3$) for LC6111_0m. U(eq) is defined as one third of the trace of the orthogonalized U^{ij} tensor.

	x	y	z	U(eq)
O(3)	534(5)	4073(4)	1645(2)	60(1)
O(1)	3794(5)	4051(4)	8704(2)	67(1)
O(2)	4879(6)	5999(5)	8696(2)	70(1)
O(4)	1521(6)	6067(5)	1625(2)	74(1)
C(4)	3382(5)	5028(5)	6800(2)	30(1)
C(1)	3924(5)	5051(5)	7891(2)	36(1)
C(15)	1747(6)	4964(5)	3539(2)	39(2)
C(18)	1312(5)	5038(5)	2448(2)	34(1)
C(7)	3102(6)	5018(5)	6233(2)	37(1)
C(3)	4154(6)	6074(5)	7064(2)	36(1)
N(1)	1894(8)	7294(6)	5154(2)	64(2)
C(5)	2893(6)	3994(5)	7102(2)	38(1)
C(10)	2555(6)	5013(6)	5126(2)	41(2)
C(19)	814(6)	3969(5)	2720(2)	37(1)
C(2)	4429(6)	6068(5)	7594(2)	34(1)
C(6)	3154(6)	3999(5)	7632(2)	34(1)
C(20)	1047(6)	3913(5)	3258(2)	36(1)
C(16)	2197(6)	6050(5)	3260(2)	40(1)
C(17)	1985(6)	6076(5)	2732(2)	41(2)
C(22)	1142(7)	5143(7)	1871(3)	50(2)
C(21)	4250(7)	5112(7)	8461(2)	48(2)
C(14)	2005(6)	4939(5)	4097(2)	44(2)
C(8)	2644(7)	6118(6)	5957(2)	50(2)
C(9)	2386(7)	6108(6)	5414(2)	54(2)
O(6)	2748(8)	7622(6)	4787(2)	113(2)
O(5)	683(9)	7902(6)	5321(3)	126(2)
C(13)	2272(7)	4981(7)	4559(3)	64(2)
C(12)	3261(7)	3934(6)	5937(3)	55(2)
C(11)	2994(7)	3920(6)	5400(3)	60(2)
C(24)	387(9)	4080(8)	1076(3)	82(2)
C(23)	4115(11)	4034(8)	9266(3)	97(3)

Table 34. Bond lengths [Å] and angles [°] for LC6111_0m.

O(3)-C(22)	1.338(7)
O(3)-C(24)	1.451(7)
O(1)-C(21)	1.337(7)
O(1)-C(23)	1.442(7)
O(2)-C(21)	1.195(7)
O(4)-C(22)	1.205(7)
C(4)-C(3)	1.401(7)
C(4)-C(5)	1.401(7)
C(4)-C(7)	1.452(7)
C(1)-C(2)	1.382(7)
C(1)-C(6)	1.399(7)
C(1)-C(21)	1.465(8)
C(15)-C(16)	1.403(7)
C(15)-C(20)	1.407(7)
C(15)-C(14)	1.429(8)
C(18)-C(19)	1.391(7)
C(18)-C(17)	1.393(7)
C(18)-C(22)	1.477(8)
C(7)-C(12)	1.383(8)
C(7)-C(8)	1.393(8)
C(3)-C(2)	1.360(7)
C(3)-H(3A)	0.9400
N(1)-O(5)	1.204(7)
N(1)-O(6)	1.215(7)
N(1)-C(9)	1.458(8)
C(5)-C(6)	1.358(7)
C(5)-H(5A)	0.9400
C(10)-C(9)	1.385(8)
C(10)-C(11)	1.383(8)
C(10)-C(13)	1.452(10)
C(19)-C(20)	1.377(7)
C(19)-H(19A)	0.9400
C(2)-H(2A)	0.9400

C(6)-H(6A)	0.9400
C(20)-H(20A)	0.9400
C(16)-C(17)	1.351(7)
C(16)-H(16A)	0.9400
C(17)-H(17A)	0.9400
C(14)-C(13)	1.187(8)
C(8)-C(9)	1.389(8)
C(8)-H(8A)	0.9400
C(12)-C(11)	1.376(8)
C(12)-H(12A)	0.9400
C(11)-H(11A)	0.9400
C(24)-H(24A)	0.9700
C(24)-H(24B)	0.9700
C(24)-H(24C)	0.9700
C(23)-H(23A)	0.9700
C(23)-H(23B)	0.9700
C(23)-H(23C)	0.9700
C(22)-O(3)-C(24)	115.6(5)
C(21)-O(1)-C(23)	116.3(5)
C(3)-C(4)-C(5)	117.6(5)
C(3)-C(4)-C(7)	121.1(5)
C(5)-C(4)-C(7)	121.3(5)
C(2)-C(1)-C(6)	118.5(5)
C(2)-C(1)-C(21)	118.6(5)
C(6)-C(1)-C(21)	123.0(5)
C(16)-C(15)-C(20)	118.7(5)
C(16)-C(15)-C(14)	120.1(5)
C(20)-C(15)-C(14)	121.2(5)
C(19)-C(18)-C(17)	118.6(5)
C(19)-C(18)-C(22)	123.5(5)
C(17)-C(18)-C(22)	117.9(5)
C(12)-C(7)-C(8)	116.4(5)
C(12)-C(7)-C(4)	122.7(5)
C(8)-C(7)-C(4)	121.0(5)
C(2)-C(3)-C(4)	120.7(5)

C(2)-C(3)-H(3A)	119.7
C(4)-C(3)-H(3A)	119.7
O(5)-N(1)-O(6)	123.8(7)
O(5)-N(1)-C(9)	118.0(6)
O(6)-N(1)-C(9)	118.1(6)
C(6)-C(5)-C(4)	121.5(5)
C(6)-C(5)-H(5A)	119.3
C(4)-C(5)-H(5A)	119.3
C(9)-C(10)-C(11)	117.1(5)
C(9)-C(10)-C(13)	122.7(6)
C(11)-C(10)-C(13)	120.2(6)
C(20)-C(19)-C(18)	120.9(5)
C(20)-C(19)-H(19A)	119.6
C(18)-C(19)-H(19A)	119.6
C(3)-C(2)-C(1)	121.5(5)
C(3)-C(2)-H(2A)	119.3
C(1)-C(2)-H(2A)	119.3
C(5)-C(6)-C(1)	120.3(5)
C(5)-C(6)-H(6A)	119.8
C(1)-C(6)-H(6A)	119.8
C(19)-C(20)-C(15)	119.8(5)
C(19)-C(20)-H(20A)	120.1
C(15)-C(20)-H(20A)	120.1
C(17)-C(16)-C(15)	120.6(5)
C(17)-C(16)-H(16A)	119.7
C(15)-C(16)-H(16A)	119.7
C(16)-C(17)-C(18)	121.4(5)
C(16)-C(17)-H(17A)	119.3
C(18)-C(17)-H(17A)	119.3
O(4)-C(22)-O(3)	123.0(6)
O(4)-C(22)-C(18)	125.0(6)
O(3)-C(22)-C(18)	112.0(6)
O(2)-C(21)-O(1)	121.9(6)
O(2)-C(21)-C(1)	124.9(6)
O(1)-C(21)-C(1)	113.2(6)

C(13)-C(14)-C(15)	176.3(6)
C(9)-C(8)-C(7)	120.9(6)
C(9)-C(8)-H(8A)	119.6
C(7)-C(8)-H(8A)	119.6
C(10)-C(9)-C(8)	121.9(6)
C(10)-C(9)-N(1)	120.4(6)
C(8)-C(9)-N(1)	117.8(6)
C(14)-C(13)-C(10)	178.5(6)
C(11)-C(12)-C(7)	122.9(6)
C(11)-C(12)-H(12A)	118.6
C(7)-C(12)-H(12A)	118.6
C(10)-C(11)-C(12)	120.9(6)
C(10)-C(11)-H(11A)	119.6
C(12)-C(11)-H(11A)	119.6
O(3)-C(24)-H(24A)	109.5
O(3)-C(24)-H(24B)	109.5
H(24A)-C(24)-H(24B)	109.5
O(3)-C(24)-H(24C)	109.5
H(24A)-C(24)-H(24C)	109.5
H(24B)-C(24)-H(24C)	109.5
O(1)-C(23)-H(23A)	109.5
O(1)-C(23)-H(23B)	109.5
H(23A)-C(23)-H(23B)	109.5
O(1)-C(23)-H(23C)	109.5
H(23A)-C(23)-H(23C)	109.5
H(23B)-C(23)-H(23C)	109.5

Table 35. Anisotropic displacement parameters ($Å^2 \times 10^3$) for LC6111_0m. The anisotropic displacement factor exponent takes the form: $-2\pi^2[h^2 a^{*2} U^{11} + ... + 2 h k a^* b^* U^{12}]$

	U^{11}	U^{22}	U^{33}	U^{23}	U^{13}	U^{12}
O(3)	70(2)	62(3)	47(3)	-4(2)	-6(2)	-2(2)
O(1)	87(3)	62(3)	51(3)	17(2)	-3(2)	-9(2)
O(2)	89(3)	59(3)	60(3)	-8(2)	-12(2)	-5(3)
O(4)	108(3)	53(3)	59(3)	15(3)	-1(2)	0(3)
C(4)	26(2)	26(4)	38(3)	2(3)	2(2)	5(2)
C(1)	28(3)	31(4)	48(4)	1(3)	1(2)	3(2)
C(15)	26(3)	43(4)	50(4)	-10(3)	8(2)	5(2)
C(18)	25(2)	32(4)	42(3)	3(3)	-2(2)	7(2)
C(7)	30(3)	18(3)	63(4)	-1(3)	6(2)	1(2)
C(3)	28(2)	19(3)	62(4)	4(3)	4(2)	1(2)
N(1)	80(4)	52(4)	60(4)	13(3)	-4(3)	0(3)
C(5)	27(2)	24(3)	61(4)	-3(3)	4(2)	-3(2)
C(10)	38(3)	44(4)	41(4)	-5(3)	2(2)	0(3)
C(19)	28(2)	26(3)	57(4)	-8(3)	2(2)	1(2)
C(2)	30(2)	29(3)	43(4)	-1(3)	0(2)	1(2)
C(6)	35(3)	22(3)	46(4)	8(3)	6(2)	0(2)
C(20)	32(3)	30(4)	49(4)	-5(3)	8(2)	-1(2)
C(16)	37(3)	32(4)	50(4)	-9(3)	3(2)	-3(2)
C(17)	33(3)	23(3)	67(4)	4(3)	5(3)	1(2)
C(22)	37(3)	48(5)	66(5)	-6(4)	-2(3)	8(3)
C(21)	44(3)	41(4)	57(4)	4(4)	0(3)	8(3)
C(14)	38(3)	53(4)	42(4)	-6(3)	6(3)	-6(3)
C(8)	47(3)	49(4)	54(4)	-7(3)	4(3)	-1(3)
C(9)	52(3)	53(5)	57(4)	2(4)	-2(3)	-2(3)
O(6)	146(5)	104(5)	89(4)	35(4)	14(4)	-11(4)
O(5)	139(5)	85(5)	155(6)	10(4)	18(4)	48(4)
C(13)	49(3)	73(6)	71(5)	-1(4)	10(3)	-5(3)
C(12)	58(3)	44(4)	64(5)	0(3)	7(3)	2(3)
C(11)	66(4)	50(5)	63(5)	-10(4)	4(3)	8(3)
C(24)	90(5)	99(6)	56(5)	-6(4)	-10(4)	6(4)
C(23)	128(6)	105(7)	56(5)	23(5)	-5(4)	-7(5)

Table 36. Hydrogen coordinates ($\times 10^4$) and isotropic displacement parameters ($Å^2 \times 10^3$) for LC6111_0m.

	x	y	z	U(eq)
H(3A)	4485	6786	6872	44
H(5A)	2372	3281	6935	45
H(19A)	312	3274	2534	44
H(2A)	4974	6772	7763	41
H(6A)	2816	3293	7826	41
H(20A)	740	3176	3437	44
H(16A)	2649	6764	3442	47
H(17A)	2299	6811	2552	49
H(8A)	2507	6878	6141	60
H(12A)	3564	3174	6111	66
H(11A)	3113	3157	5218	72
H(24A)	-55	3267	950	124
H(24B)	1564	4241	945	124
H(24C)	-448	4737	955	124
H(23A)	3744	3225	9401	145
H(23B)	3426	4703	9419	145
H(23C)	5392	4162	9355	145

BIBLIOGRAPHY

(1) Kickelbick, G. In *Hybrid Materials*; Wiley-VCH Verlag GmbH & Co. KGaA: 2007, p 1.

(2) Li, H.; Eddaoudi, M.; O'Keeffe, M.; Yaghi, O. M. *Nature* **1999**, *402*, 276.

(3) James, S. L. *Chemical Society Reviews* **2003**, *32*, 276.

(4) Rowsell, J. L. C.; Yaghi, O. M. *Microporous and Mesoporous Materials* **2004**, *73*, 3.

(5) Long, J. R.; Yaghi, O. M. *Chemical Society Reviews* **2009**, *38*, 1213.

(6) Zhou, H. C.; Long, J. R.; Yaghi, O. M. *Chemical Reviews* **2012**, *112*, 673.

(7) Furukawa, H.; Cordova, K. E.; O'Keeffe, M.; Yaghi, O. M. *Science* **2013**, *341*, 1230444.

(8) Eddaoudi, M.; Moler, D. B.; Li, H.; Chen, B.; Reineke, T. M.; O'Keeffe, M.; Yaghi, O. M. *Accounts of Chemical Research* **2001**, *34*, 319.

(9) Yaghi, O. M.; O'Keeffe, M.; Ockwig, N. W.; Chae, H. K.; Eddaoudi, M.; Kim, J. *Nature* **2003**, *423*, 705.

(10) Ockwig, N. W.; Delgado-Friedrichs, O.; O'Keeffe, M.; Yaghi, O. M. *Accounts of Chemical Research* **2005**, *38*, 176.

(11) O'Keeffe, M.; Peskov, M. A.; Ramsden, S. J.; Yaghi, O. M. *Accounts of Chemical Research* **2008**, *41*, 1782.

(12) O'Keeffe, M. *APL Mater.* **2014**, *2*, 124106.

(13) Delgado-Friedrichs, O.; O'Keeffe, M.; Yaghi, O. M. *Physical Chemistry Chemical Physics* **2007**, *9*, 1035.

(14) Tranchemontagne, D. J.; Mendoza-Cortes, J. L.; O'Keeffe, M.; Yaghi, O. M. *Chemical Society Reviews* **2009**, *38*, 1257.

(15) O'Keeffe, M.; Yaghi, O. M. *Chemical Reviews* **2012**, *112*, 675.

(16) Li, M.; Li, D.; O'Keeffe, M.; Yaghi, O. M. *Chemical Reviews* **2014**, *114*, 1343.

(17) Jiang, H.-L.; Xu, Q. *Chemical Communications* **2011**, *47*, 3351.

(18) Mueller, U.; Schubert, M.; Teich, F.; Puetter, H.; Schierle-Arndt, K.; Pastre, J. *Journal of Materials Chemistry* **2006**, *16*, 626.

(19) Kuppler, R. J.; Timmons, D. J.; Fang, Q.-R.; Li, J.-R.; Makal, T. A.; Young, M. D.; Yuan, D.; Zhao, D.; Zhuang, W.; Zhou, H.-C. *Coordination Chemistry Reviews* **2009**, *253*, 3042.

(20) Han, Y.; Li, J. R.; Xie, Y.; Guo, G. *Chemical Society Reviews* **2014**, *43*, 5952.

(21) Evans, J. D.; Sumby, C. J.; Doonan, C. J. *Chemical Society Reviews* **2014**, *43*, 5933.

(22) Deria, P.; Mondloch, J. E.; Karagiaridi, O.; Bury, W.; Hupp, J. T.; Farha, O. K. *Chemical Society Reviews* **2014**, *43*, 5896.

(23) Karagiaridi, O.; Bury, W.; Mondloch, J. E.; Hupp, J. T.; Farha, O. K. *Angewandte Chemie International Edition* **2014**, *53*, 4530.

(24) Wang, Z.; Cohen, S. M. *Chemical Society Reviews* **2009**, *38*, 1315.

(25) Tanabe, K. K.; Cohen, S. M. *Chemical Society Reviews* **2011**, *40*, 498.

(26) Cohen, S. M. *Chemical Reviews* **2012**, *112*, 970.

(27) Stock, N.; Biswas, S. *Chemical Reviews* **2012**, *112*, 933.

(28) Eddaoudi, M.; Kim, J.; Rosi, N.; Vodak, D.; Wachter, J.; O'Keeffe, M.; Yaghi, O. M. *Science* **2002**, *295*, 469.

(29) Deng, H.; Doonan, C. J.; Furukawa, H.; Ferreira, R. B.; Towne, J.; Knobler, C. B.; Wang, B.; Yaghi, O. M. *Science* **2010**, *327*, 846.

(30) Wang, L. J.; Deng, H.; Furukawa, H.; Gándara, F.; Cordova, K. E.; Peri, D.; Yaghi, O. M. *Inorganic Chemistry* **2014**, *53*, 5881.

(31) Burrows, A. D.; Frost, C. G.; Mahon, M. F.; Richardson, C. *Chemical Communications* **2009**, 4218.

(32) Ahnfeldt, T.; Gunzelmann, D.; Loiseau, T.; Hirsemann, D.; Senker, J.; Férey, G.; Stock, N. *Inorganic Chemistry* **2009**, *48*, 3057.

(33) Marshall, R. J.; Griffin, S. L.; Wilson, C.; Forgan, R. S. *Journal of the American Chemical Society* **2015**, *137*, 9527.

(34) Deshpande, R. K.; Minnaar, J. L.; Telfer, S. G. *Angewandte Chemie International Edition* **2010**, *49*, 4598.

(35) Savonnet, M.; Bazer-Bachi, D.; Bats, N.; Perez-Pellitero, J.; Jeanneau, E.; Lecocq, V.; Pinel, C.; Farrusseng, D. *Journal of the American Chemical Society* **2010**, *132*, 4518.

(36) Savonnet, M.; Aguado, S.; Ravon, U.; Bazer-Bachi, D.; Lecocq, V.; Bats, N.; Pinel, C.; Farrusseng, D. *Green Chemistry* **2009**, *11*, 1729.

(37) Sletten, E. M.; Bertozzi, C. R. *Angewandte Chemie International Edition* **2009**, *48*, 6974.

(38) Rostovtsev, V. V.; Green, L. G.; Fokin, V. V.; Sharpless, K. B. *Angewandte Chemie* **2002**, *114*, 2708.

(39) Tornøe, C. W.; Christensen, C.; Meldal, M. *The Journal of Organic Chemistry* **2002**, *67*, 3057.

(40) Moses, J. E.; Moorhouse, A. D. *Chemical Society Reviews* **2007**, *36*, 1249.

(41) Wong, C. H.; Zimmerman, S. C. *Chemical Communications* **2013**, *49*, 1679.

(42) Goto, Y.; Sato, H.; Shinkai, S.; Sada, K. *Journal of the American Chemical Society* **2008**, *130*, 14354.

(43) Gadzikwa, T.; Lu, G.; Stern, C. L.; Wilson, S. R.; Hupp, J. T.; Nguyen, S. T. *Chemical Communications* **2008**, 5493.

(44) Chen, C.; Allen, C. A.; Cohen, S. M. *Inorganic chemistry* **2011**, *50*, 10534.

(45) Roy, P.; Schaate, A.; Behrens, P.; Godt, A. *Chemistry – A European Journal* **2012**, *18*, 6979.

(46) Wang, Z.; Liu, J.; Arslan, H. K.; Grosjean, S.; Hagendorn, T.; Gliemann, H.; Bräse, S.; Wöll, C. *Langmuir* **2013**, *29*, 15958.

(47) Kim, M.; Cahill, J. F.; Su, Y.; Prather, K. A.; Cohen, S. M. *Chemical Science* **2012**, *3*, 126.

(48) Fei, H.; Cohen, S. M. *Journal of the American Chemical Society* **2015**, *137*, 2191.

(49) Kim, S.; Dawson, K. W.; Gelfand, B. S.; Taylor, J. M.; Shimizu, G. K. H. *Journal of the American Chemical Society* **2013**, *135*, 963.

(50) Park, J.; Feng, D.; Zhou, H. C. *Journal of the American Chemical Society* **2015**, *137*, 1663.

(51) Deng, H.; Grunder, S.; Cordova, K. E.; Valente, C.; Furukawa, H.; Hmadeh, M.; Gándara, F.; Whalley, A. C.; Liu, Z.; Asahina, S.; Kazumori, H.; O'Keeffe, M.; Terasaki, O.; Stoddart, J. F.; Yaghi, O. M. *Science* **2012**, *336*, 1018.

(52) Burnett, B. J.; Barron, P. M.; Hu, C.; Choe, W. *Journal of the American Chemical Society* **2011**, *133*, 9984.

(53) Karagiaridi, O.; Bury, W.; Tylianakis, E.; Sarjeant, A. A.; Hupp, J. T.; Farha, O. K. *Chemistry of Materials* **2013**, *25*, 3499.

(54) Li, T.; Kozlowski, M. T.; Doud, E. A.; Blakely, M. N.; Rosi, N. L. *Journal of the American Chemical Society* **2013**, *135*, 11688.

(55) Chui, S. S.-Y.; Lo, S. M.-F.; Charmant, J. P. H.; Orpen, A. G.; Williams, I. D. *Science* **1999**, *283*, 1148.

(56) Mondloch, J. E.; Bury, W.; Fairen-Jimenez, D.; Kwon, S.; DeMarco, E. J.; Weston, M. H.; Sarjeant, A. A.; Nguyen, S. T.; Stair, P. C.; Snurr, R. Q.; Farha, O. K.; Hupp, J. T. *Journal of the American Chemical Society* **2013**, *135*, 10294.

(57) Deria, P.; Mondloch, J. E.; Tylianakis, E.; Ghosh, P.; Bury, W.; Snurr, R. Q.; Hupp, J. T.; Farha, O. K. *Journal of the American Chemical Society* **2013**, *135*, 16801.

(58) Wu, C.-D.; Hu, A.; Zhang, L.; Lin, W. *Journal of the American Chemical Society* **2005**, *127*, 8940.

(59) Bloch, E. D.; Britt, D.; Lee, C.; Doonan, C. J.; Uribe-Romo, F. J.; Furukawa, H.; Long, J. R.; Yaghi, O. M. *Journal of the American Chemical Society* **2010**, *132*, 14382.

(60) Zhang, Z.; Gao, W.-Y.; Wojtas, L.; Ma, S.; Eddaoudi, M.; Zaworotko, M. J. *Angewandte Chemie International Edition* **2012**, *51*, 9330.

(61) Yuan, S.; Chen, Y.-P.; Qin, J.; Lu, W.; Wang, X.; Zhang, Q.; Bosch, M.; Liu, T.-F.; Lian, X.; Zhou, H.-C. *Angewandte Chemie International Edition* **2015**, *54*, 14696.

(62) Ma, L.; Abney, C.; Lin, W. *Chemical Society Reviews* **2009**, *38*, 1248.

(63) Wang, J.-L.; Wang, C.; Lin, W. *ACS Catalysis* **2012**, *2*, 2630.

(64) Nguyen, H. G. T.; Schweitzer, N. M.; Chang, C.-Y.; Drake, T. L.; So, M. C.; Stair, P. C.; Farha, O. K.; Hupp, J. T.; Nguyen, S. T. *ACS Catalysis* **2014**, *4*, 2496.

(65) Yang, D.; Odoh, S. O.; Wang, T. C.; Farha, O. K.; Hupp, J. T.; Cramer, C. J.; Gagliardi, L.; Gates, B. C. *Journal of the American Chemical Society* **2015**, *137*, 7391.

(66) Bloch, W. M.; Champness, N. R.; Doonan, C. J. *Angewandte Chemie International Edition* **2015**, *54*, 12860.

(67) Inokuma, Y.; Yoshioka, S.; Ariyoshi, J.; Arai, T.; Hitora, Y.; Takada, K.; Matsunaga, S.; Rissanen, K.; Fujita, M. *Nature* **2013**, *495*, 461.

(68) Inokuma, Y.; Yoshioka, S.; Ariyoshi, J.; Arai, T.; Fujita, M. *Nature Protocols* **2014**, *9*, 246.

(69) Ramadhar, T. R.; Zheng, S. L.; Chen, Y. S.; Clardy, J. *Acta Crystallographica Section A* **2015**, *71*, 46.

(70) Sanna, E.; Escudero-Adán, E. C.; Bauzá, A.; Ballester, P.; Frontera, A.; Rotger, C.; Costa, A. *Chemical Science* **2015**, *6*, 5466.

(71) Zhang, S. Y.; Wojtas, L.; Zaworotko, M. J. *Journal of the American Chemical Society* **2015**, *137*, 12045.

(72) Zhu, Q. L.; Li, J.; Xu, Q. *Journal of the American Chemical Society* **2013**, *135*, 10210.

(73) Volosskiy, B.; Niwa, K.; Chen, Y.; Zhao, Z.; Weiss, N. O.; Zhong, X.; Ding, M.; Lee, C.; Huang, Y.; Duan, X. *ACS Nano* **2015**, *9*, 3044.

(74) Custelcean, R.; Moyer, B. A. *European Journal of Inorganic Chemistry* **2007**, *2007*, 1321.

(75) Hoskins, B. F.; Robson, R. *Journal of the American Chemical Society* **1990**, *112*, 1546.

(76) Liu, Y.; Li, G.; Li, X.; Cui, Y. *Angewandte Chemie* **2007**, *119*, 6417.

(77) An, J.; Geib, S. J.; Rosi, N. L. *Journal of the American Chemical Society* **2009**, *131*, 8376.

(78) An, J.; Rosi, N. L. *Journal of the American Chemical Society* **2010**, *132*, 5578.

(79) Zhao, X.; Bu, X.; Wu, T.; Zheng, S.-T.; Wang, L.; Feng, P. *Nature Communications* **2013**, *4*, 2344

(80) Yu, J.; Cui, Y.; Xu, H.; Yang, Y.; Wang, Z.; Chen, B.; Qian, G. *Nature Communications* **2013**, *4*, 2719

(81) Nouar, F.; Eckert, J.; Eubank, J. F.; Forster, P.; Eddaoudi, M. *Journal of the American Chemical Society* **2009**, *131*, 2864.

(82) Genna, D. T.; Wong-Foy, A. G.; Matzger, A. J.; Sanford, M. S. *Journal of the American Chemical Society* **2013**, *135*, 10586.

(83) Lu, W.-G.; Jiang, L.; Feng, X.-L.; Lu, T.-B. *Inorganic Chemistry* **2009**, *48*, 6997.

(84) Liu, C.; Li, T.; Rosi, N. L. *Journal of the American Chemical Society* **2012**, *134*, 18886.

(85) Valtchev, V.; Majano, G.; Mintova, S.; Perez-Ramirez, J. *Chemical Society Reviews* **2013**, *42*, 263.

(86) Zhang, Z.; Yao, Z.-Z.; Xiang, S.; Chen, B. *Energy & Environmental Science* **2014**, *7*, 2868.

(87) Fang, Q.-R.; Makal, T. A.; Young, M. D.; Zhou, H.-C. *Comments on Inorganic Chemistry* **2010**, *31*, 165.

(88) Song, L.; Zhang, J.; Sun, L.; Xu, F.; Li, F.; Zhang, H.; Si, X.; Jiao, C.; Li, Z.; Liu, S.; Liu, Y.; Zhou, H.; Sun, D.; Du, Y.; Cao, Z.; Gabelica, Z. *Energy & Environmental Science* **2012**, *5*, 7508.

(89) Xuan, W.; Zhu, C.; Liu, Y.; Cui, Y.*Chemical Society Reviews* **2012**, *41*, 1677.

(90) Wang, Z. C., Seth M. *Journal of the American Chemical Society* **2007**, *129*, 12368.

(91) Ingleson, M. J.; Barrio, J. P.; Guilbaud, J. B.; Khimyak, Y. Z.; Rosseinsky, M. J. *Chemical Communications* **2008**, 2680.

(92) Morris, W.; Doonan, C. J.; Furukawa, H.; Banerjee, R.; Yaghi, O. M. *Journal of the American Chemical Society* **2008**, *130*, 12626.

(93) Deshpande, R. K.; Waterhouse, G. I.; Jameson, G. B.; Telfer, S. G. *Chemical Communications* **2012**, *48*, 1574.

(94) Tanabe, K. K.; Allen, C. A.; Cohen, S. M. *Angewandte Chemie International Edition* **2010**, *49*, 9730.

(95) Jewett, J. C.; Bertozzi, C. R. *Chemical Society Reviews* **2010**, *39*, 1272.

(96) Sletten, E. M.; Bertozzi, C. R. *Accounts of Chemical Research* **2011**, *44*, 666.

(97) Agard, N. J.; Prescher, J. A.; Bertozzi, C. R. *Journal of the American Chemical Society* **2004**, *126*, 15046.

(98) Baskin, J. M.; Prescher, J. A.; Laughlin, S. T.; Agard, N. J.; Chang, P. V.; Miller, I. A.; Lo, A.; Codelli, J. A.; Bertozzi, C. R. *Proceedings of the National Academy of Sciences* **2007**, *104*, 16793.

(99) Codelli, J. A.; Baskin, J. M.; Agard, N. J.; Bertozzi, C. R. *Journal of the American Chemical Society* **2008**, *130*, 11486.

(100) Sletten, E. M.; Bertozzi, C. R. *Organic letters* **2008**, *10*, 3097.

(101) Ning, X.; Guo, J.; Wolfert, M. A.; Boons, G. J. *Angewandte Chemie International Edition* **2008**, *47*, 2253.

(102) Jewett, J. C.; Sletten, E. M.; Bertozzi, C. R. *Journal of the American Chemical Society* **2010**, *132*, 3688.

(103) Debets, M. F.; van Berkel, S. S.; Schoffelen, S.; Rutjes, F. P. J. T.; van Hest, J. C. M.; van Delft, F. L. *Chemical Communications* **2010**, *46*, 97.

(104) Wittig, G.; Krebs, A. *Chemische Berichte* **1961**, *94*, 3260.

(105) Laughlin, S. T.; Baskin, J. M.; Amacher, S. L.; Bertozzi, C. R. *Science* **2008**, *320*, 664.

(106) Chang, P. V.; Prescher, J. A.; Sletten, E. M.; Baskin, J. M.; Miller, I. A.; Agard, N. J.; Lo, A.; Bertozzi, C. R. *Proceedings of the National Academy of Sciences* **2010**, *107*, 1821.

(107) Imaz, I.; Rubio-Martínez, M.; An, J.; Solé-Font, I.; Rosi, N. L.; Maspoch, D. *Chemical Communications* **2011**, *47*, 7287.

(108) An, J.; Farha, O. K.; Hupp, J. T.; Pohl, E.; Yeh, J. I.; Rosi, N. L. *Nature Communications* **2012**, *3*, 604.

(109) Delgado Friedrichs, O.; O'Keeffe, M.; Yaghi, O. M. *Acta Crystallographica Section A* **2003**, *59*, 515.

(110) Gordon, C. G.; Mackey, J. L.; Jewett, J. C.; Sletten, E. M.; Houk, K. N.; Bertozzi, C. R. *Journal of the American Chemical Society* **2012**, *134*, 9199.

(111) Campbell‐Verduyn, L. S.; Mirfeizi, L.; Schoonen, A. K.; Dierckx, R. A.; Elsinga, P. H.; Feringa, B. L. *Angewandte Chemie International Edition* **2011**, *50*, 11117.

(112) Cho, H.; Iwama, Y.; Sugimoto, K.; Mori, S.; Tokuyama, H. *The Journal of Organic Chemistry* **2010**, *75*, 627.

(113) Olkhovik, V. K.; Vasilevskii, D. A.; Pap, A. A.; Kalechyts, G. V.; Matveienko, Y. V.; Baran, A. G.; Halinouski, N. A.; Petushok, V. G. *ARKIVOC* **2008**, 69.

(114) Ol'khovik, V. K.; Pap, A. A.; Vasilevskii, V. A.; Galinovskii, N. A.; Tereshko, S. N. *Russian Journal of Organic Chemistry* **2008**, *44*, 1172.

(115) Sato, H.; Matsuda, R.; Sugimoto, K.; Takata, M.; Kitagawa, S. *Nature Materials* **2010**, *9*, 661.

(116) Liu, C.; Luo, T. Y.; Feura, E. S.; Zhang, C.; Rosi, N. L. *Journal of the American Chemical Society* **2015**, *137*, 10508.

(117) Burrows, A. D. *CrystEngComm* **2011**, *13*, 3623.

(118) Kim, M.; Cahill, J. F.; Prather, K. A.; Cohen, S. M. *Chemical Communications* **2011**, *47*, 7629.

(119) Li, B.; Zhang, Y.; Ma, D.; Li, L.; Li, G.; Li, G.; Shi, Z.; Feng, S. *Chemical Communications* **2012**, *48*, 6151.

(120) Dau, P. V.; Cohen, S. M. *Inorganic Chemistry* **2015**, *54*, 3134.

(121) Li, B.; Chrzanowski, M.; Zhang, Y.; Ma, S. *Coordination Chemistry Reviews* **2016**, *307, Part 2*, 106.

(122) Furukawa, H.; Muller, U.; Yaghi, O. M. *Angewandte Chemie International Edition* **2015**, *54*, 3417.

(123) Furukawa, S.; Hirai, K.; Takashima, Y.; Nakagawa, K.; Kondo, M.; Tsuruoka, T.; Sakata, O.; Kitagawa, S. *Chemical Communications* **2009**, 5097.

(124) Kong, X.; Deng, H.; Yan, F.; Kim, J.; Swisher, J. A.; Smit, B.; Yaghi, O. M.; Reimer, J. A. *Science* **2013**, *341*, 882.

(125) Katzenmeyer, A. M.; Canivet, J.; Holland, G.; Farrusseng, D.; Centrone, A. *Angewandte Chemie International Edition* **2014**, *53*, 2852.

(126) Krajnc, A.; Kos, T.; Zabukovec Logar, N.; Mali, G. *Angewandte Chemie International Edition* **2015**, *54*, 10535.

(127) Förster, T. *Annalen der Physik* **1948**, *437*, 55.

(128) Burrows, A. D.; Frost, C. G.; Mahon, M. F.; Richardson, C. *Angewandte Chemie International Edition* **2008**, *47*, 8482.

(129) Betard, A.; Fischer, R. A. *Chemical Reviews* **2012**, *112*, 1055.

(130) Choi, K. M.; Jeon, H. J.; Kang, J. K.; Yaghi, O. M. *Journal of the American Chemical Society* **2011**, *133*, 11920.

(131) Hong, D. H.; Suh, M. P. *Chemistry – A European Journal* **2014**, *20*, 426.

(132) DeCoste, J. B.; Rossin, J. A.; Peterson, G. W. *Chemistry – A European Journal* **2015**, *21*, 18029.

(133) McGuire, C. V.; Forgan, R. S. *Chemical Communications* **2015**, *51*, 5199.

(134) Koh, K.; Wong-Foy, A. G.; Matzger, A. J. *Chemical Communications* **2009**, 6162.

(135) Furukawa, S.; Hirai, K.; Nakagawa, K.; Takashima, Y.; Matsuda, R.; Tsuruoka, T.; Kondo, M.; Haruki, R.; Tanaka, D.; Sakamoto, H.; Shimomura, S.; Sakata, O.; Kitagawa, S. *Angewandte Chemie International Edition* **2009**, *48*, 1766.

(136) Yoo, Y.; Jeong, H.-K. *Crystal Growth & Design* **2010**, *10*, 1283.

(137) Liu, B.; Tu, M.; Zacher, D.; Fischer, R. A. *Advanced Functional Materials* **2013**, *23*, 3790.

(138) Meilikhov, M.; Furukawa, S.; Hirai, K.; Fischer, R. A.; Kitagawa, S. *Angewandte Chemie International Edition* **2013**, *52*, 341.

(139) Heinke, L.; Cakici, M.; Dommaschk, M.; Grosjean, S.; Herges, R.; Bräse, S.; Wöll, C. *ACS Nano* **2014**, *8*, 1463.

(140) Zhuang, J.; Chou, L. Y.; Sneed, B. T.; Cao, Y.; Hu, P.; Feng, L.; Tsung, C. K. *Small* **2015**, *11*, 5551.

(141) Zhang, J.-P.; Liao, P.-Q.; Zhou, H.-L.; Lin, R.-B.; Chen, X.-M. *Chemical Society Reviews* **2014**, *43*, 5789.

(142) Jin, R. *Nanoscale* **2010**, *2*, 343.

(143) Qian, H.; Zhu, M.; Wu, Z.; Jin, R. *Accounts of Chemical Research* **2012**, *45*, 1470.

(144) Das, A.; Liu, C.; Byun, H. Y.; Nobusada, K.; Zhao, S.; Rosi, N.; Jin, R. *Angewandte Chemie International Edition* **2015**, *54*, 3140.

(145) Zeng, C.; Liu, C.; Chen, Y.; Rosi, N. L.; Jin, R. *Journal of the American Chemical Society* **2014**, *136*, 11922.

(146) Chen, Y.; Liu, C.; Tang, Q.; Zeng, C.; Higaki, T.; Das, A.; Jiang, D.-e.; Rosi, N. L.; Jin, R.*Journal of the American Chemical Society* **2016**, *138*, 1482.

(147) Higaki, T.; Liu, C.; Zeng, C.; Jin, R.; Chen, Y.; Rosi, N. L.; Jin, R. *Angewandte Chemie International Edition* **2016**, *55*, 6694.

(148) Das, A.; Liu, C.; Zeng, C.; Li, G.; Li, T.; Rosi, N. L.; Jin, R. *The Journal of Physical Chemistry A* **2014**, *118*, 8264.

(149) Zeng, C.; Chen, Y.; Liu, C.; Nobusada, K.; Rosi, N. L.; Jin, R. *Science Advances* **2015**, *1*, e1500425.

(150) Jadzinsky, P. D.; Calero, G.; Ackerson, C. J.; Bushnell, D. A.; Kornberg, R. D. *Science* **2007**, *318*, 430.

(151) Chen, Y.; Zeng, C.; Liu, C.; Kirschbaum, K.; Gayathri, C.; Gil, R. R.; Rosi, N. L.; Jin, R. *Journal of the American Chemical Society* **2015**, *137*, 10076.

(152) Zeng, C.; Chen, Y.; Kirschbaum, K.; Appavoo, K.; Sfeir, M. Y.; Jin, R. *Science Advances* **2015**, *1*, e1500045.

(153) Dass, A.; Theivendran, S.; Nimmala, P. R.; Kumara, C.; Jupally, V. R.; Fortunelli, A.; Sementa, L.; Barcaro, G.; Zuo, X.; Noll, B. C. *Journal of the American Chemical Society* **2015**, *137*, 4610.

(154) Zhu, M.; Aikens, C. M.; Hollander, F. J.; Schatz, G. C.; Jin, R. *Journal of the American Chemical Society* **2008**, *130*, 5883.

(155) Heaven, M. W.; Dass, A.; White, P. S.; Holt, K. M.; Murray, R. W. *Journal of the American Chemical Society* **2008**, *130*, 3754.

(156) Zhu, M.; Aikens, C. M.; Hendrich, M. P.; Gupta, R.; Qian, H.; Schatz, G. C.; Jin, R. *Journal of the American Chemical Society* **2009**, *131*, 2490.

(157) Liu, Z.; Zhu, M.; Meng, X.; Xu, G.; Jin, R. *The Journal of Physical Chemistry Letters* **2011**, *2*, 2104.

(158) Venzo, A.; Antonello, S.; Gascon, J. A.; Guryanov, I.; Leapman, R. D.; Perera, N. V.; Sousa, A.; Zamuner, M.; Zanella, A.; Maran, F. *Analytical Chemistry* **2011**, *83*, 6355.

(159) Tofanelli, M. A.; Salorinne, K.; Ni, T. W.; Malola, S.; Newell, B.; Phillips, B.; Häkkinen, H.; Ackerson, C. J. *Chemical Science* **2016**, *7*, 1882.

(160) Wu, Z.; Suhan, J.; Jin, R. *Journal of Materials Chemistry* **2009**, *19*, 622.

(161) Binnemans, K. *Chemical Reviews* **2009**, *109*, 4283.

(162) Bünzli, J.-C. G. *Chemical Reviews* **2010**, *110*, 2729.

(163) Eliseeva, S. V.; Bunzli, J.-C. G. *Chemical Society Reviews* **2010**, *39*, 189.

(164) Petoud, S.; Cohen, S. M.; Bünzli, J.-C. G.; Raymond, K. N. *Journal of the American Chemical Society* **2003**, *125*, 13324.

(165) Zhang, J.; Badger, P. D.; Geib, S. J.; Petoud, S. *Angewandte Chemie International Edition* **2005**, *44*, 2508.

(166) Mahmood, U.; Weissleder, R. *Molecular Cancer Therapeutics* **2003**, *2*, 489.

(167) Lim, Y. T.; Kim, S.; Nakayama, A.; Stott, N. E.; Bawendi, M. G.; Frangioni, J. V. *Molecular Imaging* **2003**, *2*, 50.

(168) Frangioni, J. V. *Current Opinion in Chemical Biology* **2003**, *7*, 626.

(169) Foucault-Collet, A.; Gogick, K. A.; White, K. A.; Villette, S.; Pallier, A.; Collet, G.; Kieda, C.; Li, T.; Geib, S. J.; Rosi, N. L.; Petoud, S. *Proceedings of the National Academy of Sciences* **2013**, *110*, 17199.

(170) Weissman, S. I. *The Journal of Chemical Physics* **1942**, *10*, 214.

(171) Allendorf, M. D.; Bauer, C. A.; Bhakta, R. K.; Houk, R. J. T. *Chemical Society Reviews* **2009**, *38*, 1330.

(172) Rocha, J.; Carlos, L. D.; Paz, F. A. A.; Ananias, D. *Chemical Society Reviews* **2011**, *40*, 926.

(173) Cui, Y.; Yue, Y.; Qian, G.; Chen, B. *Chemical Reviews* **2012**, *112*, 1126.

(174) Cui, Y.; Chen, B.; Qian, G. *Coordination Chemistry Reviews* **2014**, *273–274*, 76.

(175) Chen, B.; Yang, Y.; Zapata, F.; Qian, G.; Luo, Y.; Zhang, J.; Lobkovsky, E. B. *Inorganic Chemistry* **2006**, *45*, 8882.

(176) White, K. A.; Chengelis, D. A.; Zeller, M.; Geib, S. J.; Szakos, J.; Petoud, S.; Rosi, N. L. *Chemical Communications* **2009**, 4506.

(177) White, K. A.; Chengelis, D. A.; Gogick, K. A.; Stehman, J.; Rosi, N. L.; Petoud, S. *Journal of the American Chemical Society* **2009**, *131*, 18069.

(178) Xu, H.; Li, Y. *Journal of Molecular Structure* **2004**, *690*, 137.

(179) Xue, D. X.; Cairns, A. J.; Belmabkhout, Y.; Wojtas, L.; Liu, Y.; Alkordi, M. H.; Eddaoudi, M. *Journal of the American Chemical Society* **2013**, *135*, 7660.

(180) Guillerm, V.; Weselinski, L.; Belmabkhout, Y.; Cairns, A. J.; D'Elia, V.; Wojtas, L.; Adil, K.; Eddaoudi, M. *Nature Chemistry* **2014**, *6*, 673.

(181) Assen, A. H.; Belmabkhout, Y.; Adil, K.; Bhatt, P. M.; Xue, D. X.; Jiang, H.; Eddaoudi, M. *Angewandte Chemie International Edition* **2015**, *54*, 14353.

(182) Luebke, R.; Belmabkhout, Y.; Weseliński, Ł. J.; Cairns, A. J.; Alkordi, M.; Norton, G.; Wojtas, Ł.; Adil, K.; Eddaoudi, M. *Chemical Science* **2015**, *6*, 4095.

(183) Alezi, D.; Peedikakkal, A. M.; Weselinski, L. J.; Guillerm, V.; Belmabkhout, Y.; Cairns, A. J.; Chen, Z.; Wojtas, L.; Eddaoudi, M. *Journal of the American Chemical Society* **2015**, *137*, 5421.

(184) Cavka, J. H.; Jakobsen, S.; Olsbye, U.; Guillou, N.; Lamberti, C.; Bordiga, S.; Lillerud, K. P. *Journal of the American Chemical Society* **2008**, *130*, 13850.

(185) Jakobsen, S.; Gianolio, D.; Wragg, D. S.; Nilsen, M. H.; Emerich, H.; Bordiga, S.; Lamberti, C.; Olsbye, U.; Tilset, M.; Lillerud, K. P. *Physical Review B* **2012**, *86*, 125429.

(186) Kandiah, M.; Nilsen, M. H.; Usseglio, S.; Jakobsen, S.; Olsbye, U.; Tilset, M.; Larabi, C.; Quadrelli, E. A.; Bonino, F.; Lillerud, K. P. *Chemistry of Materials* **2010**, *22*, 6632.

(187) Schaate, A.; Roy, P.; Godt, A.; Lippke, J.; Waltz, F.; Wiebcke, M.; Behrens, P. *Chemistry – A European Journal* **2011**, *17*, 6643.

(188) Wang, C.; Xie, Z.; deKrafft, K. E.; Lin, W. *Journal of the American Chemical Society* **2011**, *133*, 13445.

(189) Kim, M.; Cahill, J. F.; Fei, H.; Prather, K. A.; Cohen, S. M. *Journal of the American Chemical Society* **2012**, *134*, 18082.

(190) Liu, X.; Demir, N. K.; Wu, Z.; Li, K. *Journal of the American Chemical Society* **2015**, *137*, 6999.

(191) Zhang, Z.-M.; Zhang, T.; Wang, C.; Lin, Z.; Long, L.-S.; Lin, W. *Journal of the American Chemical Society* **2015**, *137*, 3197.

(192) Dang, S.; Zhang, J.-H.; Sun, Z.-M. *Journal of Materials Chemistry* **2012**, *22*, 8868.

(193) Rao, X.; Song, T.; Gao, J.; Cui, Y.; Yang, Y.; Wu, C.; Chen, B.; Qian, G. *Journal of the American Chemical Society* **2013**, *135*, 15559.

(194) Feng, X.; Wang, L.-Y.; Wang, J.-G.; Xie, C.-Z.; Zhao, J.-S.; Sun, Q. *CrystEngComm* **2010**, *12*, 3476.

(195) Fernández, B.; Oyarzabal, I.; Seco, J. M.; Sebastián, E. S.; Fairen-Jiménez, D.; Gómez-Ruiz, S.; Salinas-Castillo, A.; Calahorro, A. J.; Rodríguez-Diéguez, A. *Polymers* **2016**, *8*, 39.

(196) Shakhverdov, T. A.; Shakhverdov, P. A.; Sveshnikova, E. B. In *Photonics West'95*; International Society for Optics and Photonics: **1995**, p 280.

(197) Spek, A. *Acta Crystallographica Section A* **1990**, *46*, c34.

(198) Frey, S. T.; Chang, C. A.; Carvalho, J. F.; Varadarajan, A.; Schultze, L. M.; Pounds, K. L.; Horrocks, W. D. *Inorganic Chemistry* **1994**, *33*, 2882.

(199) Ferreira, R. A. S.; André, P. S.; Carlos, L. D. *Optical Materials* **2010**, *32*, 1397.

(200) Thibon, A.; Pierre, V. C. *Analytical & Bioanalytical Chemistry* **2009**, *394*, 107.

(201) SHELXTL (XCIF, XL, XP, XPREP, XS), 6.10 ed.; Bruker AXS Inc.: Madison WI, USA, **2002**.

(202) APEX2, SAINT, and SADABS ed.; Bruker AXS Inc.: Madison WI, USA, **2014**.

(203) Sheldrick, G. *Acta Crystallographica Section A* **2008**, *64*, 112.

(204) Sheldrick, G. *Acta Crystallographica Section C* **2015**, *71*, 3.

(205) Dolomanov, O. V.; Bourhis, L. J.; Gildea, R. J.; Howard, J. A. K.; Puschmann, H. *Journal of Applied Crystallography* **2009**, *42*, 339.

(206) Bon, V.; Senkovska, I.; Weiss, M. S.; Kaskel, S. *CrystEngComm* **2013**, *15*, 9572.

(207) Sheldrick, G. *Acta Crystallographica Section A* **2015**, *71*, 3.